University of Liège
Faculty of Science
Department of Chemistry

Advancing the Analysis of Halogenated Contaminants Using a GC-APCI-TIMS-TOFMS Platform: Development and Optimization for Targeted and Non-Targeted Approaches

---

Doctoral thesis submitted for the fulfilment of the degree of
Doctor of Philosophy in Sciences

Hugo MULLER

Under the supervision of Prof. Gauthier Eppe

Academic year 2024-2025

Jury

Supervisor	Prof. Gauthier EPPE	University of Liège, Belgium
President	Prof. Bernard Leyh	University of Liège, Belgium
Secretary	Dr. Johann Far	University of Liège, Belgium
Member	Prof. Emma Schymanski	University of Luxembourg, Luxembourg
Member	Prof. Tim Causon	University of Boku, Austria
Member	Prof. Adrian Covaci	University of Antwerp, Belgium
Member	Prof. Jean-François Focant	University of Liège, Belgium

Abstract

Environmental contamination by chemical pollutants, particularly halogenated persistent organic pollutants (POPs), remains a major concern due to their toxicity and persistence. Traditional analytical methods, such as gas chromatography-mass spectrometry (GC-MS), have been widely used for detecting and quantifying these contaminants. However, ion mobility spectrometry (IM) has emerged as a powerful complementary technique, offering enhanced separation and greater confidence in analyte identification.

This thesis focuses on developing and optimizing a gas chromatography-atmospheric pressure chemical ionization-trapped ion mobility spectrometry-time-of-flight mass spectrometry (GC-APCI-TIMS-TOFMS) system for the analysis of halogenated contaminants. The feasibility of this system is evaluated for both targeted and untargeted analyses in complex food and biological matrices.

The first and second part of the thesis details the development and optimization of the GC-APCI-TIMS-TOFMS system, including the determination of collision cross sections (CCS) for halogenated POPs, critical instrument parameter optimization, and assessment of ion mobility separation for isomeric and isobaric species. The third part evaluates the quantitative performance of the system, assessing linearity, limits of quantification (LOQs), precision, accuracy and uncertainty. The benefits of ion mobility, such as enhanced selectivity and the use of CCS for analyte confirmation, are also explored. The fourth part applies the developed method to the non-targeted analysis of halogenated compounds in a stranded killer whale, demonstrating the potential of ion mobility-mass spectrometry for pollutant characterization.

The thesis concludes with a discussion on the broader implications of these findings, emphasizing the role of ion mobility-mass spectrometry in advancing regulatory contaminant analysis and environmental monitoring.

Résumé

La contamination de l'environnement par les polluants chimiques, en particulier les polluants organiques persistants (POP) halogénés, reste une préoccupation majeure en raison de leur toxicité et de leur persistance. Les méthodes analytiques traditionnelles, telles que la chromatographie en phase gazeuse et la spectrométrie de masse (GC-MS), ont été largement utilisées pour détecter et quantifier ces contaminants. Cependant, la spectrométrie de mobilité ionique (IM) s'est imposée comme une technique complémentaire puissante, offrant une séparation améliorée, une meilleure spécificité et une plus grande confiance dans l'identification de l'analyte.

Cette thèse se concentre sur le développement et l'optimisation d'un système de « chromatographie en phase gazeuse - ionisation chimique à pression atmosphérique - spectrométrie de mobilité ionique piégée - spectrométrie de masse à temps de vol » (GC-APCI-TIMS-TOFMS) pour l'analyse des contaminants halogénés. La faisabilité de ce système est évaluée pour des analyses ciblées et non ciblées dans des matrices alimentaires et biologiques complexes.

Les deux premières parties de la thèse détaille le développement et l'optimisation du système GC-APCI-TIMS-TOFMS, y compris la détermination des sections transversales de collision (CCS) pour les POP halogénés et l'optimisation des paramètres critiques de l'instrument. La troisième partie évalue les performances quantitatives du système, en évaluant la linéarité, les limites de quantification, la précision, l'exactitude et l'incertitude. Les avantages de la mobilité ionique, tels que l'amélioration de la séparation de la mobilité ionique pour les espèces isomériques et isobariques et l'utilisation du CCS pour la confirmation des analytes, sont également explorés. La quatrième partie applique la méthode développée à l'analyse non ciblée de composés halogénés dans une orque échouée, démontrant le potentiel du couplage entre la mobilité ionique et la spectrométrie de masse pour la caractérisation des polluants.

La thèse se termine par une discussion sur les implications plus larges de ces résultats, soulignant le rôle de la spectrométrie de masse avec mobilité ionique dans l'avancement de l'analyse réglementaire des contaminants et de la surveillance de l'environnement.

Remerciements

Dans cette section, j'aimerais prendre un moment pour remercier toutes les personnes qui, de près ou de loin, ont contribué à l'accomplissement de cette thèse.

Tout d'abord, je tiens à exprimer ma gratitude envers celles et ceux qui ont eu un impact direct sur mon travail.

Je remercie en premier lieu le professeur Gauthier Eppe de m'avoir proposé de réaliser cette thèse dans son laboratoire, sur un sujet qui me passionne particulièrement. Merci pour votre encadrement, vos retours et vos conseils tout au long de ces années, et ce malgré un emploi du temps plus que chargé.

Je souhaite également remercier toutes les personnes qui m'ont aidé, à un moment ou à un autre, dans la réalisation de mes manips. Une mention toute particulière à Georges : tu as été un soutien essentiel depuis le début, toujours à l'écoute, partageant tes connaissances pointues avec générosité et bonne humeur. Je ne pourrai jamais assez te remercier. Merci également aux autres membres du labo: Johann, Domi, Chris, ainsi qu'à la 'team' du CART, Nathalie, Cédric et Philippe. J'aimerais aussi remercier les deux mémorantes que j'ai eu la chance d'encadrer, Aurore et Elisa. Ce fut un vrai plaisir de vous accompagner et de partager un peu de mon expérience.

Je voudrais aussi remercier les personnes avec qui j'ai eu l'opportunité de collaborer durant ce doctorat. Merci à Krishna Das et Catherine Adam de m'avoir permis d'analyser l'échantillon d'orque. Merci également à la team Bruker (France et Espagne) pour leur aide précieuse et l'accès à une instrumentation de pointe. Enfin, un grand merci aux 'visiteurs' avec qui j'ai pu échanger autour de notre instrumentation ici au labo: Jakob et Theresa de l'EURL POPs de Freiburg, Milagros de l'Université du Luxembourg, et Ingrid du Laberca à Nantes. Plus largement, je souhaite remercier toutes celles et ceux avec qui j'ai eu des discussions enrichissantes lors des différents congrès auxquels j'ai eu la chance de participer.

Enfin, je tiens également à remercier les membres de mon jury pour leur relecture attentive, leurs retours et leurs commentaires pertinents sur mon manuscrit.

Ensuite, il y a toutes les personnes qui, même de manière indirecte, ont eu un rôle tout aussi important durant cette aventure.

Je pense bien sûr à celles et ceux avec qui j'ai partagé l'open space pendant ces quatre années: la team MS Lab Vib du +1. Merci aux jeunes doctorantes (Aurélie et Aurore) et aux jeunes docteurs (Alexandre, Lucas, Wendy et Zouheir) pour tous les bons moments au labo et en dehors. Merci aussi aux deux 'plus vieux' du labo, Cédric (pour ta bonne humeur, ton aide pour mes répétitions, et tes brins de folie) et Stéphane (pour ta bienveillance, ton partage de culture et ton humour). Et merci de m'avoir appris à jouer à la belote!

Merci également aux autres collègues du MS Lab avec qui j'ai partagé de bons moments, notamment en conférences: Caroline, Sophie, Cédric D, Zeina, Lou, Damien, Thomas T, Evan, Clara, Bastien, Thomas C, Axel et Chris. Sans oublier Thibault et Max, mes camarades doctorants depuis le tout début du bachelier, ainsi que Maud, ma collègue biologiste bientôt devenue chimiste!

Enfin, un grand merci à ma sphère privée: mes amis et ma (belle) famille. Je tiens particulièrement à remercier mon père Bernard, ma mère Carine, mes deux frères Pol et Tom, ainsi que mes deux grands-mères, Mamy et Mutti. Et pour finir, je voudrais remercier du fond du cœur ma 'petite' famille du quotidien: mon chien Teddy, et surtout ma compagne Marie, qui m'a soutenu avec patience, courage et amour durant ces quatre années intenses de travail.

Pour terminer, je souhaite également remercier le FNRS pour le financement de ma thèse de doctorat via une bourse FRIA, ainsi que le département de Chimie de l'Université de Liège pour tout l'enseignement et l'accompagnement reçus au cours de ces neuf années de bachelier, master et doctorat.

List of abbreviations

APCI	Atmospheric pressure chemical ionization
CCS or Ω	Collision cross section
DDA	Data dependent acquisition
DIA	Data independent acquisition
DL	Dioxin like
DTIMS	Drift tube ion mobility spectrometry
eBFR	Emerging brominated flame retardants
EI	Electron ionization
EIC	Extracted ion chromatogram
ESI	Electrospray ionization
EU	European union
E/N	Reduced electric field
FAIMS	Field asymmetric ion mobility spectrometry
FWHM	Full width at half maximum
GC	Gas chromatography
HOC	Halogenated organic compounds
HNP	Halogenated natural products
HRMS	High resolution mass spectrometry
IM(S)	Ion mobility (spectrometry)
IM-MS	Ion mobility – Mass spectrometry
K	Ion mobility coefficient
K_0	Reduced ion mobility coefficient
LC	Liquid chromatography
LOQ	Limit of quantification
iLOQ	Instrumental limit of quantification
mLOQ	Method limit of quantification
ML	Machine learning
MO	Mono ortho
MS	Mass spectrometry
MS/MS	Tandem mass spectrometry
m/z	Mass-to-charge ratio
N	Gas number density
NDL	Non dioxin like
NO	Non ortho
NTA	Non targeted analysis
NTS	Non targeted screening
OCP	Organochlorinated pesticides
p_{ent}	Entrance TIMS pressure
PASEF	Parallel accumulation serial fragmentation
PAHs	Polycyclic aromatic hydrocarbons
PBDEs	Polybrominated diphenyl ethers
PCBs	Polychlorinated biphenyls

PCDDs	Polychlorinated dibenzo-p-dioxins
PCDFs	Polychlorinated dibenzofurans
PCNs	Polychlorinated naphtalenes
PFAS	Per and Poly-fluoroalkyl substances
POP	Persistent organic pollutant
PT	Proficiency test
q	Quadrupole
RF	Radio frequency
RFF	Relative response factor
RSD	Relative standard deviation
RSD_R	Intermediate precision
R_p	Resolving power
RT	Retention time
SLIM	Structures for lossless ion manipulation
SWIM	Sliding windows in ion mobility
S/N	Signal to noise ratio
TA	Targeted analysis
TEF	Toxic equivalent factor
TEQ	Toxic equivalent quantity
TIM	Total ion mobilogram
TIMS	Trapped ion mobility spectrometry
TOF	Time-of-flight
TWIMS	Travelling wave ion mobility spectrometry
U	Expended measurement uncertainty
v_g	Buffer gas velocity (TIMS)
WHO	World health organisation

List of specific terms

Congener – one of a related set of compounds that share the same base structure, e.g. there are 209 polychlorinated biphenyl (PCB) congeners where one or more chlorine atoms may be substituted in place of any of the 10 hydrogens of the biphenyl molecule.

Isotopologue – one of a set of compounds with the same chemical formula and structure but with a different isotopic composition of one or more atoms, e.g. $^{12}C_{12}H_4Ocl_4$-2,3,7,8-TCDF and $^{12}C_{11}{}^{13}C_1H_4Ocl_4$-2,3,7,8-TCDF are both isotopologues of 2,3,7,8-TCDF.

Reference: HART, Jeremy R. (2020). Measurement artefacts, ion mobility and other observations in environmental mass spectrometry analyses. Doctoral, Sheffield Hallam University.

Table of contents

JURY III

ABSTRACT IV

RESUME V

REMERCIEMENTS VI

LIST OF ABBREVIATIONS VIII

LIST OF SPECIFIC TERMS IX

TABLE OF CONTENTS X

Chapter 1: General introduction 1

1.1 CHEMICAL POLLUTION 3

1.2 ANALYSIS OF CHEMICAL POLLUTANTS 5

1.2.1 - Targeted and non-targeted analysis 5

1.2.2 - Current analytical challenges 7

1.3 ION MOBILITY AS AN EMERGING TECHNIQUE TO ANALYSE CHEMICAL POLLUTANTS 7

1.3.1 - A bit of history 7
- A. From the discovery to the first analytical applications 7
- B. From the biological revolution to the commercialization of the first IM-MS instruments 8
- C. Present status 8

1.3.2 - IM experiment 9
- A. Basic principle 9
- B. Ion mobility coefficient K 9

1.3.3 - IM technologies 14
- A. Drift tube IMS (DTIMS) 14
- B. Traveling wave IMS (TWIMS) 15
- C. Field asymmetric IMS (FAIMS) 16
- D. Trapped IMS (TIMS) 17

1.3.4 - Advantages of IM for small molecules applications 20

A. Additional separation 20
B. Identification 20
C. Structural information 21

1.3.5 - Overview of IM-MS applications for contaminants 21
A. Situation before 2020 (start of PhD thesis) 21
B. Situation after 2020 22

1.4 REFERENCES 24

Chapter 2: Objectives & outline 35

Chapter 3: Ion mobilities and collision cross sections of halogenated POPs measured on a GC-APCI-TIMS-TOF system 41

3.1 - MATERIALS AND METHODS 43

3.2 - RESULTS AND DISCUSSION 43

3.2.1 - CCS calibration procedure for GC hyphenated timsTOF systems 43
A. Calibration before ion sources switching 44
B. External calibration procedure 47
C. Internal calibration procedure 48

3.2.2 - Ion mobilities and collision cross sections of halogenated POPs 50
A. Ion mobilities of (quasi)molecular ions 50
B. Ion mobilities of fragment ions 51
C. CCS trends 58

3.3 - CONCLUSION 64

3.4 - REFERENCES 65

3.5 - SUPPORTING INFORMATION 67

Chapter 4: Optimization of trapped ion mobility performance 79

4.1 - MATERIALS AND METHODS 81

4.2 - RESULTS AND DISCUSSION 81

4.2.1 - Impact of key parameters on TIMS performance 81
A. Accumulation time 81

B. Funnel 1 RF voltage 85
C. TIMS cell DC voltages 87
D. Quadrupole and collision cell energy 88
E. Collision cell in 89

4.2.2 - Strategies for enhancing ion mobility resolving power in TIMS 90
A. Buffer gas velocity 91
B. Number of ions accumulated 91
C. Scan rate β 92

4.3 - CONCLUSION 97

4.4 - REFERENCES 98

4.5 - SUPPORTING INFORMATION 101

Chapter 5: Evaluation of the performance of GC-APCI-TIMS-TOFMS for the quantitative analysis of trace contaminants 111

5.1 - MATERIALS AND METHODS 113

5.1.1 - Chemicals 113

5.1.2 - Sample preparation 113

5.1.3 - Instrumentation 114
A. GC-APCI-TIMS-TOFMS 114
B. GC-sectorHRMS 115

5.1.4 - Data treatment 115

5.2 - RESULTS AND DISCUSSION 115

5.2.1 - Quantitative performances evaluation of GC-APCI-TIMS-TOF 115
A. Linearity and LOQs 115
B. Precision, trueness and uncertainty 118

5.2.2 - Benefits of ion mobility for the quantitative analysis of contaminants 121
A. CCS values for analyte confirmation 121
B. Increased selectivity 122

5.3 - CONCLUSION 125

5.4 - REFERENCES 126

5.5 - SUPPORTING INFORMATION 129

Chapter 6: Non targeted analysis of halogenated compounds in a stranded killer whale using TIMS hyphenated with GC-HRMS 153

6.1 - MATERIALS AND METHODS 156

6.1.1 - Sample preparation 156

6.1.2 - Analysis 156

6.1.3 - Data processing 156

6.2 - RESULTS AND DISCUSSION 157

6.2.1 - Leveraging an additional dimension of separation: mass vs mobility space 157
  A. Prioritization Strategy 157
  B. Optimized DDA selectivity 160

6.2.2 - Classes of halogenated compounds tentatively identified in the killer whale's blubber 161

6.2.3 - Evaluation of machine learning tools for predicting CCS of polyhalogenated pollutants 163

6.3 - CONCLUSION 165

6.4 - REFERENCES 165

6.5 - SUPPORTING INFORMATION 171

Chapter 7: General conclusion & outlook 179

Curriculum Vitae 191

Appendices 197

“The earliest humans, and even those living little more than a century ago, must have thought of the Earth as so vast that human activity could scarcely have any more than local effects on the soil, water, and air. Today we realize that our activities can have not only local and regional, but also global, consequences.”

Colin Baird & Michael Cann
Environmental chemistry textbook 5th ed.

Chapter 1:
General introduction

Chapter 1: General introduction

1.1 CHEMICAL POLLUTION 3

1.2 ANALYSIS OF CHEMICAL POLLUTANTS 5

1.2.1 - Targeted and non-targeted analysis 5

1.2.2 - Current analytical challenges 7

1.3 ION MOBILITY AS AN EMERGING TECHNIQUE TO ANALYSE CHEMICAL POLLUTANTS 7

1.3.1 - A bit of history 7
- A. From the discovery to the first analytical applications 7
- B. From the biological revolution to the commercialization of the first IM-MS instruments 8
- C. Present status 8

1.3.2 - IM experiment 9
- A. Basic principle 9
- B. Ion mobility coefficient K 9

1.3.3 - IM technologies 14
- A. Drift tube IMS (DTIMS) 14
- B. Traveling wave IMS (TWIMS) 15
- C. Field asymmetric IMS (FAIMS) 16
- D. Trapped IMS (TIMS) 17

1.3.4 - Advantages of IM for small molecules applications 20
- A. Additional separation 20
- B. Identification 20
- C. Structural information 21

1.3.5 - Overview of IM-MS applications for contaminants 21
- A. Situation before 2020 (start of PhD thesis) 21
- B. Situation after 2020 22

1.4 REFERENCES 24

1.1 Chemical pollution

Over the last century, technological and economic development has led to a dramatic, though uneven, improvement in living standards worldwide. These advances have transformed how we travel, produce food, dress, use energy, communicate, and treat disease. However, alongside a nearly seven-fold increase in the global population over the past two centuries, anthropogenic activities have placed immense pressure on the planet's sustainability. Current global environmental challenges include the depletion of natural resources, accelerated species extinction, ocean acidification, land-use and climate change, and widespread chemical pollution[1,2].

Chemistry plays a central role in modern society. The production of diverse chemicals has contributed to longer, healthier, and more comfortable lives[3]. Yet, until recently, insufficient attention was paid to the environmental consequences of chemical emissions into the air, water, and soil[4]. For much of the 20th century, chemical pollution was largely regarded as a problem that could be solved through dilution. However, a series of environmental disasters and the growing awareness among scientists[*] about the long-term effects of pollutants led to the first formal regulations on the manufacture, use, and disposal of chemicals in the 1970s[6]. Today, common control measures include monitoring the presence of chemicals in the environment and organisms, regulating or banning hazardous substances, registering new chemicals before their release on the market, and implementing remediation strategies at contaminated sites[3].

Now more than ever, concerns are growing about the release of certain substances into the environment, commonly referred to as micropollutants[7]. These are chemicals present at concentrations above natural levels that can negatively impact the environment and living organisms. Micropollutants encompass a wide range of substances[8,9], including inorganic compounds (e.g., heavy metals, nitrates), organic pollutants, gaseous compounds (e.g., CO_2, NO_x, CFCs), radioactive isotopes, and nanomaterials. They can be further classified by their source or use (e.g., industrial, agricultural, pharmaceutical, personal care products), their chemical properties (e.g., persistence, mobility, bioaccumulation, and toxicity), and their regulatory status (e.g., regulated or emerging contaminants).

Among organic micropollutants is a class of extensively halogenated compounds containing fluorine, chlorine, or bromine, commonly referred to as environmental halogenated pollutants or halogenated organic compounds (HOCs)[10]. Most HOCs are synthetic and have been produced for a wide range of industrial applications[11] (**Table 1.1**). However, some are generated unintentionally as by-products of industrial processes (e.g., dioxins during waste incineration[11]), while others also occur naturally, produced by organisms such as sponges, algae, and bacteria (i.e., halogenated natural products, HNPs[12]), or during natural events like wildfires and volcanic eruptions[13].

Table 1.1 – Industrial use and year of entry in the Stockholm convention of regulated classes of HOCs.

Class name	Industrial use(s)	Year of entry in Stockholm convention
Polychlorinated biphenyls (PCBs)	- Flame retardants - Capacitors and transformers	**2001**

---

[*] Among which the biologist Rachel Carson is renowned for initiating widespread concern about chemical pollution and its effects on the environment and human health through the publication of her book 'Silent Spring' in 1962[5].

	- Paints - Lubricants - Plasticizers	
Halogenated flame retardants (HFRs)	- Flame retardants	**2009** (Tetra, Penta, Hexa and Hepta brominated diphenyl ethers; Hexabromobiphenyls); **2013** (Hexabromocyclododecane); **2017** (DecaBDE); **2023** (Dechlorane plus)
Organochlorinated pesticides (OCPs)	- Pesticides	**2001** (Aldrin, Chlordane, DDT, Dieldrin, Endrin, Heptachlor, Hexachlorobenzene, Mirex, Toxaphenes); **2009** (α,β,γ-Hexachlorocyclohexanes, Chlordecone, Pentachlorobenzene); **2011** (Endosulfan); **2015** (Pentachlorophenols); **2019** (Dicofol); **2023** (Metoxychlor)
Polychlorinated naphthalenes (PCNs)	- Dielectric fluids - Insulators	**2015**
Short-chain chlorinated paraffins (SCCPs)	- Metalworking industry - Sealants	**2017**
Per and Poly-fluoroalkyl substances (PFAS)	- Nonstick cookware - Stain-resistant material - Food-contact paper coating - Aqueous film-forming foam	**2009** (PFOS & POSF); **2019** (PFOA); **2022** (PFHxS)
Hexachlorobutadiene (HCBD)	- Solvent	**2015**

The high degree of halogenation imparts specific physical and chemical properties to these compounds:

- Resistance to degradation
- Ability to be transported over long distances via air and water
- High potential for bioaccumulation and biomagnification due to strong lipophilicity (i.e., Log K_{OW})
- Toxicity to humans and other organisms

Because of these characteristics, many industrial HOCs have been classified as persistent organic pollutants (POPs)[11,14] and are now tightly regulated under the Stockholm Convention, an international treaty that came into force in 2004[15]. This treaty, signed by nearly all countries with the notable exception of the United States, aims to control the anthropogenic release of POPs into the environment. It currently regulates over 34 harmful substances (33 of which are halogenated, Table 1.1), with four additional classes of compounds under review for potential inclusion.

Besides these regulated POPs, many other unregulated substances with POP-like characteristics have been identified in various national and international chemical inventories by multiple research groups, the vast majority of which are halogenated compounds[16].

1.2 Analysis of chemical pollutants

The chemical monitoring of pollutants is a critical step that supports every stage of the policy cycle, from defining environmental problems to developing, implementing, and evaluating measures aimed at reducing emissions and limiting exposure[6]. Interest in the analysis of environmental pollutants truly began in the 1960s[2,11,17]. During this time, the first analytical data revealed widespread contamination of the environment (including top predator species) with several persistent organic pollutants, such as organochlorine pesticides and PCBs[17]. These initial measurements were made using gas chromatography coupled with a newly developed, highly sensitive detector: the electron capture detector (ECD), invented by James Lovelock in the late 1950s[11]. In the 1970s, mass spectrometry, particularly single quadrupole and magnetic sector instruments using electron impact (EI) ionization, rapidly replaced the ECD as the preferred GC detector[18]. GC-MS then became the gold standard for the targeted analysis of environmental pollutants in complex matrices[2].

The 1990s were marked by several key advancements[18]. One major development was the introduction of soft ionization techniques (typically ESI) and interface that enabled liquid chromatography to be coupled with MS. This innovation allowed for the analysis of polar and hydrophilic contaminants that were not amenable to GC. Similar interfaces were later developed for GC, such as atmospheric pressure chemical ionization (APCI)[19,20] and atmospheric pressure photoionization (APPI)[21] in the 2000s. Significant progress was also made in tandem MS technologies[2], particularly with ion trap and triple quadrupole instruments. Additionally, the advent of the internet during this period revolutionized how scientists shared and processed analytical data[18].

Since the 2000s, GC and LC coupled with triple quadrupole instruments have become the standard platforms for targeted contaminant analysis[2]. At the same time, developments in high-resolution mass spectrometry (HRMS), including orthogonal time-of-flight (oTOF) and Orbitrap systems, have enabled the rise of non-targeted analysis (NTA)[18].

1.2.1 - Targeted and non-targeted analysis

Unlike targeted methods, which focus on detecting and quantifying a predefined list of contaminants for which reference standards are available, NTA seeks to comprehensively characterize both known and unknown compounds in a sample[6,18,22]. This broader screening is achieved using generic, universal parameters for both sample preparation and analysis, making NTA a powerful complement to traditional targeted approaches. An overview of the general characteristics of both types of approaches is presented in **Table 1.2**.

Table 1.2 – Comparison between targeted and non-targeted analysis approaches for the detection of environmental contaminants.

	Targeted analysis	**Non-targeted analysis**
Sample preparation	Thorough, to remove matrix interferences	Minimal, to avoid the loss of chemicals of interest
Analytical parameters	Optimized for the targeted analytes	Generic, to ensure performance for as many classes of contaminants as possible
Mass spectrometry	Low resolution Single or multiple ion/fragment monitoring e.g.: Triple quadrupoles	High resolution Full-scan + tandem MS e.g.: q-TOF & q-Orbitrap
Prior information about contaminants	Chemical structure, mass, isotopic pattern, retention time, fragmentation spectrum, CCS (from reference standard)	<u>Suspect screening (SS)</u>: Chemical structure, mass, isotopic pattern. Retention time, fragmentation spectrum and CCS may be found in online libraries or predicted with in-silico tools. <u>Non-targeted screening (NTS)</u>: None
Final outpout	Quantitative	Qualitative or semi-quantitative[23]
Number of contaminants	Tens to a hundred	Hundreds to thousands

Following data acquisition, the general data treatment workflow in non-targeted analysis (NTA) involves the following steps[6,22]:

- <u>Data pre-processing</u>: This step may include several processes, the most critical being feature detection (i.e., identifying signals that could correspond to specific compounds) and componentization (grouping related signals such as adducts, isotopologues, and fragments into a single compound representation). The outcome of this step is a comprehensive list of individual features detected in the sample.
- <u>Prioritization</u>: This a crucial step aimed at filtering the feature list to retain only those signals relevant to the research question. Prioritization strategies can generally be grouped into three main categories: chemical signature-based approaches (e.g., suspect screening, mass defect filtering), statistical methods (e.g., principal component analysis (PCA), heatmaps), and effect-directed methods (e.g., bioassays, biomarker).
- <u>Features identification</u>: The final step involves identifying the prioritized features using all available data, including exact mass, isotopic pattern, (tandem) mass spectra (including EI spectra when available), diagnostic fragments, retention time and retention index, collision cross section (CCS), meta-information, and data from complementary techniques (e.g., NMR, IR). Confidence in the proposed structure is typically expressed using a multi-level classification system, such as the five-level system proposed by Schymanski et al[24]. Achieving the highest confidence level (Level 1) requires confirmation of the structure using the corresponding reference standard.

1.2.2 - Current analytical challenges

Despite continuous analytical advances in sample preparation, chromatographic performance, mass spectrometry, and data treatment[25], the monitoring of chemical pollutants in complex matrices -such as environmental, food, and biological samples - remains challenging in many respects.

Indeed, the number of anthropogenic molecules used by modern society is enormous, estimated to be in the hundreds of thousands[3,16]. Moreover, thousands of new synthetic chemicals are developed and marketed each year, sometimes as replacements for substances that have been phased out[17]. Globally, only a small fraction of these chemicals have been well characterized or included in regulatory programs. For the majority, information on their physicochemical properties and potential ecological impact is still lacking. In addition, the (a)biotic degradation of these chemicals in the environment can give rise to numerous unknown transformation products (TPs), which may also be harmful[26].

This immense and ever-increasing number of chemicals poses several challenges to the field of contaminants analysis. First, the wide diversity of physicochemical properties exhibited by these substances necessitates the use of complementary analytical techniques[22,25], including various approaches to sample preparation, chromatographic separations (e.g., reversed-phase and HILIC LC, GC, SFC, ion chromatography), and ionization methods (e.g., ESI, APCI, APPI, EI). Furthermore, the broad range of contaminant concentrations, often spanning several orders of magnitude, requires highly sensitive and dynamic detection systems[25]. Finally, the complexity of the matrices demands instrumentation with high selectivity[25]. Increasing the method selectivity can for instance be achieved through multidimensional chromatography (e.g., GC×GC[27,28] and LC×LC[29]).

1.3 Ion mobility as an emerging technique to analyse chemical pollutants

In addition to the recent analytical advances in sample preparation, chromatography and mass spectrometry, an emerging technology termed ion mobility (IM) has recently become increasingly prevalent in several research fields, including contaminants analysis[30,31]. Easily nested between chromatography and mass spectrometry[32], this approach provides an additional dimension of separation according to the 'size' of ions, offering enhanced method selectivity as well as further identification capabilities for both targeted and non-targeted workflows. In this section, we give a broad overview of this method.

1.3.1 - A bit of history

A. From the discovery to the first analytical applications

The origins of the technique of ion mobility spectrometry (IMS) are generally traced back to experiments carried out around 1896 by J.J. Thompson and E. Rutherford to study of the formation and behavior of ions generated through electrical discharges in various gases[33,34]. Among other things, the two scientists discovered that gaseous ions would travel at a constant speed through a gas when placed under the influence of an external electric field. They observed that this speed, called the drift velocity, was proportional to the magnitude of the electric field through a coefficient, the ion mobility K. Following this discovery, the first tables of ion mobilities measured for different atomic ions were soon published by E. Rutherford (1897) and J. Zeleny (1898)[34]. During the first half of the twentieth century, the instrumentation, experiments and theories of ion mobility were gradually refined[33].

The period from the 1960s to the 1970s saw the advent of the use of IM for chemical measurements[33]. Until then, IM had remained a niche technique used only by some research groups to study the gas phase behavior and reactivity of ions. After several years of development by E. Mc Daniels and colleagues, the first drift-tube IMS (Section 1.3.3A) was conceived in the mid-1960s[34]. A few years later in 1970, the first commercial IM instrument, known as "plasma chromatograph (PC)", was introduced based on that technology[35,36]. This was followed by almost a decade of research by the group of F.W. Karasek's at the University of Waterloo in Canada, whose work demonstrated the broad applicability of PC to the analysis of a wide range of compounds, including PCBs[37].

In addition to research in academic laboratories, unpublicized research programmes were initiated in the military and security fields to develop portable, hand-held IM instruments[33]. The high sensitivity, small size, and rapid screening capability of the developed stand-alone IM instruments led to their widespread use for military applications (e.g., detection of traces of chemical warfare agents and other hazardous materials) as early as the early 1980s[33,38,39]. A decade later, the first benchtop IMS analysers were deployed at several airports to detect explosives[40], in response to several aircraft bombing incidents[33]. Today, modern versions of these early devices are still in use by most airports and military units[33].

B. From the biological revolution to the commercialization of the first IM-MS instruments

While most research and applications in the field of IM had been focused on stand-alone IM systems for security and military venues, renewed interest in the use of IM as an analytical tool in academic settings occurred in the 1990s as part of the worldwide effort to characterize biological molecules[33]. This period, dubbed the 'biological revolution'[33], marked the onset of a growing interest in the technique of ion mobility. IMS was combined with the then emerging soft macromolecular ionization sources: electrospray ionization (ESI) and later, matrix-assisted laser desorption ionization (MALDI)[33,41] Most importantly, IMS was recoupled[†] to its close relative[‡], mass spectrometry (MS), giving rise to hyphenated IM-MS systems that could provide details on the size and shape of biomolecules in addition to their mass[33,41].

This period of increased visibility for IMS has been the catalyst for an important period of technology development over the last two decades[33]. The quest for increased ion mobility resolution[44] and transmission led to the development of a myriad of ion mobility technologies, some of which have been commercialized by major instruments companies[45]: travelling wave IMS (TWIMS) in 2006 by Waters, drift tube IMS (DTIMS) in 2014 by Agilent, trapped IMS (TIMS) in 2016 by Bruker and field asymmetric IMS (FAIMS) in 2018 by Thermo Scientific. Higher resolving power versions of the TWIMS technology were recently commercialized in 2019 by Waters (cyclic TWIMS) and in 2021 by MOBILion systems (structures for lossless ion manipulation SLIM TWIMS).

C. Present status

Advances in the performance and accessibility of commercial instruments have made ion mobility spectrometry an increasingly established technique with broad utility in both physical and analytical chemistry[46]. Current applications in the latter field are typically divided into the structural

---

[†] The coupling of IM and MS was first performed in the 1960s to study the chemistry of gas-phase ions in more detail[42]. However, with the subsequent development of stand-alone IM instruments, the two techniques went their separate ways once again.

[‡] Mass spectrometry and ion mobility were discovered around the same time (discovery of MS in 1912 by the same J.J. Thompson) in the Cavendish laboratory at Cambridge University[43].

characterization of large (bio)molecules by IM-MS[47,48] (e.g., proteins) and the separation and identification of diverse analytes in complex samples by both IMS and IM-MS, often coupled with a chromatographic front end[32] (e.g., “omics” fields[45], including environmental pollutants monitoring[30,31,49,50]). Although several challenges remain (e.g., higher resolving power and sensitivity[44], user-friendly softwares, accurate theoretical and numerical tools[34,51] …), continual advances in technology is expected to further improve and expand the capabilities of IM-MS in the future[52].

1.3.2 - IM experiment

A. Basic principle

During a typical ion mobility experiment, ensembles of gaseous ions (referred to as ion swarms) are sent into a region filled with a neutral gas (called the buffer or drift gas), under the influence of an external electric field[33]. Under such conditions, the charged ions will be submitted to two opposing forces:

- The electric force $\overrightarrow{F_{el}} = q\vec{E}$, which will accelerate the ions in the direction of the electric field
- The drag force $\overrightarrow{F_{drag}}$, which will decelerate the ions through repeated collisions with the buffer gas, in a direction opposite to the electric field.

Quickly, a stationary state will be reached where, on average, the two forces balance each other through repeated acceleration (between collisions) and deceleration (during collisions) events[53] (**Figure 1.1**).

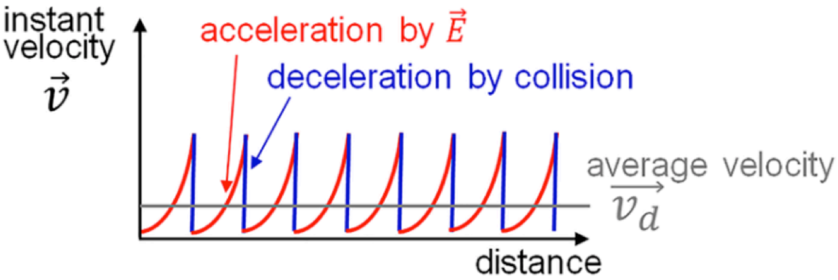

Figure 1.1 – Simplified representation of the variation in instantaneous ion velocity due to alternating field acceleration and collision-induced deceleration events, resulting in an overall constant drift velocity. Adapted from reference [53].

Consequently, the average speed of the ion swarms along the electric field lines, called the drift speed v_d, will be constant and proportional to the electric field[53]:

$$\overrightarrow{v_d} = K\vec{E} \tag{1.1}$$

The proportionality coefficient, K, is referred to as the ion mobility coefficient.

B. Ion mobility coefficient K

Fundamental low-field ion mobility equation

Initially developed a few years after the discovery of ion mobility by Paul Langevin, theoretical models to describe the ion mobility experiment were gradually refined by several investigators throughout the 20th century[34,51] (S. Chapman, D. Enskog, H. Hasse, E. Mc Daniels, H. Revercomb, E. Mason, to name but a few). Currently, the most widely used equation in the analytical community to express the ion mobility coefficient in terms of physico-chemical parameters and constants is the fundamental low-field ion mobility equation[43,§]:

$$K\ (p,T) = \frac{3}{16}\sqrt{\frac{2\pi}{\mu k_b T_{gas}}}\ \frac{q}{N}\ \frac{1}{\overline{\Omega}(\mathrm{T})} \qquad (1.2)$$

where:

- $\mu = \frac{m_{ion}.m_{gas}}{m_{ion}+m_{gas}}$ is the reduced mass of the ion-buffer gas system (in kg)
- k_b is the Boltzmann constant ($1.38\mathrm{x}10^{-23}$ J/K)
- T_{gas} is the temperature of the buffer gas (in K)
- q is the ion charge (in C)
- N is the gas number density, the number of gas particle per unit of volume (in m^{-3}). For a perfect gas, $N = \frac{p}{k_b T_{gas}}$ where *p* is the pressure in Pa.
- $\overline{\Omega}(\mathrm{T})$ is the orientationally averaged momentum transfer collision integral (in m^2)

Some notable features of this equation are:

- Buffer gas dependency[53]: through its pressure (N) and temperature (N, T_{gas} and $\overline{\Omega}(\mathrm{T})$). For a given temperature, the K coefficient decreases linearly with the pressure, due to the increasing number of collisions between the ions and the buffer gas molecules. The dependence on the gas temperature is less straightforward because the momentum transfer collision integral also depends on the temperature in a complex way. To correct for the pressure dependency, the ion mobility coefficient *K (p,T)* is often reported in a reduced form $K_0(T) = K\ \frac{N}{N_0} = K\ \frac{p}{101325\ Pa}\ \frac{273.15\ K}{T_{gas}}$. In this equation, the Loschmidt constant N_0, is equal to $2.687\mathrm{x}10^{25}$ m^{-3}. Note that the reduced mobility coefficient is still dependent on the temperature of the gas through the $(\sqrt{T_{gas}})^{-1}$ factor and the momentum transfer collision integral.
- Ion dependency: through its charge q. However, the ion mobility coefficient of a given ion will not necessarily double if its charge is doubled because the momentum transfer collision integral Ω also depends to some extent on the ion charge (again, in a complex way)[54,55].
- Ion-buffer gas pair dependency: through the reduced mass factor μ and the momentum transfer collision integral Ω. While the ion mobility coefficient depends directly on the mass of the ion through the μ factor, in the case of $m_{ion} >> m_{gas}$, its impact is not very significant since the reduced mass simplifies to $\mu \simeq m_{gas}$ (e.g., the $(\sqrt{\mu})^{-1}$ factor varies from 0.20 for an ion with m/z 200 to 0.19 for an ion with m/z 1000). The impact of the Ω factor will be developed in details in a later section.

Meaning in terms of resisting force

From the theories of resisting force developed long ago by P. Langevin, M. Knudsen, R. Milikan, G. Stokes and others, it is known that for a particle traveling at constant speed *v* through a buffer gas medium with mean thermal velocity v_t and density *d*, the magnitude of the drag force on the particle is given by[56]:

[§] Also referred to in the literature as the *Mason-Schamp equation*, although this terminology is debated in the IMS community.

$$F_{drag} = \frac{4}{3}\,\pi a^2 d\ v\ v_t \tag{1.3}$$

Where a is the collision radius (i.e., the sum of the radius of the collision partners: $r_{particule} + r_{gas}$). The quantity πa^2 thus represents the area of a circle with radius a, the collision cross section σ.

For ions drifting through a buffer during an ion mobility experiment, we know that the drag force is equal in magnitude to the electric force acting on the ions:

$$F_{drag\ IM} = F_{el} = qE \tag{1.4}$$

Because $v_d = KE$ (equation 1.1), the drag force can be written as:

$$F_{drag\ IM} = q\,\frac{v_d}{K} = \frac{4}{3}\,\bar{\Omega}(T)\ N\mu\ v_d\sqrt{\frac{8k_bT_{gas}}{\pi\mu}} \tag{1.5}$$

where K was replaced by equation 1.2.

Written in this form, the equivalence with equation 1.3 becomes readily apparent and enables one to identify the ion mobility coefficient as a fundamental transport property closely linked to the amount of friction an ion will experience while drifting through a gas under the influence of an electric field[56], with:

- The orientationally averaged momentum transfer collision integral $\bar{\Omega}(\mathrm{T})$ of an ion being the equivalent to the collision cross section σ of a perfectly spherical particle that would experience a similar drag while drifting at the same speed in the same buffer gas[56].
- The product $N\mu$ being the equivalent to the buffer gas density d (as long as $m_{ion} >> m_{gas}$, $N\mu \simeq Nm_{gas} = d_{gas}$).
- The drift speed v_d being the equivalent to the particle speed v.
- The factor $\sqrt{8k_bT_{gas}/\pi\mu}$ being the equivalent to the mean thermal agitation velocity v_t.

Momentum transfer collision integral Ω(T)

In the previous section, we saw that in the frame of the simple model of hard spheres collisions, the collision cross section σ is defined as the area of a circle with radius equal to the collision diameter (IUPAC definition, **Figure 1.2**)[56]. This definition is appropriate to describe whether a collision between two particles will take place or not. The higher σ, the higher the probability of collision[53].

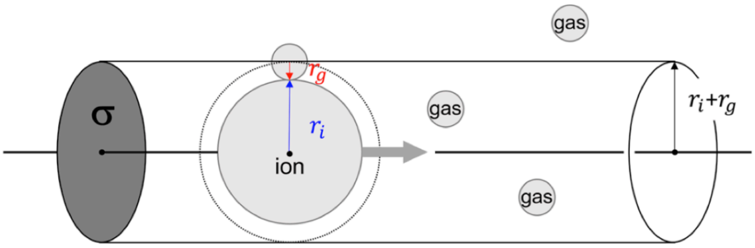

Figure 1.2 – Schematic representation of the collision cross section σ in the simplified model of hard sphere collisions. Adapted from reference [53].

However, the model of hard-sphere collisions is too simplistic to describe the interaction of molecular ion with buffer gas molecules in IMS for the following reasons[53,56]:

- Molecules are not hard spheres with defined boundaries. Rather, they tend to interact attractively at long distances and repulsively at shorter distances, without a sharp boundary. Therefore, collisions in IMS are better described in terms of the magnitude of the change in ion velocity due to the interaction potential (i.e. momentum transfer between the ion and the buffer gas molecule), instead of hit-or-miss events. Indeed, even if a collision is not a direct hit (e.g., a glancing collision), there will be a momentum transfer (**Figure 1.3**).
- Real molecules are not perfectly symmetric like hard speres. The interaction potential is therefore dependent on the relative orientation of the buffer gas – ion pair (collisions occur from all directions).

Therefore in IMS, the impact of collisions are better described by a parameter related to (but not equal to) the collision cross section σ, known as the momentum transfer collision integral Ω[56]. For a given relative orientation of the ion, it is formally defined as follows[34,51,56]:

$$\Omega(T) = \int_{0}^{\infty} Q(g)\ \omega(g,T) dg \tag{1.6}$$

In this equation:

- $\mathrm{Q}(g) = 2\pi \int_0^\infty [1 - \cos\chi] b\, db$ is called the momentum transfer cross section where:
    - χ is the deflection angle: the angle by which a given buffer gas molecule is deflected after it has interacted with the ion. It depends on the ion-gas interaction potentials Φ, the collision velocity g[**], the impact parameter b and the orientation of the ion.
    - $[1 - \cos\chi]$ is the magnitude of the momentum transfer in a single collision. Maximum momentum transfer occurs for head-on collisions (i.e., backward scattering $\chi < 90°$) and decrease for glancing collisions (i.e., forward scattering $\chi > 90°$). As glancing collisions are more likely than head-on collisions, their overall contribution to the total moment transfer is significant[56].
    - b is the impact parameter
- $\omega(g,T)$ is the distribution of relative collision velocities g at gas temperature T (e.g., Maxwellian distribution). The temperature dependance of Ω comes from this distribution.

To obtain the orientationally averaged Ω (i.e., $\overline{\Omega}$), the integral in equation 1.6 must be evaluated over all the relative ion-buffer gas orientations[34,51] (generally assuming equal orientations probabilities).

Overall, the orientationally averaged momentum transfer collision integral $\overline{\Omega}$ thus corresponds to a measure of the momentum transfer by collisions averaged over all possible impact parameters, relative collision velocities (weighted by a temperature dependent velocity distribution) and ion orientations[51]. Due to its similarity to the collision cross section σ, Ω is usually described in the literature as being related only to the size and shape of ions in the gas phase. While it is indeed expected that larger, more extended ions should undergo a higher number of collisions with significantly more momentum transfer than smaller, more compact ions, we have seen that Ω actually depends on the ion-neutral interaction potential. Therefore, any parameter other than size and shape that affects this potential will also affect Ω, especially for small molecules. These are, for example, buffer gas polarizability, ion charge and ion charge distribution[54,55]. In addition, for historical reasons,

---

[**] As the relative collision velocity increases (i.e., as T_{gas} increases), the ion and the gas molecules have less time to interact. Therefore, the deflection is less significant.

the similarity between σ and Ω also led to the latter being referred to as the collision cross section (CCS), and this terminology is still used today. While both terminologies are accepted in the IMS community, it should be kept in mind that the CCS truly represents orientationally averaged momentum transfer collision integral $\overline{\Omega}$, not σ[43,53]. In this manuscript, for simplicity, we will use the collision cross section terminology (abbreviated as CCS or Ω), when we really mean the orientationally averaged momentum transfer collision integral $\overline{\Omega}$.

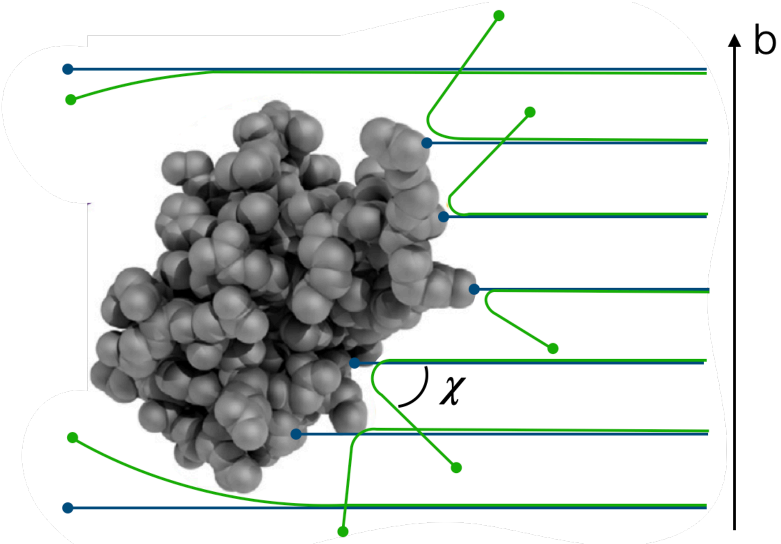

Figure 1.3 – Schematic illustration of collisions between a spherical ion and buffer gas molecules, comparing the simplified hard sphere model (blue trajectories) with a more realistic model that accounts for both short-range and long-range interactions (green trajectories). Post-collision buffer gas trajectories are shown for various impact parameters *b*. Adapted from reference [55]

Low-field and high field mobility

The theory discussed so far has been made, without properly mentioning it, within the framework of the so-called low-field limit. Indeed, for equation 1.2 to hold, it is mandatory that the energy acquired by the ions from the electric field be small relative to its thermal energy (i.e., the ions must be thermalized)[57]. The translational energy E_{trans} of the ion in IM is given by[34,51,56]:

$$E_{trans} = \frac{3}{2}RT_{gas} + \frac{1}{2}\, m_{gas}v_d^2 \quad (1.7)$$

where:

- The first term is the thermal energy of the ion in the buffer gas at temperature T_{gas}
- The second term is the random kinetic energy acquired by the electric field

For ions to be thermalized, the condition is:

$$E_{trans} \approx \frac{3}{2}RT_{gas} \quad (1.8)$$

Which therefore requires that[††]:

$$\frac{3}{2}RT_{gas} \gg \frac{1}{2}\, m_{gas}v_d^2 \qquad (1.9)$$

$$\Leftrightarrow\ v_d \to 0$$

$$\Leftrightarrow\ KE \to 0$$

$$\Leftrightarrow\ K_0N_0\frac{E}{N} \to 0$$

$$\Leftrightarrow\ \frac{E}{N} \to 0$$

Therefore, the last equation tells us that in order for ions to be thermalized, the ratio between the electric field strength and the gas number density, also called the reduced electric field and expressed in Townsend (1 Td = 10^{-21} Vm^2), must be as small as possible[58]. This can be achieved either by using a low electric field (to reduce the energy gained by the ions during the acceleration phase between collisions) or by working at high pressure (i.e., high N, to increase the collision frequency and reduce the acceleration time between collisions). Under these conditions, the ion mobility is independent of the reduced electric field and the fundamental low-field ion mobility equation applies[53].

Above a certain value of the reduced electric field, the energy gained by the ion from the electric field can no longer be considered negligible with respect to the thermal energy and the reduced ion mobility K_0 begins to depend on this experimental parameter in a complex way[‡‡]. The corresponding reduced ion mobility coefficients are then referred to as the high field ion mobility coefficients. These coefficients can increase, decrease, or both, as E/N increases[33,34].

1.3.3 - IM technologies

As discussed in Section 1.3.1B, the decades that followed the biological revolution were marked by a proliferation of new IMS techniques[59]. Despite their varied designs and working principles, all these methods have in common that they allow the separation of ions on the basis of their ion mobility coefficient K_0. In this section, we will briefly describe and compare the operating principle, figures of merit and advantages/disadvantages of the four most widely used IM-MS technologies for contaminant applications: DTIMS, TWIMS, FAIMS and TIMS (**Table 1.3**).

A. Drift tube IMS (DTIMS)

DTIMS is the earliest IMS technology that was developed, but also the simplest. Ions separation takes place in a drift tube filled with a stationary buffer gas and operated with a constant electric field in both space and time[53] (**Figure 1.4**). The main advantage of DTIMS is that it is the only of the four technologies where reduced mobilities and CCS values can be measured without the use of calibration[43] (i.e., it is a primary method of measurement). It is also the one that operates at the lowest reduced electric fields E/N[55]. For these reasons, DTIMS is the gold standard method for measuring CCS

[††] The requirement for operating in the low-field limit can also be expressed as v_t >> v_d, where v_t is the relative thermal speed of the ion and the buffer gas molecules $\sqrt{\frac{8k_bT_{gas}}{\pi\mu}}$. At 300K in N_2, the relative thermal speed of an ion with m/z 500 is 489 m/s.

[‡‡] Since the fundamental ion mobility equation no longer holds, more elaborated theoretical models must be used. These include the two-temperatures and the three-temperatures models[34,51]. These models take into account the fact that at high reduced field, the ions are no longer thermalized to the buffer gas temperature and thus possess their own temperature(s), T_{ion}.

values[45]. On the other hand, its resolving power and sensitivity are not very high[44], although a method known as high resolution demultiplexing (HRdm) allows them to be significantly improved[60].

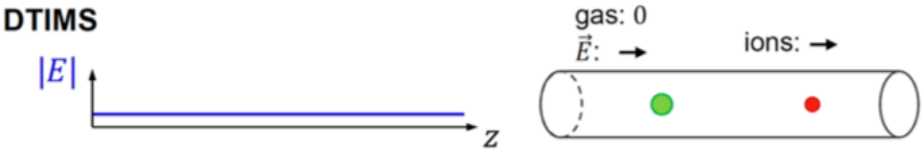

Figure 1.4 – Technical characteristics of DTIMS. Left panel: electric field magnitude as a function of distance along the drift cell. Right panel: schematic showing the direction of buffer gas flow (0 = no gas flow), electric field, ion movement, and elution order (red = low CCS ion, green = high CCS ion). Adapted from reference [53].

B. Traveling wave IMS (TWIMS)

Key instrument in the popularization of IMS during the biological revolution, the TWIMS Synapt HDMS was the first IM-MS platform to become commercially available in 2006[33].

In TWIMS, ions are propelled trough a drift cell by a series of voltage pulses, akin to “waves”[33] (**Figure 1.5**). In analogy to an object floating in the sea, ions may ‘surf’ on a wavefront for a certain period of time before being overtaken by the wave. The number of ‘waves’ (technically called ‘bins’) necessary to push an ion through the cell is dependent on its ion mobility: high mobility ions will spend a larger amount of time surfing an a specific ‘wave’ before falling behind, compared to low mobility ions, due to the lower friction their experience with the buffer gas. They will thus experience a lower number of ‘roll overs’.

Probably the main advantage of TWIMS over DTIMS is that it does not require an increase in voltage to increase the length of a mobility cell, allowing ions to be separated over long path lengths[44]. As the resolving power in TWIMS and DTIMS increases with the square root of the separation length, this allows a significant increase in separation performance. This has been technically realized in the last decade with the development of cyclic[61] and SLIM TWIMS[62] instruments. These allow ions to be separated over very large distances in a multi-pass loop and serpentine path, respectively.

While these longer path separations greatly improve the poor resolving power classically achieved on linear TWIMS instruments, they come at the cost of increased separation time, loss of sensitivity[§§] and reduced IM analysis range[44,***]. In addition, a common disadvantage of all instruments based on the TWIMS technique is that, owing to the complex ion motion, a calibration procedure is required to determine the CCS values, with the choice of the calibrant being of considerable importance[43,55] (it is recommended that the calibrant used be as close as possible to the class of compounds analyzed). Moreover, the reduced electric field at the top of a ‘wave’ can reach values close to 150 Td, raising questions about the validity of the fundamental low-field ion mobility equation[63].

[§§] A loss of sensitivity of ~2% per cycle has been reported on the cyclic TWIMS[61]. The SLIM technology is deemed ‘lossless’[62].

[***] Due to ‘wrap-around effects’ for multi-pass experiments (i.e., the overtaking of lower mobility ions by the higher mobility ions)[45].

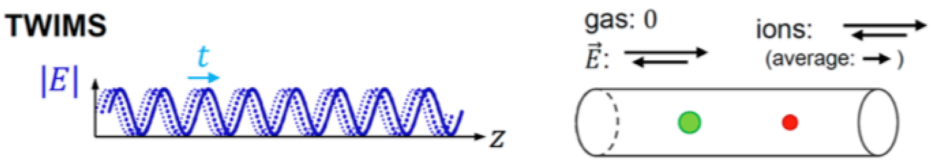

Figure 1.5 - Technical characteristics of TWIMS. Left panel: electric field magnitude as a function of distance along the drift cell. Right panel: schematic showing the direction of buffer gas flow (0 = no gas flow), electric field, ion movement, and elution order (red = low CCS ion, green = high CCS ion). Adapted from reference [53].

C. Field asymmetric IMS (FAIMS)

The initial development of FAIMS[†††] originates from Russian scientist circa 1980[45]. The technology then reached the United States and started to be commercialized by several vendors at the start of the 21st century[33,34].

In FAIMS, the ions are pushed by a gas flow parallel to the drift cell[34,44] (**Figure 1.6**). Perpendicular to this cell, an asymmetric waveform electric field is generated by the combination of a low magnitude electric field (the compensation voltage CV) and high magnitude electric field (the dispersion voltage DV), in opposite directions. During the low electric field phase, ions will drift in the direction of the field (downwards in the example in figure 1.6) with a drift velocity fixed by the low-field ion mobility coefficient. Conversely, during the strong electric field phase, they will drift in the opposite direction (upwards in figure 1.6) with a velocity fixed by the high-field ion mobility coefficient (characterizing the ion at the specific value of E/N). Since the relative duration of the two alternating fields is initially such that the areas in the 'time-electric field intensity' domain are equal, only ions having identical low field and high field mobility will make it through the drift cell. The other ions, characterized by a high-field mobility that is either higher or lower than the low-field mobility, will be neutralized on the side parts of the drift cell (upper parts and lower parts in figure 1.6, respectively). To allow these ions to be passed through the cell and analyzed, the intensity of the compensation voltage is gradually scanned. The result is an ion mobility spectrum where the abscissa is the value of the compensation voltage.

This IMS technique therefore differs from the other three in that: a) ions are separated spatially, rather than temporally[42]; b) the separation of ions is based on their difference in ion mobility at low and high field rather than on their low field mobility[34]. These features make the FAIMS a powerful device for filtering and reducing chemical noise prior to mass spectrometric detection[53]. Furthermore, its different separation principle makes it orthogonal and complementary to other low field IMS techniques: some IM separations of ions that are not possible at low field can be improved at higher fields[44]. However, the obvious limitations of this technique are that the majority of the ions are discarded during the separation and that CCS cannot be determined[45] (due to the high field).

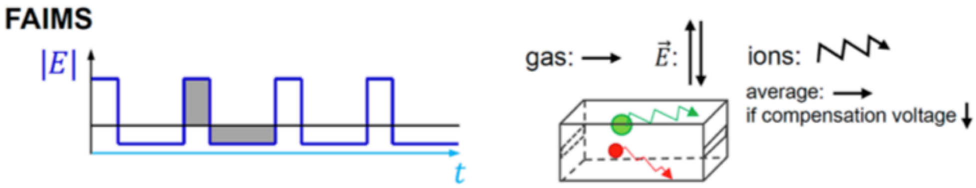

Figure 1.6 - Technical characteristics of FAIMS. Left panel: electric field magnitude as a function of time. Right panel: schematic showing the direction of buffer gas flow, electric field, and ion movement. Adapted from reference [53].

[†††] Equivalent names for this technology are: Differential Mobility Spectrometry (DMS), Differential Ion Mobility Spectrometry (DIMS) and Ion Mobility Increment Spectrometry (IMIS)[43].

D. Trapped IMS (TIMS)

Inspired by former experiments performed by several scientists in IMS (J. Zeleny; A. Loboda; G. Baykut), capillary electropheris (Z. Huang and C. Ivory) and electrodynamic ion funnel (R. Smith), the technique of trapped IMS was developed in 2011 by M. Park, D. Kaplan and F. Fernandez-Lima[64,65]. About 5 years later, the technology was made commercially available by Bruker during the 2016 ASMS conference with the launch of the *timsTOF* instrument, a modified q-TOF instrument (*impact II*) featuring and additional IM cell incorporated in its first pumping stage. Since then, Bruker has released a dozen updated versions of their first *timsTOF* instrument featuring technological improvements or tailored for a specific application.

The IM experiment in TIMS has two main distinctive features[66]. Firstly, ions are pushed through the IM cell by a flow of buffer gas and, in the absence of external forces, travel with the gas at a velocity v_g. Secondly, the electric field is directed in the opposite direction to the gas flow, towards the entrance of the cell (**Figure 1.7**). In addition, the intensity of this electric field is not constant but increases linearly as a function of the position in the analysis region (the region of the cell where the IM separation occurs) up to a point where it becomes constant over a certain distance (called the plateau region).

TIMS separations typically occur in two consecutive phases[66]: the trapping phase and the elution phase (Figure 1.7):

- During the trapping phase, ions pushed by the flow of gas enter the analysis region. There, ions will be subjected to the influence of the electric field and start to drift in the opposite direction to the moving buffer gas with a drift velocity given by equation 1.1. The resulting velocity of the ions in the laboratory reference frame will therefore be given by the sum of the gas velocity v_g and the drift velocity v_d:

  $$\overrightarrow{v_{ion}} = \overrightarrow{v_g} + \overrightarrow{v_d} \tag{1.10}$$

  Because of the electric field gradient, the drift velocity v_d will increase as ions progress further in the cell, up to a point of equilibrium where it will reach the magnitude of the gas velocity v_g. At this moment, the two velocities will cancel each other out and the resulting speed v_{ion} will be zero (i.e., the ions will become trapped). The intensity of the electric field E_{trap} necessary to trap an ion of ion mobility K is therefore given by:

  $$v_d = KE_{trap} = v_g$$

  $$\Leftrightarrow E_{trap} = \frac{v_g}{K} \tag{1.11}$$

  Equation 1.11 tells us that an ion characterized by an ion mobility coefficient K will be trapped at a position in the cell where the magnitude of the electric field E_{trap} is exactly equal to the ratio v_g/K. Since under given experimental conditions v_g is constant, the trapping position is only K-dependent and therefore, ions with different mobilities will be trapped at different positions inside the TIMS tunnel. Note that in order to fulfill the equilibrium condition (equation 1.11), higher K ions will be trapped at a position closer to the entrance of the cell (lower E_{trap}) whereas low K ions will be trapped at a position closer to its exit (higher E_{trap}). Thus, the trapping phase of a TIMS experiment allows ions to be spatially separated according to their ion mobility coefficients K.

- After ions have been trapped and separated according to their mobilities, they will be released from the cell towards the mass spectrometer in a subsequent step called the elution phase. To this end, the strength of the electric field gradient will be decreased over time at a fixed, user-defined scan rate β. Under these conditions, ions of a given K will remain in the cell until the magnitude of the electric field on the plateau region $E_{plateau}$ reaches the trapping electric field E_{trap} value characteristics of these ions. Past this moment, the weaker electric field will no longer be able to hold the ions against the flow of buffer gas, resulting in their sequential release out of the TIMS cell by order of increasing K (i.e., decreasing CCS). Once all trapped ions have been eluted, the initial electric field gradient is restored to perform another cycle of trapping/elution.

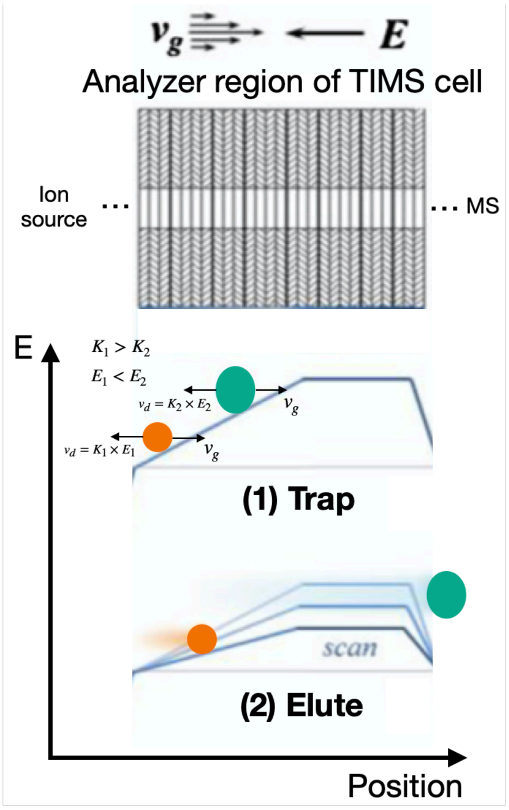

Figure 1.7 – Schematic representation of the electric field gradient magnitude as a function of position and time during the two main phases of TIMS: ion trapping and elution. Adapted from reference [67].

Compared to the other types of common low-field IMS (i.e., DTIMS and linear TWIMS), the 'trap-and-release' approach of the TIMS offers added flexibility[‡‡‡]. Indeed, contrary to these techniques, the speed, duty cycle and ion mobility range of an IM scan can be easily fine-tuned to meet the requirements of a specific application[67]. For example, while high resolution separations (>80) are routinely obtained in TIMS, ultra-high resolving power (>200) can be achieved in some cases, at the expense of longer separation times, lower sensitivity and/or limited mobility ranges. However, as with TWIMS, the only way that CCS measurements can currently be made is by using a calibration procedure[43]. The E/N regime is also thought to be quite high, but less than in TWIMS[68].

[‡‡‡] The more recent cyclic and SLIM versions of the TWIMS techniques are also characterized by a higher degree of flexibility.

Table 1.3 - Comparison of the technical characteristics and figures of merit of DTIMS, TWIMS, FAIMS and TIMS technologies.

	DTIMS	**TWIMS**	**FAIMS**	**TIMS**
CCS measurable?	Yes	Yes	No	Yes
Calibration required?	No, but performed when multi-field primary measurement method is not possible (e.g., for chromatography hyphenated analysis)	Yes	/	Yes
Typical E/N[55]	Low: 7-15 Td	Variable Low to high: ≤~150 Td	Low (CV) to high (DV)	Intermediate: 40 – 85 Td
Typical drift velocity[55]	10-80 m/s	200-300 m/s	/	120-170 m/s[69]
Resolving power (*Δ*CCS/CCS)[44]	Low: <80 (up to 200 after hrDM reprocessing[60] or using high pressure instruments)	Linear TWIMS Low: < 50 Cyclic TWIMS Low (single pass): 60-80 High to ultra-high (multi passes): 100-750[61] SLIM TWIMS High to ultra-high (13m single pass): 100-300[70]	Not comparable	High to ultra-high (tunable): 80-350
Sensitivity	Low to intermediate (up to 50% duty cycle[§§§] with multiplexing)	Intermediate	Fixed CV: High Scan mode: Low	Low to high (tunable duty cycle up to 100%)
Separation time	Dozens of ms	Linear TWIMS Dozens of ms Cyclic TWIMS Dozens (single pass) to hundreds of ms (multi passes) SLIM TWIMS Hundreds of ms (13m single pass)	Scan mode: seconds to minutes	Hundreds of ms
IM range	Full range	Linear TWIMS Full range Cyclic TWIMS Single pass: full range Multi passes: shorter range (tunable) SLIM TWIMS 13m single pass: full range	Fixed CV: single value (ΔK) Stepped CV: several values (ΔK) Scan mode: full range (ΔK)	Full range or shorter range (tunable)

[§§§] The duty cycle is the fraction of the continuous beam of ions that is collected for IM separation (i.e., a 50%$_{dc}$ means that, overall, half of the ions entering the IM-MS instruments will be send to the IM cell for analysis while the other half will be discarded).

Reference instrument(s)	6560 IMS-Q-ToF (Agilent)	Linear TWIMS Synapt G2-Si and Vion IMS-Q-ToF (Waters) Cyclic TWIMS Select cTWIMS (Waters) SLIM TWIMS MOBIE (MOBILion)	Faims Pro (Thermo) SelexION (Sciex)	timsTOF (Bruker)

1.3.4 - Advantages of IM for small molecules applications

Since IMS typically operates in the millisecond time frame, it can be easily integrated into traditional LC/GC-MS configurations[32]. Initially limited to the analysis of (large) biomolecules[47,71] (proteins, peptides, lipids, carbohydrates…), these workflows are now increasingly being used for the evaluation of small molecules such as metabolites[72], drugs[73] and, more recently, environmental contaminants[30,31].

IMS offers several advantages for small molecule applications when coupled to chromatography hyphenated MS: additional separation, enhanced identification and structural information.

A. Additional separation

During the ion mobility experiment, the compounds are separated according to their ion mobility coefficients *K*, which are partly orthogonal to retention time and m/z[74]. Therefore, IM adds another dimension of separation, resulting in an overall improvement of the peak capacity of the system[53]. This allows for the separation of some isomeric/isobaric compounds[75] as well as the cleaning of the MS and MS/MS spectra by IM filtering of interfering signals[76].

B. Identification

The CCS derived from the determination of the ion mobility coefficient of ions is a robust parameter that is not influenced by the type of sample matrix nor the type or conditions of chromatography[77]. In addition, the CCS is highly reproducible, both intralab[78,79] (short and long term precision) and interlab[78] (using the same IM technologies). Moreover, good agreement is also usually reported between the different commercially available platforms[80–82] (DTIMS, TWIMS and TIMS).

Taken together, these advantages make CCS a very useful and reliable parameter for increasing confidence in the identification of a compound. Experimental CCS values can indeed be compared with database values[83] (generated in-house or publicly available). However, due to the limited number of standards available and the time-consuming process of measuring CCS values, the number of available empirical CCS values is currently limited. To fill this gap, machine-learning based software have been developed to enable the large-scale prediction of CCS values for small molecules, typically with an acceptable error of less than 6%[84]. More advanced, but also more computationally intensive, computational modelling software can also be used for that purpose, the most accurate of which is the Trajectory Method (TM)[34,85]. Comparison of experimental CCS values with empirical and theoretical database values has been shown to reduce the number of false positives and the number of candidates in screening[83,86] and non-targeted workflows[87], respectively.

C. Structural information

Since the collision cross section is related to the size and shape of the ions, it can give an indication of their conformation in the gas phase[53]. Again, computational modelling software can be helpful to relate the experimentally measured CCS to putative ion conformation(s)[88].

1.3.5 - Overview of IM-MS applications for contaminants

The number of publications dealing with the analysis of contaminants by IM-MS has been steadily increasing since 2015, as indicated in **Figure 1.8**. This has coincided with the release of most of the current commercial instruments[33,45].

A. Situation before 2020 (start of PhD thesis)

The first applications of IM-MS for pollutants were dominated by LC-IM-MS workflows for the screening of pesticides[89–91] and drug residues[92,93] (human and veterinary) on TWIMS and DTIMS systems (**Figure 1.9**). These studies already highlighted the benefit of CCS as a robust ion parameter that could provide enhanced confidence in analyte annotation[90,94,95]. In addition, the analysis of several classes of compounds by direct infusion IM-MS demonstrated the potential of this analytical method to achieve very fast separations of analytes, including some isomers[96,97].

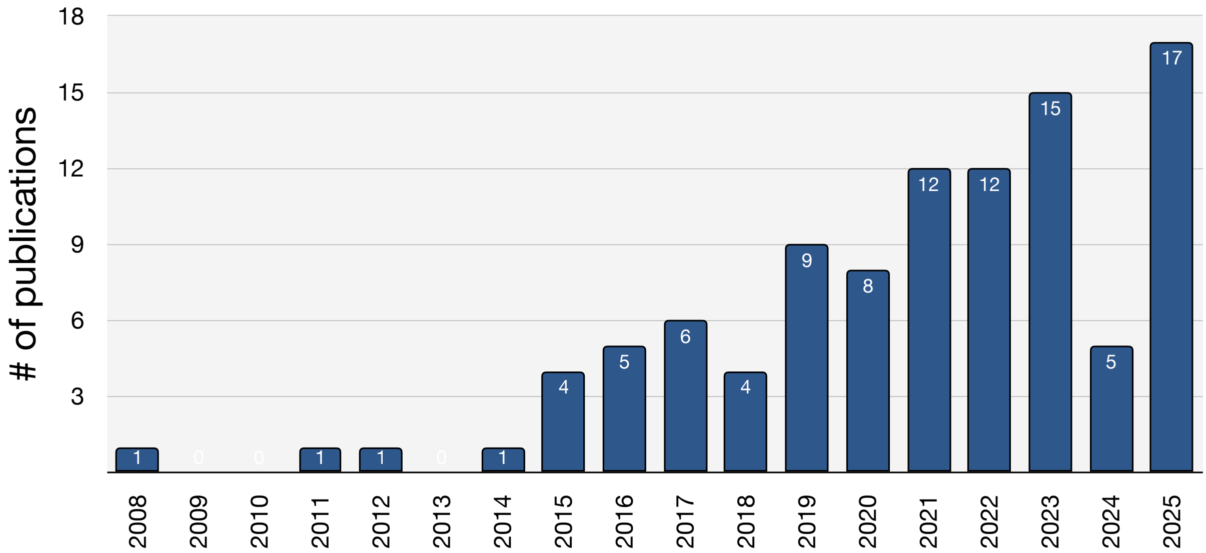

Figure 1.8 – Annual number of scientific publications related to contaminant analysis using IM-MS platforms from 2008 to the first half of 2025, based on a Scopus database search.

During this period, LC-hyphenated IM-MS applications clearly dominated GC-hyphenated ones (Figure 1.9): only a single study had reported the use of GC as a pre-separation technique coupled to IM-MS to analyse pesticides[98]. This observation can be extended to the other applications of IM-MS in general. While GC-IMS systems have historically been (and still are) very common[99,100], GC-IM-MS applications have been scarce. Moreover, the analysis of other types of contaminants, including halogenated POPs and emerging contaminants, had hardly been explored.

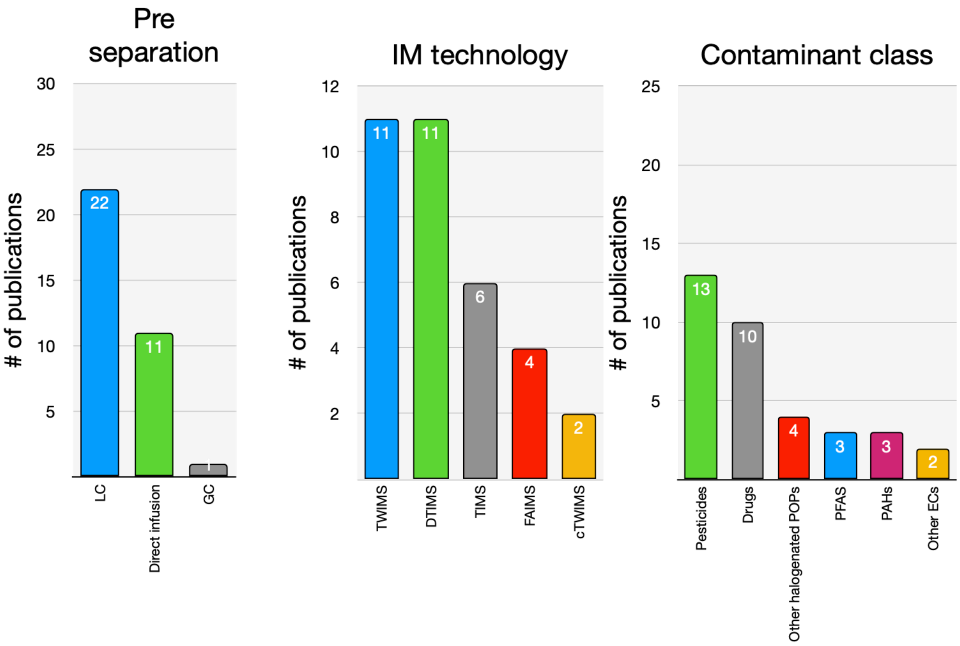

Figure 1.9 – Classification of pre-2020 applications by type of pre-separation, ion mobility technology, and class of contaminants.

B. Situation after 2020

Over the past five years, there has been a significant surge in IM-MS publications focused on contaminant analysis[30,31]. While liquid chromatography has remained the predominant front-end separation technique, a few GC-IM-MS systems were developed[79,101–107] (**Figure 1.10**). Notably, supercritical fluid chromatography (SFC) has been employed for the first time in this context[108]. In contrast, direct infusion approaches have seen more limited application.

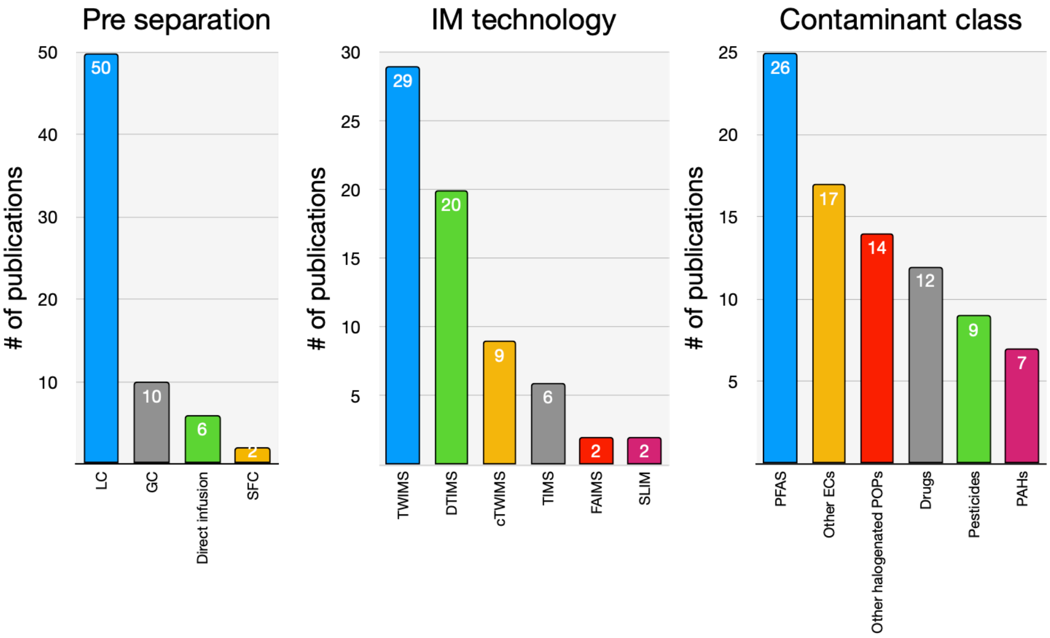

Figure 1.10 – Classification of post-2020 applications by type of pre-separation, ion mobility technology, and class of contaminants.

The adoption of high-resolution ion mobility technologies such as TIMS, cyclic and SLIM TWIMS has increased, underscoring their enhanced performance in distinguishing structurally similar analytes[109–111]. Additionally, there has been a clear shift in focus toward the analysis of emerging contaminants, with particular emphasis on per- and polyfluoroalkyl substances[103,112–115].

Overall, IM-MS applications in the field of contaminants have been dominated by the use of low resolution IM-MS systems coupled with liquid chromatography for the analysis of a wide range of contaminants.

1.4 References

(1) Rockström, J.; Steffen, W.; Noone, K.; Persson, Å.; Chapin, F. S. I.; Lambin, E.; Lenton, T. M.; Scheffer, M.; Folke, C.; Schellnhuber, H. J.; Nykvist, B.; De Wit, C. A.; Hughes, T.; Van Der Leeuw, S.; Rodhe, H.; Sörlin, S.; Snyder, P. K.; Costanza, R.; Svedin, U.; Falkenmark, M.; Karlberg, L.; Corell, R. W.; Fabry, V. J.; Hansen, J.; Walker, B.; Liverman, D.; Richardson, K.; Crutzen, P.; Foley, J. Planetary Boundaries: Exploring the Safe Operating Space for Humanity. *Ecol. Soc.* **2009**, *14* (2), art32. https://doi.org/10.5751/ES-03180-140232.

(2) *Mass Spectrometry in Food and Environmental Chemistry*; Picó, Y., Campo, J., Eds.; The Handbook of Environmental Chemistry; Springer International Publishing: Cham, 2023; Vol. 119. https://doi.org/10.1007/978-3-031-19093-3.

(3) Wang, Z.; Walker, G. W.; Muir, D. C. G.; Nagatani-Yoshida, K. Toward a Global Understanding of Chemical Pollution: A First Comprehensive Analysis of National and Regional Chemical Inventories. *Environ. Sci. Technol.* **2020**, *54* (5), 2575–2584. https://doi.org/10.1021/acs.est.9b06379.

(4) Persson, L.; Carney Almroth, B. M.; Collins, C. D.; Cornell, S.; De Wit, C. A.; Diamond, M. L.; Fantke, P.; Hassellöv, M.; MacLeod, M.; Ryberg, M. W.; Søgaard Jørgensen, P.; Villarrubia-Gómez, P.; Wang, Z.; Hauschild, M. Z. Outside the Safe Operating Space of the Planetary Boundary for Novel Entities. *Environ. Sci. Technol.* **2022**, *56* (3), 1510–1521. https://doi.org/10.1021/acs.est.1c04158.

(5) Carson, R. *Silent Spring*; Houghton Mifflin Company: Boston, 1962.

(6) Hollender, J.; Van Bavel, B.; Dulio, V.; Farmen, E.; Furtmann, K.; Koschorreck, J.; Kunkel, U.; Krauss, M.; Munthe, J.; Schlabach, M.; Slobodnik, J.; Stroomberg, G.; Ternes, T.; Thomaidis, N. S.; Togola, A.; Tornero, V. High Resolution Mass Spectrometry-Based Non-Target Screening Can Support Regulatory Environmental Monitoring and Chemicals Management. *Environ. Sci. Eur.* **2019**, *31* (1), 42. https://doi.org/10.1186/s12302-019-0225-x.

(7) Schwarzenbach, R. P.; Escher, B. I.; Fenner, K.; Hofstetter, T. B.; Johnson, C. A.; Von Gunten, U.; Wehrli, B. The Challenge of Micropollutants in Aquatic Systems. *Science* **2006**, *313* (5790), 1072–1077. https://doi.org/10.1126/science.1127291.

(8) Baird, C.; Cann, M. *Environmental Chemistry*, 5. ed., international ed.; Freeman: New York, 2012.

(9) Sauvé, S.; Desrosiers, M. A Review of What Is an Emerging Contaminant. *Chem. Cent. J.* **2014**, *8* (1), 15. https://doi.org/10.1186/1752-153X-8-15.

(10) Shaul, N. J.; Dodder, N. G.; Aluwihare, L. I.; Mackintosh, S. A.; Maruya, K. A.; Chivers, S. J.; Danil, K.; Weller, D. W.; Hoh, E. Nontargeted Biomonitoring of Halogenated Organic Compounds in Two Ecotypes of Bottlenose Dolphins (*Tursiops Truncatus*) from the Southern California Bight. *Environ. Sci. Technol.* **2015**, *49* (3), 1328–1338. https://doi.org/10.1021/es505156q.

(11) Jones, K. C. Persistent Organic Pollutants (POPs) and Related Chemicals in the Global Environment: Some Personal Reflections. *Environ. Sci. Technol.* **2021**, *55* (14), 9400–9412. https://doi.org/10.1021/acs.est.0c08093.

(12) Vetter, W. Marine Halogenated Natural Products of Environmental Relevance. In *Reviews of Environmental Contamination and Toxicology*; Ware, G. W., Whitacre, D. M., Albert, L. A., De Voogt, P., Gerba, C. P., Hutzinger, O., Knaak, J. B., Mayer, F. L., Morgan, D. P., Park, D. L., Tjeerdema, R. S., Yang, R. S. H., Gunther, F. A., Eds.; Reviews of Environmental Contamination and Toxicology; Springer New York: New York, NY, 2006; Vol. 188, pp 1–57. https://doi.org/10.1007/978-0-387-32964-2_1.

(13) Lay, J. O.; Liyanage, R.; Gidden, J. A. THE DEVELOPMENT OF A HIGH-RESOLUTION MASS SPECTROMETRY METHOD FOR ULTRA-TRACE ANALYSIS OF CHLORINATED DIOXINS IN

ENVIRONMENTAL AND BIOLOGICAL SAMPLES INCLUDING VIET NAM ERA VETERANS. *Mass Spectrom. Rev.* **2021**, *40* (3), 236–254. https://doi.org/10.1002/mas.21639.

(14) Jones, K. C.; De Voogt, P. Persistent Organic Pollutants (POPs): State of the Science. *Environ. Pollut.* **1999**, *100* (1–3), 209–221. https://doi.org/10.1016/S0269-7491(99)00098-6.

(15) *Stockholm Convention on Persistent Organic Pollutants (POPs)*. Stockholm Convention. https://www.pops.int (accessed 2025-06-16).

(16) Muir, D. C. G.; Howard, P. H. Are There Other Persistent Organic Pollutants? A Challenge for Environmental Chemists. *Environ. Sci. Technol.* **2006**, *40* (23), 7157–7166. https://doi.org/10.1021/es061677a.

(17) Arp, H. P. H.; Aurich, D.; Schymanski, E. L.; Sims, K.; Hale, S. E. Avoiding the Next Silent Spring: Our Chemical Past, Present, and Future. *Environ. Sci. Technol.* **2023**, *57* (16), 6355–6359. https://doi.org/10.1021/acs.est.3c01735.

(18) Hollender, J.; Schymanski, E. L.; Singer, H. P.; Ferguson, P. L. Nontarget Screening with High Resolution Mass Spectrometry in the Environment: Ready to Go? *Environ. Sci. Technol.* **2017**, *51* (20), 11505–11512. https://doi.org/10.1021/acs.est.7b02184.

(19) Schiewek, R.; Lorenz, M.; Giese, R.; Brockmann, K.; Benter, T.; Gäb, S.; Schmitz, O. J. Development of a Multipurpose Ion Source for LC-MS and GC-API MS. *Anal. Bioanal. Chem.* **2008**, *392* (1–2), 87–96. https://doi.org/10.1007/s00216-008-2255-x.

(20) McEwen, C. N.; McKay, R. G. A Combination Atmospheric Pressure LC/MS:GC/MS Ion Source: Advantages of Dual AP-LC/MS:GC/MS Instrumentation. *J. Am. Soc. Mass Spectrom.* **2005**, *16* (11), 1730–1738. https://doi.org/10.1016/j.jasms.2005.07.005.

(21) Revelsky, I. A.; Yashin, Y. S.; Sobolevsky, T. G.; Revelsky, A. I.; Miller, B.; Oriedo, V. Electron Ionization and Atmospheric Pressure Photochemical Ionization in Gas Chromatography-Mass Spectrometry Analysis of Amino Acids. *Eur. J. Mass Spectrom.* **2003**, *9* (5), 497–507. https://doi.org/10.1255/ejms.581.

(22) Hollender, J.; Schymanski, E. L.; Ahrens, L.; Alygizakis, N.; Béen, F.; Bijlsma, L.; Brunner, A. M.; Celma, A.; Fildier, A.; Fu, Q.; Gago-Ferrero, P.; Gil-Solsona, R.; Haglund, P.; Hansen, M.; Kaserzon, S.; Kruve, A.; Lamoree, M.; Margoum, C.; Meijer, J.; Merel, S.; Rauert, C.; Rostkowski, P.; Samanipour, S.; Schulze, B.; Schulze, T.; Singh, R. R.; Slobodnik, J.; Steininger-Mairinger, T.; Thomaidis, N. S.; Togola, A.; Vorkamp, K.; Vulliet, E.; Zhu, L.; Krauss, M. NORMAN Guidance on Suspect and Non-Target Screening in Environmental Monitoring. *Environ. Sci. Eur.* **2023**, *35* (1), 75. https://doi.org/10.1186/s12302-023-00779-4.

(23) Aalizadeh, R.; Nikolopoulou, V.; Alygizakis, N. A.; Thomaidis, N. S. First Novel Workflow for Semiquantification of Emerging Contaminants in Environmental Samples Analyzed by Gas Chromatography–Atmospheric Pressure Chemical Ionization–Quadrupole Time of Flight–Mass Spectrometry. *Anal. Chem.* **2022**, *94* (27), 9766–9774. https://doi.org/10.1021/acs.analchem.2c01432.

(24) Schymanski, E. L.; Jeon, J.; Gulde, R.; Fenner, K.; Ruff, M.; Singer, H. P.; Hollender, J. Identifying Small Molecules via High Resolution Mass Spectrometry: Communicating Confidence. *Environ. Sci. Technol.* **2014**, *48* (4), 2097–2098. https://doi.org/10.1021/es5002105.

(25) Ayala-Cabrera, J. F.; Santos, F. J.; Moyano, E. Recent Advances in Analytical Methodologies Based on Mass Spectrometry for the Environmental Analysis of Halogenated Organic Contaminants. *Trends Environ. Anal. Chem.* **2021**, *30*, e00122. https://doi.org/10.1016/j.teac.2021.e00122.

(26) Hernández, F.; Bakker, J.; Bijlsma, L.; De Boer, J.; Botero-Coy, A. M.; Bruinen De Bruin, Y.; Fischer, S.; Hollender, J.; Kasprzyk-Hordern, B.; Lamoree, M.; López, F. J.; Laak, T. L. T.; Van Leerdam, J. A.; Sancho, J. V.; Schymanski, E. L.; De Voogt, P.; Hogendoorn, E. A. The Role of Analytical Chemistry in Exposure Science: Focus on the Aquatic Environment. *Chemosphere* **2019**, *222*, 564–583. https://doi.org/10.1016/j.chemosphere.2019.01.118.

(27) Vaye, O.; Ngumbu, R. S.; Xia, D. A Review of the Application of Comprehensive Two-Dimensional Gas Chromatography MS-Based Techniques for the Analysis of Persistent Organic

Pollutants and Ultra-Trace Level of Organic Pollutants in Environmental Samples. *Rev. Anal. Chem.* **2022**, *41* (1), 63–73. https://doi.org/10.1515/revac-2022-0034.

(28) Muscalu, A. M.; Górecki, T. Comprehensive Two-Dimensional Gas Chromatography in Environmental Analysis. *TrAC Trends Anal. Chem.* **2018**, *106*, 225–245. https://doi.org/10.1016/j.trac.2018.07.001.

(29) Ouyang, X.; Leonards, P.; Legler, J.; Van Der Oost, R.; De Boer, J.; Lamoree, M. Comprehensive Two-Dimensional Liquid Chromatography Coupled to High Resolution Time of Flight Mass Spectrometry for Chemical Characterization of Sewage Treatment Plant Effluents. *J. Chromatogr. A* **2015**, *1380*, 139–145. https://doi.org/10.1016/j.chroma.2014.12.075.

(30) Celma, A.; Alygizakis, N.; Belova, L.; Bijlsma, L.; Fabregat-Safont, D.; Menger, F.; Gil-Solsona, R. Ion Mobility Separation Coupled to High-Resolution Mass Spectrometry in Environmental Analysis – Current State and Future Potential. *Trends Environ. Anal. Chem.* **2024**, *43*, e00239. https://doi.org/10.1016/j.teac.2024.e00239.

(31) Song, X.-C.; Canellas, E.; Dreolin, N.; Goshawk, J.; Lv, M.; Qu, G.; Nerin, C.; Jiang, G. Application of Ion Mobility Spectrometry and the Derived Collision Cross Section in the Analysis of Environmental Organic Micropollutants. *Environ. Sci. Technol.* **2023**, *57* (51), 21485–21502. https://doi.org/10.1021/acs.est.3c03686.

(32) Zheng, X.; Wojcik, R.; Zhang, X.; Ibrahim, Y. M.; Burnum-Johnson, K. E.; Orton, D. J.; Monroe, M. E.; Moore, R. J.; Smith, R. D.; Baker, E. S. Coupling Front-End Separations, Ion Mobility Spectrometry, and Mass Spectrometry For Enhanced Multidimensional Biological and Environmental Analyses. *Annu. Rev. Anal. Chem.* **2017**, *10* (1), 71–92. https://doi.org/10.1146/annurev-anchem-061516-045212.

(33) Eiceman, G. A.; Karpas, Z.; Hill Jr., H. H. *Ion Mobility Spectrometry*, 0 ed.; CRC Press, 2013. https://doi.org/10.1201/b16109.

(34) Viehland, L. A. *Gaseous Ion Mobility, Diffusion, and Reaction*; Springer Series on Atomic, Optical, and Plasma Physics Ser; Springer: Cham, 2018.

(35) Cohen, M. J.; Karasek, F. W. Plasma Chromatography --A New Dimension for Gas Chromatography and Mass Spectrometry. *J. Chromatogr. Sci.* **1970**, *8* (6), 330–337. https://doi.org/10.1093/chromsci/8.6.330.

(36) Karasek, F. W. Plasma Chromatography. *Anal. Chem.* **1974**, *46* (8), 710A-720A. https://doi.org/10.1021/ac60344a724.

(37) Karasek, F. W. Plasma Chromatography of the Polychlorinated Biphenyls. *Anal. Chem.* **1971**, *43* (14), 1982–1986. https://doi.org/10.1021/ac60308a024.

(38) Puton, J.; Namieśnik, J. Ion Mobility Spectrometry: Current Status and Application for Chemical Warfare Agents Detection. *TrAC Trends Anal. Chem.* **2016**, *85*, 10–20. https://doi.org/10.1016/j.trac.2016.06.002.

(39) Mäkinen, M. A.; Anttalainen, O. A.; Sillanpää, M. E. T. Ion Mobility Spectrometry and Its Applications in Detection of Chemical Warfare Agents. *Anal. Chem.* **2010**, *82* (23), 9594–9600. https://doi.org/10.1021/ac100931n.

(40) Ewing, R. A Critical Review of Ion Mobility Spectrometry for the Detection of Explosives and Explosive Related Compounds. *Talanta* **2001**, *54* (3), 515–529. https://doi.org/10.1016/S0039-9140(00)00565-8.

(41) Bohrer, B. C.; Merenbloom, S. I.; Koeniger, S. L.; Hilderbrand, A. E.; Clemmer, D. E. Biomolecule Analysis by Ion Mobility Spectrometry. *Annu. Rev. Anal. Chem.* **2008**, *1* (1), 293–327. https://doi.org/10.1146/annurev.anchem.1.031207.113001.

(42) May, J. C.; McLean, J. A. Ion Mobility-Mass Spectrometry: Time-Dispersive Instrumentation. *Anal. Chem.* **2015**, *87* (3), 1422–1436. https://doi.org/10.1021/ac504720m.

(43) Gabelica, V.; Shvartsburg, A. A.; Afonso, C.; Barran, P.; Benesch, J. L. P.; Bleiholder, C.; Bowers, M. T.; Bilbao, A.; Bush, M. F.; Campbell, J. L.; Campuzano, I. D. G.; Causon, T.; Clowers, B. H.; Creaser, C. S.; De Pauw, E.; Far, J.; Fernandez-Lima, F.; Fjeldsted, J. C.; Giles, K.; Groessl, M.; Hogan, C. J.; Hann, S.; Kim, H. I.; Kurulugama, R. T.; May, J. C.; McLean, J. A.; Pagel, K.;

Richardson, K.; Ridgeway, M. E.; Rosu, F.; Sobott, F.; Thalassinos, K.; Valentine, S. J.; Wyttenbach, T. Recommendations for Reporting Ion Mobility Mass Spectrometry Measurements. *Mass Spectrom. Rev.* **2019**, *38* (3), 291–320. https://doi.org/10.1002/mas.21585.

(44) Kirk, A. T.; Bohnhorst, A.; Raddatz, C.-R.; Allers, M.; Zimmermann, S. Ultra-High-Resolution Ion Mobility Spectrometry—Current Instrumentation, Limitations, and Future Developments. *Anal. Bioanal. Chem.* **2019**, *411* (24), 6229–6246. https://doi.org/10.1007/s00216-019-01807-0.

(45) Delafield, D. G.; Lu, G.; Kaminsky, C. J.; Li, L. High-End Ion Mobility Mass Spectrometry: A Current Review of Analytical Capacity in Omics Applications and Structural Investigations. *TrAC Trends Anal. Chem.* **2022**, *157*, 116761. https://doi.org/10.1016/j.trac.2022.116761.

(46) D'Atri, V.; Causon, T.; Hernandez-Alba, O.; Mutabazi, A.; Veuthey, J.; Cianferani, S.; Guillarme, D. Adding a New Separation Dimension to MS and LC–MS: What Is the Utility of Ion Mobility Spectrometry? *J. Sep. Sci.* **2018**, *41* (1), 20–67. https://doi.org/10.1002/jssc.201700919.

(47) Lanucara, F.; Holman, S. W.; Gray, C. J.; Eyers, C. E. The Power of Ion Mobility-Mass Spectrometry for Structural Characterization and the Study of Conformational Dynamics. *Nat. Chem.* **2014**, *6* (4), 281–294. https://doi.org/10.1038/nchem.1889.

(48) Christofi, E.; Barran, P. Ion Mobility Mass Spectrometry (IM-MS) for Structural Biology: Insights Gained by Measuring Mass, Charge, and Collision Cross Section. *Chem. Rev.* **2023**, *123* (6), 2902–2949. https://doi.org/10.1021/acs.chemrev.2c00600.

(49) Metz, T. O.; Baker, E. S.; Schymanski, E. L.; Renslow, R. S.; Thomas, D. G.; Causon, T. J.; Webb, I. K.; Hann, S.; Smith, R. D.; Teeguarden, J. G. Integrating Ion Mobility Spectrometry Into Mass Spectrometry-Based Exposome Measurements: What Can It Add and How Far Can It Go? *Bioanalysis* **2017**, *9* (1), 81–98. https://doi.org/10.4155/bio-2016-0244.

(50) Burnum-Johnson, K. E.; Zheng, X.; Dodds, J. N.; Ash, J.; Fourches, D.; Nicora, C. D.; Wendler, J. P.; Metz, T. O.; Waters, K. M.; Jansson, J. K.; Smith, R. D.; Baker, E. S. Ion Mobility Spectrometry and the Omics: Distinguishing Isomers, Molecular Classes and Contaminant Ions in Complex Samples. *TrAC Trends Anal. Chem.* **2019**, *116*, 292–299. https://doi.org/10.1016/j.trac.2019.04.022.

(51) Larriba-Andaluz, C.; Prell, J. S. Fundamentals of Ion Mobility in the Free Molecular Regime. Interlacing the Past, Present and Future of Ion Mobility Calculations. *Int. Rev. Phys. Chem.* **2020**, *39* (4), 569–623. https://doi.org/10.1080/0144235X.2020.1826708.

(52) Dodds, J. N.; Baker, E. S. Ion Mobility Spectrometry: Fundamental Concepts, Instrumentation, Applications, and the Road Ahead. *J. Am. Soc. Mass Spectrom.* **2019**, *30* (11), 2185–2195. https://doi.org/10.1007/s13361-019-02288-2.

(53) Gabelica, V. CHAPTER 1. Ion Mobility–Mass Spectrometry: An Overview. In *New Developments in Mass Spectrometry*; Ashcroft, A. E., Sobott, F., Eds.; Royal Society of Chemistry: Cambridge, 2021; pp 1–25. https://doi.org/10.1039/9781839162886-00001.

(54) Lalli, P. M.; Corilo, Y. E.; Fasciotti, M.; Riccio, M. F.; De Sa, G. F.; Daroda, R. J.; Souza, G. H. M. F.; McCullagh, M.; Bartberger, M. D.; Eberlin, M. N.; Campuzano, I. D. G. Baseline Resolution of Isomers by Traveling Wave Ion Mobility Mass Spectrometry: Investigating the Effects of Polarizable Drift Gases and Ionic Charge Distribution. *J. Mass Spectrom.* **2013**, *48* (9), 989–997. https://doi.org/10.1002/jms.3245.

(55) Gabelica, V.; Marklund, E. Fundamentals of Ion Mobility Spectrometry. *Curr. Opin. Chem. Biol.* **2018**, *42*, 51–59. https://doi.org/10.1016/j.cbpa.2017.10.022.

(56) Wyttenbach, T.; Bleiholder, C.; Bowers, M. T. Factors Contributing to the Collision Cross Section of Polyatomic Ions in the Kilodalton to Gigadalton Range: Application to Ion Mobility Measurements. *Anal. Chem.* **2013**, *85* (4), 2191–2199. https://doi.org/10.1021/ac3029008.

(57) Bleiholder, C.; Liu, F. C.; Chai, M. Comment on Effective Temperature and Structural Rearrangement in Trapped Ion Mobility Spectrometry. *Anal. Chem.* **2020**, *92* (24), 16329–16333. https://doi.org/10.1021/acs.analchem.0c02052.

(58) Bleiholder, C. Towards Measuring Ion Mobilities in Non-Stationary Gases and Non-Uniform and Dynamic Electric Fields (I). Transport Equation. *Int. J. Mass Spectrom.* **2016**, *399–400*, 1–9. https://doi.org/10.1016/j.ijms.2016.01.003.

(59) Cumeras, R.; Figueras, E.; Davis, C. E.; Baumbach, J. I.; Gràcia, I. Review on Ion Mobility Spectrometry. Part 1: Current Instrumentation. *The Analyst* **2015**, *140* (5), 1376–1390. https://doi.org/10.1039/C4AN01100G.

(60) May, J. C.; Knochenmuss, R.; Fjeldsted, J. C.; McLean, J. A. Resolution of Isomeric Mixtures in Ion Mobility Using a Combined Demultiplexing and Peak Deconvolution Technique. *Anal. Chem.* **2020**, *92* (14), 9482–9492. https://doi.org/10.1021/acs.analchem.9b05718.

(61) Giles, K.; Ujma, J.; Wildgoose, J.; Pringle, S.; Richardson, K.; Langridge, D.; Green, M. A Cyclic Ion Mobility-Mass Spectrometry System. *Anal. Chem.* **2019**, *91* (13), 8564–8573. https://doi.org/10.1021/acs.analchem.9b01838.

(62) Tolmachev, A. V.; Webb, I. K.; Ibrahim, Y. M.; Garimella, S. V. B.; Zhang, X.; Anderson, G. A.; Smith, R. D. Characterization of Ion Dynamics in Structures for Lossless Ion Manipulations. *Anal. Chem.* **2014**, *86* (18), 9162–9168. https://doi.org/10.1021/ac502054p.

(63) Morsa, D.; Gabelica, V.; De Pauw, E. Effective Temperature of Ions in Traveling Wave Ion Mobility Spectrometry. *Anal. Chem.* **2011**, *83* (14), 5775–5782. https://doi.org/10.1021/ac201509p.

(64) Fernandez-Lima, F.; Kaplan, D. A.; Suetering, J.; Park, M. A. Gas-Phase Separation Using a Trapped Ion Mobility Spectrometer. *Int. J. Ion Mobil. Spectrom.* **2011**, *14* (2–3), 93–98. https://doi.org/10.1007/s12127-011-0067-8.

(65) Hernandez, D. R.; DeBord, J. D.; Ridgeway, M. E.; Kaplan, D. A.; Park, M. A.; Fernandez-Lima, F. Ion Dynamics in a Trapped Ion Mobility Spectrometer. *The Analyst* **2014**, *139* (8), 1913–1921. https://doi.org/10.1039/C3AN02174B.

(66) Hernandez, D. R.; DeBord, J. D.; Ridgeway, M. E.; Kaplan, D. A.; Park, M. A.; Fernandez-Lima, F. Ion Dynamics in a Trapped Ion Mobility Spectrometer. *The Analyst* **2014**, *139* (8), 1913–1921. https://doi.org/10.1039/C3AN02174B.

(67) Ridgeway, M. E.; Lubeck, M.; Jordens, J.; Mann, M.; Park, M. A. Trapped Ion Mobility Spectrometry: A Short Review. *Int. J. Mass Spectrom.* **2018**, *425*, 22–35. https://doi.org/10.1016/j.ijms.2018.01.006.

(68) Morsa, D.; Hanozin, E.; Eppe, G.; Quinton, L.; Gabelica, V.; Pauw, E. D. Effective Temperature and Structural Rearrangement in Trapped Ion Mobility Spectrometry. *Anal. Chem.* **2020**, *92* (6), 4573–4582. https://doi.org/10.1021/acs.analchem.9b05850.

(69) Silveira, J. A.; Michelmann, K.; Ridgeway, M. E.; Park, M. A. Fundamentals of Trapped Ion Mobility Spectrometry Part II: Fluid Dynamics. *J. Am. Soc. Mass Spectrom.* **2016**, *27* (4), 585–595. https://doi.org/10.1007/s13361-015-1310-z.

(70) May, J. C.; Leaptrot, K. L.; Rose, B. S.; Moser, K. L. W.; Deng, L.; Maxon, L.; DeBord, D.; McLean, J. A. Resolving Power and Collision Cross Section Measurement Accuracy of a Prototype High-Resolution Ion Mobility Platform Incorporating Structures for Lossless Ion Manipulation. *J. Am. Soc. Mass Spectrom.* **2021**, *32* (4), 1126–1137. https://doi.org/10.1021/jasms.1c00056.

(71) McLean, J. A.; Ruotolo, B. T.; Gillig, K. J.; Russell, D. H. Ion Mobility–Mass Spectrometry: A New Paradigm for Proteomics. *Int. J. Mass Spectrom.* **2005**, *240* (3), 301–315. https://doi.org/10.1016/j.ijms.2004.10.003.

(72) Paglia, G.; Smith, A. J.; Astarita, G. Ion Mobility Mass Spectrometry in the Omics Era: Challenges and Opportunities for Metabolomics and Lipidomics. *Mass Spectrom. Rev.* **2022**, *41* (5), 722–765. https://doi.org/10.1002/mas.21686.

(73) Ross, D. H.; Xu, L. Determination of Drugs and Drug Metabolites by Ion Mobility-Mass Spectrometry: A Review. *Anal. Chim. Acta* **2021**, *1154*, 338270. https://doi.org/10.1016/j.aca.2021.338270.

(74) Causon, T. J.; Hann, S. Theoretical Evaluation of Peak Capacity Improvements by Use of Liquid Chromatography Combined with Drift Tube Ion Mobility-Mass Spectrometry. *J. Chromatogr. A* **2015**, *1416*, 47–56. https://doi.org/10.1016/j.chroma.2015.09.009.

(75) Dodds, J. N.; May, J. C.; McLean, J. A. Correlating Resolving Power, Resolution, and Collision Cross Section: Unifying Cross-Platform Assessment of Separation Efficiency in Ion Mobility Spectrometry. *Anal. Chem.* **2017**, *89* (22), 12176–12184. https://doi.org/10.1021/acs.analchem.7b02827.

(76) Menger, F.; Celma, A.; Schymanski, E. L.; Lai, F. Y.; Bijlsma, L.; Wiberg, K.; Hernández, F.; Sancho, J. V.; Ahrens, L. Enhancing Spectral Quality in Complex Environmental Matrices: Supporting Suspect and Non-Target Screening in Zebra Mussels with Ion Mobility. *Environ. Int.* **2022**, *170*, 107585. https://doi.org/10.1016/j.envint.2022.107585.

(77) Celma, A.; Sancho, J. V.; Schymanski, E. L.; Fabregat-Safont, D.; Ibáñez, M.; Goshawk, J.; Barknowitz, G.; Hernández, F.; Bijlsma, L. Improving Target and Suspect Screening High-Resolution Mass Spectrometry Workflows in Environmental Analysis by Ion Mobility Separation. *Environ. Sci. Technol.* **2020**, *54* (23), 15120–15131. https://doi.org/10.1021/acs.est.0c05713.

(78) Stow, S. M.; Causon, T. J.; Zheng, X.; Kurulugama, R. T.; Mairinger, T.; May, J. C.; Rennie, E. E.; Baker, E. S.; Smith, R. D.; McLean, J. A.; Hann, S.; Fjeldsted, J. C. An Interlaboratory Evaluation of Drift Tube Ion Mobility–Mass Spectrometry Collision Cross Section Measurements. *Anal. Chem.* **2017**, *89* (17), 9048–9055. https://doi.org/10.1021/acs.analchem.7b01729.

(79) Izquierdo-Sandoval, D.; Fabregat-Safont, D.; Lacalle-Bergeron, L.; Sancho, J. V.; Hernández, F.; Portoles, T. Benefits of Ion Mobility Separation in GC-APCI-HRMS Screening: From the Construction of a CCS Library to the Application to Real-World Samples. *Anal. Chem.* **2022**, *94* (25), 9040–9047. https://doi.org/10.1021/acs.analchem.2c01118.

(80) Hinnenkamp, V.; Klein, J.; Meckelmann, S. W.; Balsaa, P.; Schmidt, T. C.; Schmitz, O. J. Comparison of CCS Values Determined by Traveling Wave Ion Mobility Mass Spectrometry and Drift Tube Ion Mobility Mass Spectrometry. *Anal. Chem.* **2018**, *90* (20), 12042–12050. https://doi.org/10.1021/acs.analchem.8b02711.

(81) Belova, L.; Celma, A.; Van Haesendonck, G.; Lemière, F.; Sancho, J. V.; Covaci, A.; Van Nuijs, A. L. N.; Bijlsma, L. Revealing the Differences in Collision Cross Section Values of Small Organic Molecules Acquired by Different Instrumental Designs and Prediction Models. *Anal. Chim. Acta* **2022**, *1229*, 340361. https://doi.org/10.1016/j.aca.2022.340361.

(82) Belova, L.; Caballero-Casero, N.; Ballesteros, A.; Poma, G.; Van Nuijs, A. L. N.; Covaci, A. Trapped and Drift-tube Ion-mobility Spectrometry for the Analysis of Environmental Contaminants: Comparability of Collision Cross-section Values and Resolving Power. *Rapid Commun. Mass Spectrom.* **2024**, *38* (21), e9901. https://doi.org/10.1002/rcm.9901.

(83) Celma, A.; Ahrens, L.; Gago-Ferrero, P.; Hernández, F.; López, F.; Lundqvist, J.; Pitarch, E.; Sancho, J. V.; Wiberg, K.; Bijlsma, L. The Relevant Role of Ion Mobility Separation in LC-HRMS Based Screening Strategies for Contaminants of Emerging Concern in the Aquatic Environment. *Chemosphere* **2021**, *280*, 130799. https://doi.org/10.1016/j.chemosphere.2021.130799.

(84) Zhou, Z.; Tu, J.; Zhu, Z.-J. Advancing the Large-Scale CCS Database for Metabolomics and Lipidomics at the Machine-Learning Era. *Curr. Opin. Chem. Biol.* **2018**, *42*, 34–41. https://doi.org/10.1016/j.cbpa.2017.10.033.

(85) Kartowikromo, K. Y.; Olajide, O. E.; Hamid, A. M. Collision Cross Section Measurement and Prediction Methods in Omics. *J. Mass Spectrom.* **2023**, *58* (9), e4973. https://doi.org/10.1002/jms.4973.

(86) Regueiro, J.; Negreira, N.; Hannisdal, R.; Berntssen, M. H. G. Targeted Approach for Qualitative Screening of Pesticides in Salmon Feed by Liquid Chromatography Coupled to Traveling-Wave Ion Mobility/Quadrupole Time-of-Flight Mass Spectrometry. *Food Control* **2017**, *78*, 116–125. https://doi.org/10.1016/j.foodcont.2017.02.053.

(87) Zhou, Z.; Luo, M.; Chen, X.; Yin, Y.; Xiong, X.; Wang, R.; Zhu, Z.-J. Ion Mobility Collision Cross-Section Atlas for Known and Unknown Metabolite Annotation in Untargeted Metabolomics. *Nat. Commun.* **2020**, *11* (1), 4334. https://doi.org/10.1038/s41467-020-18171-8.

(88) Schneiders, A. L.; Far, J.; Belova, L.; Fry, A.; Covaci, A.; Baker, E. S.; De Pauw, E.; Eppe, G. Structural Characterization of Dimeric Perfluoroalkyl Carboxylic Acid Using Experimental and Theoretical Ion Mobility Spectrometry Analyses. *J. Am. Soc. Mass Spectrom.* **2025**, *36* (4), 850–861. https://doi.org/10.1021/jasms.5c00007.

(89) Bauer, A.; Luetjohann, J.; Hanschen, F. S.; Schreiner, M.; Kuballa, J.; Jantzen, E.; Rohn, S. Identification and Characterization of Pesticide Metabolites in Brassica Species by Liquid Chromatography Travelling Wave Ion Mobility Quadrupole Time-of-Flight Mass Spectrometry (UPLC-TWIMS-QTOF-MS). *Food Chem.* **2018**, *244*, 292–303. https://doi.org/10.1016/j.foodchem.2017.09.131.

(90) Goscinny, S.; Joly, L.; De Pauw, E.; Hanot, V.; Eppe, G. Travelling-Wave Ion Mobility Time-of-Flight Mass Spectrometry as an Alternative Strategy for Screening of Multi-Class Pesticides in Fruits and Vegetables. *J. Chromatogr. A* **2015**, *1405*, 85–93. https://doi.org/10.1016/j.chroma.2015.05.057.

(91) Goscinny, S.; McCullagh, M.; Far, J.; De Pauw, E.; Eppe, G. Towards the Use of Ion Mobility Mass Spectrometry Derived Collision Cross Section as a Screening Approach for Unambiguous Identification of Targeted Pesticides in Food. *Rapid Commun. Mass Spectrom.* **2019**, *33* (S2), 34–48. https://doi.org/10.1002/rcm.8395.

(92) Emhofer, L.; Himmelsbach, M.; Buchberger, W.; Klampfl, C. W. High-Performance Liquid Chromatography Drift-Tube Ion-Mobility Quadrupole Time-of-Flight/Mass Spectrometry for the Identity Confirmation and Characterization of Metabolites from Three Statins (Lipid-Lowering Drugs) in the Model Plant Cress (Lepidium Sativum) after Uptake from Water. *J. Chromatogr. A* **2019**, *1592*, 122–132. https://doi.org/10.1016/j.chroma.2019.01.049.

(93) Hinnenkamp, V.; Balsaa, P.; Schmidt, T. C. Quantitative Screening and Prioritization Based on UPLC-IM-Q-TOF-MS as an Alternative Water Sample Monitoring Strategy. *Anal. Bioanal. Chem.* **2019**, *411* (23), 6101–6110. https://doi.org/10.1007/s00216-019-01994-w.

(94) Regueiro, J.; Negreira, N.; Berntssen, M. H. G. Ion-Mobility-Derived Collision Cross Section as an Additional Identification Point for Multiresidue Screening of Pesticides in Fish Feed. *Anal. Chem.* **2016**, *88* (22), 11169–11177. https://doi.org/10.1021/acs.analchem.6b03381.

(95) Bijlsma, L.; Berntssen, M. H. G.; Merel, S. A Refined Nontarget Workflow for the Investigation of Metabolites through the Prioritization by in Silico Prediction Tools. *Anal. Chem.* **2019**, *91* (9), 6321–6328. https://doi.org/10.1021/acs.analchem.9b01218.

(96) Adams, K. J.; Montero, D.; Aga, D.; Fernandez-Lima, F. Isomer Separation of Polybrominated Diphenyl Ether Metabolites Using nanoESI-TIMS-MS. *Int. J. Ion Mobil. Spectrom.* **2016**, *19* (2–3), 69–76. https://doi.org/10.1007/s12127-016-0198-z.

(97) Zheng, X.; Dupuis, K. T.; Aly, N. A.; Zhou, Y.; Smith, F. B.; Tang, K.; Smith, R. D.; Baker, E. S. Utilizing Ion Mobility Spectrometry and Mass Spectrometry for the Analysis of Polycyclic Aromatic Hydrocarbons, Polychlorinated Biphenyls, Polybrominated Diphenyl Ethers and Their Metabolites. *Anal. Chim. Acta* **2018**, *1037*, 265–273. https://doi.org/10.1016/j.aca.2018.02.054.

(98) Lipok, C.; Hippler, J.; Schmitz, O. J. A Four Dimensional Separation Method Based on Continuous Heart-Cutting Gas Chromatography with Ion Mobility and High Resolution Mass Spectrometry. *J. Chromatogr. A* **2018**, *1536*, 50–57. https://doi.org/10.1016/j.chroma.2017.07.013.

(99) Márquez-Sillero, I.; Aguilera-Herrador, E.; Cárdenas, S.; Valcárcel, M. Ion-Mobility Spectrometry for Environmental Analysis. *TrAC Trends Anal. Chem.* **2011**, *30* (5), 677–690. https://doi.org/10.1016/j.trac.2010.12.007.

(100) Vautz, W.; Franzke, J.; Zampolli, S.; Elmi, I.; Liedtke, S. On the Potential of Ion Mobility Spectrometry Coupled to GC Pre-Separation – A Tutorial. *Anal. Chim. Acta* **2018**, *1024*, 52–64. https://doi.org/10.1016/j.aca.2018.02.052.

(101) Olanrewaju, C. A.; Ramirez, C. E.; Fernandez-Lima, F. Comprehensive Screening of Polycyclic Aromatic Hydrocarbons and Similar Compounds Using GC–APLI–TIMS–TOFMS/GC–EI–MS. *Anal. Chem.* **2021**, *93* (15), 6080–6087. https://doi.org/10.1021/acs.analchem.0c04525.

(102) MacNeil, A.; Li, X.; Amiri, R.; Muir, D. C. G.; Simpson, A.; Simpson, M. J.; Dorman, F. L.; Jobst, K. J. Gas Chromatography-(Cyclic) Ion Mobility Mass Spectrometry: A Novel Platform for the Discovery of Unknown Per-/Polyfluoroalkyl Substances. *Anal. Chem.* **2022**, *94* (31), 11096–11103. https://doi.org/10.1021/acs.analchem.2c02325.

(103) Steeves, K. L.; Bissram, M. J.; Kleywegt, S.; Stevens, D.; Dorman, F. L.; Simpson, A. J.; Simpson, M. J.; Cahill, L. S.; Jobst, K. J. Nontargeted Screening Reveals Fluorotelomer Ethoxylates in Indoor Dust and Industrial Wastewater. *Environ. Int.* **2023**, *171*, 107634. https://doi.org/10.1016/j.envint.2022.107634.

(104) Singh, R. R.; Aminot, Y.; Héas-Moisan, K.; Preud'homme, H.; Munschy, C. Cracked and Shucked: GC-APCI-IMS-HRMS Facilitates Identification of Unknown Halogenated Organic Chemicals in French Marine Bivalves. *Environ. Int.* **2023**, *178*, 108094. https://doi.org/10.1016/j.envint.2023.108094.

(105) Izquierdo-Sandoval, D.; Sancho, J. V.; Hernández, F.; Portoles, T. Approaches for GC-HRMS Screening of Organic Microcontaminants: GC-APCI-IMS-QTOF versus GC-EI-QOrbitrap. *Environ. Sci. Technol.* **2025**, *59* (5), 2436–2448. https://doi.org/10.1021/acs.est.4c11032.

(106) Shi, X.; Langberg, H. A.; Sobek, A.; Benskin, J. P. Exploiting Molecular Ions for Screening Hydrophobic Contaminants in Sediments Using Gas Chromatography-Atmospheric Pressure Chemical Ionization-Ion Mobility-Mass Spectrometry. *Environ. Sci. Technol.* **2025**, *59* (9), 4699–4708. https://doi.org/10.1021/acs.est.4c13059.

(107) González-Hernández, M.; Portolés, T.; Mokh, S.; Sancho, J. V.; Calduch-Giner, J.; Nacher-Mestre, J.; Pérez-Sánchez, J.; Ibáñez, M. Comprehensive Screening of the Contaminants in Feeds and Gilthead Sea Bream (Sparus Aurata) Fillets by GC and LC Coupled to HRMS Technique. *Microchem. J.* **2025**, *213*, 113854. https://doi.org/10.1016/j.microc.2025.113854.

(108) Shi, Y.; Jin, H.-F.; Shi, M.-Z.; Cao, J.; Ye, L.-H. Carbon Black-Assisted Miniaturized Solid-Phase Extraction of Carbamate Residues from Ginger by Supercritical Fluid Chromatography Combined with Ion Mobility Quadrupole Time-of-Flight Mass Spectrometry. *Microchem. J.* **2023**, *194*, 109335. https://doi.org/10.1016/j.microc.2023.109335.

(109) McCullagh, M.; Goscinny, S.; Palmer, M.; Ujma, J. Investigations into Pesticide Charge Site Isomers Using Conventional IM and cIM Systems. *Talanta* **2021**, *234*, 122604. https://doi.org/10.1016/j.talanta.2021.122604.

(110) Wijayahena, M. K.; Moreira, I. S.; Castro, P. M. L.; Dowd, S.; Marciesky, M. I.; Ng, C.; Aga, D. S. PFAS Biodegradation by Labrys Portucalensis F11: Evidence of Chain Shortening and Identification of Metabolites of PFOS, 6:2 FTS, and 5:3 FTCA. *Sci. Total Environ.* **2025**, *959*, 178348. https://doi.org/10.1016/j.scitotenv.2024.178348.

(111) Sabatini, H. M.; Pettit-Bacovin, T.; Aderorho, R.; Chouinard, C. D. Multidimensional Separations for Characterization of Isomeric PFAS Using SLIM High-Resolution Ion Mobility and Tandem Mass Spectrometry. *Anal. Chem.* **2025**, *97* (12), 6727–6734. https://doi.org/10.1021/acs.analchem.4c06985.

(112) Dodds, J. N.; Hopkins, Z. R.; Knappe, D. R. U.; Baker, E. S. Rapid Characterization of Per- and Polyfluoroalkyl Substances (PFAS) by Ion Mobility Spectrometry–Mass Spectrometry (IMS-MS). *Anal. Chem.* **2020**, *92* (6), 4427–4435. https://doi.org/10.1021/acs.analchem.9b05364.

(113) Kirkwood, K. I.; Fleming, J.; Nguyen, H.; Reif, D. M.; Baker, E. S.; Belcher, S. M. Utilizing Pine Needles to Temporally and Spatially Profile Per- and Polyfluoroalkyl Substances (PFAS). *Environ. Sci. Technol.* **2022**, *56* (6), 3441–3451. https://doi.org/10.1021/acs.est.1c06483.

(114) Kirkwood-Donelson, K. I.; Dodds, J. N.; Schnetzer, A.; Hall, N.; Baker, E. S. Uncovering Per- and Polyfluoroalkyl Substances (PFAS) with Nontargeted Ion Mobility Spectrometry–Mass Spectrometry Analyses. *Sci. Adv.* **2023**, *9* (43), eadj7048. https://doi.org/10.1126/sciadv.adj7048.

(115) Smolinski, R.; Koelmel, J. P.; Stelben, P.; Weil, D.; Godri, D.; Schiessel, D.; Kummer, M.; Stow, S. M.; Mohsin, S.; Royer, L.; McKenzie-Coe, A.; Lubinsky, T.; DeBord, D.; Chevallier, O.; Rennie, E. E.; Godri Pollitt, K. J.; McDonough, C. FluoroMatch IM: An Interactive Software for PFAS Analysis by Ion Mobility Spectrometry. *Environ. Sci. Technol.* **2025**, *59* (13), 6636–6648. https://doi.org/10.1021/acs.est.4c13846.

Chapter 2:
Objectives & outline

Environmental contamination by chemical pollutants, particularly halogenated persistent organic pollutants, remains a major concern due to their toxicity and persistence[1,2]. Traditional analytical methods, such as gas chromatography-mass spectrometry, have been widely used for detecting and quantifying these contaminants, in particular GC-QqQ, GC-quadrupole and GC-sector configurations[3]. However, ion mobility spectrometry has recently emerged as a promising complementary technique which could offer enhanced separation and greater confidence in analyte identification[4,5].

At the outset of this PhD thesis, the use of IMS coupled to MS instruments to analyze environmental contaminants was still in its infancy (Section 1.3.5A). Furthermore, existing applications and developments were primarily limited to[4,5]:

- Hyphenation with liquid chromatography (LC)
- LC-compatible contaminants (e.g., pesticides and drug residues)
- Low-resolution IM technologies (e.g., drift tube and linear travelling wave IMS)
- Qualitative studies

In order to further expand the analytical scope of IM-MS, this doctoral thesis was guided by the following main objectives:

I. To develop and optimize a GC-hyphenated IM-MS system to enable the application of ion mobility–mass spectrometry to GC-amenable compounds
II. To characterize the ion mobilities and CCS of GC-amenable halogenated POPs
III. To evaluate the analytical benefits of using a higher resolution IM technology (TIMS) for both the targeted and untargeted analysis of these contaminants.
IV. To assess the performances of the developed platform for quantitative analysis of trace halogenated POPs in complex matrices

The research conducted to achieve these objectives is summarized in this thesis manuscript, which is structured into four distinct research chapters (**Figure 2.1**).

- **Chapter 3** describes the implementation of a CCS calibration procedure and on the IM characterization of several classes of POPs.
- **Chapter 4** focuses on optimizing critical parameters for IM separation and ion transfer within the instrument. A novel method, termed 'Sliding Windows in Ion Mobility' (SWIM) is introduced, significantly improving TIMS resolving power.
- **Chapter 5** evaluates the system's quantitative performance, assessing linearity, limits of quantification (LOQs), precision, accuracy and measurement uncertainty for the targeted analysis of dioxins and PCBs in several food samples. The advantages of ion mobility, such as enhanced selectivity and CCS based for confirmation, are also discussed .
- **Chapter 6** applies the developed method to the non-targeted analysis of halogenated compounds in a stranded killer whale, showcasing the potential of high-resolution ion mobility-mass spectrometry and advanced IM-enhanced MS/MS fragmentation mode (PASEF) for the characterization of unknown pollutant in complex biological matrices.

The thesis concludes with a discussion on the broader implications of these findings, emphasizing the value of gas chromatography-ion mobility-mass spectrometry in advancing regulatory contaminant analysis and environmental monitoring.

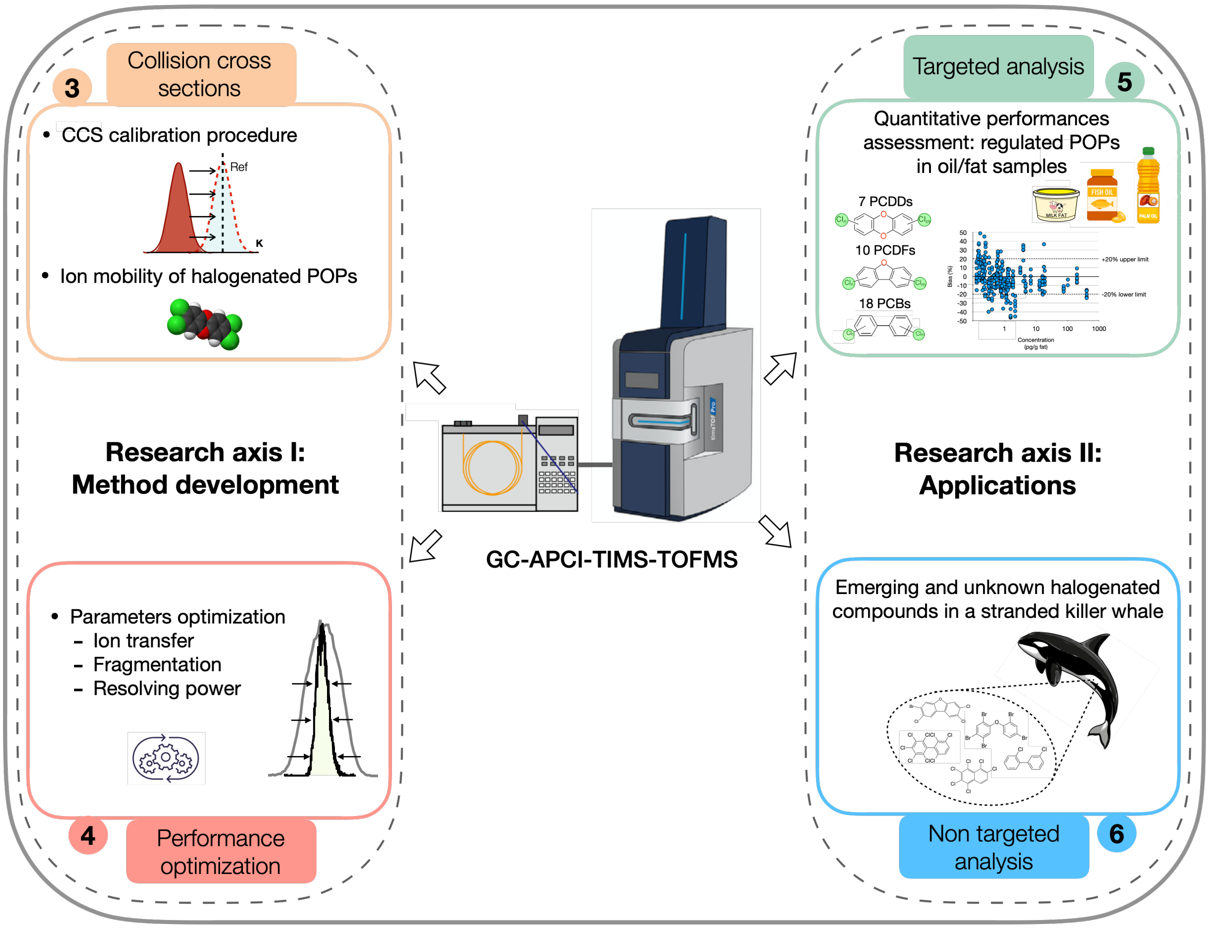

Figure 2.1 - Graphical abstract of PhD project

References

(1) Jones, K. C.; De Voogt, P. Persistent Organic Pollutants (POPs): State of the Science. *Environ. Pollut.* **1999**, *100* (1–3), 209–221. https://doi.org/10.1016/S0269-7491(99)00098-6.

(2) Jones, K. C. Persistent Organic Pollutants (POPs) and Related Chemicals in the Global Environment: Some Personal Reflections. *Environ. Sci. Technol.* **2021**, *55* (14), 9400–9412. https://doi.org/10.1021/acs.est.0c08093.

(3) *Mass Spectrometry in Food and Environmental Chemistry*; Picó, Y., Campo, J., Eds.; The Handbook of Environmental Chemistry; Springer International Publishing: Cham, 2023; Vol. 119. https://doi.org/10.1007/978-3-031-19093-3.

(4) Song, X.-C.; Canellas, E.; Dreolin, N.; Goshawk, J.; Lv, M.; Qu, G.; Nerin, C.; Jiang, G. Application of Ion Mobility Spectrometry and the Derived Collision Cross Section in the Analysis of Environmental Organic Micropollutants. *Environ. Sci. Technol.* **2023**, *57* (51), 21485–21502. https://doi.org/10.1021/acs.est.3c03686.

(5) Celma, A.; Alygizakis, N.; Belova, L.; Bijlsma, L.; Fabregat-Safont, D.; Menger, F.; Gil-Solsona, R. Ion Mobility Separation Coupled to High-Resolution Mass Spectrometry in Environmental Analysis – Current State and Future Potential. *Trends Environ. Anal. Chem.* **2024**, *43*, e00239. https://doi.org/10.1016/j.teac.2024.e00239.

Research axis I: Development and optimization of a GC-APCI-TIMS-TOFMS system for halogenated contaminants

Chapter 3:
Ion mobilities and collision cross sections of halogenated POPs measured on a GC-APCI-TIMS-TOF system

Portions of this chapter are based on the following publication:

Muller, H. B.; Scholl, G.; Far, J.; De Pauw, E.; Eppe, G. Sliding Windows in Ion Mobility (SWIM): A New Approach to Increase the Resolving Power in Trapped Ion Mobility-Mass Spectrometry Hyphenated with Chromatography. *Anal. Chem.* **2023**, *95* (48), 17586–17594

Chapter 3: Ion mobilities and collision cross sections of halogenated POPs measured on a GC-APCI-TIMS-TOF system

3.1 - MATERIALS AND METHODS 43

3.2 - RESULTS AND DISCUSSION 43

3.2.1 - CCS calibration procedure for GC hyphenated timsTOF systems 43
A. Calibration before ion sources switching 44
B. External calibration procedure 47
C. Internal calibration procedure 48

3.2.2 - Ion mobilities and collision cross sections of halogenated POPs 50
A. Ion mobilities of (quasi)molecular ions 50
B. Ion mobilities of fragment ions 51
C. CCS trends 58

3.3 - CONCLUSION 64

3.4 - REFERENCES 65

3.5 - SUPPORTING INFORMATION 67

This chapter focuses on the characterization of ion mobilities and collision cross sections of selected classes of halogenated persistent organic pollutants. It begins by introducing a CCS calibration procedure compatible with the GC-APCI–coupled timsTOF system. The chapter then examines the ion mobility behavior of APCI-generated (quasi)molecular and fragment ions. Finally, it provides a comparative overview of CCS values across a broad range of halogenated POP classes, many of which are reported here for the first time.

3.1 - Materials and methods

The development of the IM calibration procedure was performed on a commercial timsTOF Pro 2 mass spectrometer with various ion sources (Bruker, Bremen): ESI, LC-APCI and GC-APCI. Agilent tune mix and PAHs standards were purchased from Agilent Technologies (Santa Clara, USA) and Wellington Laboratories (Ontario, Canada), respectively.

All POPs standards measurements were performed on a commercial timsTOF Pro 2 mass spectrometer (Bruker, Bremen) equipped with a Scion 456-GC connected to an atmospheric pressure chemical ionization (APCI) source (GC- APCI II, Bruker, Bremen) (see Appendix A for photographs of the instrument setup). Appendices C, D and E provide the general principles of GC, APCI and TOF-MS, respectively.

The standards were purchased from Wellington Laboratories (Ontario, Canada) and CIL (Tewksbury, MA). IM and MS calibration were performed using the internal calibration procedure described in this chapter.

3.2 - Results and discussion

3.2.1 - CCS calibration procedure for GC hyphenated timsTOF systems

Although attempts have been made to determine CCS on timsTOF instruments from first principles (i.e., without a calibration procedure), accurately measuring key experimental parameters, such as temperature, pressure, and gas velocity inside the TIMS tunnel, currently limits this approach[5]. Therefore, the determination of K_0 and CCS values on TIMS is currently performed via a calibration procedure based on the following equation[6]:

$$\Delta V_{detection} \simeq a + b\frac{1}{K_0} \tag{3.1}$$

This equation stems from the fact that in TIMS, the potential drop across the plateau at which an ion is detected is approximately linearly proportional to the inverse of its reduced mobility coefficient[7] (see Appendix B for the complete derivation of this equation). In practice, the detection voltages of several calibrant ions with known reduced mobilities are measured and the empirical coefficients a and b are determined through a linear fit[6]. Then, the reduced mobility coefficient of any ion can be retrieved through the calibration equation by measuring its detection voltage. The CCS can also be obtained based on the fundamental low-field ion mobility equation (equation 1.2, Section 1.3.2B).

In general, the calibration of ${}^{TIMS}K_0$ is performed using a mixture of calibrant molecules known as the Agilent ESI tune mix. This mixture contains nine fluorinated compounds and betaine, yielding up to ten ions in positive and in negative modes within the mass range 100 – 3000 m/z. The collision cross sections of these ions have been accurately determined using a drift tube instrument[8] and are in the range from approximately 100 to 500 Å^2. To calibrate the instrument, a diluted solution of this mix is directly infused into the ion source (e.g., ESI source) and the calibration coefficients are automatically determined based on the linear regression.

Unfortunately, the Bruker GC-APCI II source is not designed to infuse solutions directly into the ionization region. As a result, calibration through direct infusion of the Agilent tune mix (or any calibration mix) is not possible. Therefore, alternative calibration strategies had to be found. This section describes and discusses several calibration procedures that were investigated.

A. Calibration before ion sources switching

The first method we investigated involved the following straightforward procedure. First, the instrument was calibrated with the Agilent tune mix using a compatible ion source. Second, the ion source was removed and replaced with the GC-APCI source. To test this procedure, the instrument was calibrated with the LC-APCI source[†] and the Agilent tune mix. Next, a standard solution of 2,3,7,8-TCDD was directly infused into the source and the inverse of its reduced ion mobility was measured[‡] (red peak in **Figure 3.1**). Then, the LC-APCI source was replaced by the GC-APCI source and a diluted solution of the TCDD solution was injected and its $1/K_0$ was measured once again (orange peak in Figure 3.1). As is apparent in Figure 3.1, a significant shift towards lower $1/K_0$ values was observed for the mobility measurement performed with the GC-APCI source configuration, compared with the reference LC-APCI measurement.

To try to explain the observed shift, two hypotheses were formulated:

- Impact of helium: The GC separations were performed with helium as the carrier gas. After the compounds are separated in the GC column, they are transferred from the gas chromatograph to the inside of the APCI source via the transfer line (see **Figures A2** and **A3** in Appendix A). There, the helium carrier gas mixes with nitrogen that originates from the nebulizer (used to perform the corona ionization) and the spray shield ('dry gas flow'). The gas mixture is then transferred into the mass spectrometer through the glass transfer capillary. Some of the gas is pumped out of the mass spectrometer while the rest is forced through the TIMS cell, where it serves as the buffer gas. Since the reduced mobility coefficient K_0 depends heavily on the gas composition (Section 1.3.2B), the presence of helium in the nitrogen buffer gas could therefore contribute to the observed shift.
- Changes in the thermodynamic properties of the buffer gas: The calibration coefficients are valid for a specific gas velocity, temperature, and pressure (see Appendix B). Gas velocity affects the drag force experienced by ions and therefore the trapping voltage. Pressure and temperature directly affect the ion mobility coefficient K (equation 1.2, Section 1.3.2B). Consequently, a change in any of these properties after connecting the GC-APCI to the instrument would result in a an apparent[§] shift of the mobility peaks.

[†] In contrast to the GC version, this ion source allows solutions to be directly infused, and thus, calibration to be performed with the Agilent tune mix. Moreover, it also allows the ionization of halogenated POPs (more readily so than the ESI source).

[‡] In TIMS, mobility spectra are reported as a function of the inverse reduced mobility ($1/K_0$), which is proportional to CCS.

[§] The shift is considered apparent because the reduced ion mobility coefficient (and thus $1/K_0$) is theoretically independent of pressure and drift gas velocity (though it remains dependent on temperature). However, changes in pressure or drift gas velocity influence the detection voltage. Since $1/K_0$ values are calculated from the detection voltage and predefined calibration parameters, any change in voltage without updating the calibration parameters to reflect the new experimental conditions will lead to an inaccurate $1/K_0$ measurement. In this case, the true $1/K_0$ remains unchanged, but the measured value appears shifted. This results in an apparent shift in ion mobility.

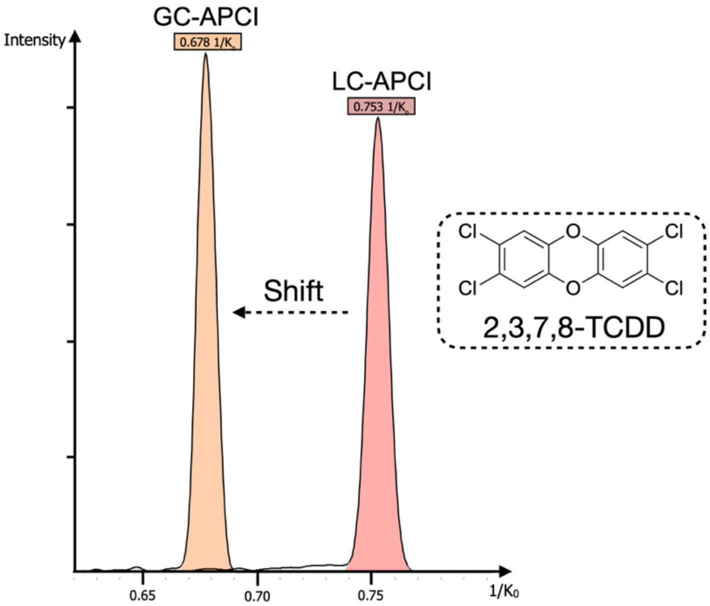

Figure 3.1 – Overlaid ion mobility spectra of the 2,3,7,8-TCDD measured with the LC-APCI source (in red) and the GC-APCI source (in orange).

To test the first hypothesis, we monitored the relative ion mobility of siloxane background ions across a range of helium flow rates, from 0.1 to 6.0 mL/min. As shown in **Figure 3.2**, increasing the helium concentration in the ion source resulted in only minimal changes to the measured ion mobilities. This suggests that the observed mobility shift cannot be attributed to the presence of helium in the nitrogen buffer gas. This is likely due to the very low helium flow rate (~60 mL/hour) relative to the total nitrogen flow in the source (~150 L/hour), resulting in an expectedly low helium concentration in the buffer gas.

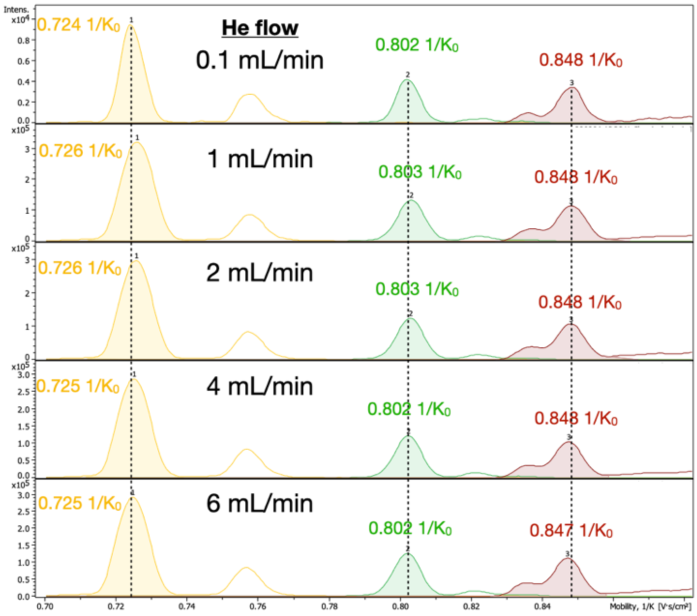

Figure 3.2 – Listed ion mobility spectra of three siloxane background ions (m/z 355, 429 and 503) recorded at various helium carrier gas flow.

Testing the second hypothesis proved more challenging in the first place, as the analytical[**] drift gas velocity, temperature, and pressure are not measured on timsTOF instruments. However, the pressure at the entrance of the tunnel (p_{ent}, around the first funnel) is recorded. Both the analytical drift gas velocity and pressure are related to this pressure: they both increase with increasing p_{ent}. Therefore, although the direct impact of the GC-APCI source on drift gas conditions inside the TIMS tunnel could not be measured, variations in p_{ent} provided an indirect means of assessing such effects.

Thus, in order to investigate this effect, the entrance pressure p_{ent} was monitored before and after installing the GC-APCI source. A measurable drop was observed, from 2.55 mBar (before) to 2.40 mBar (after), indicating a likely decrease in both the analytical pressure and buffer gas velocity within the TIMS cell. This finding aligns with the apparent mobility shift previously observed, as the detection voltage is expected to decrease with reductions in both buffer gas velocity and analytical pressure (as described by equation A7 in Appendix B). As a result, the apparent mobility shift observed using this calibration method can be attributed primarily to a change in the analytical drift gas pressure and velocity when the GC-APCI is installed. A potential contribution from a change in analytical temperature cannot be excluded, although this parameter could not be assessed in the this experiment.

To further investigate the experimental parameter(s) responsible for the observed pressure drop, the entrance pressure p_{ent} was monitored while individually varying key GC-APCI parameters: transfer line temperature, ion source temperature, nebulizer pressure, dry gas flow, and dry gas temperature (see Appendix A). Among these, only one parameter significantly impacted the entrance pressure and the corresponding apparent shift in $1/K_0$: the ion source temperature (**Figure 3.3** and **Figures S3.1-S3.4**). As shown in Figure 3.3A, the entrance pressure decreased markedly as the ion source temperature was raised to its operational value of 300 °C. The high temperature of the GC-APCI ion source was therefore identified as the primary cause of the apparent shift in measured reduced mobility, in contrast to ESI and LC-APCI sources, which are not heated[††].

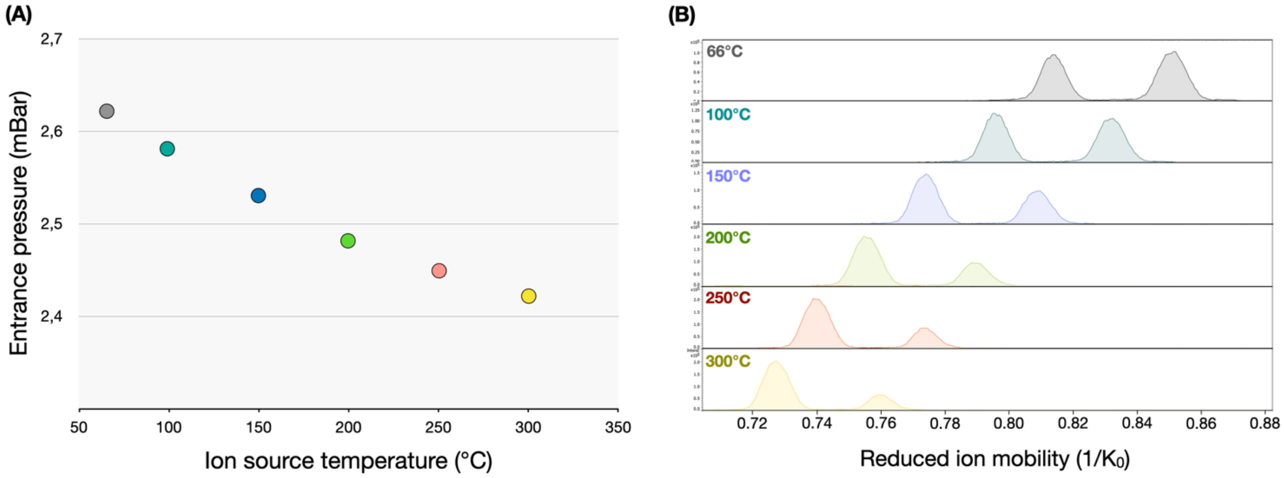

Figure 3.3 – **(A)** Variation of the TIMS entrance pressure (p_{ent}) as a function of the temperature of the ion source. **(B)** Corresponding ion mobility spectra from a background siloxane ion (m/z 355).

[**] The drift gas pressure, temperature and gas velocity vary throughout the TIMS tunnel[9]. Those present at the elution position (i.e., the location between the ramp and the plateau region, see Figure 1.7 in Chapter 1) are referred to as 'analytical'.

[††] In the LC-APCI source, only the nebulizer part is heated to vaporize the droplets.

B. External calibration procedure

The findings from the previous section demonstrated the need to recalibrate ion mobility measurements after installing the GC-APCI source on the timsTOF instrument. Since direct infusion of a calibrant solution is not possible with this configuration, we investigated an external calibration procedure where the calibrant is introduced through the GC. For this purpose, calibrant compounds that were GC-compatible and had published reference ^{DTIMS}CCS values had to be found. After consulting several databases, a set of eleven polycyclic aromatic hydrocarbons (PAHs) was identified as suitable candidates[10]. A standard mixture of these compounds was prepared and analyzed using the GC-TIMS-MS system. The uncalibrated TIMS $1/K_0$ and CCS values of the radical $M^{+\cdot}$ ions were determined. As shown in **Figure 3.4**, plotting the experimental ^{TIMS}CCS values against the reference ^{DTIMS}CCS values revealed a strong linear correlation ($R^2 = 0.9981$). This confirmed the suitability of using these PAHs for recalibrating the ion mobilities and CCS on the timsTOF instrument after installing the GC-APCI source, using the corresponding regression curves.

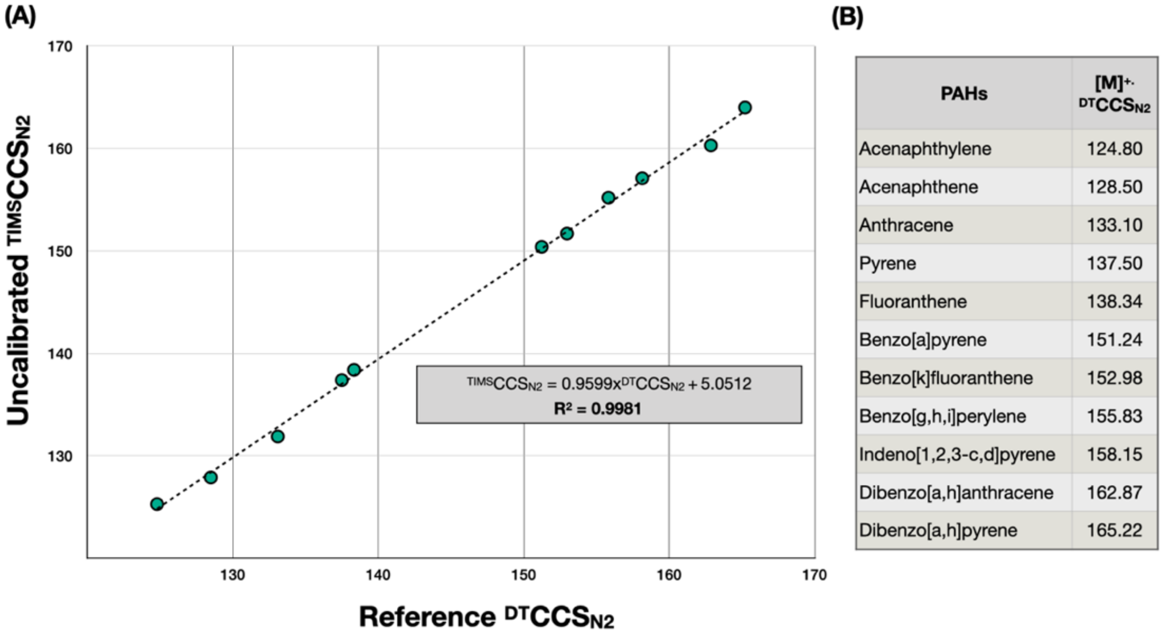

PAHs	$[M]^{+\cdot}$ $^{DT}CCS_{N2}$
Acenaphthylene	124.80
Acenaphthene	128.50
Anthracene	133.10
Pyrene	137.50
Fluoranthene	138.34
Benzo[a]pyrene	151.24
Benzo[k]fluoranthene	152.98
Benzo[g,h,i]perylene	155.83
Indeno[1,2,3-c,d]pyrene	158.15
Dibenzo[a,h]anthracene	162.87
Dibenzo[a,h]pyrene	165.22

Figure 3.4 - **(A)** Experimentally measured $^{TIMS}CCS_{N2}$ of the radical molecular ion $M^{+\cdot}$ of eleven PAHs against their corresponding reference $^{DTIMS}CCS_{N2}$. **(B)** Reference $^{DTIMS}CCS_{N2}$ of the eleven radical $M^{+\cdot}$ PAH ions taken from ref. [10].

However, although this recalibration procedure is effective, it presents several practical disadvantages. First, the calibrant molecules are both costly and toxic (PAHs are well known suspected carcinogenic environmental contaminants[11]). Second, a full GC-TIMS-MS analysis of the PAH calibrant mixture must be performed each time ion mobility recalibration is required. This may be necessary, for example, if the scan rate β is modified (i.e., when adjusting the IM range or analysis time), or more generally whenever drift gas properties fluctuate over time. A recent study has shown that daily variations in atmospheric pressure can influence the entrance pressure of the TIMS cell (and consequently, the drift gas velocity) leading to slight apparent shifts in measured ion mobilities throughout the day[12]. Given that a full GC-TIMS-MS analysis takes approximately 30 minutes, this recalibration approach is relatively time-consuming and impractical on the long term. In addition, the ion mobilities and CCS cannot be calibrated directly in real time on the acquisition software. Recalibration can only be done manually post acquisition using the regression curves created after the analysis of the mix of PAHs calibrants, contributing to additional workload and an increased risk of introducing manual errors during data processing.

C. Internal calibration procedure

To overcome these issues, we investigated the use of background ions as internal calibrants. Cyclic siloxanes are well-known thermal degradation products of polydimethylsiloxane (PDMS), the polymer material commonly used in GC stationary phases[13]. During a typical GC analysis, these volatile molecules are continuously emitted and dominate the signals in full-scan MS spectra. **Figure 3.5** shows a mass spectrum recorded at high GC oven temperature on our system, where the release of siloxanes (commonly referred to as 'GC column bleed') was particularly intense. Numerous peaks were observed across the mass range from 200 to 1000 m/z. Among these, several series of siloxanes, separated by a constant m/z difference of 74 (corresponding to a repeating $OSi(CH_3)_2$ unit), were identified (**Figure S3.5**).

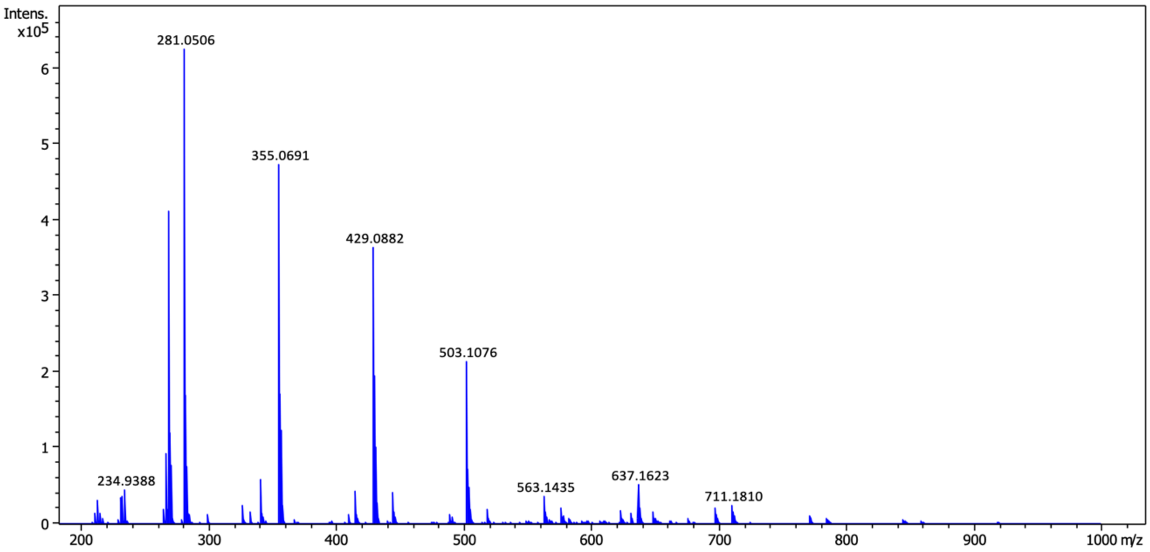

Figure 3.5 – Average background mass spectrum recorded on the timsTOF instrument with the GC oven temperature set to 300 °C.

The ion mobilities of these siloxanes were investigated in detail. It was found that lower-mass siloxane ions (<500 m/z) generally exhibited well-defined IM peaks, with CCS values that increased steadily with ion mass (**Figure 3.6**). For some siloxane ions, the mobility spectra displayed multiple peaks. These additional peaks are likely the result of post-TIMS fragmentation of higher-mass precursor ions; for example, the loss of methane from the m/z 297 siloxane ion ($C_8H_{25}Si_4O_4$) to form the fragment ion with m/z 281 ($C_7H_{21}Si_4O_4$) (**Figure S3.6**). A similar reasoning can be applied to m/z siloxane ions 371 – 355 and 445 – 429. The behavior of fragment ions in TIMS will be provided in detail in Section 3.3.2B.

Ultimately, five siloxane ions (highlighted in **Figure S3.7**) were selected as internal calibration ions. As their ion mobility coefficients and CCS values were not available in the literature, their CCS were determined using the external calibration procedure described in the previous section. The calibrated $1/K_0$ values for these siloxanes[‡‡] ranged from 0.693 to 0.992 V·s/cm^2, corresponding to CCS values between 147.2 and 204.1 Å^2. The use of these background ions as internal IM calibrants offers several advantages:

[‡‡] As will be discussed in a later chapter (Section 5.2.2A), ion mobility peaks tend to shift slightly toward higher CCS values when the number of trapped ions becomes excessive. To avoid this effect, the CCS values of the siloxanes were determined at a low temperature (140 °C) and an intermediate accumulation time (75 ms). Consequently, when performing IM calibration, it is important to select similar conditions to minimize CCS shifts and ensure calibration accuracy.

- Calibration is fast and can be performed in real time once the GC is connected to the instrument.
- Recalibration can be applied post-acquisition to improve reproducibility and correct for run-to-run fluctuations in buffer gas properties.
- As background ions, they are freely available and do not require additional cost or sample preparation.
- The range of CCS values covered closely matches that of the halogenated POPs analyzed in this thesis (see Section 3.2.2C).
- In addition to calibrating the ion mobility, they can also be used to calibrate the mass to charge ratio. These five ions and six other higher-mass siloxane ions were selected for that purpose (**Table S3.1**).

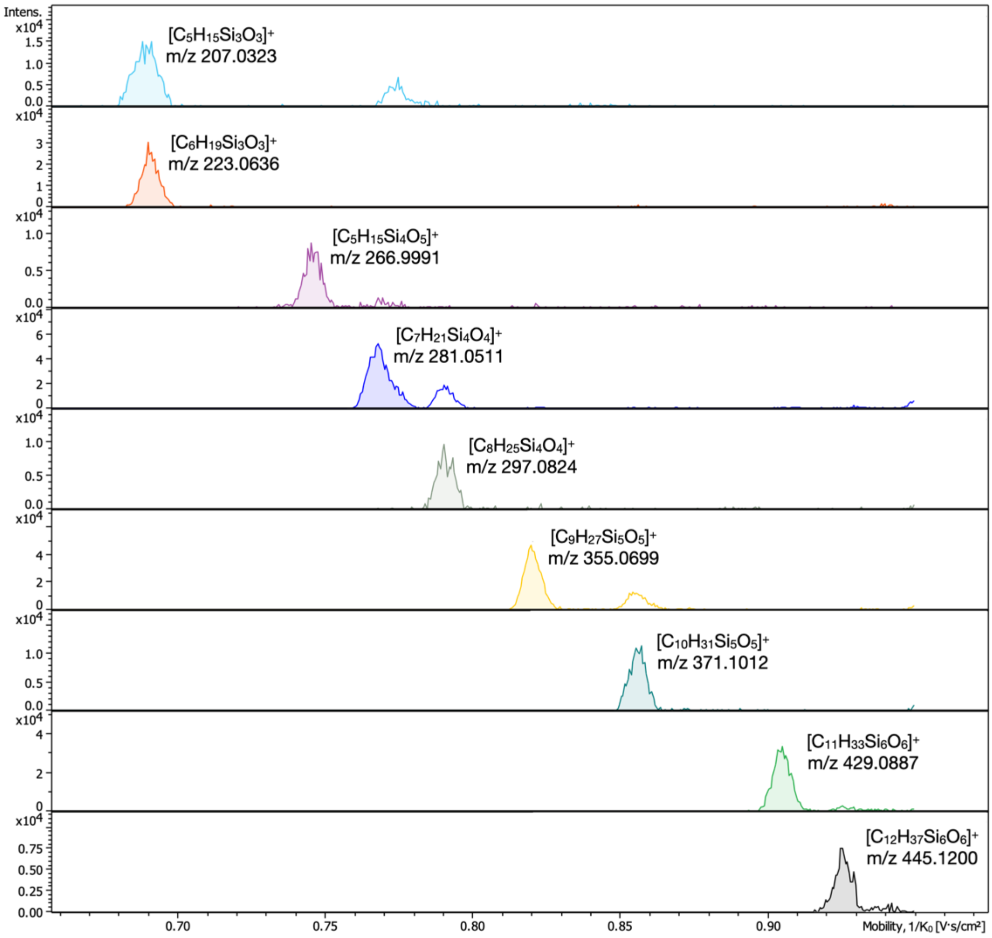

Figure 3.6 – Listed ion mobility spectra of selected lower-mass siloxane ions.

However, a major drawback is that siloxanes are only ionized in positive mode, limiting their use for IM calibration in negative mode.

3.2.2 - Ion mobilities and collision cross sections of halogenated POPs

Throughout this PhD thesis, a wide range of GC-amenable POP classes were investigated using the developed GC-APCI-TIMS-MS system. The classes of POPs considered were:

- Chlorinated, brominated and mixed chlorinated-brominated dibenzodioxins (PCDDs, PBDDs and PXDDs)
- Chlorinated, brominated and mixed chlorinated-brominated dibenzofurans (PCDFs, PBDFs and PXDFs)
- Chlorinated, brominated and mixed chlorinated-brominated biphenyls (PCBs, PBBs and PXBs)
- Polybrominated diphenyl ethers (PBDEs)
- Polychlorinated naphthalenes (PCNs)
- Emerging brominated flame retardants (eBFRs)
- Organochlorine pesticides (OCPs)

This section presents a detailed discussion of the trapped ion mobility analysis of these halogenated POPs. A complete list of these compounds, along with their measured $^{TIMS}CCS_{N2}$ values, is provided in Appendix F.

A. Ion mobilities of (quasi)molecular ions

In atmospheric pressure chemical ionization (APCI), two main positive ionization mechanisms have been reported: proton transfer and charge transfer[13,14] (see Appendix D for details). For all classes of POPs investigated, both ionization pathways were observed, although charge transfer was the dominant mechanism for nearly all compounds. The relative contribution of each mechanism was found to depend on the chemical class. As illustrated in **Figure 3.7**, PCBs exhibited the lowest average proportion of proton transfer ionization (less than 15%), while brominated dioxins, furans, and diphenyl ethers showed the highest (exceeding 25%). All other classes listed in Figure 3.7 (i.e., chlorinated dioxins and furans, brominated biphenyls, PCNs, and mixed Cl-Br classes) displayed an average proton transfer contribution of between 15 and 20%. Overall, these results suggest that halogenated biphenyls are less prone to proton transfer ionization compared to halogenated dioxins, furans, naphthalenes, and diphenyl ethers. Additionally, the presence of bromine atoms appears to favor proton transfer ionization more than chlorine atoms.

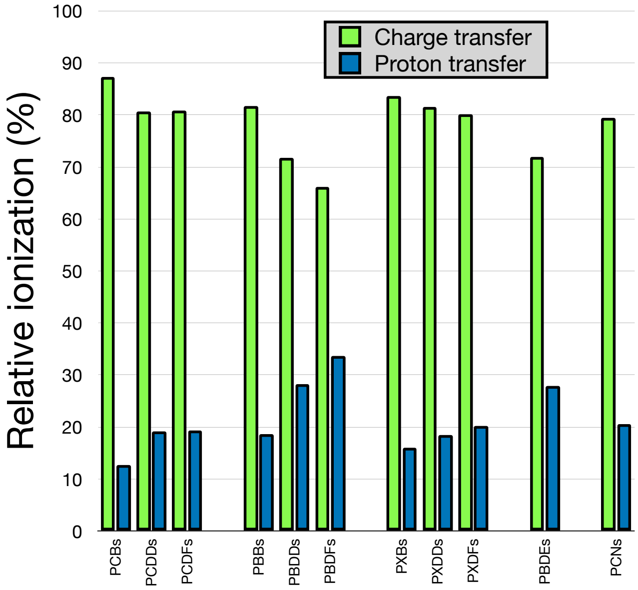

Figure 3.7 – Comparison of the relative proportions of charge transfer and proton transfer ionization mechanisms across different POP congener classes. Relative ionization was calculated by comparing the areas of the IM peaks corresponding to

the most intense isotopologue of the (quasi)molecular ions. When relevant, the contribution of their corresponding fragment ions was also included. For example, the total IM area for the $[M+H]^+$ ion of PCDDs was calculated as the sum of the areas of the protonated ion and the corresponding $[M+H-Cl]^{+\cdot}$ fragment ion. The area of the most intense isotopologue of the fragment ions was corrected to account for differences in absolute isotopic abundance (e.g., the absolute isotopic abundance of the M+2 isotopologue of the $[M+H]^+$ ion of hexachlorodibenzo-p-dioxin is 32.0%, while that of the M+2 isotopologue of the corresponding $[M+H-Cl]^{+\cdot}$ fragment ion is 35.2%). Further details regarding the fragmentation of these ions are provided in the next section (3.2.2B).

Within each chemical class, the relative proportions of the two ionization mechanisms were found to be further influenced by the degree of halogenation, with lower-halogenated congeners generally exhibiting a higher proportion of proton transfer ionization (**Figure S3.8A**). In some cases, the specific halogen substitution pattern (i.e., isomers) also affected the ionization behavior (Figure S3.8B). For a given compound, the relative contributions of each ionization mechanism were found to be reproducible over time (Figure S3.8C).

In terms of ion mobility, the spectra of radical molecular ions ($M^{+\cdot}$) for most POP classes - including halogenated dioxins, furans, biphenyls, diphenyl ethers, naphthalenes, simple OCPs such as hexachlorobenzene, and eBFRs (with the exception of dechloranes) - were typically characterized by a single Gaussian peak (**Figure 3.8**, upper ion mobility traces). This suggests the adoption of either a single conformation (e.g., for rigid molecules like halogenated dioxins, furans, naphthalenes, and substituted-benzene-type eBFRs and OCPs) or a weighted average of rapidly interconverting conformations relative to the timescale of ion mobility separation[1] (e.g., for molecules having flexible bonds such as halogenated biphenyls and diphenyl ethers).

In contrast, the ion mobility spectra of the corresponding protonated species ($[M+H]^+$) were usually more complex, sometimes showing distorted peaks (Figure 3.8B) or even multiple peaks (Figure 3.8C). Most of the time, the CCS values of these ions were slightly higher than those of the corresponding radical molecular ions, often merging partly with the ion mobility peak of the latter[§§] (e.g., Figure 3.8B), although a few exceptions showed lower CCS values (e.g., HxBB 153, **Figure S3.9**). The underlying reasons for these observations remain unclear. The asymmetric peak shapes and multiple features may arise from various factors[1,6], including the presence of multiple protomers depending on the protonation site (e.g., heteroatoms or π-electron systems), the existence of multiple conformers, or dynamic equilibria with adducts (e.g., ion–water clustering) during separation.

For classes of POPs with more complex structures, such as OCPs and dechloranes, the spectra of their radical molecular ions ($M^{+\cdot}$) were sometimes characterized by the presence of multiple peaks, which could be attributed to the adoption of multiple stable gas-phase conformations (**Figure 3.9**, see also **Table A2** in Appendix F). The ion mobility spectra of their corresponding protonated ions ($[M+H]^+$) were also usually similarly complex (**Figure S3.10**).

B. Ion mobilities of fragment ions

APCI is considered a soft ionization technique in the sense that it yields to reduced in-source fragmentation compared to hard ionization technique such as EI. This is primarily due to the low energy transfer between the reactant ion and the analyte during chemical ionization, as well as the high rate of collisions (up to 10^6 per millisecond) at atmospheric pressure, which enables efficient ion

---

[§§] Since radical molecular ions ($M^{+\cdot}$) and protonated ions ($[M+H]^+$) of halogenated POPs differ only by the presence of a hydrogen atom, their isotopic clusters overlap, with an m/z offset of one unit. In most cases, the resolving power of the TOF mass spectrometer was sufficient to differentiate the two ions at m/z values corresponding to the even N+x isotopologues of the $M^{+\cdot}$ ion (i.e., the odd N+x isotopologues of the $[M+H]^+$ ion). However, it was not sufficient to fully separate the two ions at m/z values corresponding to the odd N+x isotopologues of the $M^{+\cdot}$ ion (i.e., the even N+x isotopologues of the $[M+H]^+$ ion) (Figure 3.8).

thermalization through collisional cooling[13,14]. However, ionization is not the only source of energy input; subsequent steps such as ion mobility separation and ion transfer can also impart energy to the ions, potentially causing additional fragmentation[15,16].

(A) Gaussian $[M+H]^+$ peak

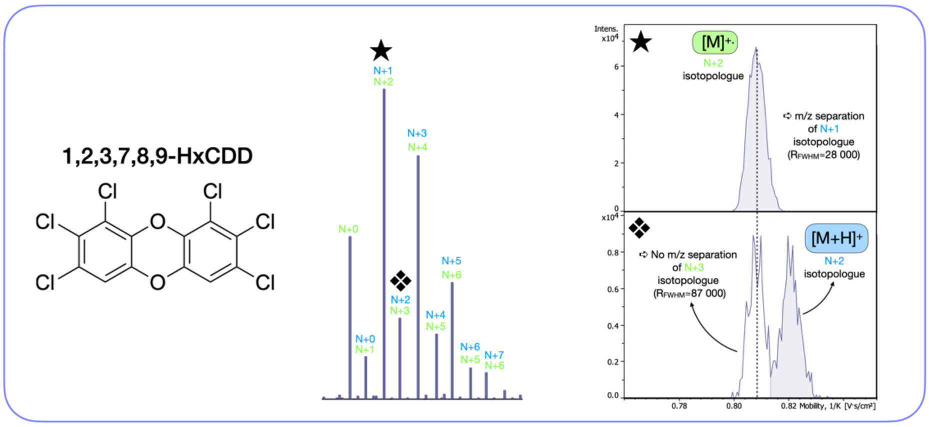

(B) Distorted $[M+H]^+$ peak

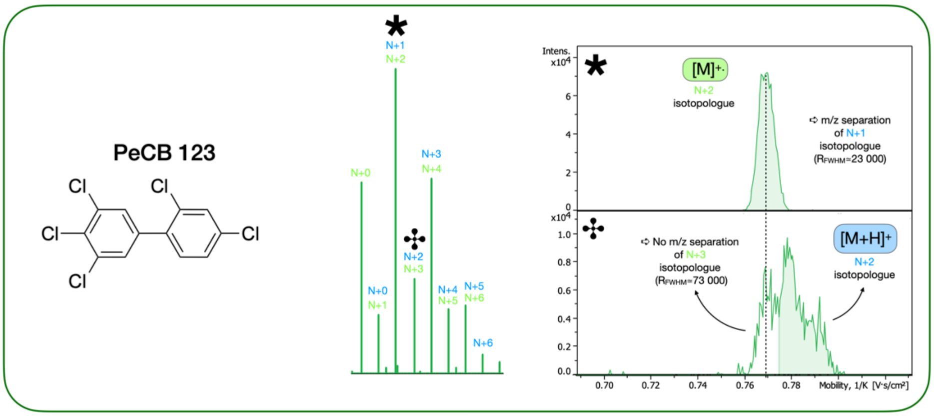

(C) Multiple $[M+H]^+$ peaks

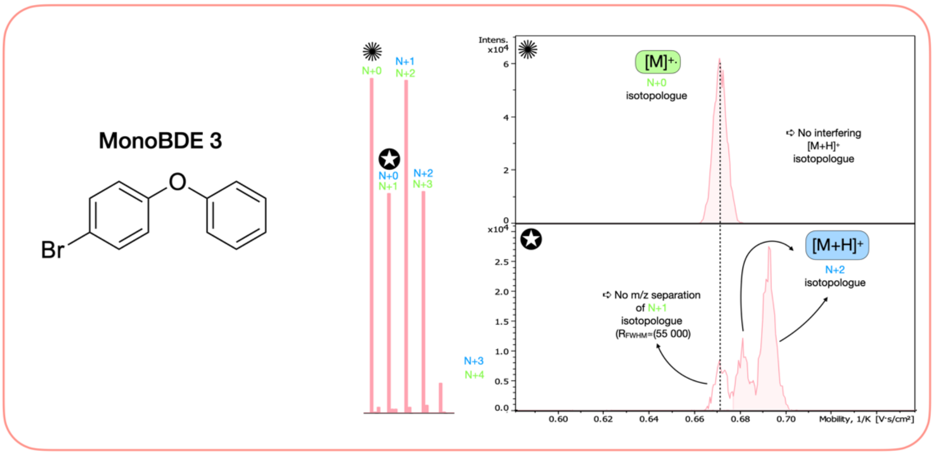

Figure 3.8 – Typical ion mobility spectra of radical molecular ($M^{+\cdot}$) and protonated ($[M+H]^+$) ions for halogenated POPs with simple chemical structures. In most cases, both types of ions produced a single Gaussian peak (example A). However, in some instances, the ion mobility peak of the protonated ion appeared distorted (B) or even split into multiple peaks (C). In each example, the ion mobility spectrum corresponds to the most intense isotopologue of each ion, with a symbol linking the spectrum to its associated m/z peak within the overlapping isotopic cluster. For the protonated ions, signal interference from the radical molecular ion is consistently observed, due to the mass spectrometer's limited resolving power ($R_{TOF} \simeq 50\ 000$) in distinguishing these isobaric species at those m/z values (the required resolving power R_{FWHM} to separate the signal of the two ions at half height is indicated in parenthesis). For the radical molecular ions, the resolving power was sufficient to resolve the isobaric interferences.

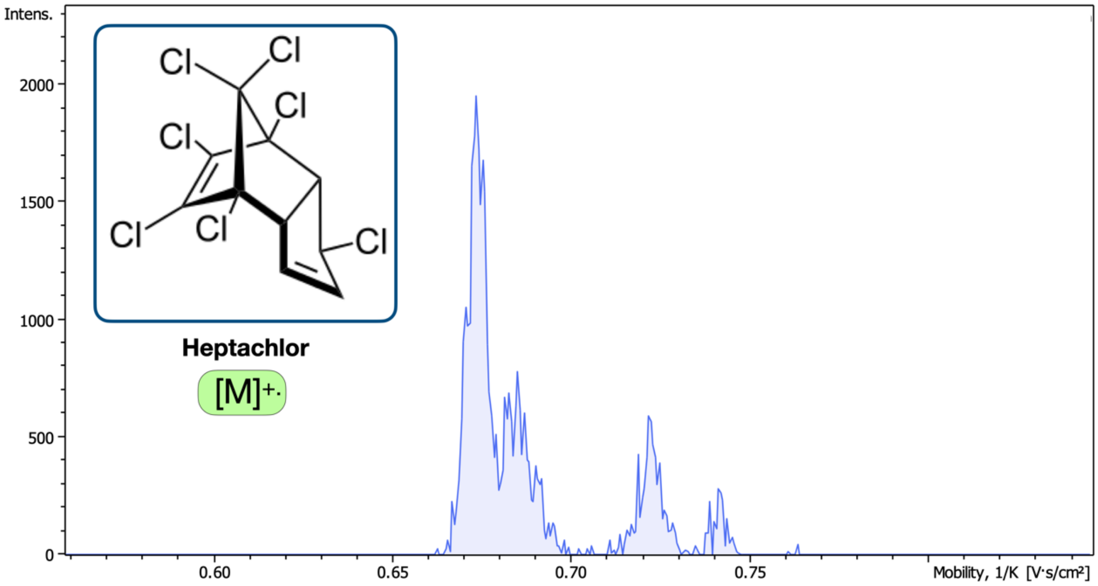

Figure 3.9 – Ion mobility spectrum of the radical molecular ion ($M^{+\cdot}$) of the organochlorine pesticide heptachlor, showing four distinct peaks.

For the classes of compounds investigated in this project, it was observed that:

- Compounds with simple chemical structures (i.e., all POPs except Dechloranes and most OCPs) exhibited low to moderate fragmentation - typically less than 20% of the total number of ions, on average (**Figure S3.11**) - and produced a limited variety of fragment ions (either 1 or 2).
- Compounds with more complex chemical structures (i.e., Dechloranes and most OCPs) exhibited extensive fragmentation (up to 100%) and generated a wide variety of fragment ions (see **Table A2** in Appendix F).

Simple chemical structure with a single fragment

In the simplest cases, only a single type of fragment was observed. This was true for PCDDs, PCDFs, PBDDs, PBDFs, PXBs, PXDFs, PCNs, most eBFRs, and hexachlorobenzene (an OCP). **Figure 3.11** illustrates the typical resulting ion mobility spectra of both the precursor and fragment ions, using 2,3,7,8-TCDD as an example.

As shown in this figure, the ion mobility spectrum of the fragment ($[M+H-Cl]^{+\cdot}$) was characterized by two distinct ion mobility distributions: one at lower CCS values and another at higher CCS values, the latter closely matching the CCS of the $[M+H]^+$ ion. The first distribution most likely corresponds to the CCS of the fragment itself, which formed before (e.g., in source, during transfer to the TIMS cell…) or during the ion mobility separation[15]. Since the loss of a halogen atom from a polyhalogenated structure can occur at different sites, this sometimes resulted in multiple peaks within the lower CCS region, representing isomeric fragment ions (**Figure S3.12**). The second distribution likely corresponds to the CCS of the parent ion, which underwent fragmentation after the ion mobility separation[15] (i.e., post-IM fragmentation).

Interestingly, if this interpretation holds true, it suggests that by matching the high CCS distribution of fragment ions with the corresponding CCS distribution of the (quasi)molecular ions, one can identify the precursor ion(s) from which the fragments originate. For example, the perfect alignment between the high CCS peak of the 2,3,7,8-TCDD fragment ions and that of the protonated ion ($[M+H]^+$) strongly suggests that the $[M+H-Cl]^{+\cdot}$ fragment originates exclusively from the fragmentation of $[M+H]^{+}$, rather than from the radical molecular ion ($M^{+\cdot}$). This latter observation can likely be extended to all other congeners of PCDDs, as well as nearly all other classes of POPs mentioned in the previous paragraph, as summarized in **Table 3.1**.

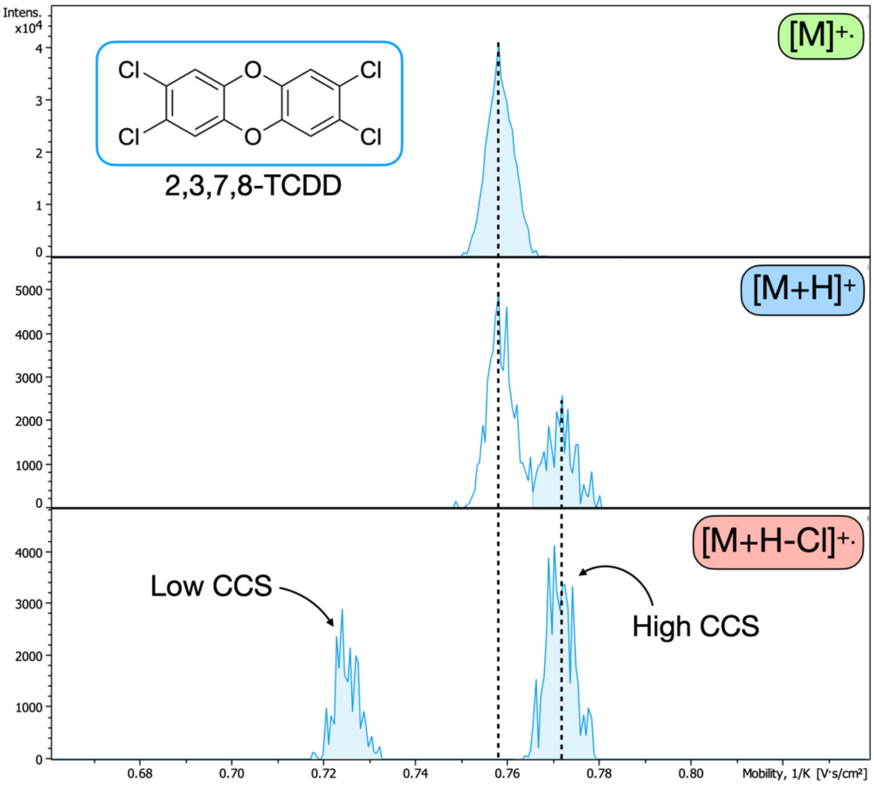

Figure 3.11 – Ion mobility spectra of the radical molecular ion (top), protonated ion (middle), and fragment ion (bottom) of 2,3,7,8-tetrachlorodibenzo-p-dioxin.

Table 3.1 – Type of fragment, precursor ion and average extent of fragmentation observed for the classes of POPs giving rise to a single fragment ion. (PBBz= 1,2,3,4,5-pentabromobenzene; PBT= Pentabromotoluene; PBEB= Pentabromoethylbenzene; HBBz= Hexabromobenzene; pTBX= 2,3,5,6-tetrabromo-p-xylene; HCB=Hexachlorobenzene)

Classes of POP		**Fragment type**	**Precursor ion** (as suggested by alignment of the IM peaks)		**Average extent of fragmentation**
			Protonated ion $[M+H]^{+}$	**Radical molecular ion $M^{+\cdot}$**	
PCDDs		$[M+H-Cl]^{+\cdot}$	x		57%
PCDFs		$[M+H-Cl]^{+\cdot}$	x		7%
PBDDs		$[M+H-Br]^{+\cdot}$	x		74%
PBDFs		$[M+H-Br]^{+\cdot}$	x		58%
PCNs		$[M+H-Cl]^{+\cdot}$	x		62%
eBFRs	PBBz, PBT, PBEB & HBBz	$[M+H-Br]^{+\cdot}$	x		
	pTBX	$[M-Br]^{+}$		x	
OCP	HCB	$[M-Cl+NH_3]^{+}$		x	

Fragmentation of the protonated ion is proposed to occur via the loss of a halogen radical (X°, either bromine or chlorine), according to the following scheme:

$$[M+H]^{+} \rightarrow [M+H-X]^{+\cdot} + X^{\cdot}$$

However, the formation of a radical fragment from a protonated ion, as suggested by this mechanism, is somewhat questionable. According to the even-electron rule, even-electron ions (such as protonated molecules) typically do not undergo fragmentation pathways that yield odd-electron (radical) cations[13]. Nevertheless, exceptions to this rule have been documented, particularly when the resulting radical fragment is highly stabilized[13], which may be the case here.

To further confirm the identity of the precursor ion giving rise to $[M+H-X]^{+\cdot}$ fragments, a tandem MS experiment was conducted using PBDEs. As discussed in the next section, PBDEs generate two types of fragments, one of which, $[M+H-Br]^{+\cdot}$, is believed to originate from the protonated ion, based on alignment of the ion mobility peaks. In this experiment, a mixture of five tetrabromodiphenyl ethers (TBDEs) was analyzed using the GC-TIMS-MS system. For the first three eluting isomers, the quadrupole was configured to isolate the first isotopologue (N+0) of the radical molecular ion ($M^{+\cdot}$), which was then fragmented in the collision cell at intermediate energy (20 eV) followed by full-scan analysis of the fragments in the TOF. This specific isotopologue was selected because it is the only one of the $M^{+\cdot}$ ion that does not overlap with any isotopologues of the protonated ion $[M+H]^{+}$ due to the one mass unit difference. For the last two eluting isomers, the most intense isotopologue of the protonated ion (N+4) was isolated and fragmented. However, in this case, complete isolation of the $[M+H]^{+}$ isotopologue was not possible, as the isobaric N+5 isotopologue of the radical molecular ion was also present, albeit at a lower relative abundance (approximately 30%).

The resulting tandem mass spectra are shown in **Figure 3.12**. As depicted, the top three spectra, corresponding to the isolation and fragmentation of one isotopologue of the radical molecular ion, were characterized by the presence of a fragment of the type $[M-2Br]^{+}$, while no signal corresponding to the $[M+H-Br]^{+\cdot}$ fragment was detected. In contrast, the bottom two tandem mass spectra, resulting from the isolation and fragmentation of a mixture of both the radical and protonated ions, were dominated by an intense signal corresponding to the $[M+H-Br]^{+\cdot}$ fragment. Additionally, low-intensity signals corresponding to $[M-2Br]^{+}$ fragments were observed, consistent with the concomitant presence of the radical molecular ion. This experiment thus confirms that the $[M+H-Br]^{+\cdot}$ fragment, and more generally the $[M+H-X]^{+\cdot}$ fragment, originates from the fragmentation of the protonated ion, in agreement with the conclusions drawn from the analysis of the ion mobility spectra.

Simple chemical structure with two fragments

For the classes of PCBs, PBBs, PBDEs, PXDDs, PXDFs, and PXBs, two types of fragment ions were sometimes observed in their respective mass spectra. Inspection of the corresponding ion mobility spectra revealed two distinct cases regarding the origin of the precursor ions:

- Both fragment ions originate from the same precursor ion (**Figure 3.13A**). This was observed for PXDDs, PXDFs, PXBs, and some PCBs and PBBs.
- Each fragment ion originates from a different precursor ion (Figure 3.13B). This was the case for PBDEs.

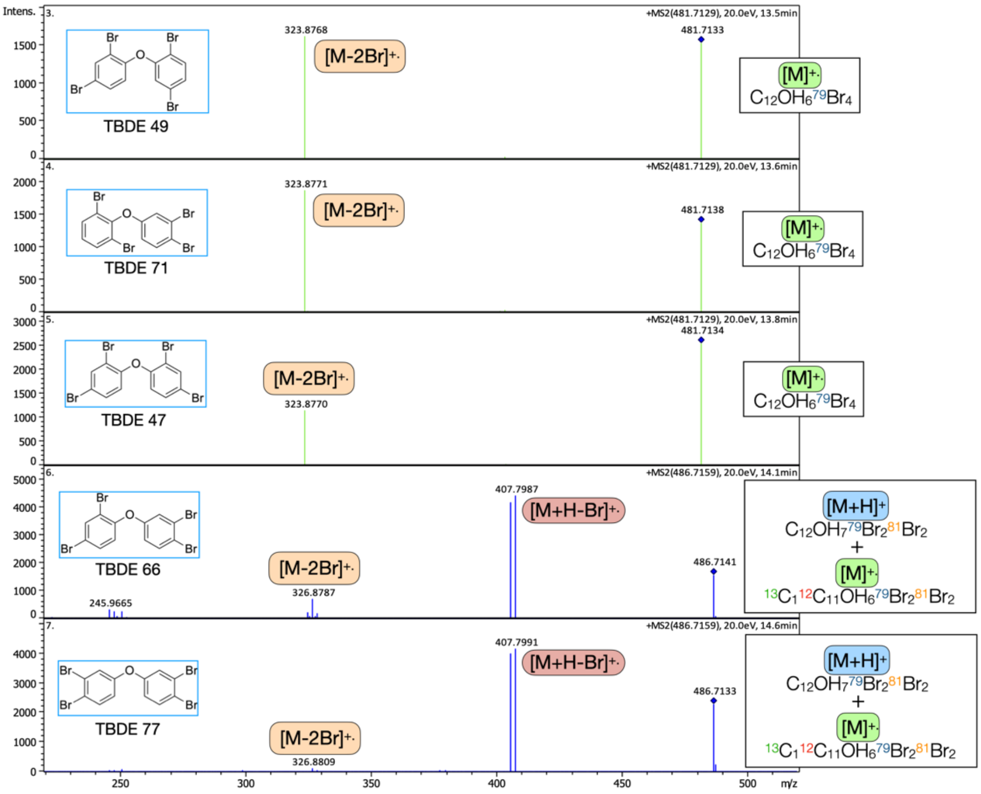

Figure 3.12 – Tandem mass spectra of the five tetrabromodiphenyl ethers. In the top three spectra, the N+0 isotopologue ($C_{12}OH_6{}^{79}Br_4$) of the radical molecular ion was isolated and fragmented. In the bottom two spectra, the N+4 isotopologue ($C_{12}OH_7{}^{79}Br_2{}^{81}Br_2$) of the protonated ion and the N+5 isotopologue ($^{13}C_1{}^{12}C_{11}OH_6{}^{79}Br_2{}^{81}Br_2$) of the radical molecular ion were isolated and fragmented simultaneously.

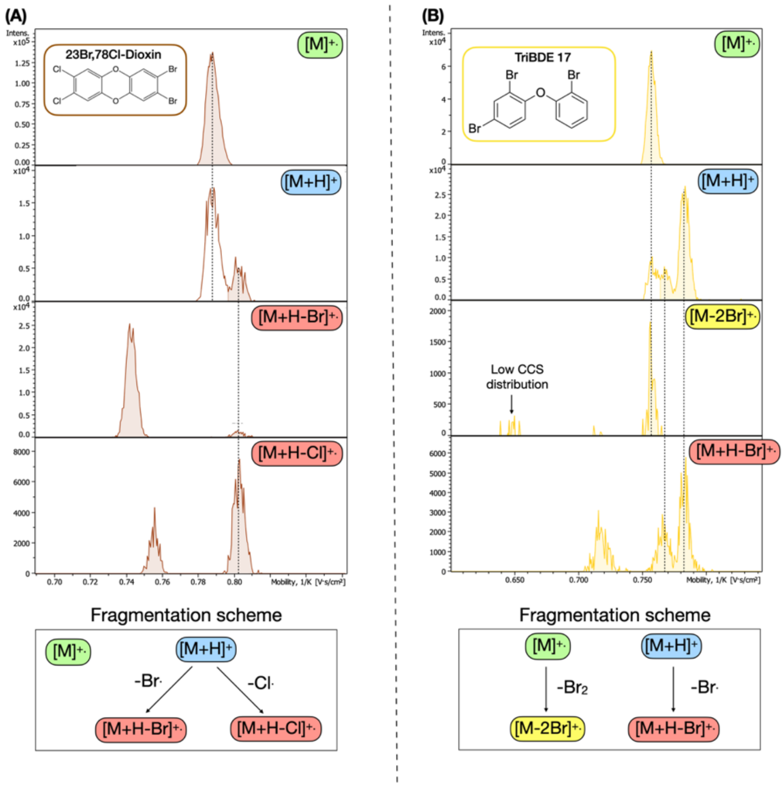

Figure 3.13 – Ion mobility spectra of the radical molecular ion (top), protonated ion (second), and fragment ions (bottom two) of **(A)** 2,3-Br,7,8-Cl-dioxin and **(B)** TriBDE-17. The proposed fragmentation schemes are shown at the bottom of each panel.

An interesting mixed case was observed for PCBs and PBBs. Congeners without halogens at the ortho positions of both aromatic rings (i.e., non-ortho, mono-ortho, and some di-ortho substituted congeners) as well as tetra-ortho substituted congeners produced two fragment ions ($[M+H-X]^{+\cdot}$ and $[M-X]^{+}$) from the same precursor ion (the protonated ion), in accordance with the first case described above (**Figure 3.14A**). However, congeners bearing halogens at the ortho positions of both aromatic rings (excluding the tetra-ortho congeners) also showed additional formation of the $[M-X]^{+}$ ion fragment through the fragmentation of the radical molecular ion ($M^{+\cdot}$), resulting in the hybrid fragmentation scheme shown in Figure 3.14B.

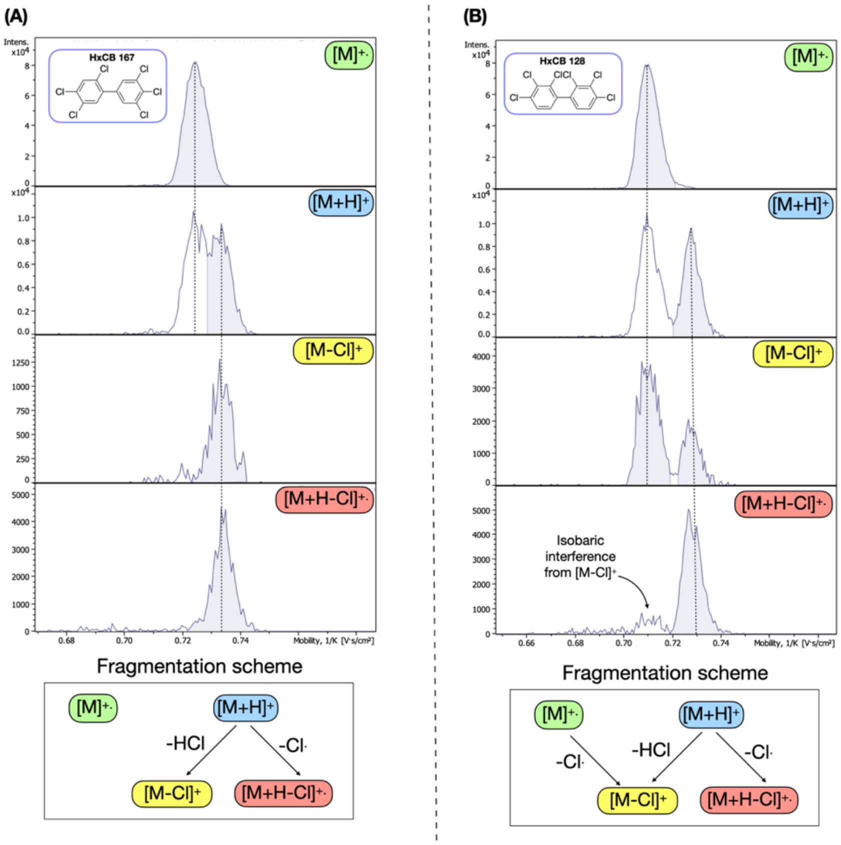

Figure 3.14 – Ion mobility spectra of the radical molecular ion (top), protonated ion (second), and fragment ions (bottom two) of **(A)** HxCB 167 and **(B)** HxCB 128. The proposed fragmentation schemes are shown at the bottom of each panel.

The fragmentation characteristics of the classes of POPs examined in this section is summarized in **Table 3.2**.

Comment on the average extent of fragmentation

Across POP classes with multiple congeners, significant fragmentation was observed primarily for the protonated ions, while radical molecular ions consistently showed minimal fragmentation, with average extents below 3% (Table 3.2).

Bromine substitution markedly increased the fragmentation of protonated species. For example, the average fragmentation extent of $[M+H]^{+}$ ions rose from 5% in chlorinated biphenyls (PCBs) to 44% in brominated biphenyls (PBBs). This trend was also evident in mixed-halogenated classes, where $[M+H-Br]^{+\cdot}$ fragments were consistently more abundant than $[M+H-Cl]^{+\cdot}$ fragments, even when chlorine atoms were more prevalent than bromine in the molecule (Tables 3.1 and 3.2). Overall, $[M+H]^{+}$ fragmentation appeared to be most pronounced in halogenated naphthalenes and dibenzo-p-dioxins, least in halogenated diphenyl ethers, and intermediate in halogenated biphenyls and dibenzofurans.

Complex structures

The wide variety of fragments and extensive fragmentation observed for most OCPs and dechloranes typically gave rise to complex ion mobility spectra. **Figure 3.15** illustrates a representative example using the OCP endosulfan sulfate. As shown, the numerous fragments were generally characterized by a distribution of ion mobility peaks in the lower CCS region (i.e., pre- or intra-IM fragmentation), which may result from the formation of multiple isomeric fragments or the presence of several stable conformers[17].

Table 3.2 – Type of fragment, precursor ion and average extent of fragmentation observed for the classes of POPs giving rise to two fragment ions.

Classes of POP	**Fragment types**	**Precursor ion** (as suggested by alignment of the IM peaks)		**Average extent of fragmentation**	
		Protonated ion $[M+H]^+$	**Radical molecular ion $M^{+\cdot}$**	**Protonated ion $[M+H]^+$**	**Radical molecular ion $M^{+\cdot}$**
PCBs	$[M+H-Cl]^{+\cdot}$	x		2%	
	$[M-Cl]^+$	x	x	3%	~0%
PBBs	$[M+H-Br]^{+\cdot}$	x		44%	
	$[M-Br]^+$	x	x	~0%	3%
PXDDs	$[M+H-Br]^{+\cdot}$	x		58%	
	$[M+H-Cl]^{+\cdot}$	x		29%	
PXDFs	$[M+H-Br]^{+\cdot}$	x		47%	
	$[M+H-Cl]^{+\cdot}$	x		~0%	
PXBs	$[M+H-Br]^{+\cdot}$	x		44%	
	$[M+H-Cl]^{+\cdot}$	x		~0%	
PBDEs	$[M+H-Br]^{+\cdot}$	x		26%	
	$[M-2Br]^+$		x		~0%

In some cases, it was also possible to identify post-IM fragmentation links between fragments and their precursor ions, which may be (quasi)molecular ions or even other fragments. For instance, the $[M-CCl_2-H]^+$ fragment appears to be derived from the radical molecular ion ($M^{+\cdot}$), while the $[C_8Cl_4O]^+$ and $[C_9Cl_4H_3]^+$ fragments seem to originate from the $[M-HSO_4-HCl]^+$ fragment, which itself appears to be linked to the $[M-Cl]^+$ and $[M-HSO_4]^+$ fragments. Interestingly, the ion mobility spectrum of the $[M-Cl]^+$ fragment illustrates that fragment ions can sometimes exhibit larger CCS values than their precursor ion (in this case, $M^{+\cdot}$), possibly due to the adoption of a more extended conformation following fragmentation[17] (e.g., by ring opening).

Overall, the complexity of the resulting spectra makes accurate identification of the fragmentation pathways significantly more difficult and less reliable than the simpler fragmentation patterns discussed in the previous sections.

C. CCS trends[***]

Halogen type comparison

A plot of the measured $^{TIMS}CCS_{N2}$ of different classes of pollutants as function of their mass is shown in **Figure 3.16**. It can be observed that each class of halogenated POPs displays a distinct trend lines in

---

[***] The following discussion applies solely to congener-type POP classes

the CCS vs m/z dimension (Figure 3.16A), which is consistent with other IM studies performed on PCBs, PBDEs and PAHs[10,18]. As discussed in several papers, these specific m/z vs CCS trendlines can be used as an additional tool in nontargeted applications; for example to help in the identification of the chemical class of an unknown compound[19], but also to pre-filter complex data when specific class of compounds are search for[20] (i.e., PFAS).

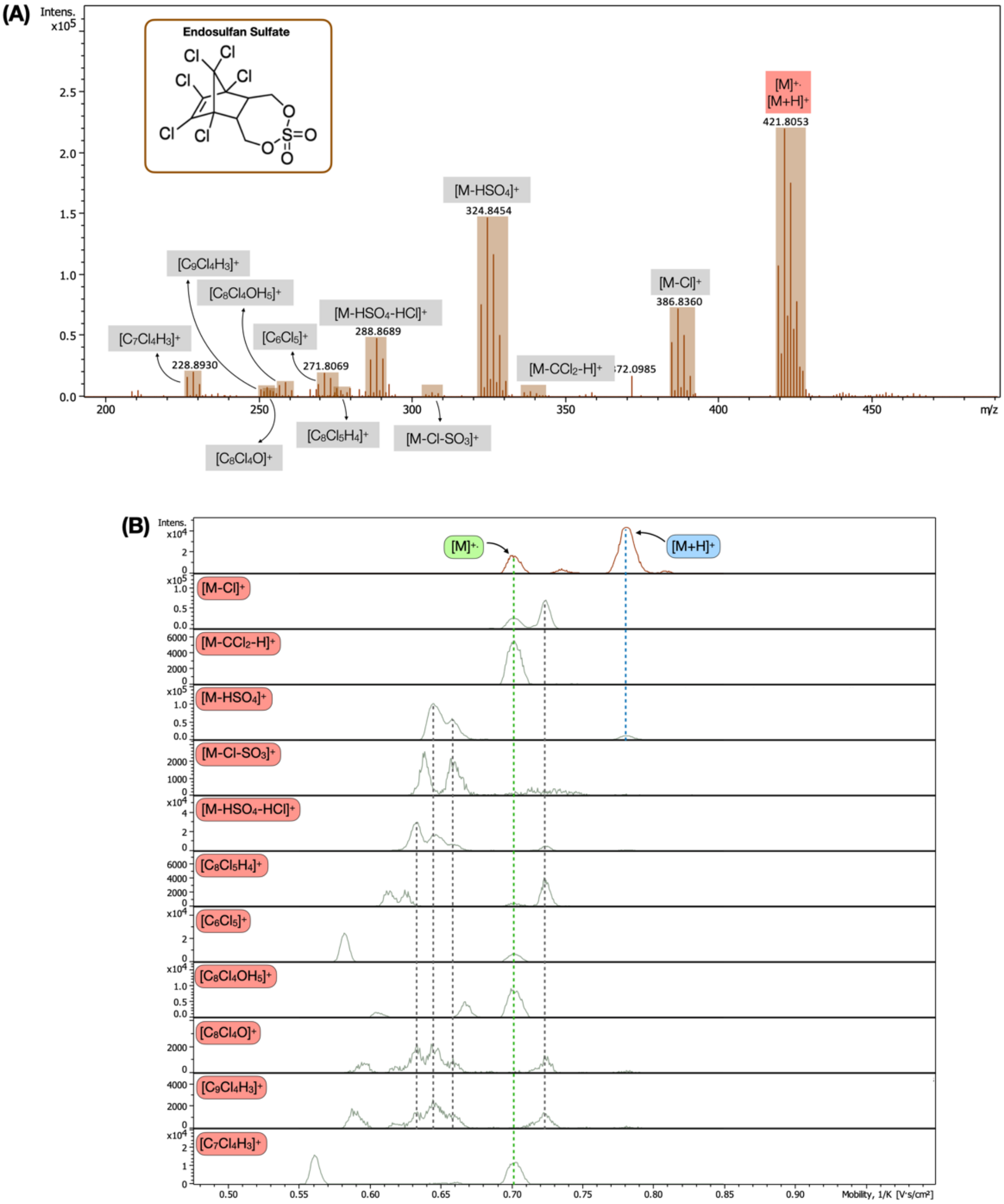

Figure 3.15 – **(A)** APCI(+) mass spectrum of endosulfan sulphate highlighting the diversity of fragments formed before reaching the detector. **(B)** Ion mobility spectra of precursor (top) and fragment (bottom) ions.

Notably, we observe a clear segregation of the trend lines between brominated POPs, chlorinated POPs, and the nonhalogenated class of PAHs (Figure 3.16B). The distinct separation between halogenated and non-halogenated compounds is largely due to the greater atomic mass of halogens (F, Cl, Br) compared to typical elements in organic molecules (such as C, H, O, N, P, and S)[18,21,22]. This results in fewer atoms for a given molecular mass, leading to more compact structures and higher overall ‘mass density’ (i.e., mass/CCS).

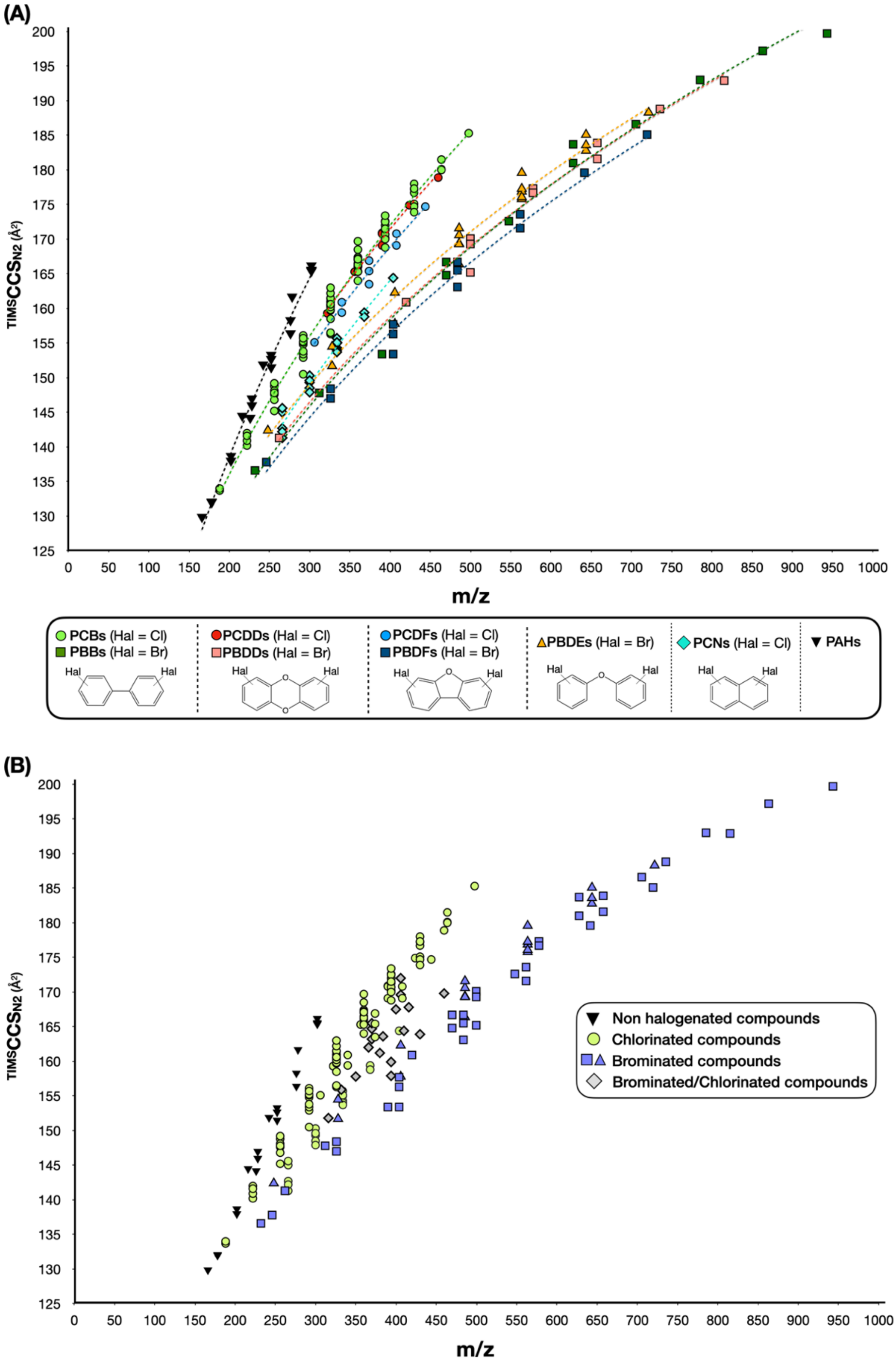

Figure 3.16 – CCS vs m/z plots of different POP classes analysed in this thesis. Panel **(A)** represents the data as a function of the different classes of POPs. Data were fitted with power trendlines of the type CCS = a x $(m/z)^b$. Panel **(B)** represents the same data as a function of halogenation type. Note that the classes of OCPs and eBFRs, which display high intra-diversity in the chemical structures, were not included. CCS values are shown for the molecular ions ($M^{+\cdot}$).

The higher mass density of brominated compounds compared to chlorinated ones further explains their clear segregation observed in Figure 3.16B. Indeed, although the incorporation of bulky bromine atoms tends to increase the CCS more than chlorine atoms do (**Figure S3.13**), the accompanying gain in mass is significantly greater in the case of bromine (average atomic mass 79.9 Da) than chlorine atoms (35.4 Da). As a result, brominated compounds exhibit a smaller increase in CCS relative to mass (reflected as a shallower slope in such plots) compared to their chlorinated counterparts. As expected, contaminant classes containing both chlorine and bromine substituents (i.e., PXDDs, PXDFs and PXBs) were positioned between the chlorinated and brominated regions in Figure 3.16B.

Contaminant class comparison

As shown in **Figure 3.17**, for a given degree of halogenation, the average CCS of the different POP classes approximately followed the order: $CCS_{dibenzodioxins} \simeq CCS_{diphenyl\ ethers} > CCS_{dibenzofurans} \simeq CCS_{biphenyls} > CCS_{naphthalenes}$. This relative ordering was consistent with the one observed for the non-halogenated analogs (i.e., the corresponding skeletal structures, **Figure S3.14**). Additionally, the curves for halogenated dioxins, furans, diphenyl ethers, and naphthalenes were found to be roughly parallel, indicating a similar average rate of CCS increase with increasing halogenation. In contrast, the curve for halogenated biphenyls was slightly steeper, suggesting that, on average, the addition of each halogen atom leads to a greater increase in CCS compared to the other classes.

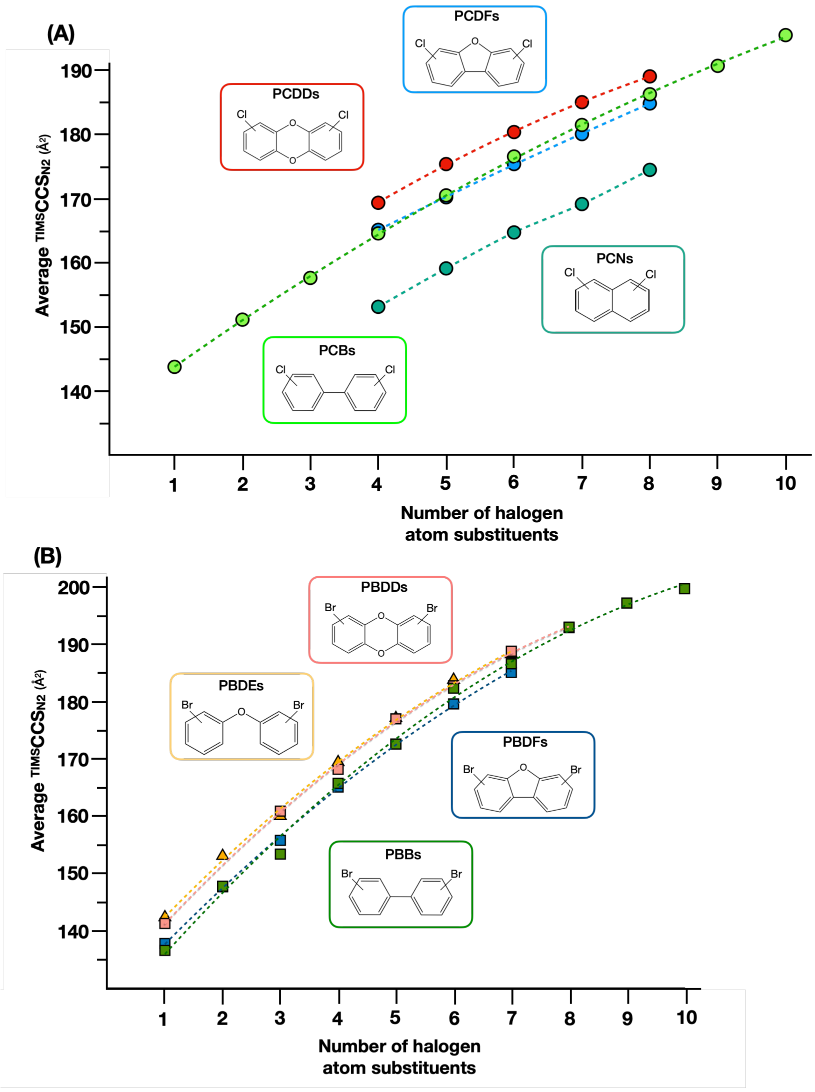

Figure 3.17 - Average $^{TIMS}CCS_{N2}$ of chlorinated **(A)** and brominated **(B)** POPs classes per halogenation degree. Data were fitted with a second order polynomial regression (dotted curves). CCS values are shown for the molecular ions ($M^{+\cdot}$).

Congener-level comparison

Within a compound class, the CCS of the congeners was, as expected, primarily dependent on the number of halogen atom substituents. For a given halogenation degree (i.e., among isomeric congeners), a less pronounced but still noticeable dependence on the halogen substitution pattern could also be observed. **Figure 3.18** illustrates this observation for the class of PCBs. Note the larger average difference in $1/K_0$ between PCB congeners with different degrees of chlorination compared to those with the same number of chlorine atoms. This behavior is similar to what is typically seen in the gas chromatographic retention times of these POPs[23] (i.e., the RT is primarily dependent on the halogenation degree).

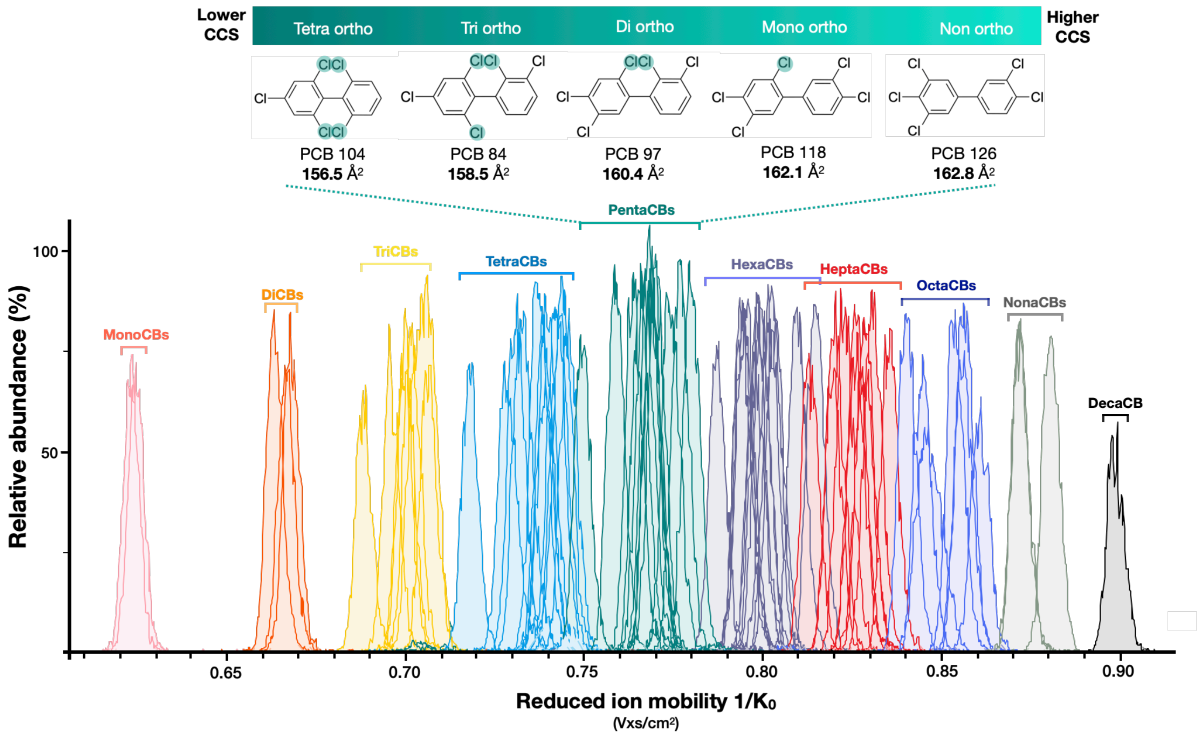

Figure 3.18 – Overlaid ion mobility spectrum of 82 PCBs congeners analysed in this thesis. The inset illustrates the trend of decreasing CCS with increasing chlorine substitution at the ortho positions for a few selected pentachlorobiphenyl isomers. CCS values are shown for the molecular ions ($M^{+\cdot}$).

For some compound classes, notable CCS trends were observed among isomeric congeners based on their substitution patterns. For example, halogenated biphenyl isomers generally exhibited lower CCS values as the degree of halogen substitution at the ortho positions increased (see inset in Figure 3.18). This trend is likely due to the adoption of more compact, non-coplanar conformations by biphenyls with a higher number of ortho halogens. In contrast, biphenyls with few or no ortho halogens are believed to adopt more extended, coplanar conformations, resulting in larger CCS values[10]. Interestingly, the influence of ortho substitution on the CCS of PCB congeners parallels its effect on their gas chromatographic retention times, where greater ortho substitution typically results in lower retention times (**Figure S3.15**). The ability to separate PCBs in both the GC and IM dimensions based on their degree of ortho substitution is particularly relevant, as this structural feature also governs their toxicity, non-ortho congeners being the most toxic.

CCS trends were also observed for isomers belonging to other classes of POPs. For example, in the case of hexa 2,3,7,8-substituted dibenzodioxins (PCDDs and PBDDs), isomers having the two extra halogen atoms on opposite sides of the dibenzodioxin moiety displayed a higher CCS compared to those having them on the same side (**Figures 3.19** and **S3.16**).

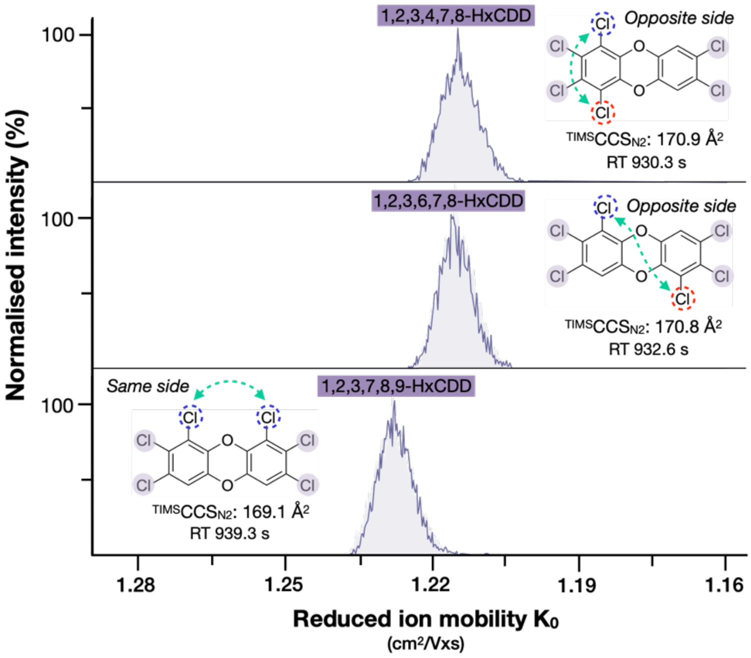

Figure 3.19 - Ion mobility spectra of hexa substituted 2,3,7,8-PCDDs. CCS values are shown for the molecular ions ($M^{+\cdot}$).

Similarly, for the corresponding penta and hexa 2,3,7,8-substituted dibenzo furans (PCDFs and PBDFs), isomers with extra halogen atom(s) on the same side of the oxygen atom (positions 4 and 6, **Figures 3.20** and **S3.17**) generally displayed higher CCS values. This could be attributed to the fact that halogens in those positions lead to more extended structures compared to halogens in positions 1 and 9 (on the opposite side of the oxygen atom).

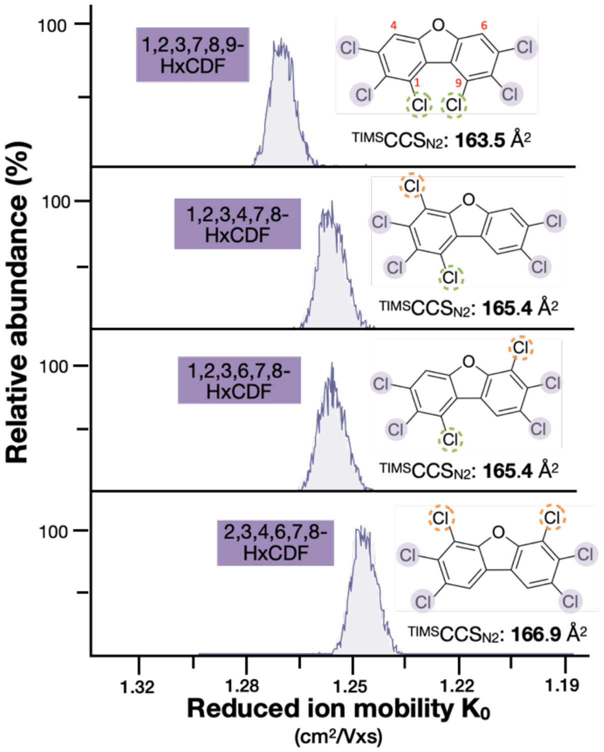

Figure 3.20 - Ion mobility spectra of hexa-substituted 2,3,7,8-PCDFs. Halogen atoms that are on the same side of the dibenzo furan moiety as the oxygen atom (positions 4 and 6) are circled in orange, while those on the opposite side (positions 1 and 9) are circled in green. CCS values are shown for the molecular ions ($M^{+\cdot}$).

3.3 - Conclusion

In conclusion, the establishment of a robust CCS calibration procedure for GC-hyphenated timsTOF systems proved to be essential due to the specific challenges introduced by the GC-APCI ion source (inability to perform direct infusion-based calibrations and changes in the analytical drift gas properties). The internal calibration strategy based on background siloxane ions described in this chapter provides a fast, cost-free, and real-time calibration solution that also enables post-acquisition recalibration and extends to mass calibration.

Furthermore, the GC-APCI-TIMS-MS measurements conducted on various classes of POPs demonstrated that factors such as halogen type and number, substitution pattern, molecular rigidity, and ionization mechanism significantly influence their ion mobility and collision cross section values. Since charge transfer generally predominated over proton transfer for most classes and typically resulted in simpler, single-peak mobility spectra, radical molecular ions appear as the most suitable candidates for quantitative applications. However, the rich information provided by the more complex ion mobility signatures of both protonated and fragment ions offers valuable potential for compound identification in non-targeted analytical workflows.

3.4 - References

(1) Gabelica, V. CHAPTER 1. Ion Mobility–Mass Spectrometry: An Overview. In *New Developments in Mass Spectrometry*; Ashcroft, A. E., Sobott, F., Eds.; Royal Society of Chemistry: Cambridge, 2021; pp 1–25. https://doi.org/10.1039/9781839162886-00001.

(2) Dodds, J. N.; Baker, E. S. Ion Mobility Spectrometry: Fundamental Concepts, Instrumentation, Applications, and the Road Ahead. *J. Am. Soc. Mass Spectrom.* **2019**, *30* (11), 2185–2195. https://doi.org/10.1007/s13361-019-02288-2.

(3) Song, X.-C.; Canellas, E.; Dreolin, N.; Goshawk, J.; Lv, M.; Qu, G.; Nerin, C.; Jiang, G. Application of Ion Mobility Spectrometry and the Derived Collision Cross Section in the Analysis of Environmental Organic Micropollutants. *Environ. Sci. Technol.* **2023**, *57* (51), 21485–21502. https://doi.org/10.1021/acs.est.3c03686.

(4) Celma, A.; Alygizakis, N.; Belova, L.; Bijlsma, L.; Fabregat-Safont, D.; Menger, F.; Gil-Solsona, R. Ion Mobility Separation Coupled to High-Resolution Mass Spectrometry in Environmental Analysis – Current State and Future Potential. *Trends Environ. Anal. Chem.* **2024**, *43*, e00239. https://doi.org/10.1016/j.teac.2024.e00239.

(5) Bleiholder, C. Towards Measuring Ion Mobilities in Non-Stationary Gases and Non-Uniform and Dynamic Electric Fields (I). Transport Equation. *Int. J. Mass Spectrom.* **2016**, *399–400*, 1–9. https://doi.org/10.1016/j.ijms.2016.01.003.

(6) Gabelica, V.; Shvartsburg, A. A.; Afonso, C.; Barran, P.; Benesch, J. L. P.; Bleiholder, C.; Bowers, M. T.; Bilbao, A.; Bush, M. F.; Campbell, J. L.; Campuzano, I. D. G.; Causon, T.; Clowers, B. H.; Creaser, C. S.; De Pauw, E.; Far, J.; Fernandez-Lima, F.; Fjeldsted, J. C.; Giles, K.; Groessl, M.; Hogan, C. J.; Hann, S.; Kim, H. I.; Kurulugama, R. T.; May, J. C.; McLean, J. A.; Pagel, K.; Richardson, K.; Ridgeway, M. E.; Rosu, F.; Sobott, F.; Thalassinos, K.; Valentine, S. J.; Wyttenbach, T. Recommendations for Reporting Ion Mobility Mass Spectrometry Measurements. *Mass Spectrom. Rev.* **2019**, *38* (3), 291–320. https://doi.org/10.1002/mas.21585.

(7) Michelmann, K.; Silveira, J. A.; Ridgeway, M. E.; Park, M. A. Fundamentals of Trapped Ion Mobility Spectrometry. *J. Am. Soc. Mass Spectrom.* **2015**, *26* (1), 14–24. https://doi.org/10.1007/s13361-014-0999-4.

(8) Stow, S. M.; Causon, T. J.; Zheng, X.; Kurulugama, R. T.; Mairinger, T.; May, J. C.; Rennie, E. E.; Baker, E. S.; Smith, R. D.; McLean, J. A.; Hann, S.; Fjeldsted, J. C. An Interlaboratory Evaluation of Drift Tube Ion Mobility–Mass Spectrometry Collision Cross Section Measurements. *Anal. Chem.* **2017**, *89* (17), 9048–9055. https://doi.org/10.1021/acs.analchem.7b01729.

(9) Silveira, J. A.; Michelmann, K.; Ridgeway, M. E.; Park, M. A. Fundamentals of Trapped Ion Mobility Spectrometry Part II: Fluid Dynamics. *J. Am. Soc. Mass Spectrom.* **2016**, *27* (4), 585–595. https://doi.org/10.1007/s13361-015-1310-z.

(10) Zheng, X.; Dupuis, K. T.; Aly, N. A.; Zhou, Y.; Smith, F. B.; Tang, K.; Smith, R. D.; Baker, E. S. Utilizing Ion Mobility Spectrometry and Mass Spectrometry for the Analysis of Polycyclic Aromatic Hydrocarbons, Polychlorinated Biphenyls, Polybrominated Diphenyl Ethers and Their Metabolites. *Anal. Chim. Acta* **2018**, *1037*, 265–273. https://doi.org/10.1016/j.aca.2018.02.054.

(11) Srogi, K. Monitoring of Environmental Exposure to Polycyclic Aromatic Hydrocarbons: A Review. *Environ. Chem. Lett.* **2007**, *5* (4), 169–195. https://doi.org/10.1007/s10311-007-0095-0.

(12) Steidel, M.; Knecht, S.; Sweetman, G.; Klös-Hudak, M.; Kammerer, K.; Bantscheff, M.; Zinn, N. Impact of Local Air Pressure on Ion Mobilities and Data Consistency in diaPASEF-Based High Throughput Proteomics. *J. Proteome Res.* **2025**, *24* (2), 966–973. https://doi.org/10.1021/acs.jproteome.4c00932.

(13) Gross, J. H. *Mass Spectrometry*; Springer International Publishing: Cham, 2017. https://doi.org/10.1007/978-3-319-54398-7.

(14) Li, D.-X.; Gan, L.; Bronja, A.; Schmitz, O. J. Gas Chromatography Coupled to Atmospheric Pressure Ionization Mass Spectrometry (GC-API-MS): Review. *Anal. Chim. Acta* **2015**, *891*, 43–61. https://doi.org/10.1016/j.aca.2015.08.002.

(15) Morsa, D.; Hanozin, E.; Eppe, G.; Quinton, L.; Gabelica, V.; Pauw, E. D. Effective Temperature and Structural Rearrangement in Trapped Ion Mobility Spectrometry. *Anal. Chem.* **2020**, *92* (6), 4573–4582. https://doi.org/10.1021/acs.analchem.9b05850.

(16) Bleiholder, C.; Liu, F. C.; Chai, M. Comment on Effective Temperature and Structural Rearrangement in Trapped Ion Mobility Spectrometry. *Anal. Chem.* **2020**, *92* (24), 16329–16333. https://doi.org/10.1021/acs.analchem.0c02052.

(17) Palm, E. H.; Engelhardt, J.; Tshepelevitsh, S.; Weiss, J.; Kruve, A. Gas Phase Reactivity of Isomeric Hydroxylated Polychlorinated Biphenyls. *J. Am. Soc. Mass Spectrom.* **2024**, *35* (5), 1021–1029. https://doi.org/10.1021/jasms.4c00035.

(18) Foster, M.; Rainey, M.; Watson, C.; Dodds, J. N.; Kirkwood, K. I.; Fernández, F. M.; Baker, E. S. Uncovering PFAS and Other Xenobiotics in the Dark Metabolome Using Ion Mobility Spectrometry, Mass Defect Analysis, and Machine Learning. *Environ. Sci. Technol.* **2022**, *56* (12), 9133–9143. https://doi.org/10.1021/acs.est.2c00201.

(19) Picache, J. A.; Rose, B. S.; Balinski, A.; Leaptrot, K. L.; Sherrod, S. D.; May, J. C.; McLean, J. A. Collision Cross Section Compendium to Annotate and Predict Multi-Omic Compound Identities. *Chem. Sci.* **2019**, *10* (4), 983–993. https://doi.org/10.1039/C8SC04396E.

(20) Kirkwood-Donelson, K. I.; Dodds, J. N.; Schnetzer, A.; Hall, N.; Baker, E. S. Uncovering Per- and Polyfluoroalkyl Substances (PFAS) with Nontargeted Ion Mobility Spectrometry–Mass Spectrometry Analyses. *Sci. Adv.* **2023**, *9* (43), eadj7048. https://doi.org/10.1126/sciadv.adj7048.

(21) MacNeil, A.; Li, X.; Amiri, R.; Muir, D. C. G.; Simpson, A.; Simpson, M. J.; Dorman, F. L.; Jobst, K. J. Gas Chromatography-(Cyclic) Ion Mobility Mass Spectrometry: A Novel Platform for the Discovery of Unknown Per-/Polyfluoroalkyl Substances. *Anal. Chem.* **2022**, *94* (31), 11096–11103. https://doi.org/10.1021/acs.analchem.2c02325.

(22) Mullin, L.; Jobst, K.; DiLorenzo, R. A.; Plumb, R.; Reiner, E. J.; Yeung, L. W. Y.; Jogsten, I. E. Liquid Chromatography-Ion Mobility-High Resolution Mass Spectrometry for Analysis of Pollutants in Indoor Dust: Identification and Predictive Capabilities. *Anal. Chim. Acta* **2020**, *1125*, 29–40. https://doi.org/10.1016/j.aca.2020.05.052.

(23) Van Leeuwen, S. P. J.; De Boer, J. Advances in the Gas Chromatographic Determination of Persistent Organic Pollutants in the Aquatic Environment. *J. Chromatogr. A* **2008**, *1186* (1–2), 161–182. https://doi.org/10.1016/j.chroma.2008.01.044.

3.5 - Supporting information

FIGURES

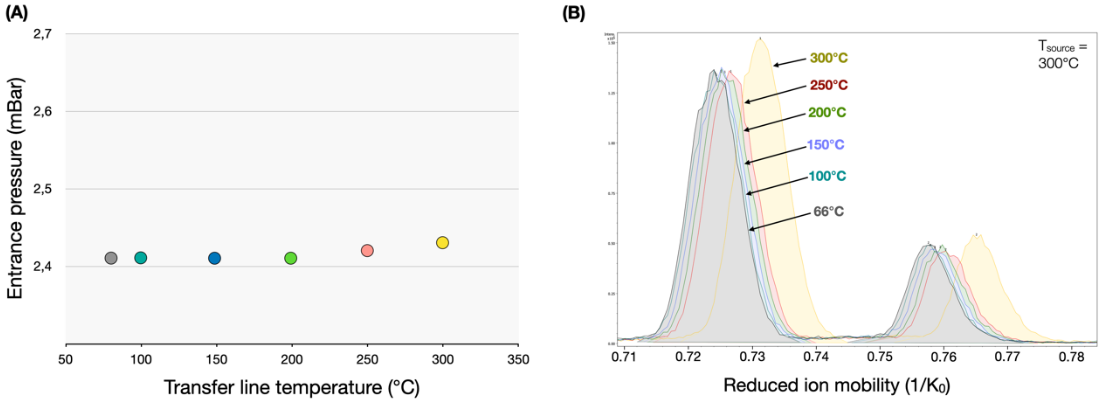

Figure S3.1 – (A) Variation of the TIMS entrance pressure (p_{ent}) as a function of the temperature of the transfer line; (B) Corresponding ion mobility spectra from a background siloxane ion (m/z 355).

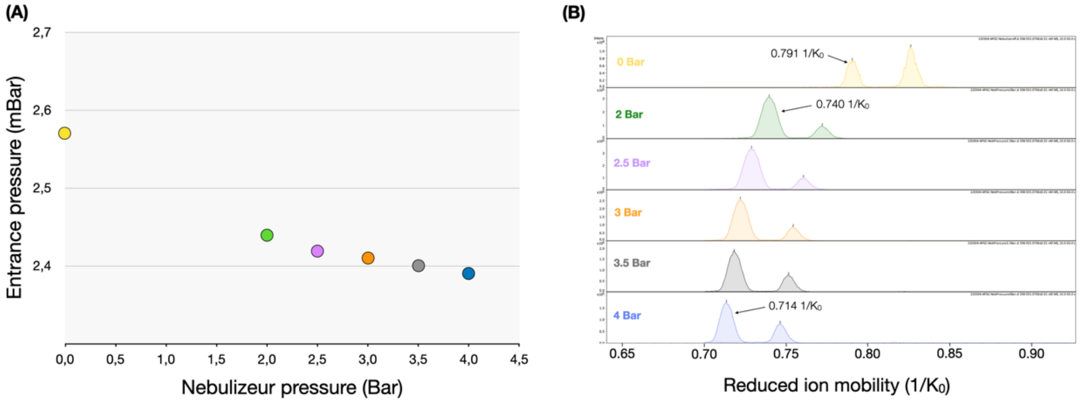

Figure S3.2 – (A) Variation of the TIMS entrance pressure (p_{ent}) as a function of the temperature of the nebulizeur pressure; (B) Corresponding ion mobility spectra from a background siloxane ion (m/z 355).

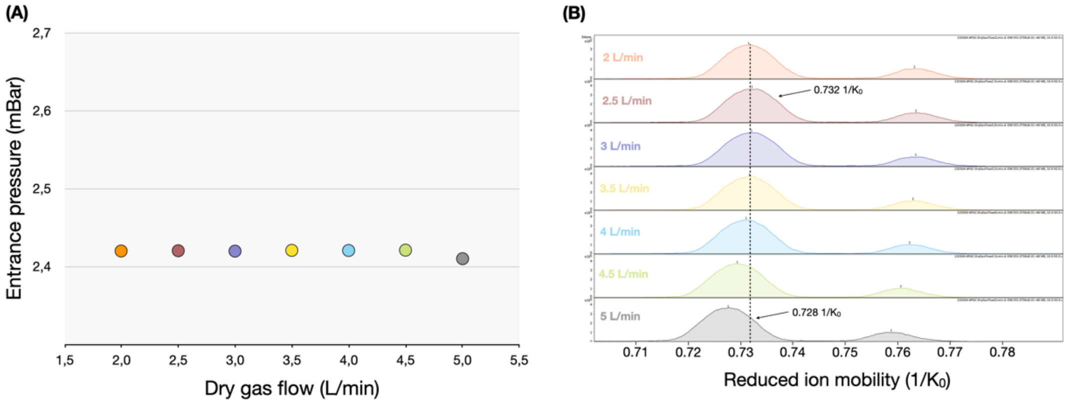

Figure S3.3 – (A) Variation of the TIMS entrance pressure (p_{ent}) as a function of the temperature of the dry gas flow; (B) Corresponding ion mobility spectra from a background siloxane ion (m/z 355).

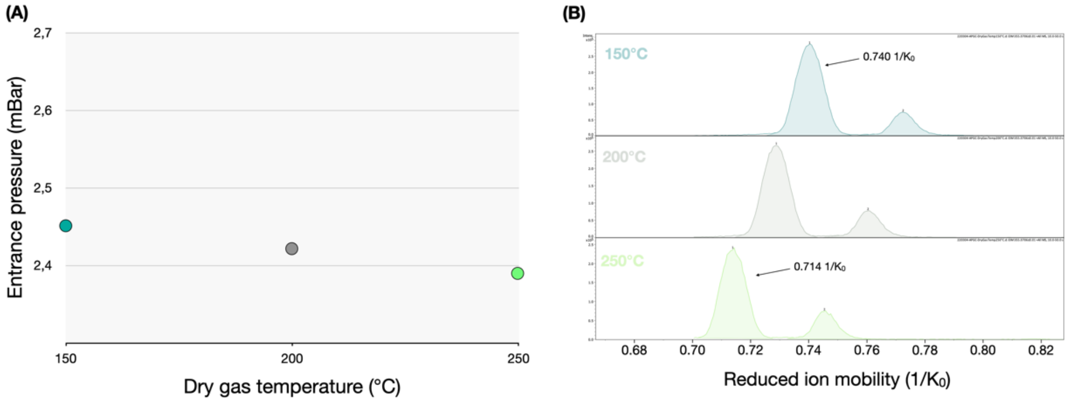

Figure S3.4 – (A) Variation of the TIMS entrance pressure (p_{ent}) as a function of the temperature of the dry gas temperature; (B) Corresponding ion mobility spectra from a background siloxane ion (m/z 355).

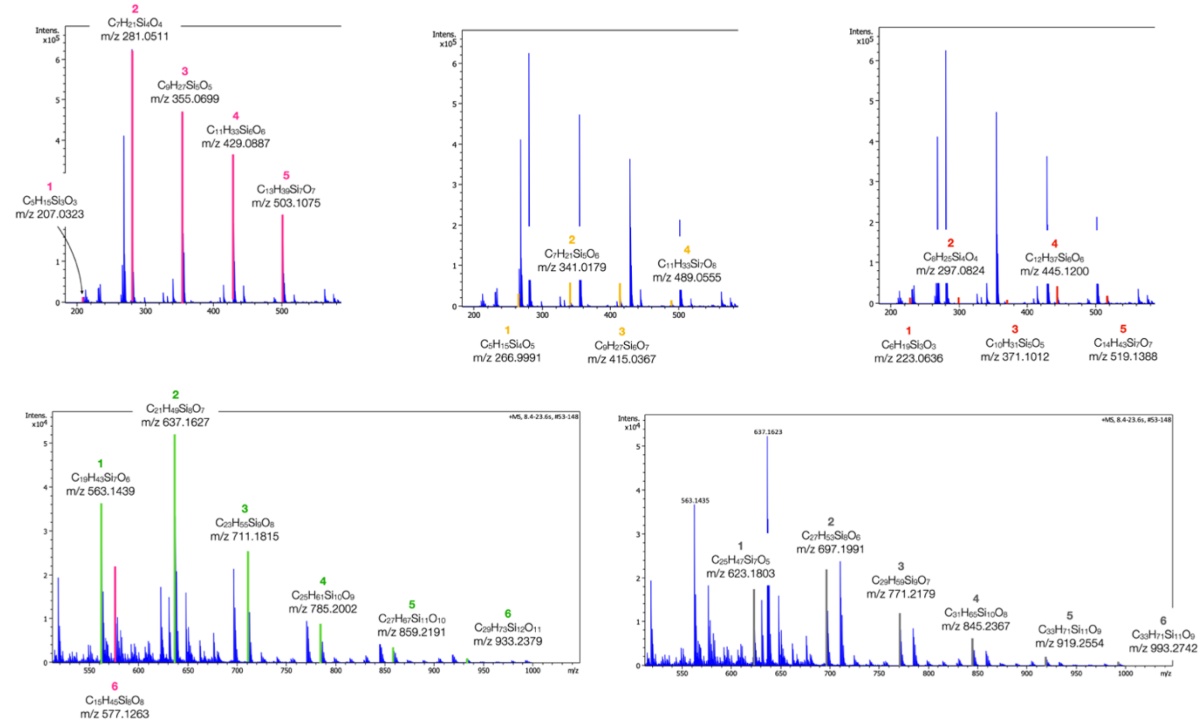

Figure S3.5 – Series of siloxane ions identified in the background GC bleeding.

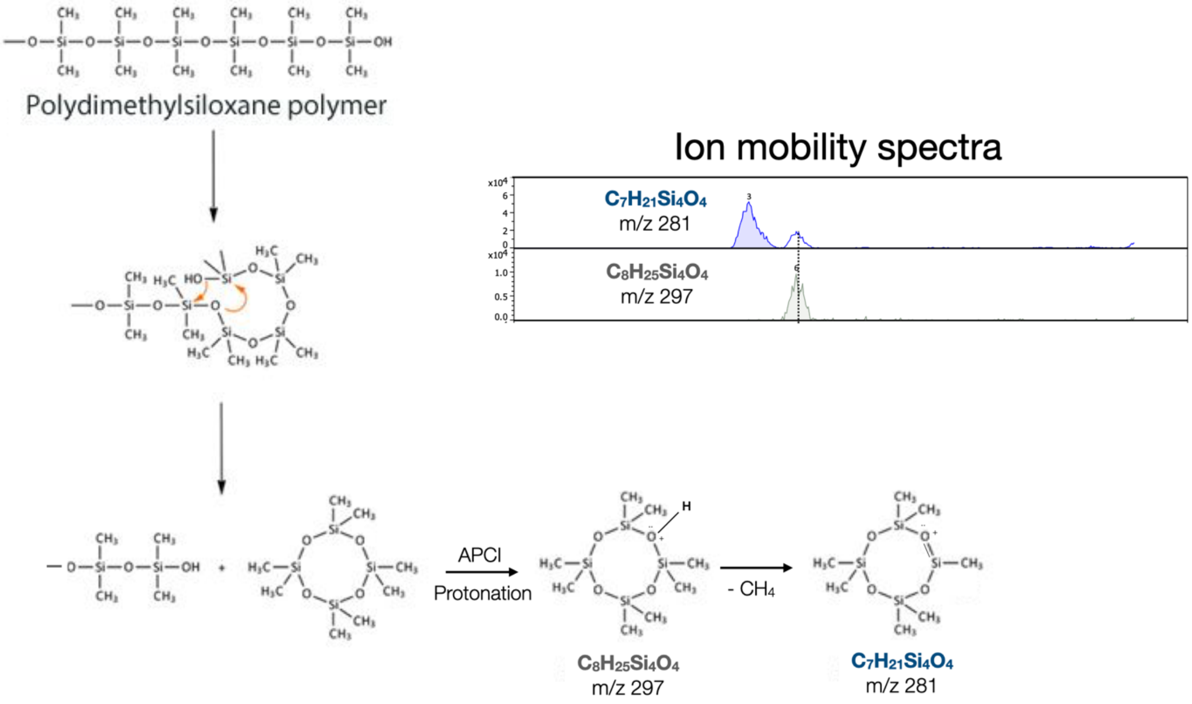

Figure S3.6 – Proposed formation mechanism of siloxane background ions m/z 281 and 297 from polydimethylsiloxane polymer. The inset shows the ion mobility spectra of both ions. The alignment of their IM peaks suggests that m/z ion 297 is the precursor ion of m/z ion 281, consistent with the proposed mechanism.

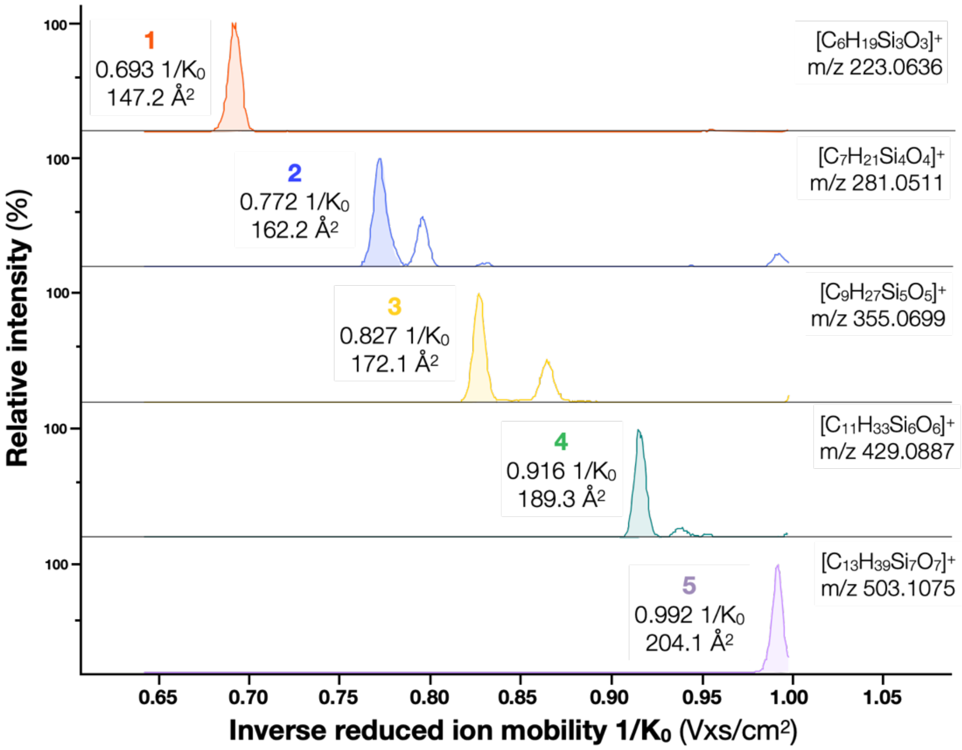

Figure S3.7 – Ion mobility spectra of the five siloxane ions used as internal IM calibrants. The reported CCS values were determined using the calibration curve shown in Figure 1.3.

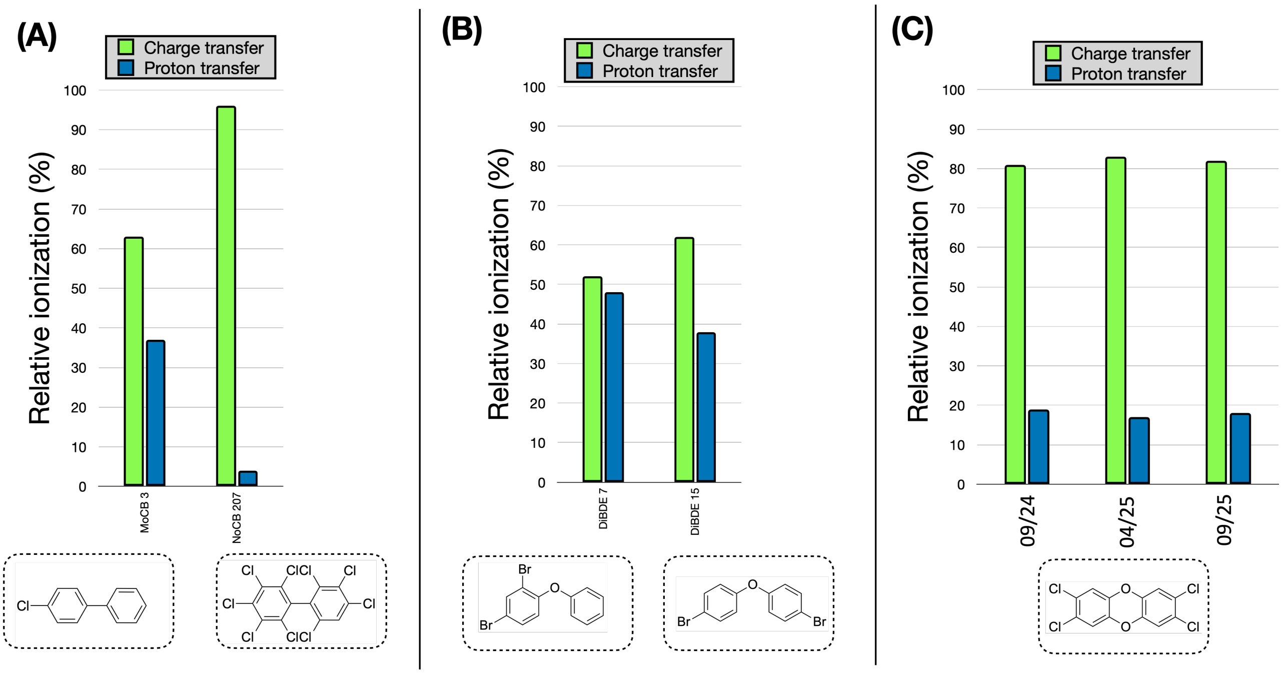

Figure S3.8 – Illustration of the impact of **(A)** halogenation degree, **(B)** halogenation substitution pattern and **(C)** time on the relative proportions of charge transfer and proton transfer.

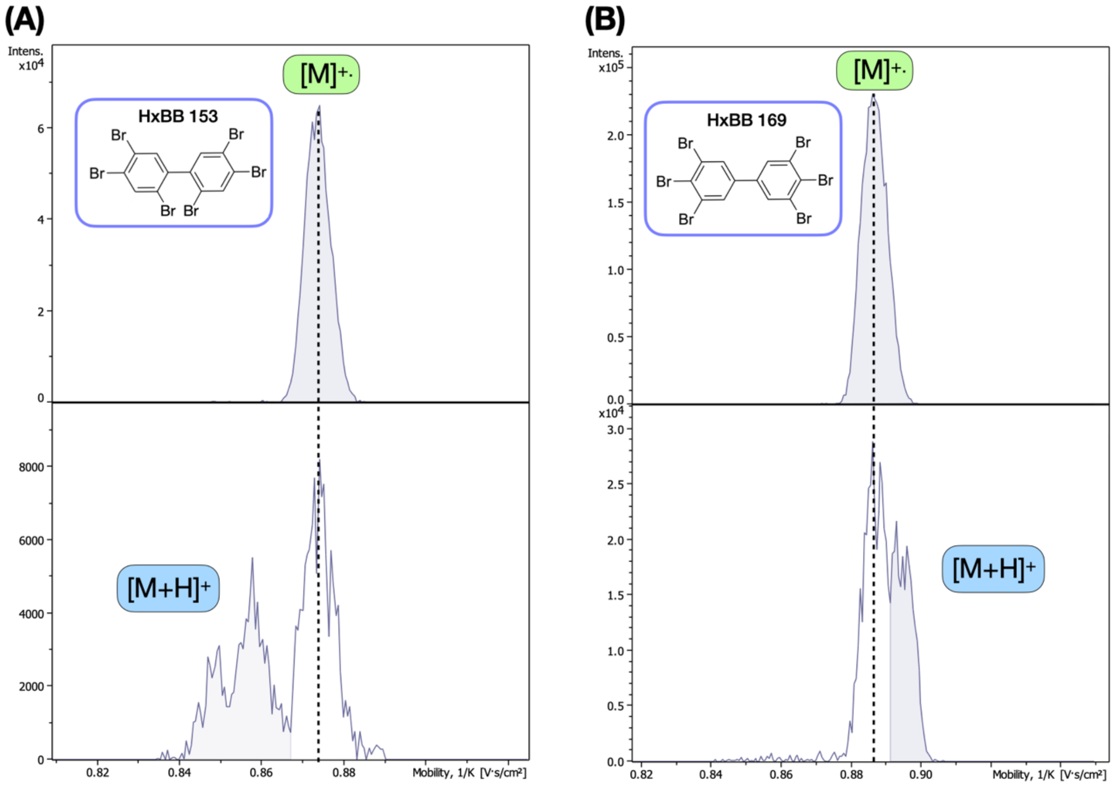

Figure S3.9 – **(A)** Example of a compound (Hexabromobiphenyl 153) where the CCS of the protonated ion [M+H]$^+$ is lower than that of the corresponding radical molecular ion M$^{+\cdot}$. Similar cases were observed for two other polybrominated biphenyls (HpBB 180 and OBB 194) and some organochlorinated pesticides (e.g., p,p'-DDE and Dieldrin). **(B)** In contrast, for the structurally similar Hexabromobiphenyl 169, the more typical case is observed, with the protonated ion having a higher CCS than the radical ion.

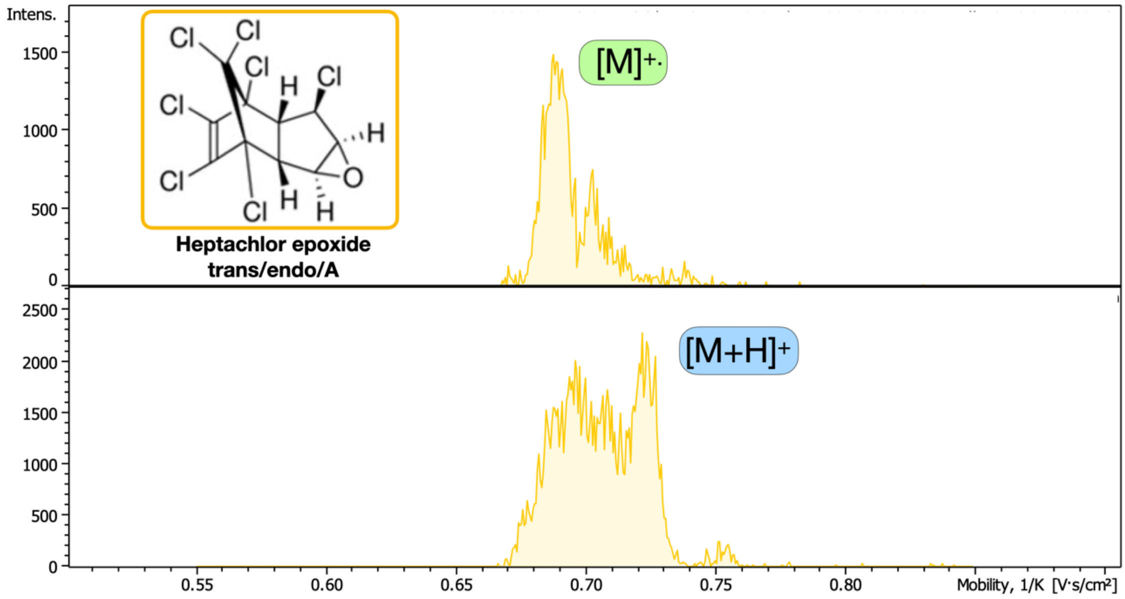

Figure S3.10 - Ion mobility spectra of the radical molecular ion and the protonated ion of the organochlorine pesticide heptachlor epoxide endo. Both ions are characterized by complex peak patterns.

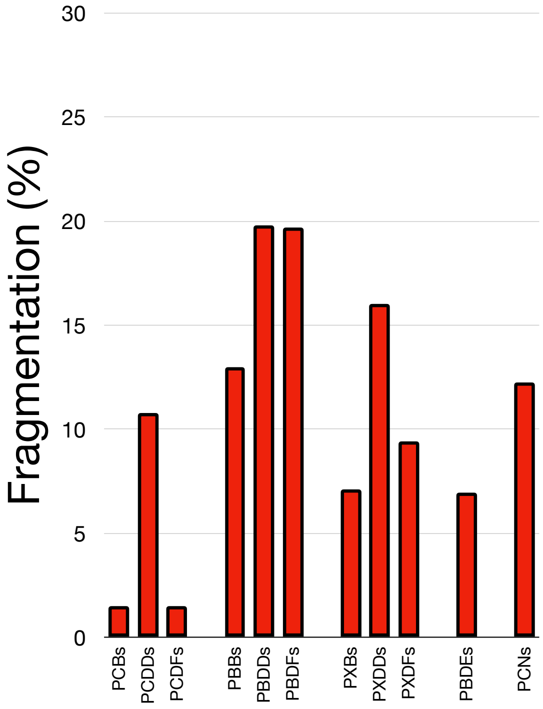

Figure S3.11 – Average fragmentation percentages across different POP congener classes. Percentages were calculated by comparing the sum of the IM peak areas of the most intense isotopologue of the fragment ions to the sum of the IM peak areas of both the fragment ions and the (quasi)molecular ions. Fragment ion areas were corrected to account for differences in absolute isotopic abundance relative to the (quasi)molecular ions.

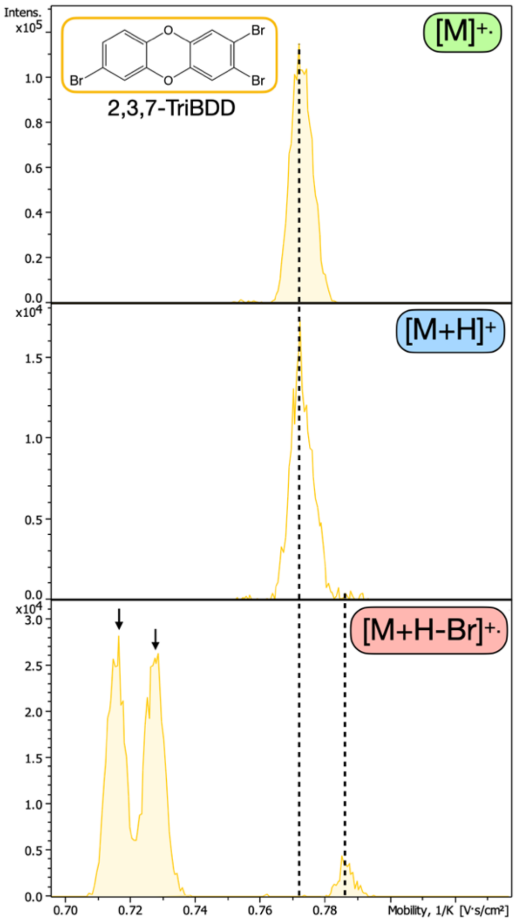

Figure S3.12 - Ion mobility spectra of the radical molecular ion (top), protonated ion (middle), and fragment ion (bottom) of 2,3,7-tribromodibenzo-p-dioxin. Two distinct peaks are clearly observed in the low CCS region of the fragment ion spectrum.

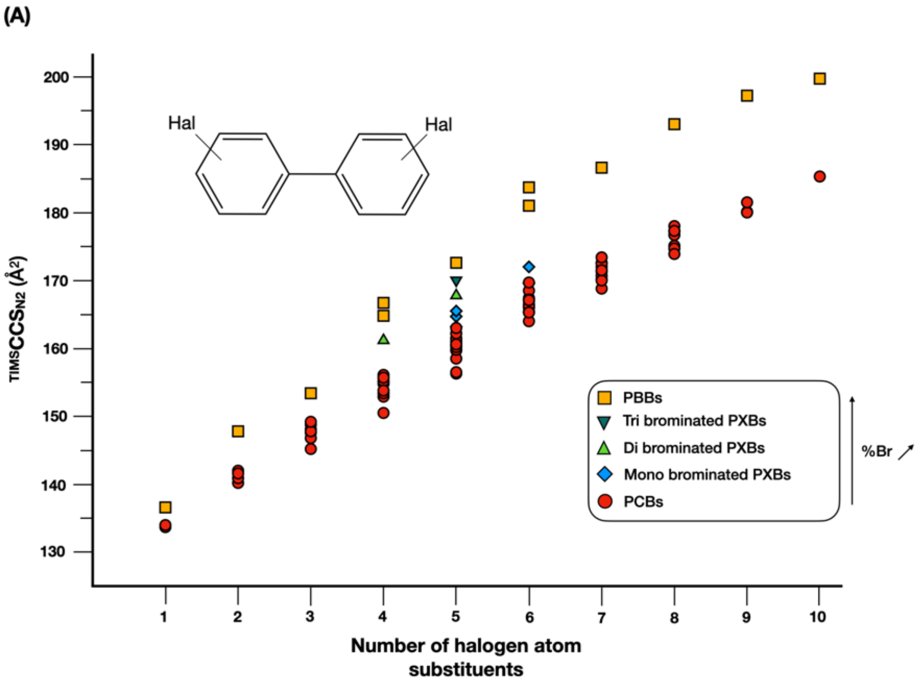

(B)

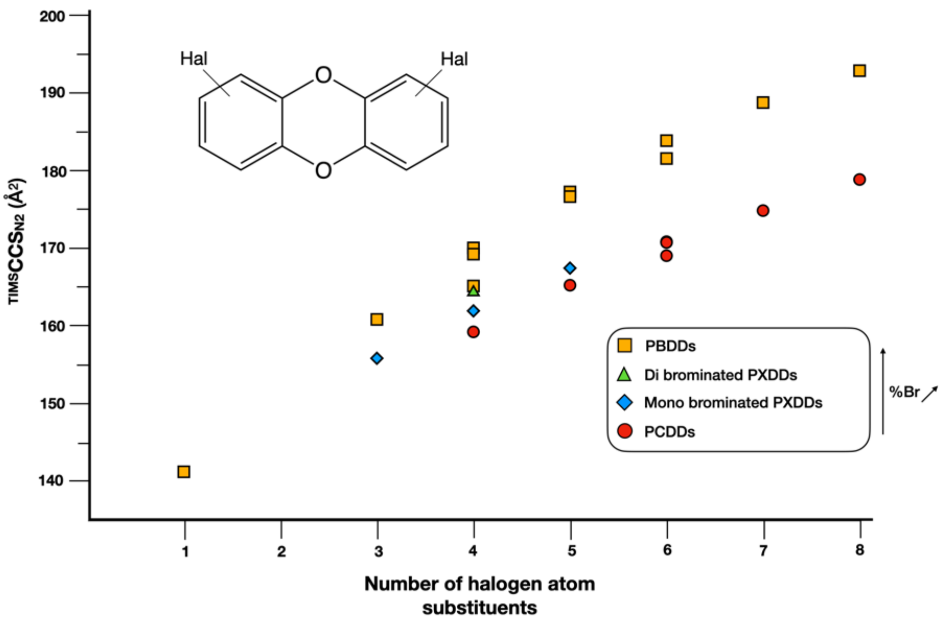

(C)

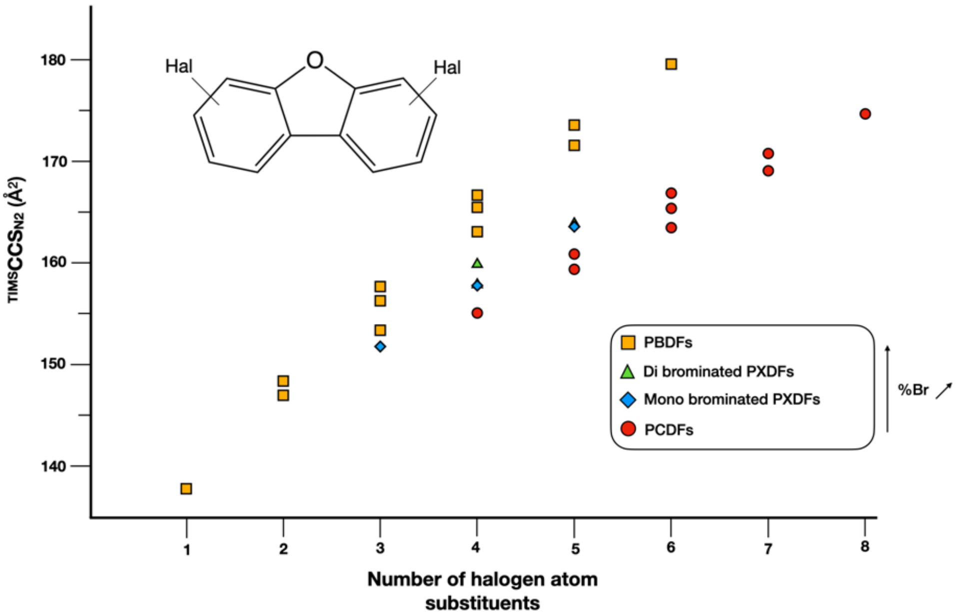

Figure S3.13 – CCS vs. degree of halogenation plots for different classes of halogenated biphenyls **(A)**, halogenated dibenzo-p-dioxins **(B)**, and halogenated dibenzofurans **(C)**. These plots highlight the following trends: (1) the increase in CCS with each additional bromine atom (i.e., the slope) is greater than that observed for chlorine atoms; and (2) for a given total number of halogen atoms, CCS increases with the proportion of bromine atoms.

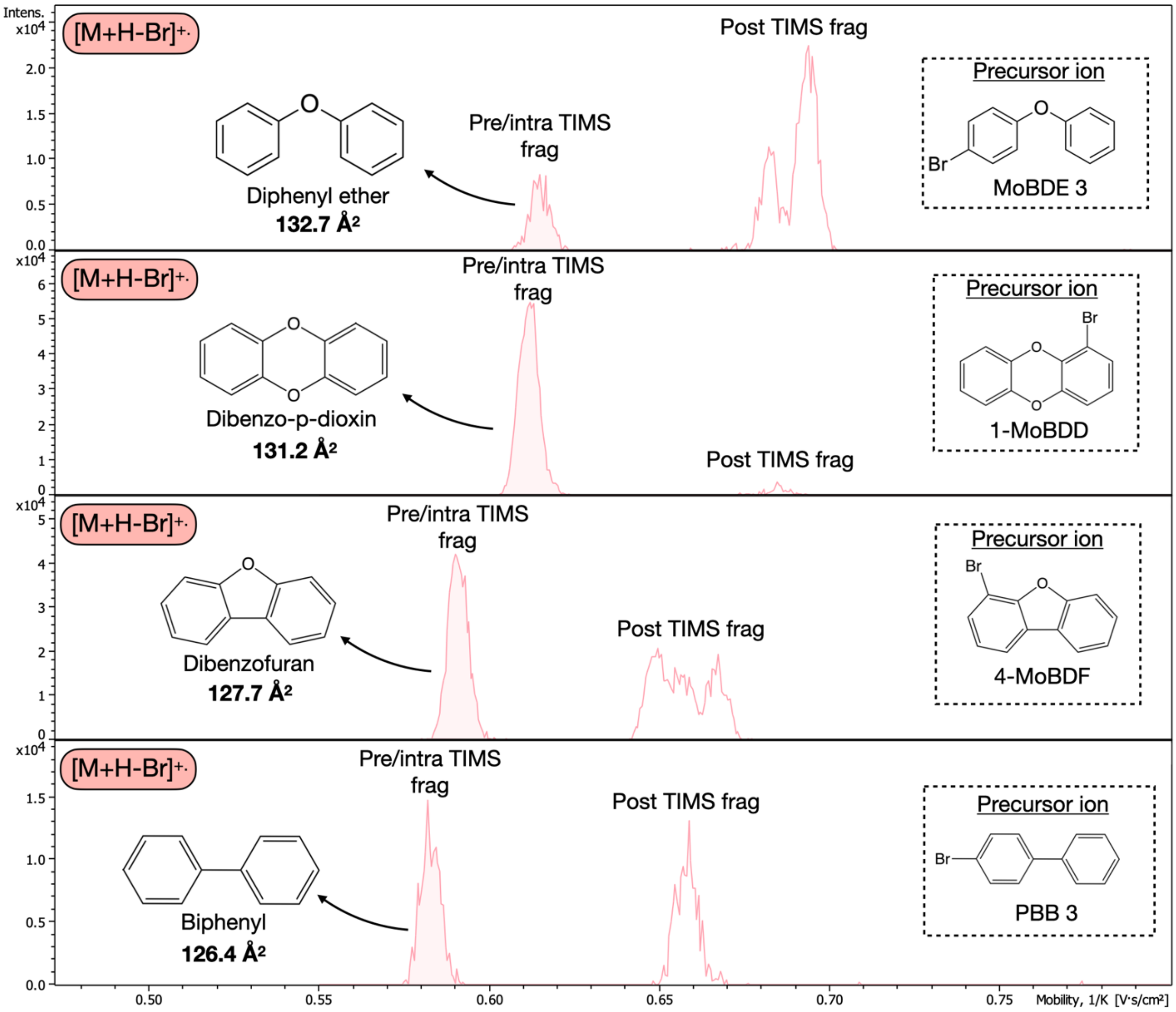

Figure S3.14 – Collision cross sections of the skeletal structures of the classes of PXDEs (diphenyl ether), PXDDs (dibenzo-p-dioxin), PXDFs (dibenzofuran) and PXBs (biphenyl). As the corresponding standards were not available in our laboratory, these CCS values were inferred from the peaks corresponding to the pre/intra-TIMS fragmentation of monobromo-substituted analogs (with the assumption that the vacant position from the lost bromine atom is effectively replaced by the additional hydrogen atom from protonation).

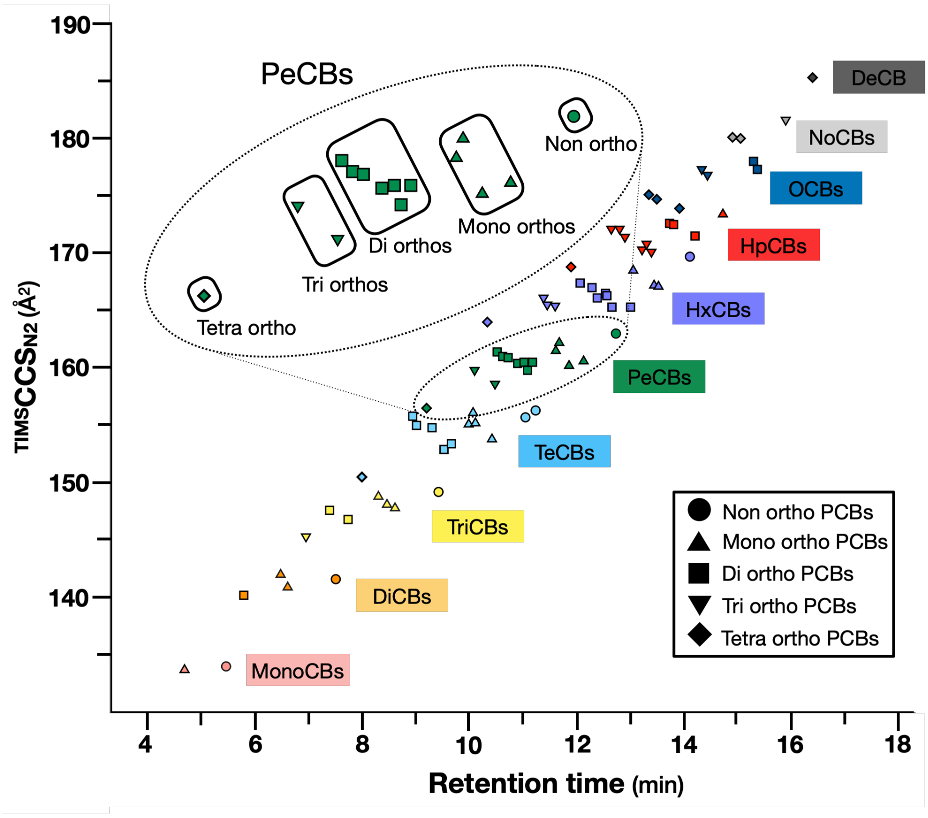

Figure S3.15 – Retention time versus CCS of PCBs (n=82). Color and shape respectively refer to halogenation and ortho substitution degree of the PCBs. The inset is a close-up view of the data of pentachloro substituted biphenyls (PeCBs).

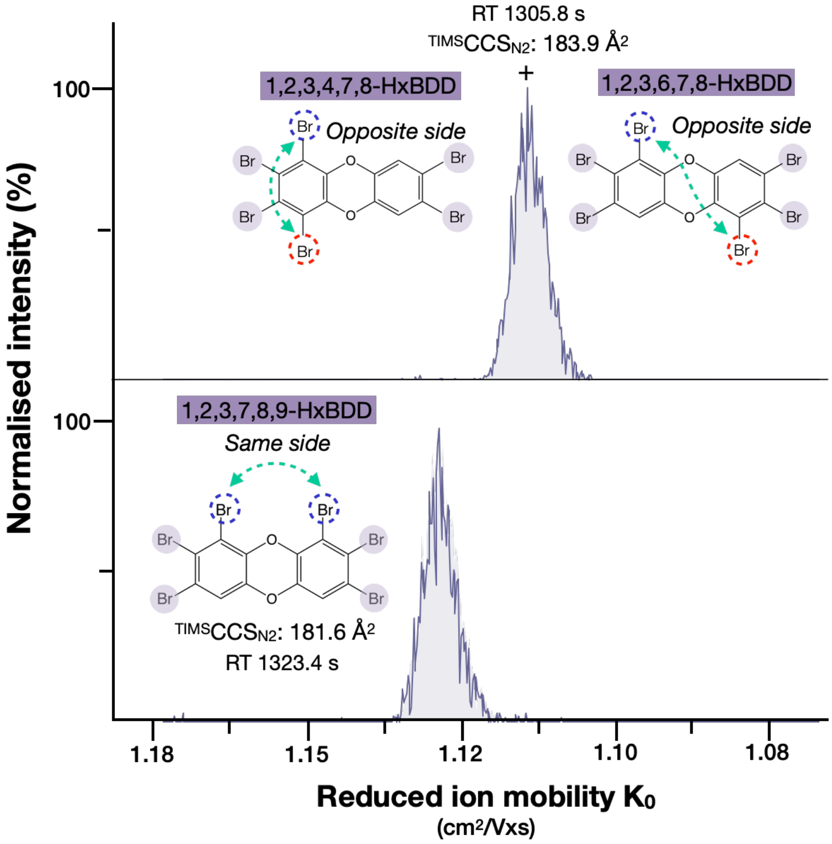

Figure S3.16 - Ion mobility spectra of hexa substituted 2,3,7,8-PBDDs.

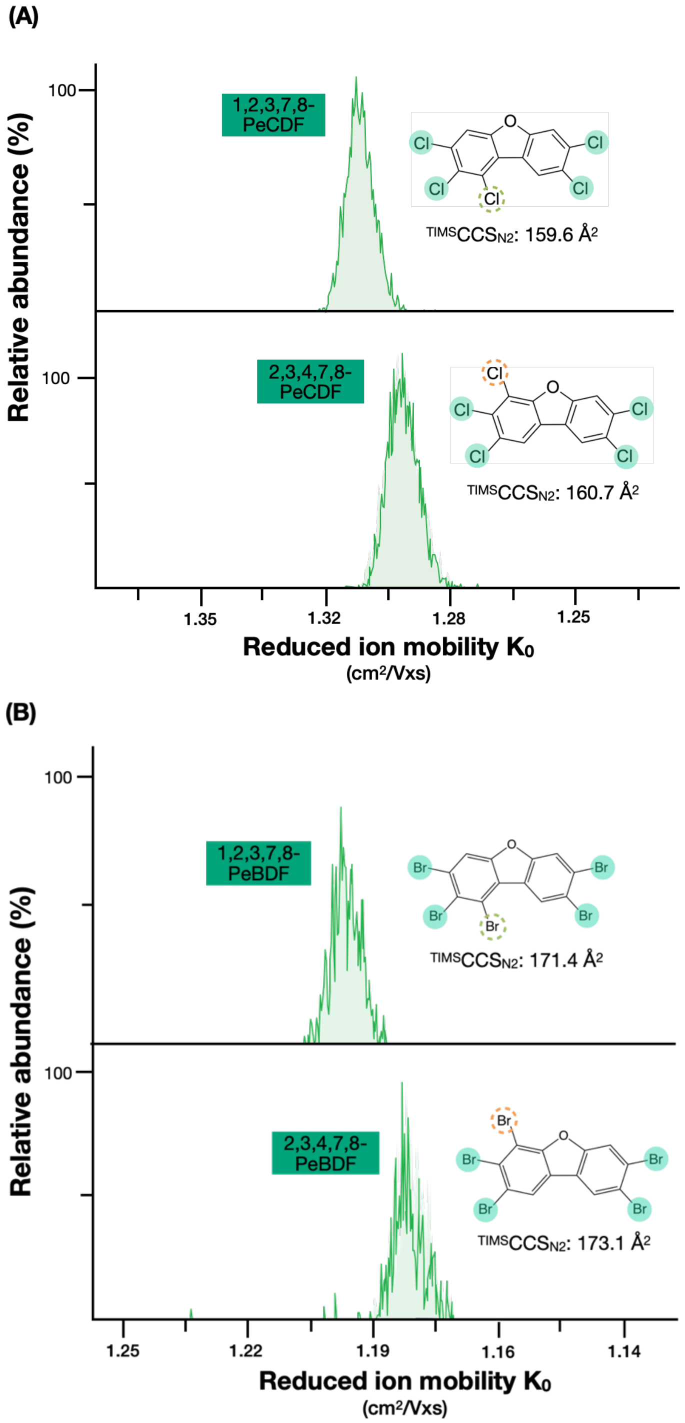

Figure S3.17 - Ion mobility spectra of PCDFs **(A)** penta-substituted 2,3,7,8-PCDFs and **(B)** penta-substituted 2,3,7,8-PBDFs. Halogen atoms that are on the same side of the dibenzo furan moiety as the oxygen atom (positions 4 and 6) are circled in orange, while those on the opposite side (positions 1 and 9) are circled in green.

TABLES

Table S3.1: Siloxane ions used for mass and ion mobility calibration.

Formula	CCS [Å^2]	m/z
$[C_6H_{19}Si_3O_3]^+$	147.2	223.0636
$[C_7H_{21}Si_4O_4]^+$	162.2	281.0511
$[C_9H_{27}Si_5O_5]^+$	172.1	355.0699
$[C_{11}H_{33}Si_6O_6]^+$	189.3	429.0887
$[C_{13}H_{39}Si_7O_7]^+$	-	503.1075
$[C_{19}H_{43}Si_7O_6]^+$	-	563.1439
$[C_{21}H_{49}Si_8O_7]^+$	-	637.1627
$[C_{23}H_{55}Si_9O_8]^+$	-	711.1815
$[C_{29}H_{59}Si_9O_7]^+$	-	771.2179
$[C_{31}H_{65}Si_{10}O_8]^+$	-	845.2367
$[C_{33}H_{71}Si_{11}O_9]^+$	-	919.2554

Chapter 4:
Optimization of trapped ion mobility performance

Portions of this chapter are based on the following publications:

Muller, H. B.; Scholl, G.; Far, J.; De Pauw, E.; Eppe, G. Sliding Windows in Ion Mobility (SWIM): A New Approach to Increase the Resolving Power in Trapped Ion Mobility-Mass Spectrometry Hyphenated with Chromatography. *Anal. Chem.* **2023**, *95* (48), 17586–17594

Muller, H. B.; Scholl, G.; Eppe, G. Gas Chromatography–Trapped Ion Mobility Mass Spectrometry: A Highly Specific and Ultra-Sensitive Platform for Quantifying Sub-ppt Levels of Dioxins and PCBs in Food. *Chemosphere* **2025**, 385, 144557

Chapter 4: Optimization of trapped ion mobility performance

4.1 - MATERIALS AND METHODS 81

4.2 - RESULTS AND DISCUSSION 81

4.2.1 - Impact of key parameters on TIMS performance 81
  A. Accumulation time 81
  B. Funnel 1 RF voltage 85
  C. TIMS cell DC voltages 87
  D. Quadrupole and collision cell energy 88
  E. Collision cell in 89

4.2.2 - Strategies for enhancing ion mobility resolving power in TIMS 90
  A. Buffer gas velocity 91
  B. Number of ions accumulated 91
  C. Scan rate β 92

4.3 - CONCLUSION 97

4.4 - REFERENCES 98

4.5 - SUPPORTING INFORMATION 101

This chapter examines the influence of various parameters on the performance of TIMS analysis, with a focus on ion transfer efficiency, fragmentation extent, and resolving power. The first part presents a systematic evaluation of general instrumental parameters affecting TIMS performance. The second part explores strategies to further enhance the ion mobility resolving power.

4.1 - Materials and methods

Unless otherwise specified, optimization of transfer and resolving power parameters was carried out using a mixture of polybrominated diphenyl ethers (PBDEs), while fragmentation assessment was performed with a mixture of five polychlorinated dibenzo-p-dioxins (PCDDs). PBDEs were selected for the optimization task due to their wide range of m/z values and ion mobilities, thereby supporting greater generalizability of the results. PCDDs, on the other hand, were chosen for fragmentation studies because they exhibit a simple fragmentation pattern, typically producing a single fragment ion from a single precursor ion (see Section 3.2.2B).

For the setting up of the SWIM method (Section 4.2.2C), a mixture of ca. 175 halogenated POPs (5−20 pg/µL in n-nonane) was prepared from standards of halogenated dioxins (PCDD/ Fs, PBDD/Fs and PXDD/Fs), biphenyls (PCBs, PBBs and PXBs), and diphenyl ether (PBDEs). Standards were purchased from Wellington (Ontario, CA) and CIL (Tewksbury, MA). The standard mixture of fatty acid methyl esters (FAMEs) was purchased from Merck.

Measurements were performed on a timsTOF Pro II mass spectrometer (Bruker, Bremen) equipped with the GC-APCI ion source (GC-APCI II, Bruker, Bremen). Injections were performed in splitless mode on a Bruker 456-GC equipped with a low polarity Rxi-5Sil MS column (30 m × 0.25 mm × 0.25 µm, Restek). Helium was used as the GC carrier gas. Ion mobility and mass (re)calibration were performed according to procedure described in the previous chapter (Section 3.2.1C).

4.2 - Results and discussion

4.2.1 - Impact of key parameters on TIMS performance

A. Accumulation time

Since the release of the "pro" version of timsTOF instrument by Bruker, the ion mobility cells are equipped with a dual stage design that enables ions to be accumulated and analyzed simultaneously in parallel for up to 100% ion utilization (i.e., when the accumulation time is set equal to the analysis time), resulting in maximum method sensitivity[1] (**Figure A4**, Appendix A). However, increasing the accumulation time and therefore the number of ions sent to the TIMS cell can also negatively impacts the resolving power since higher ion densities can lead to charge repulsion and peaks broadening[1–4] (commonly referred to as space charge effects). Also, the TIMS cell, like any ion trap, is limited in its capacity to store ions. Above a certain value, the cell reaches a saturation point and can no longer store more ions[1,3]. Thus, a compromise must be found between sensitivity (number of ions accumulated) and selectivity (resolving power).

To find the optimal accumulation time, the PBDEs mixture was analyzed multiple times with increasing accumulation times (from 10 to 250 ms) for a fixed analysis time (250 ms). As expected, the results indicated an overall increase in signal intensity and decrease in resolving power with increasing accumulation time for all congeners (**Figure 4.1A**). However, for some congeners, the increase in signal intensity was linearly proportional to accumulation time, whereas for others, the signal increased linearly until a saturation point (around 100 ms). At first, this contrasting trend was not expected since equal amounts of the different congeners were injected on the system (20 pg each).

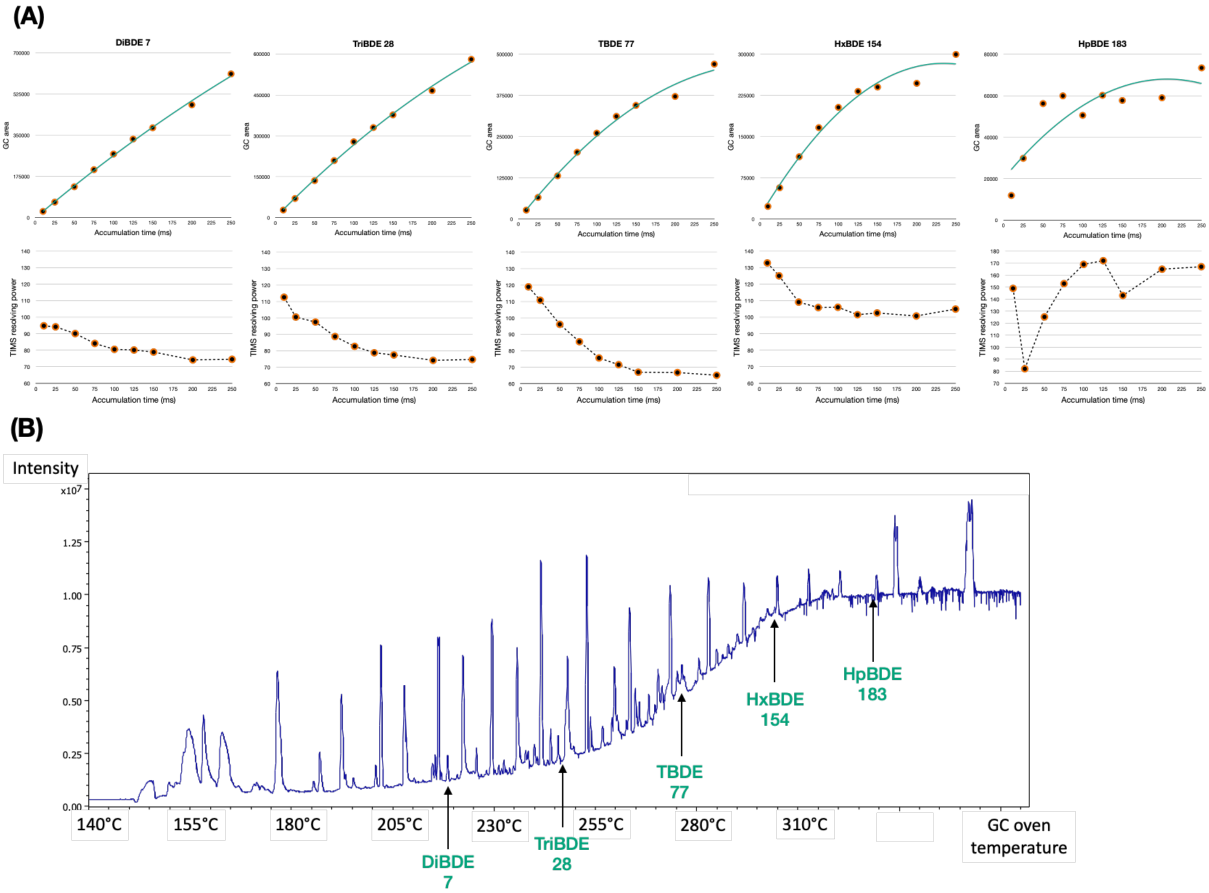

Figure 4.1: **(A)** Signal intensity (upper plots) and TIMS resolving power (lower plots) versus accumulation time for five different PBDE standards in positive mode. **(B)** Total signal intensity (TIC) versus GC oven temperature. The elution temperature of the five PBDE standards is indicated by the corresponding arrows. The series of intense peaks throughout the chromatogram corresponds to artefacts peaks that originate from impurities within the GC system (injector, caps, septa etc.).

After further examination of the data, it was found that the extent of signal saturation correlated well with the retention time: the higher the retention time, the stronger the saturation effect (Figure 4.1B). Based on this observation, we hypothesize that the onset of a saturation point for later eluting compounds could be due to the increase in GC column bleed at higher temperature. Indeed, as can be seen in Figure 4.1B, the background signal from siloxanes ions started to increase significantly around 250°C. Such an increase in the total number of ions could gradually lead to the saturation of the TIMS cell which would then reduce the trapping efficiency of the PBDE ions, accounting for the behavior observed in this experiment.

To further test this hypothesis, the same experiment was performed in negative APCI mode. Under this more selective ionization mode, most siloxane molecules were not ionized and this led to a 100-fold reduction in the background signal (**Figure 4.2B**). This time, a linear increase in signal intensity with increasing accumulation time was observed for all the congeners, including the late eluting ones, strongly supporting our previous hypothesis (Figure 4.2A). However, despite the absence of TIMS cell saturation, the absolute signal intensity in negative mode was orders of magnitude lower than in positive mode, so this ionization polarity was not further considered in the method development.

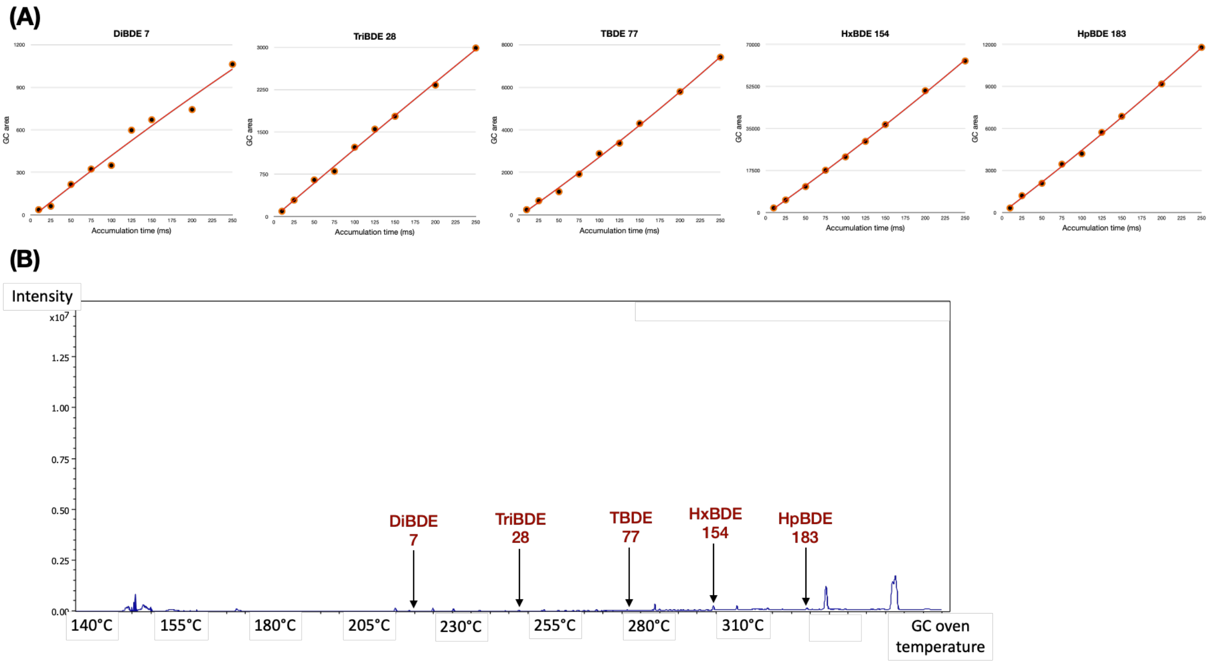

Figure 4.2: **(A)** Signal intensity versus accumulation time for the same five PBDE standards in negative mode. **(B)** Total signal intensity (TIC) versus GC oven temperature. The elution temperature of the PBDE standards is indicated by the corresponding arrows.

In addition to these observations, it was also noted that when an analyte coeluted with a large amount of another matrix constituent, increasing the accumulation time could lead to a decrease in the analyte's signal intensity. **Figure 4.3A** illustrates this effect in the analysis of tetrachlorobiphenyls (TCBs). As shown, the signal intensities of two TCB isomers (TCBs 74 and 77) decreased relative to other congeners as accumulation time increased. Both analytes coeluted with a significant amount of other compounds, producing several intense ions (m/z 235, 277, 295, 327, and 401, Figure 4.3B). A closer examination of the corresponding total ion mobilograms (TIMs) during the elution of TCB 74 (Figure 4.3C, top spectrum) revealed that its molecular ion signal was strongly interfered with by matrix ions, particularly those with m/z 277 and 295, which had similar ion mobility coefficients. These strong interfering signals were absent in the TIM of the TCB isomer eluting immediately after TCB 74 (TCB 70, Figure 4.3C, bottom spectrum), which did not coelute with the aforementioned matrix components and showed no decrease in signal intensity with increasing accumulation time. Similar observations were made for other PCB congeners (**Figure S4.1-S4.3**). These results suggest that the accumulation of large amounts of interfering ions with ion mobilities similar to that of the analyte (thus occupying similar trapping positions in the TIMS tunnel) can reduce the relative signal intensity of the analyte as accumulation time increases, likely due to enhanced space charge effects (e.g., ion repulsion).

Concerning fragmentation, it was observed that increased accumulation (and analysis) time generally led to higher levels of pre/intra-TIMS fragmentation (**Figure 4.4**). This could be attributed to the longer time available for metastable ions to fragment[5], as well as to the increase in internal energy caused by space charge effects and field heating during trapping[2,6].

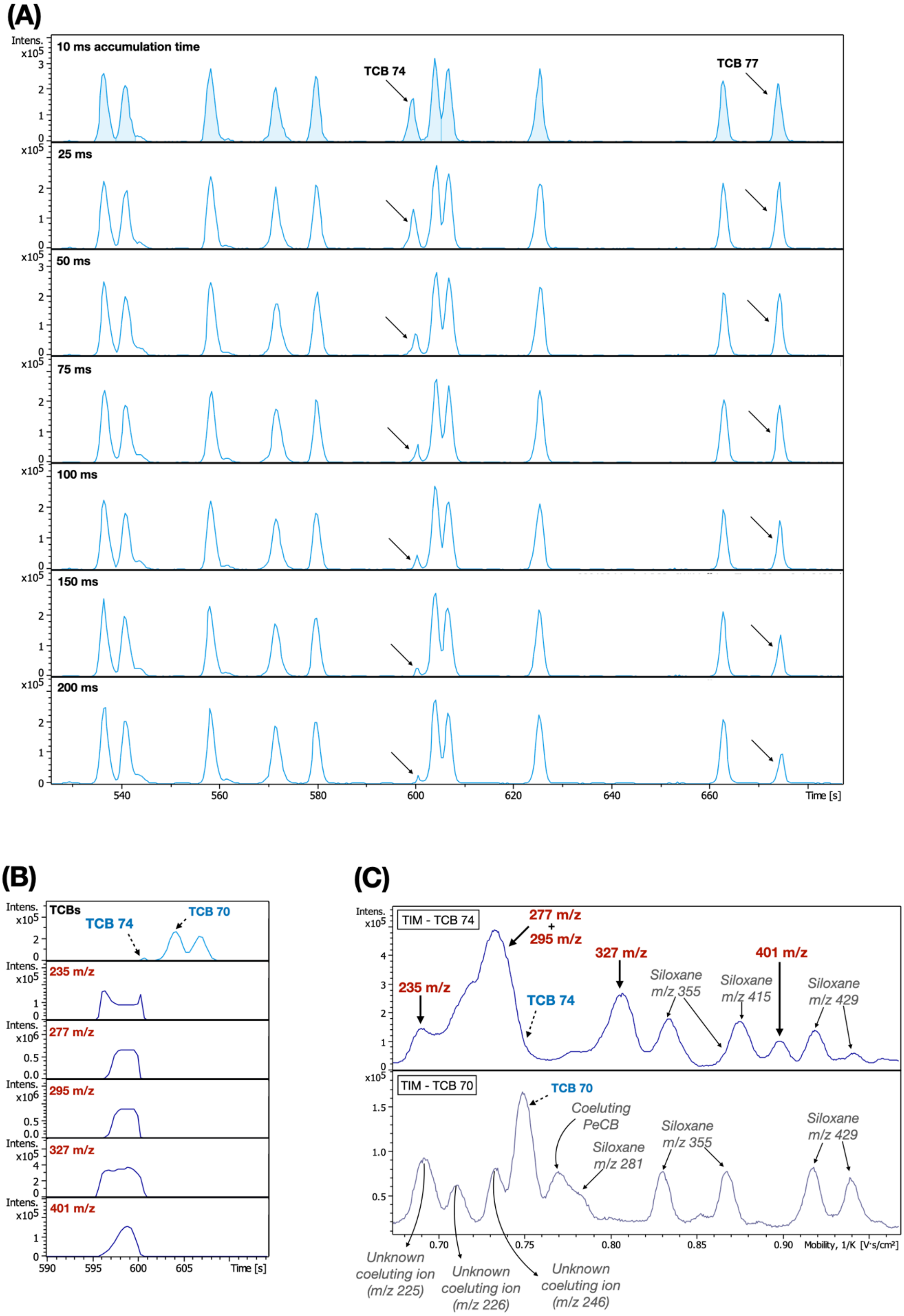

Figure 4.3 – **(A)** Extracted ion chromatograms (EICs) of a mixture of tetrachlorobiphenyls (TCBs) recorded at different accumulation times. The analysis time was fixed at 200 ms. **(B)** EICs of TCBs and matrix interferences, highlighting the coelution of the latter with TCB 74, but not with TCB 70. **(C)** Total ion mobilograms (TIMs) generated during the elution windows of TCB 74 (top) and TCB 70 (bottom). Peaks corresponding to the intense coeluting matrix interference are highlighted in dark red. Other peaks in the TIMs are annotated in grey.

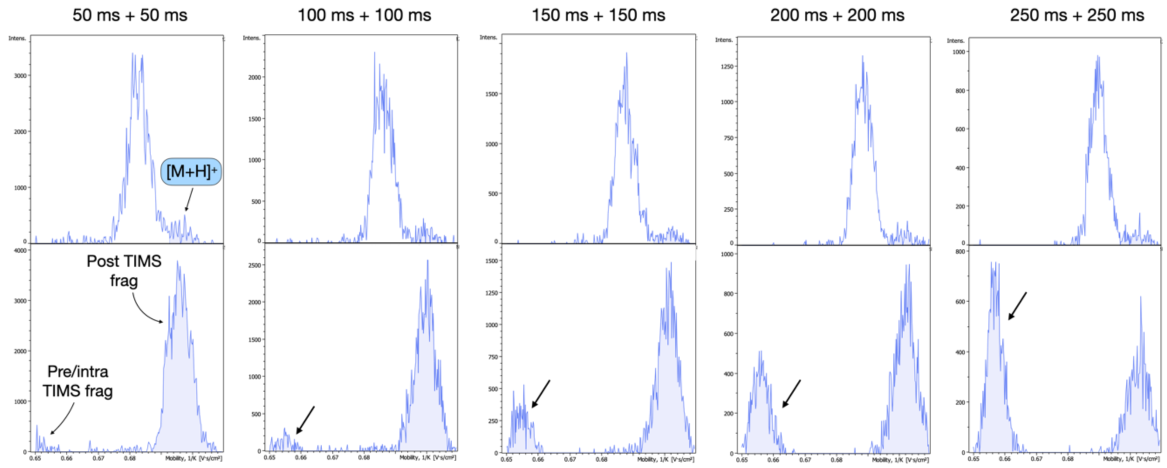

Figure 4.4 – Ion mobility spectra of precursor ($[M+H]^+$) and fragment ion ($[M+H-Cl]^{+\cdot}$) of octachlorodibenzo-p-dioxin (OCDD) measured at five different combinations of accumulation time and analysis time (indicated on top of each spectrum). Note the significant relative increase in the peak corresponding to pre/intra-TIMS fragmentation of OCDD with increasing total separation time.

Overall, the different experiments suggest that in positive APCI mode, an accumulation time above 50 ms and below 100 ms usually represents an optimal balance between sensitivity (signal intensity) and selectivity (resolving power) for must purposes. Indeed, for most analytes, increasing the accumulation time above this value will not result in any increase in the signal intensity due to the outbreak of a saturation effect. Moreover, it will decrease the resolving power due to increased space charge effects within the TIMS cell and lead to a higher level of fragmentation.

However, for the targeted analysis of compounds present at very low level, we still recommend using an accumulation time that is as close as possible to the analysis time (i.e., a high duty cycle). This is because we observed that for compounds injected in very low amounts, the signal quality was somewhat better at higher duty cycle (**Figure S4.4**), thus ensuring more accurate peak integrations (see next chapter). Moreover, we also suggest setting an accumulation time that is not too low, otherwise compounds present at trace level might not be detected (**Figure S4.5**).

Finally, one should mention that the option of the ion charge control (ICC) was also investigated. When enabled, this mode automatically adjusts the accumulation time according to the total signal intensity in order to avoid overloading of the TIMS cell and ensuing space charge effects. However, we observed that due to the intense background signal from the GC column bleed, with ICC set to the recommended target value (7.5 MiO), the accumulation time was forced to decrease to very low values (<20 ms) when the bleeding of the column increased at higher temperature (**Figure S4.6**), leading to a decrease in the sensitivity for late eluting analytes[7]. Thus, while being an interesting option for some applications, we do not recommend the use of ICC for GC-hyphenated applications.

B. Funnel 1 RF voltage

During a TIMS experiment, radial migration of ions toward the electrodes is prevented by applying radial confining radio frequency (RF) voltages. The higher this voltage (technically referred to as the "Funnel 1 RF voltage") the greater the ion confinement toward the center of the cell[4,8] (Figure A4, Appendix A).

On our system, peak-to-peak voltages (V_{pp}) between 150 and 250 volts transmitted all PBDE congeners with similar efficiency (**Figure 4.5**, left panel). However, at lower voltage (100 V_{pp}), a decrease in the transmission of all ions was observed, likely due to insufficient ion confinement. Conversely, at higher voltages (300 and 350 V_{pp}), a significant drop in the transmission efficiency of lower-mass ions (Di- and TriBDEs) was noted, possibly due to reduced stability of low m/z ions under high RF voltage[9]. Importantly, no significant effect on ion fragmentation was observed (Figure 4.5, right panel).

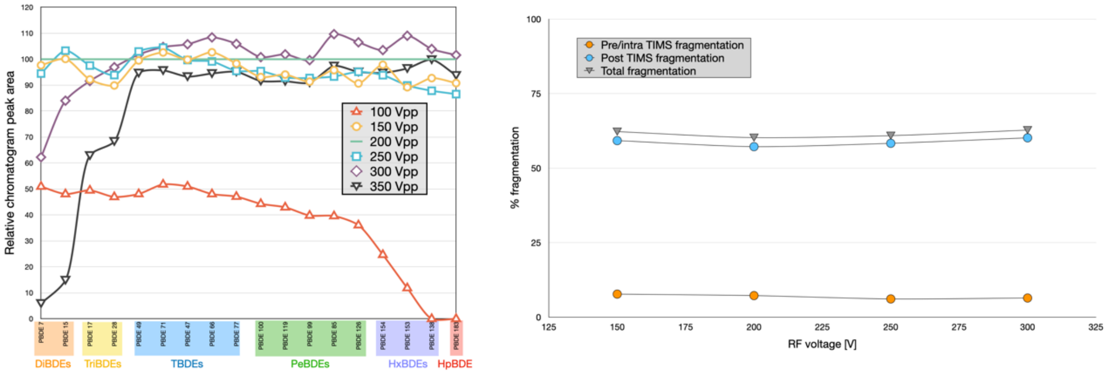

Figure 4.5 – Impact of funnel 1 RF voltage on ion transmission (left panel) and fragmentation (right panel). For the assessment of signal intensity, areas were normalized to the signal obtained at 200 Vpp. Fragmentation extent represents the average fragmentation of the protonated ion $[M+H]^+$ of five PCDD compounds with different chlorination degree.

In terms of resolving power, different behaviors were observed depending on the ions' mass. For lower m/z ions (di- to tetra-BDEs), a slight and gradual decrease in resolving power was observed as the RF voltage increased (**Figure 4.6A**). For higher m/z ions (penta- to hepta-BDEs), a pronounced drop in resolving power occurred at lower RF voltages (Figure 4.6B).

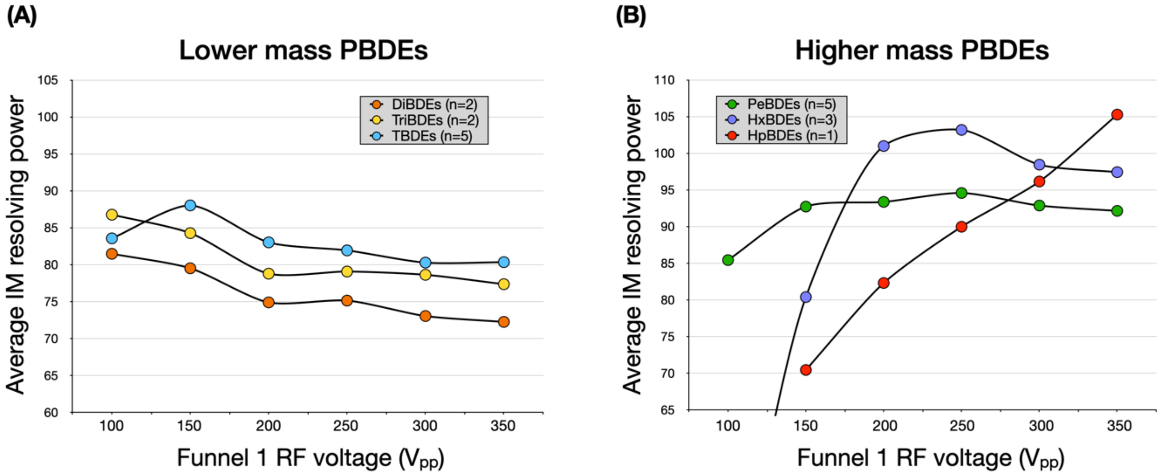

Figure 4.6 – Average ion mobility resolving power of **(A)** lower mass PBDEs and **(B)** higher mass PBDEs analyzed at different funnel 1 RF voltages.

The trend observed for low m/z ions could be explained by the fact that charged molecules cannot be concentrated indefinitely within a confined space. Thus, when the confining voltages is too high, the ion cloud has no other choice but to spread out in the axial direction, resulting in slightly broader ion mobility peaks and thus, lower resolving powers[4] (**Figure 4.7**).

In contrast, the drop in resolving power for high m/z ions at lower RF voltages can be attributed to the parabolic gas velocity profile within the TIMS cell. Ions near the central axis experience higher gas velocities than those closer to the cell walls. As a result, ions not tightly confined to the center are trapped at slightly lower axial electric field (i.e., at a position slightly closer to the tunnel entrance) than those near the axis, producing a left-sided tailing of the mobility peaks[10] (Figure 4.7). Since higher m/z ions tend to be less well-confined at a given RF voltage[3], they are more susceptible to this tailing effect and, thus, to reduced resolving power when confinement is insufficient.

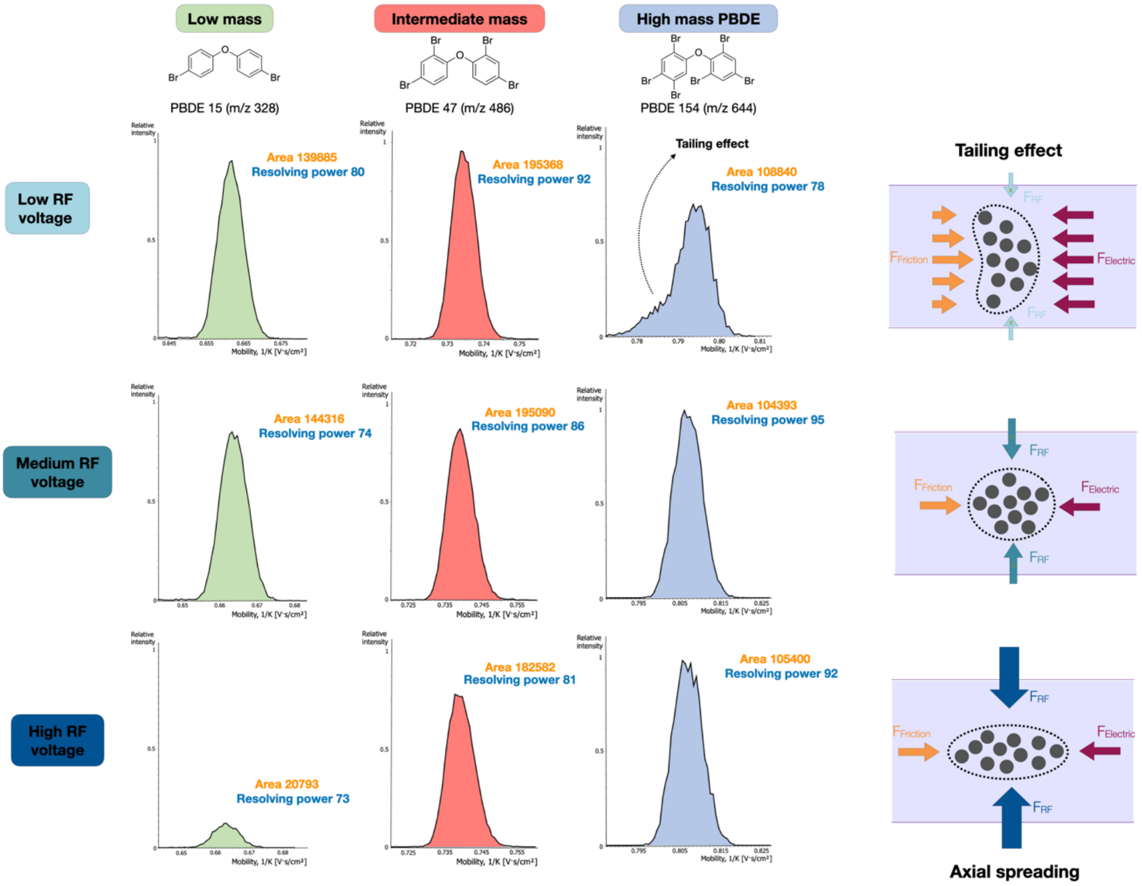

Figure 4.7 – Summary of the impact of RF voltage on the IM resolving power of PBDEs of varying masses. The ion mobility spectra of PBDEs 15, 47, and 154 are shown as examples to illustrate these effects. The figures on the right schematically represent the different forces involved and their influence on the spatial distribution of the ion cloud at different RF field strengths.

For POPs applications, an RF voltage between 150 V and 250 V therefore appears to be the most suitable, as this intermediate range offers a good trade-off between ion transmission and resolving power for a broad range of m/z values.

C. TIMS cell DC voltages

To transmit ions into and through the TIMS cell, several DC voltages are applied. Three key voltages are (Figure A4, Appendix A):

- D3 voltage: the potential difference between the deflection plate and the entrance funnel, which deflects ions from the capillary transfer into the TIMS cell.
- D4 voltage: the potential difference across the entrance funnel, which pushes ions toward the TIMS tunnel.
- D6 voltage: the potential difference between the accumulation and analyzer regions of the TIMS tunnel, responsible for transmitting ions into the analyzer after the accumulation period.

Overall, increasing the D3 and D4 voltages led to a significant improvement in ion transmission (**Figures 4.8A** and **B**, left panels). In contrast, D6 voltage showed consistent transmission efficiency across its range of tested values (Figure 4.8C, left panel). However, the enhanced transmission at higher D3 voltages was accompanied by a slight increase in pre/intra-TIMS fragmentation[6,11] (Figure 4.8A, right panel). A similar increase in fragmentation was observed for D6, but only at the highest voltages (Figure 4.8C, right panel), consistent with a previous report[6]. In contrast, D4 had no apparent effect on fragmentation (Figure 4.8B, right panel). Therefore, to optimize ion transmission while minimizing ion heating, a combination of intermediate D3 (e.g., 50 V), high D4 (e.g., 100 V) and low to intermediate D6 (e.g., 20 V) appears suitable for the analysis of POPs.

(A) - D3 voltage

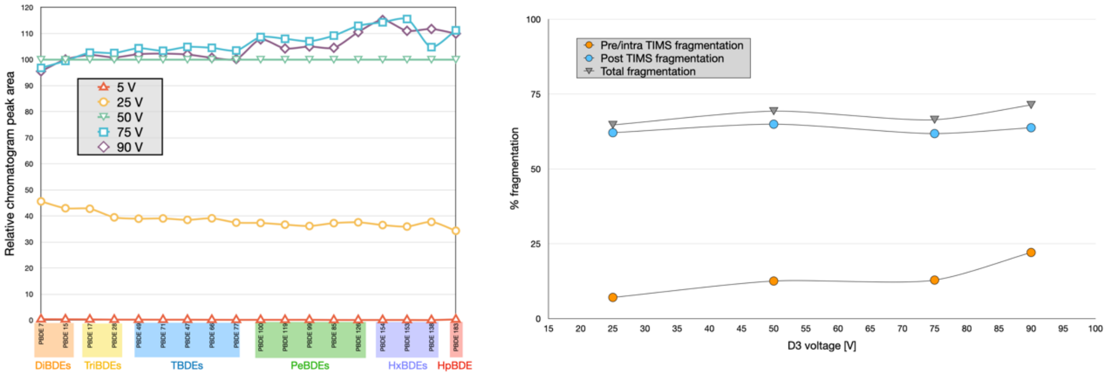

(B) - D4 voltage

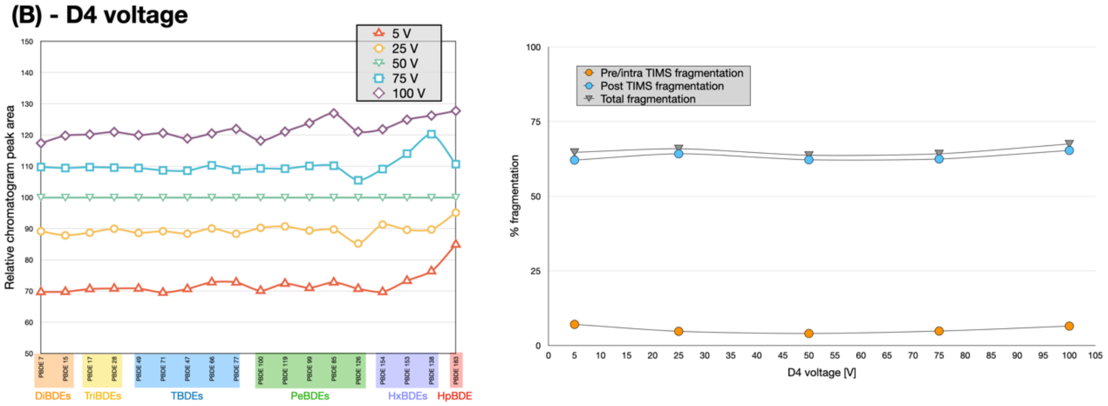

(C) - D6 voltage

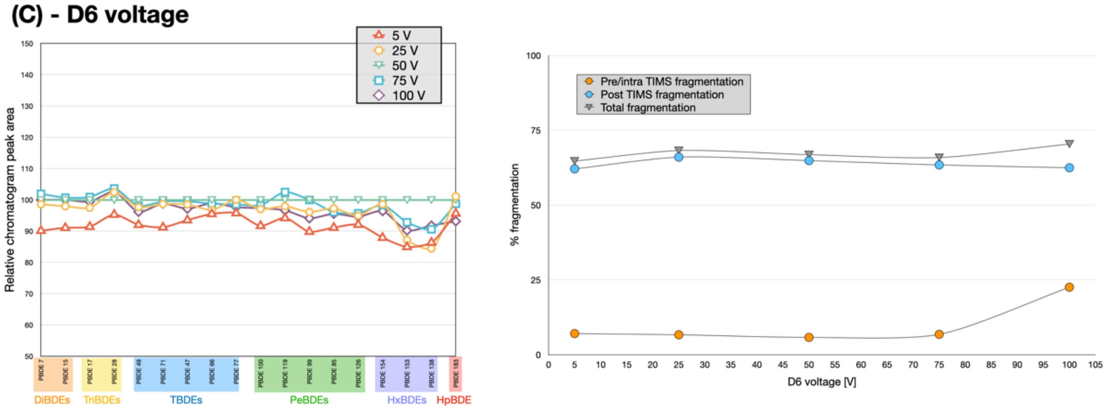

Figure 4.8 – Impact of TIMS cell voltages D3 **(A)**, D4 **(B)**, and D6 **(C)** on ion transmission (left panels) and fragmentation (right panels). For the assessment of signal intensity, areas were normalized to the signal obtained at 50 V. Fragmentation extent represents the average fragmentation of the protonated ion $[M+H]^+$ of five PCDD compounds with different chlorination degree.

D. Quadrupole and collision cell energy

Similar to the DC voltages applied in the TIMS cell, quadrupole and collision* voltages are used to transmit ions toward the TOF analyzer after elution from the TIMS cell (Figure A4, Appendix A).

---

* Note that a DC voltage is applied at the entrance of the collision cell even when tandem MS is not performed. In MS/MS mode, this voltage is substantially increased to promote fragmentation through collisions with the collision gas (N_2).

Increasing the energy of transfer led to improved ion transmission up to a plateau (around 10 eV for both parameters, **Figures 4.9A** and **B**, left panels). As expected, higher energy of transfer also caused a significant increase in post-TIMS fragmentation (Figure 4.9A and B, right panels). Intermediate values (e.g., 8-9 eV) provide a good compromise between ion transmission and fragmentation.

(A) - Quadrupole energy

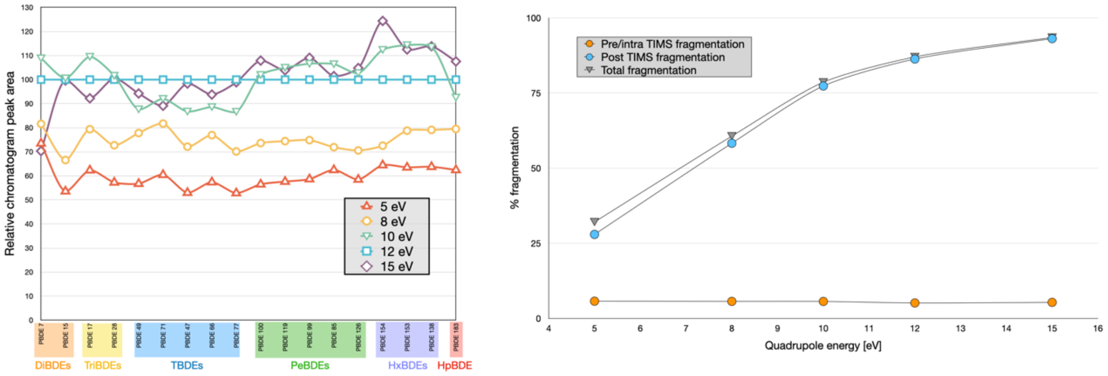

(B) - Collision cell energy

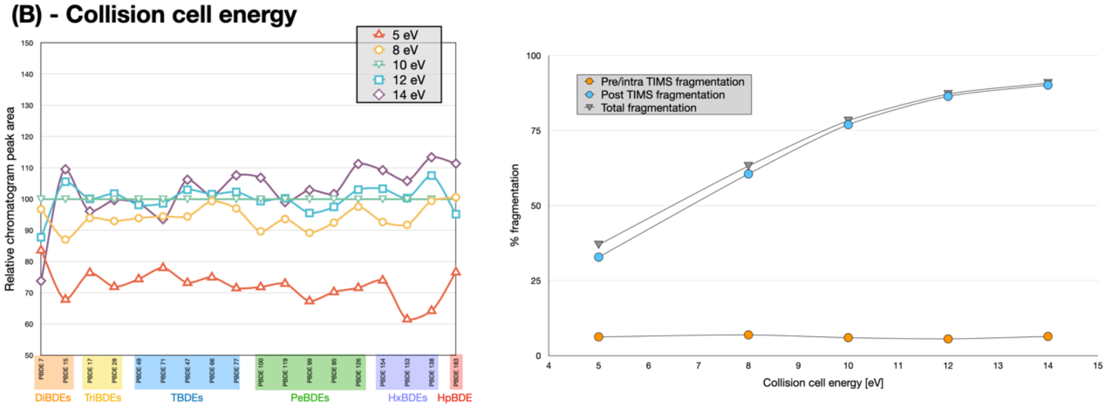

Figure 4.9 – Impact of quadrupole **(A)** and collision cell energy **(B)** on ion transmission (left panels) and fragmentation (right panels). For the assessment of signal intensity, areas were normalized to the signal obtained at 10 eV. Fragmentation extent represents the average fragmentation of the protonated ion $[M+H]^+$ of five PCDD compounds with different chlorination degree.

E. Collision cell in

The 'collision cell in' parameter corresponds to an axial electric field gradient applied throughout the collision cell to accelerate ion transit through the cell[12] (Figure A4, Appendix A). This parameter was found to significantly impact TIMS separation performance:

- Ion transmission (**Figure 4.10A**): Higher voltages enhanced the transmission of higher m/z ions while reducing that of lower m/z ions, and vice versa.
- Fragmentation (Figure 4.10B): Higher voltages led to a significant decrease in post-TIMS fragmentation, likely due to the reduced residence time of ions in the collision cell.
- Resolving power (Figure 4.10C): At lower voltages, ion mobility peaks showed pronounced tailing on the left side, possibly due to inefficient ion extraction from the collision cell, resulting in axial spreading of the mobility resolved ion clouds[3].

Overall, these findings indicate that the 'collision cell in' voltage must be sufficiently high to ensure effective ion extraction. A voltage in the range of 200-250 V achieves this while maintaining adequate transmission of both low and high m/z ions.

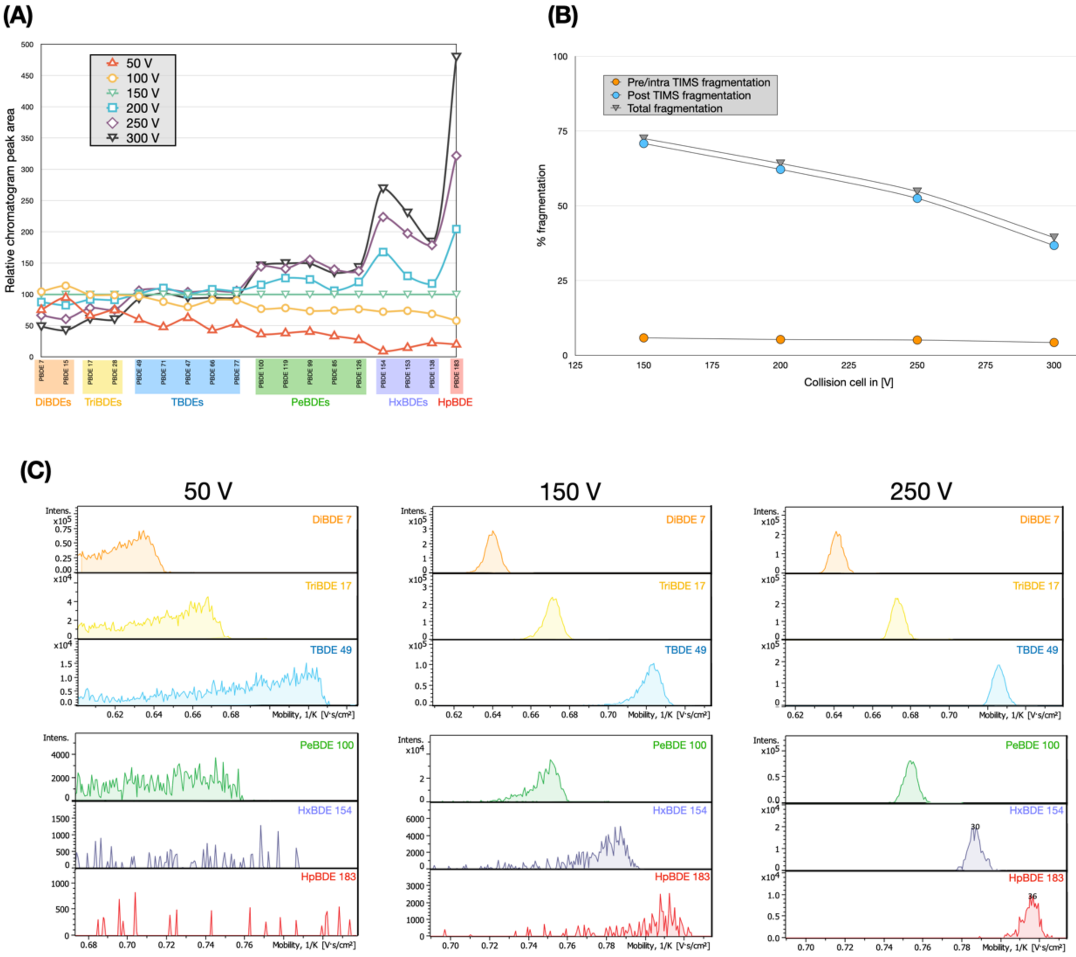

Figure 4.10 – Impact of collision cell in on ion transmission **(A)**, fragmentation **(B)** and resolving power **(C)**. For the assessment of signal intensity, areas were normalized to the signal obtained at 150 V. Fragmentation extent represents the average fragmentation of the protonated ion $[M+H]^+$ of five PCDD compounds with different chlorination degree.

4.2.2 - Strategies for enhancing ion mobility resolving power in TIMS

Over the past decade, significant improvements have been made in the separation capability of IMS instruments[13,14]. While the resolving power (R_p) values of most commercially available IM-MS platforms rarely exceed 80[15], state-of-the-art IM technologies, such as trapped ion mobility spectrometry (TIMS)[16], cyclic traveling wave ion mobility spectrometry (cTWIMS)[17] and structure for lossless ion manipulation (SLIM)[18] platforms, have demonstrated R_p values well over 200. These high resolving powers significantly improve overall separation capability[13].

However, achieving such high resolving powers in TIMS requires extended IM separation times and/or IM analysis over a restricted ion mobility range[13], posing serious challenges for IM-MS applications that involve front-end chromatography to analyze compounds characterized by a broad range of CCS values in complex samples. For instance, while high resolving powers in the range of 150–400 have been achieved for singly charged ions in direct infusion mode[19], R_p values below 100 have been more commonly reported for LC[20–22] and GC-TIMS-MS applications[23].

In TIMS, the resolving power has been shown theoretically and experimentally to depend mainly on the ramp speed β_V (i.e., the rate at which the voltage is decreased during the elution step, see Appendix B) and the drift gas velocity v_g[8–10], as shown in a simplified form in the following equation:

$$R_p \propto \frac{v_g}{\sqrt[4]{\beta_V}} \tag{4.1}$$

Other experimental parameters that also significantly impact the resolving power and require careful optimization are the RF confinement amplitude (Section 4.2.1B) and the ion density at the position of trapping (i.e., the number of ions accumulated in the TIMS analyzer, Section 4.2.1A).

This section describes how optimizing buffer gas velocity, ion accumulation, and scan rate can further enhance ion mobility resolving power.

A. Buffer gas velocity

In practice, changes in buffer gas velocity are achieved by adjusting the entrance pressure of the TIMS tunnel (p_{ent}, Section 3.2.1A) using a butterfly valve[4]. Since drift gas velocity is directly proportional to entrance pressure, increasing p_{ent} increases the gas velocity[24].

While increasing gas velocity can greatly improve resolving power, it can also lead to complications at higher flow rates, as reported in the literature[24]. As a result, gas velocity is typically kept at the default value set by the manufacturer (such that the detection voltage of the protonated ion of hexakis(2,2-difluoroethoxy)phosphazine, one of the compound of the Agilent ESI tune mix calibrant, equals 132 ± 1 V). This corresponds to an entrance pressure near 2.55 mBar.

As discussed in the previous chapter (Section 3.2.1A), replacing the ESI source with the GC-APCI source led to a reduction in p_{ent} (to ~2.4 mBar), thereby decreasing gas velocity (v_g) and reducing resolving power compared to standard ESI conditions. To address this, the effect of increasing p_{ent} (up to 3.4 mBar) on TIMS performance (resolving power, ion transmission, ion mobility values, and fragmentation) was assessed using a PBDE mixture. As shown in **Figure 4.11A**, resolving power increased linearly with p_{ent}, consistent with equation 4.1. Importantly, this improvement did not affect ion transmission (Figure 4.11B) or relative ion mobility values (linear regressions between calibrated $1/K_0$ at 2.4 mBar and non-calibrated $1/K_0$ at higher pressures yielded strong correlations, Figure 4.11C). Additionally, pre/intra-TIMS fragmentation appeared to decrease slightly with increasing pressure (Figure 4.11D), likely due to enhanced collisional cooling and reduced internal energy, as previously suggested by Naylor et al[25].

These findings indicate that, for POPs, TIMS resolving power can be enhanced by operating at entrance pressures higher than those recommended by the manufacturer, without compromising overall separation performance.

B. Number of ions accumulated

The impact of ion charge density on resolving power has generally not been considered in the various theoretical models developed to relate resolving power to key experimental parameters in TIMS[19–21]. However, in practice, we observed that the number of ions trapped within the TIMS tunnel had a substantial influence on resolving power. This effect stems from axial spreading of the radially confined ion cloud when ion density becomes excessive, resulting in Coulombic repulsion and broadening of ion mobility peaks (Section 4.2.1A).

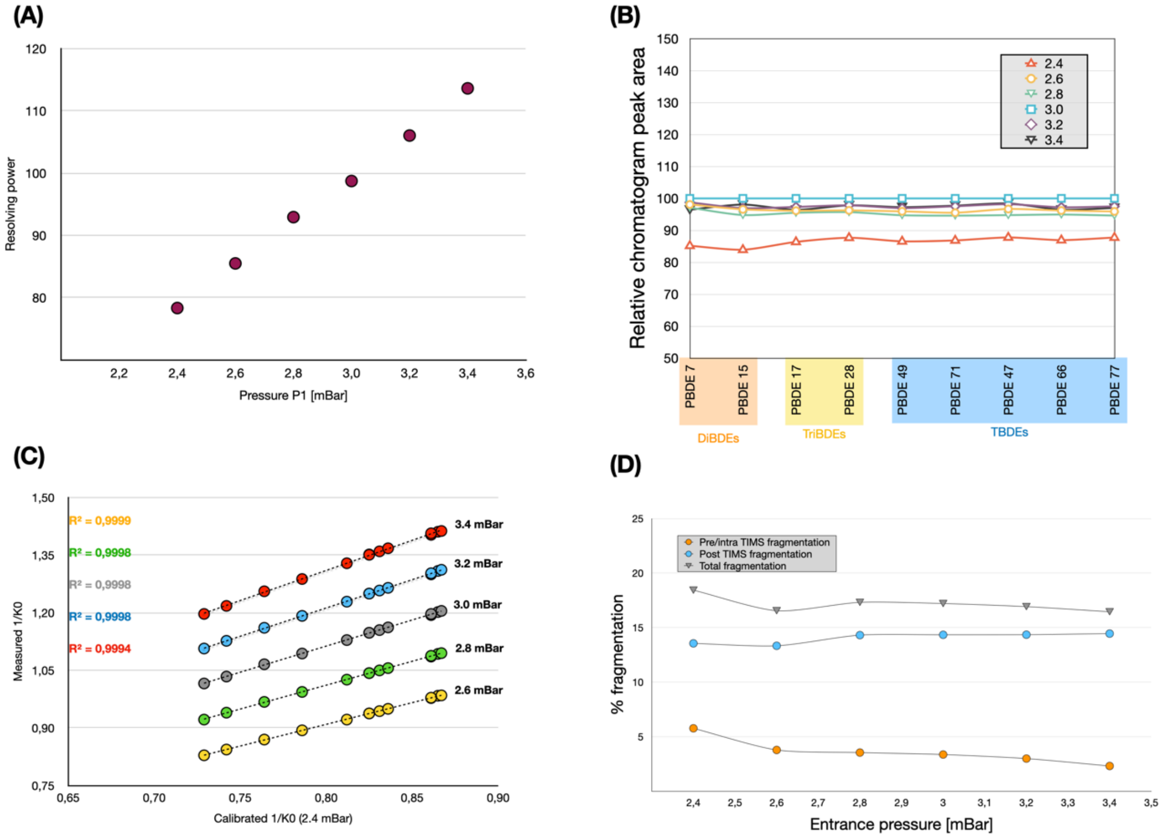

Figure 4.11 – Impact of entrance TIMS tunnel pressure on resolving power **(A)**, ion transmission **(B)**, ion mobility measurement **(C)**, and fragmentation **(D)** of PBDEs. For the assessment of signal intensity, areas were normalized to the signal obtained at 3 mBar.

To maximize resolving power, it is therefore important to minimize ion density by controlling the number of ions entering the TIMS cell. This can be achieved by adjusting the accumulation time (Section 4.2.1A). However, the number of ions trapped also strongly depends on the ion concentration in the incoming ion beam from the source. The amount of analyte injected into the GC-TIMS-MS system was indeed found to have a pronounced effect on resolving power (**Figure 4.12**). Therefore, to achieve optimal resolving powers, we advise injecting dilute samples whenever possible, without compromising the dynamic range.

C. Scan rate β

Adjusting the ramp speed is the primary means of fine-tuning the resolving power to meet the needs of a particular TIMS application. This flexibility is enabled by the unique ‘trap and release’ scheme of the TIMS experiment, which allows ions within a selected mobility range to be selectively trapped and mobility analyzed for a user-defined time. This remarkable feature enables the use of shorter ion mobility ranges (ΔV_{trap}) and/or longer analysis times (t_{ramp}) to achieve decreased ramp speeds ($\beta_v = \Delta V_{trap}/t_{ramp}$) and increased resolving powers for the analytes of interest[8] (as described in equation 4.1).

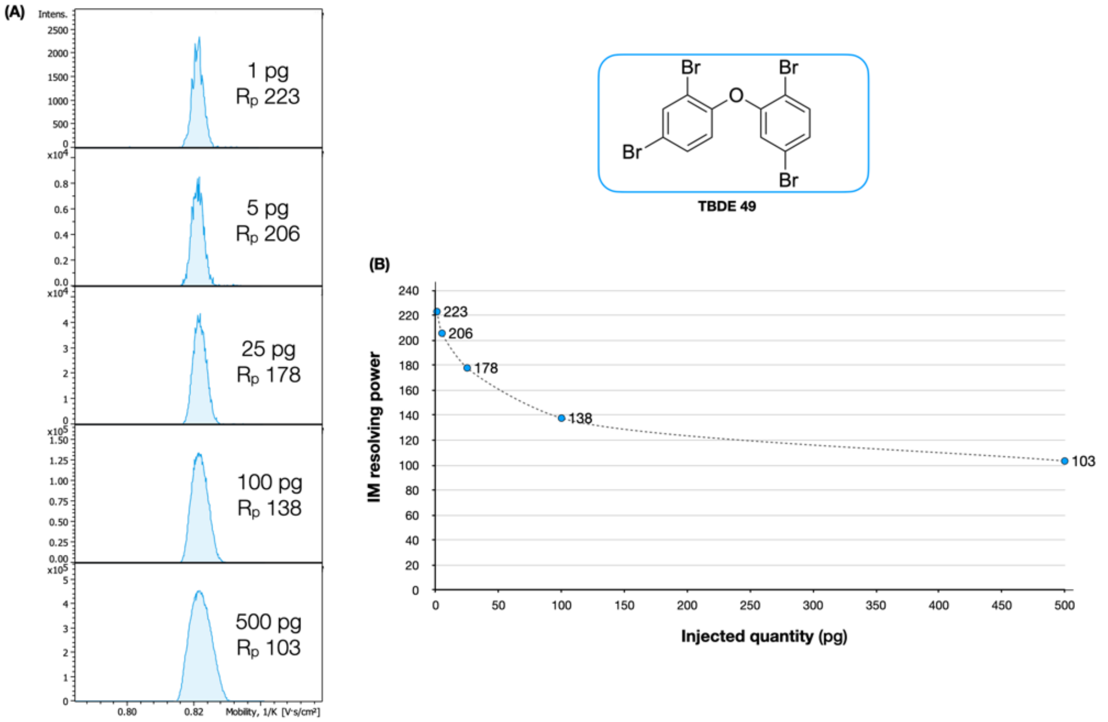

Figure 4.12 - **(A)** Ion mobility spectra of a tetrabromo diphenylether standard (TBDE 49) analysed in increasing amounts. **(B)** Corresponding plot of resolving power versus injected quantity demonstrating a significant trend of decreasing resolving power with increasing injected quantity.

While the flexibility of TIMS to tune the separation efficiency allows the achievement of high resolving power by setting a combination of long analysis time and short ion mobility range[19–21], the use of slow scan rate is compromised when (1) relatively fast coupling front end separation techniques, such as liquid and, specifically, gas chromatography, prevent the use of arbitrarily long analysis time (2) target analytes possess a broad range of CCS values, requiring the use of an extended ion mobility range.

For instance, for the GC-TIMS-MS analysis of a mixture of 174 POPs standards representative of a complex sample, the chromatographic peaks had a baseline elution width of about 4 s, which limited the maximum analysis time to approximately 350 ms in order to ensure adequate sampling of each peak (about 11 TIMS separations per peak, **Figure S4.7**). Additionally, the compounds of interest displayed a wide range of CCS values, from as low as 133 Å^2 (for 2-chlorobiphenyl, a singly chlorinated biphenyl) to as high as 200 Å^2 (for the decabrominated biphenyl PBB 209), requiring a minimum trapping voltage range (ΔV_{trap}) of 51 V. Under these constraints, the analysis of the POPs mix achieved an average resolving power of 100 (average CCS_{fwhm} 1.7 Å^2), as shown in **Figure 4.13A**. This is comparable to the R_p obtained in other TIMS studies using a similar scan rate[22,23] (β_v = 51/0.350 = 145 V/s) and already higher than most R_p values reported for DTIMS and linear TWIMS instruments for these types of compounds[26,27].

Concept of 'SWIM'

Principle

As discussed in the previous section, the diverse range of CCS values displayed by the different POP classes required the use of a relatively wide ion mobility range (ΔV_{trap} = 51 V). However, upon examination of the ion mobility versus retention time profiles of halogenated POPs (Figure 4.13B), it becomes clear that the use of such a broad and fixed ion mobility range throughout the chromatographic separation ("standard TIMS mode", blue rectangle) does not efficiently trap and analyze the compounds of interest. Indeed, as depicted in the figure, the analytes tend to elute in an orderly, rather than random, manner, from higher ion mobilities (low CCS) to lower ion mobilities (high CCS), such that at any given retention time, the compounds of interest that elute from the GC column and enter the TIMS cell are characterized by a range of ion mobilities that is only a small fraction of the total ion mobility range actually covered by all these pollutants. Consequently, a significant portion of a given TIMS scan, and thus valuable analytical effort, is spent analyzing ion mobility regions that do not contain the targeted analytes (shaded areas), thus limiting the achievable resolving power.

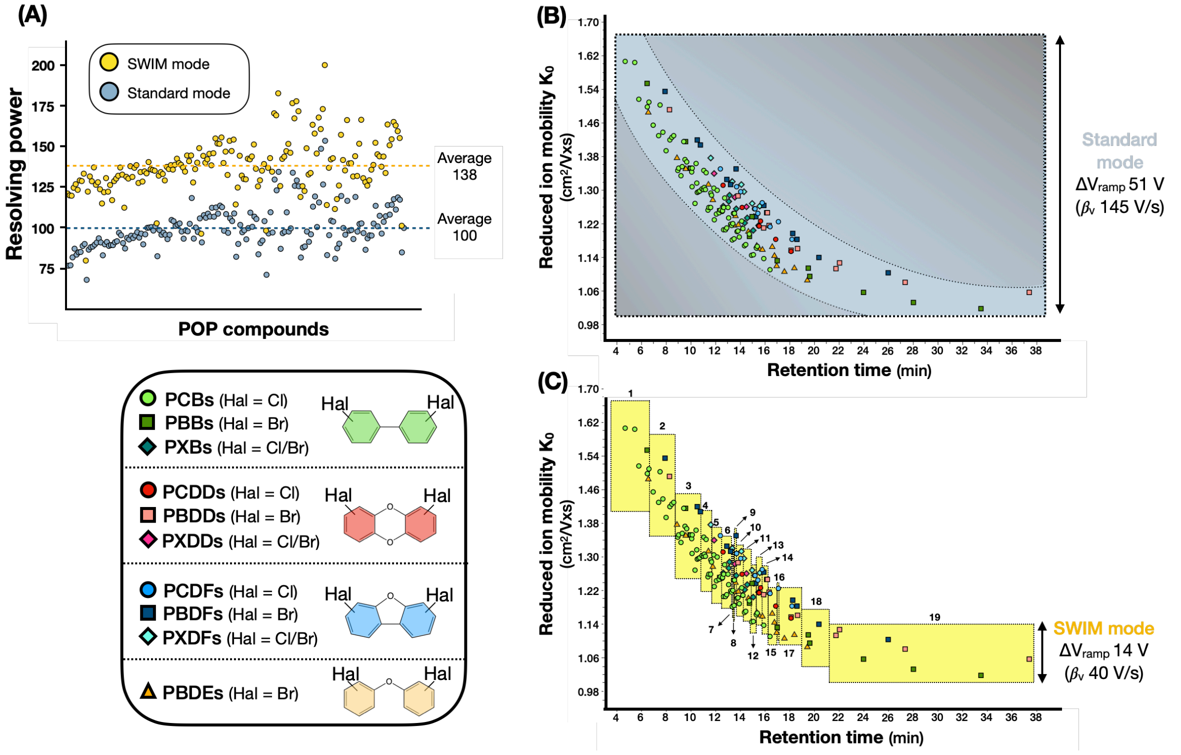

Figure 4.13 - **(A)** Comparison of the individual IM resolving power of POPs (n=174) achieved in standard (blue dots) and SWIM mode (yellow dots). **(B)(C)** Experimentally measured reduced ion mobility values K_0 of POPs as a function of their GC retention time. In panel **(B)**, the constant ion mobility range (between 1.00 and 1.66 cm²/V.s) that was used throughout the gas chromatographic separation in standard mode is represented by the blue rectangle. The dotted curves have been added to highlight the observed trend of decreasing ion mobilities with increasing retention times. In panel **(C)**, the 19 "ion mobility windows" that were used in SWIM mode are represented by the yellow rectangles.

The clear correlation of decreasing ion mobilities with increasing retention times observed in Figure 4.13B can be attributed to the relationship between the halogenation degree and both retention time and CCS in halogenated compounds. Specifically, as the degree of halogenation increases, so do the boiling point (RT) and size (CCS) of the compounds (**Figure 4.14**). As a result, compounds with lower halogenation degrees, characterized by lower CCS values, tend to elute before those with higher degrees of halogenation and higher CCS values.

Based on these correlations, we developed the concept of sliding windows in ion mobility (SWIM), which is depicted in Figure 4.13C. The rationale of SWIM is to divide the total analysis time of the GC run into small retention time segments that are each configured to trap and analyze ions within a narrow range of ion mobilities that effectively match those of the compounds of interest eluting during that time window. Technically, this can be achieved since in TIMS, the voltages on the different electrodes of the tunnel can be independently adjusted for each retention time segment in order to only trap and separate ions with the desired range of ion mobilities[28]. We refer to these narrow ion mobility ranges as 'ion mobility windows' that 'slide' and adapt to the elution profile of the targeted analytes throughout the gas chromatographic analysis, hence the name of the concept.

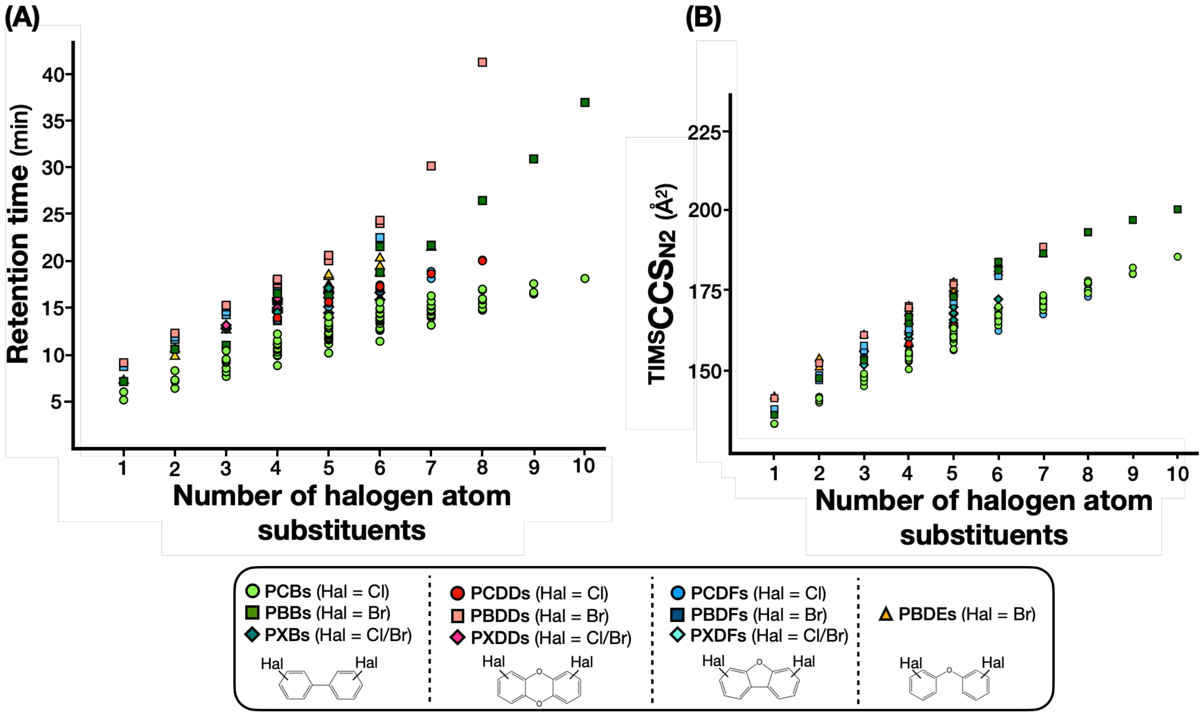

Figure 4.14 – Relationship between halogenation degree and GC retention time **(A)** and CCS **(B)**. For a given type of POP, we observe an overall increase in both retention times and CCS with increasing number of halogen subsituents, due to the concomitent increase in boiling point and molecular size, respectively.

By using narrower IM ranges at a time, the scan rate is decreased, thereby enhancing the separation power[8]. This is indeed what was observed experimentally on the mixture of halogenated POPs. Based on the ion mobility vs retention time profile of these compounds, the GC run was divided into 19 segments, each optimized to selectively separate the ions of interest (Figure 4.13C and **Table S4.1**). The first IM windows were set to selectively analyze the more volatile and lower CCS pollutants. Then, they were set to gradually analyze the higher boiling points and higher CCS compounds. This 'SWIM mode' enabled a nearly 4-fold decrease in the scan rate (40 V/s, with ΔV_{trap} = 14 V and t_{ramp} = 350 ms) compared to the traditional 'standard mode', which used a wider and fixed ion mobility range. This resulted in a ~40% increase in the average resolving power (on the order of 138, average CCS_{fwhm} 1.2 Å^2, Figure 4.13A). Moreover, this result is consistent to the expected ~40% enhancement in R_p based on theory and equation 4.1 for such a decrease in scan rate (R_p SWIM/R_p Std $\simeq \sqrt[4]{145/40}$ = 1.4). Importantly, the SWIM method did not affect the accuracy of the experimentally measured CCS values (average absolute ΔCCS of 0.07%, **Figure S4.8**) or the signal intensity (**Figure S4.9**) compared to that of the standard mode of operation.

Interestingly, the concept of segregating the chromatographic analysis into several retention time segments shares similarities with the chromatographic segments commonly employed for the single ion monitoring (SIM) and multiple reaction monitoring (MRM) of POPs such as dioxins and PCBs on "high" resolution magnetic sector[29] and triple quadrupole mass spectrometers[30], respectively. However, while in these methods, the different chromatographic segments are configured to isolate ions based on their m/z ratio, in SWIM, they are configured to isolate ions based on their ion mobilities (i.e., CCS), regardless of their mass. Furthermore, it is worth noting that that the concept of scanning the ion mobility range of interest in TIMS using narrow ranges of trapping voltages has been previously investigated with the oversampling accumulation (OSA)[31] and gated TIMS[32] modes of operation. These modes employ small elution steps and nonlinear scans to selectively transmit ions of narrow ion mobility range at a time. Both types of experiments were developed to allow the hybridization of TIMS with slow mass analyzing FT-ICR instruments. Overall, the present SWIM concept can therefore be thought of as a hybrid method that incorporates both the concepts of chromatographic segments in GC-HRMS and GC-QqQ and scanned trapping IM range in OSA and gated TIMS. However, it should be mentioned that the ion mobility windows in SWIM differ from those used in parallel accumulation-serial fragmentation (PASEF) methods[33–35] in that they are based on the isolation of a narrow range of ion mobility during a given chromatographic retention time whereas those in PASEF are based on the isolation of a narrow m/z range during a given ion mobility "elution time".

Selectivity improvement

Although most pollutants in the standard POPs mixture were fully resolved in the GC and/or m/z dimensions (78%), we observed a considerable fraction of coeluting or partially coeluting isobars and isomers (10% and 12%, respectively).

One notable example of such coelution was observed with the partially coeluting isomeric PeCBs (84, 90, and 101, m/z = 325.8799) and the isobaric DiBDF (2,4-DiBDF, m/z = 325.8760), as shown in **Figure 4.15A**. The small mass difference ($\Delta m/z = 3.9\times10^{-3}$ Da) between these species required a mass resolving power on the order of 84 000 to achieve complete resolution in the m/z dimension. However, the resolving power of the TOF spectrometer (~50 000) was not sufficient to achieve this separation. Consequently, none of the four species could be fully resolved in either the GC or the m/z dimension in this specific case.

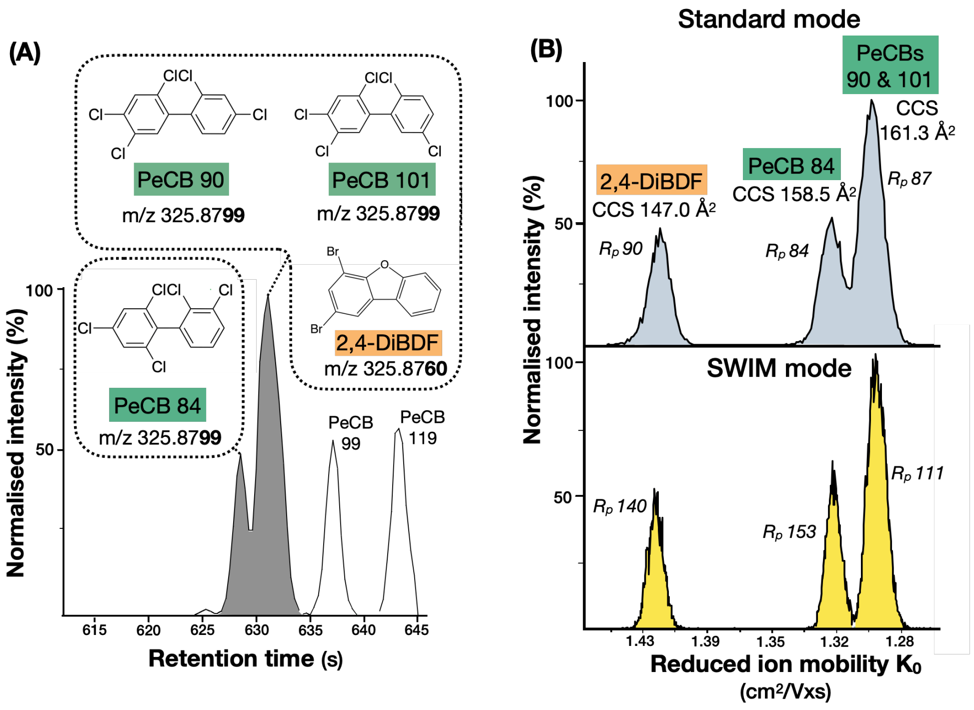

Figure 4.15 – **(A)** GC chromatogram of pentachloro biphenyls (PeCBs) and dibromodibenzofuran (DiBDFs) highlighting the (partial) coelution of PeCBs 84, 90, 101 (isomers) and 2,4-DiBDF (isobar). **(B)** Corresponding ion mobility spectra in standard mode (upper spectrum) and SWIM mode (lower spectrum).

However, the ion mobility dimension provided additional separation, as depicted in Figure 4.15B. In standard mode (upper mobility spectrum), the radical $M^{+\cdot}$ ion of the dibromo-substituted furan was clearly distinguished from the three isomeric pentachloro substituted biphenyls due to the notable differences in halogenation degree (2 bromine vs 5 chlorine atoms), which resulted in considerable differences in CCS (>7%). On the other hand, for the three isomeric PCBs, only partial separation was achieved between the partially coeluting PeCB 84 and PeCBs 90−101, while no distinction was noted for the latter isomeric pair (that perfectly coeluted in the GC dimension). However, in SWIM mode (lower mobility spectrum in Figure 4.15B), baseline separation of PeCB 84 from PeCBs 90−101 was achieved, owing to the increased separation efficiency provided by this method. **Figure S4.10** provides another example of the selectivity improvement offered by the higher resolution of the SWIM mode compared to the standard mode.

4.3 - Conclusion

This chapter highlighted the critical influence of multiple instrumental parameters on the performance of the TIMS analyzer, particularly in terms of resolving power, ion transmission, and fragmentation. As is usually the case when optimizing an analytical system, a fine balance between several interdependent parameters must be found, and no single set of conditions is ideal for all applications. For example, the accumulation time emerged as a particularly sensitive parameter, requiring a compromise between maximizing sensitivity and minimizing space charge effects such as peak broadening. The guidelines established in this chapter offer a robust foundation for tailoring method parameters to specific analytical goals.

Furthermore, by leveraging the trends in CCS versus retention time to dynamically adapt the mobility range during chromatographic separation, the novel sliding windows in ion mobility (SWIM) approach introduced in this chapter addresses key limitations of complex sample analysis, where broad ion mobility coverage and short analysis times are both critical. This targeted yet flexible strategy enhances resolving power and method selectivity without sacrificing sensitivity or CCS accuracy and holds strong potential for extending to other compound classes and separation techniques.

4.4 - References

(1) Silveira, J. A.; Ridgeway, M. E.; Laukien, F. H.; Mann, M.; Park, M. A. Parallel Accumulation for 100% Duty Cycle Trapped Ion Mobility-Mass Spectrometry. *Int. J. Mass Spectrom.* **2017**, *413*, 168–175. https://doi.org/10.1016/j.ijms.2016.03.004.

(2) Bleiholder, C.; Liu, F. C.; Chai, M. Comment on Effective Temperature and Structural Rearrangement in Trapped Ion Mobility Spectrometry. *Anal. Chem.* **2020**, *92* (24), 16329–16333. https://doi.org/10.1021/acs.analchem.0c02052.

(3) Fernandez-Lima, F. A.; Kaplan, D. A.; Park, M. A. Note: Integration of Trapped Ion Mobility Spectrometry with Mass Spectrometry. *Rev. Sci. Instrum.* **2011**, *82* (12), 126106. https://doi.org/10.1063/1.3665933.

(4) Hernandez, D. R.; DeBord, J. D.; Ridgeway, M. E.; Kaplan, D. A.; Park, M. A.; Fernandez-Lima, F. Ion Dynamics in a Trapped Ion Mobility Spectrometer. *The Analyst* **2014**, *139* (8), 1913–1921. https://doi.org/10.1039/C3AN02174B.

(5) Vékey, K. Internal Energy Effects in Mass Spectrometry. *J. Mass Spectrom.* **1996**, *31* (5), 445–463. https://doi.org/10.1002/(SICI)1096-9888(199605)31:5<445::AID-JMS354>3.0.CO;2-G.

(6) Morsa, D.; Hanozin, E.; Eppe, G.; Quinton, L.; Gabelica, V.; Pauw, E. D. Effective Temperature and Structural Rearrangement in Trapped Ion Mobility Spectrometry. *Anal. Chem.* **2020**, *92* (6), 4573–4582. https://doi.org/10.1021/acs.analchem.9b05850.

(7) Lindemann, V.; Schmidt, J.; Cramer, B.; Humpf, H.-U. Detection of Mycotoxins in Highly Matrix-Loaded House-Dust Samples by QTOF-HRMS, IM-QTOF-HRMS, and TQMS: Advantages and Disadvantages. *Anal. Chem.* **2022**, *94* (10), 4209–4217. https://doi.org/10.1021/acs.analchem.1c04254.

(8) Michelmann, K.; Silveira, J. A.; Ridgeway, M. E.; Park, M. A. Fundamentals of Trapped Ion Mobility Spectrometry. *J. Am. Soc. Mass Spectrom.* **2015**, *26* (1), 14–24. https://doi.org/10.1007/s13361-014-0999-4.

(9) Silveira, J. A.; Michelmann, K.; Ridgeway, M. E.; Park, M. A. Fundamentals of Trapped Ion Mobility Spectrometry Part II: Fluid Dynamics. *J. Am. Soc. Mass Spectrom.* **2016**, *27* (4), 585–595. https://doi.org/10.1007/s13361-015-1310-z.

(10) Larriba-Andaluz, C.; Chen, X.; Nahin, M.; Wu, T.; Fukushima, N. Analysis of Ion Motion and Diffusion Confinement in Inverted Drift Tubes and Trapped Ion Mobility Spectrometry Devices. *Anal. Chem.* **2019**, *91* (1), 919–927. https://doi.org/10.1021/acs.analchem.8b03930.

(11) Ridgeway, M. E.; Wolff, J. J.; Silveira, J. A.; Lin, C.; Costello, C. E.; Park, M. A. Gated Trapped Ion Mobility Spectrometry Coupled to Fourier Transform Ion Cyclotron Resonance Mass Spectrometry. *Int. J. Ion Mobil. Spectrom.* **2016**, *19* (2–3), 77–85. https://doi.org/10.1007/s12127-016-0197-0.

(12) Beck, S.; Michalski, A.; Raether, O.; Lubeck, M.; Kaspar, S.; Goedecke, N.; Baessmann, C.; Hornburg, D.; Meier, F.; Paron, I.; Kulak, N. A.; Cox, J.; Mann, M. The Impact II, a Very High-Resolution Quadrupole Time-of-Flight Instrument (QTOF) for Deep Shotgun Proteomics *. *Mol. Cell. Proteomics* **2015**, *14* (7), 2014–2029. https://doi.org/10.1074/mcp.M114.047407.

(13) Kirk, A. T.; Bohnhorst, A.; Raddatz, C.-R.; Allers, M.; Zimmermann, S. Ultra-High-Resolution Ion Mobility Spectrometry—Current Instrumentation, Limitations, and Future Developments. *Anal. Bioanal. Chem.* **2019**, *411* (24), 6229–6246. https://doi.org/10.1007/s00216-019-01807-0.

(14) Delafield, D. G.; Lu, G.; Kaminsky, C. J.; Li, L. High-End Ion Mobility Mass Spectrometry: A Current Review of Analytical Capacity in Omics Applications and Structural Investigations. *TrAC Trends Anal. Chem.* **2022**, *157*, 116761. https://doi.org/10.1016/j.trac.2022.116761.

(15) Dodds, J. N.; May, J. C.; McLean, J. A. Correlating Resolving Power, Resolution, and Collision Cross Section: Unifying Cross-Platform Assessment of Separation Efficiency in Ion Mobility Spectrometry. *Anal. Chem.* **2017**, *89* (22), 12176–12184. https://doi.org/10.1021/acs.analchem.7b02827.

(16) Ridgeway, M. E.; Lubeck, M.; Jordens, J.; Mann, M.; Park, M. A. Trapped Ion Mobility Spectrometry: A Short Review. *Int. J. Mass Spectrom.* **2018**, *425*, 22–35. https://doi.org/10.1016/j.ijms.2018.01.006.

(17) Giles, K.; Ujma, J.; Wildgoose, J.; Pringle, S.; Richardson, K.; Langridge, D.; Green, M. A Cyclic Ion Mobility-Mass Spectrometry System. *Anal. Chem.* **2019**, *91* (13), 8564–8573. https://doi.org/10.1021/acs.analchem.9b01838.

(18) Garimella, S. V. B.; Nagy, G.; Ibrahim, Y. M.; Smith, R. D. Opening New Paths for Biological Applications of Ion Mobility - Mass Spectrometry Using Structures for Lossless Ion Manipulations. *TrAC Trends Anal. Chem.* **2019**, *116*, 300–307. https://doi.org/10.1016/j.trac.2019.04.021.

(19) Adams, K. J.; Montero, D.; Aga, D.; Fernandez-Lima, F. Isomer Separation of Polybrominated Diphenyl Ether Metabolites Using nanoESI-TIMS-MS. *Int. J. Ion Mobil. Spectrom.* **2016**, *19* (2–3), 69–76. https://doi.org/10.1007/s12127-016-0198-z.

(20) Adams, K. J.; Smith, N. F.; Ramirez, C. E.; Fernandez-Lima, F. Discovery and Targeted Monitoring of Polychlorinated Biphenyl Metabolites in Blood Plasma Using LC-TIMS-TOF MS. *Int. J. Mass Spectrom.* **2018**, *427*, 133–140. https://doi.org/10.1016/j.ijms.2017.11.009.

(21) Adams, K. J.; Ramirez, C. E.; Smith, N. F.; Muñoz-Muñoz, A. C.; Andrade, L.; Fernandez-Lima, F. Analysis of Isomeric Opioids in Urine Using LC-TIMS-TOF MS. *Talanta* **2018**, *183*, 177–183. https://doi.org/10.1016/j.talanta.2018.02.077.

(22) Jeanne Dit Fouque, K.; Ramirez, C. E.; Lewis, R. L.; Koelmel, J. P.; Garrett, T. J.; Yost, R. A.; Fernandez-Lima, F. Effective Liquid Chromatography–Trapped Ion Mobility Spectrometry–Mass Spectrometry Separation of Isomeric Lipid Species. *Anal. Chem.* **2019**, *91* (8), 5021–5027. https://doi.org/10.1021/acs.analchem.8b04979.

(23) Olanrewaju, C. A.; Ramirez, C. E.; Fernandez-Lima, F. Comprehensive Screening of Polycyclic Aromatic Hydrocarbons and Similar Compounds Using GC–APLI–TIMS–TOFMS/GC–EI–MS. *Anal. Chem.* **2021**, *93* (15), 6080–6087. https://doi.org/10.1021/acs.analchem.0c04525.

(24) Silveira, J. A.; Michelmann, K.; Ridgeway, M. E.; Park, M. A. Fundamentals of Trapped Ion Mobility Spectrometry Part II: Fluid Dynamics. *J. Am. Soc. Mass Spectrom.* **2016**, *27* (4), 585–595. https://doi.org/10.1007/s13361-015-1310-z.

(25) Naylor, C. N.; Ridgeway, M. E.; Park, M. A.; Clowers, B. H. Evaluation of Trapped Ion Mobility Spectrometry Source Conditions Using Benzylammonium Thermometer Ions. *J. Am. Soc. Mass Spectrom.* **2020**, *31* (7), 1593–1602. https://doi.org/10.1021/jasms.0c00151.

(26) Zheng, X.; Dupuis, K. T.; Aly, N. A.; Zhou, Y.; Smith, F. B.; Tang, K.; Smith, R. D.; Baker, E. S. Utilizing Ion Mobility Spectrometry and Mass Spectrometry for the Analysis of Polycyclic Aromatic Hydrocarbons, Polychlorinated Biphenyls, Polybrominated Diphenyl Ethers and Their Metabolites. *Anal. Chim. Acta* **2018**, *1037*, 265–273. https://doi.org/10.1016/j.aca.2018.02.054.

(27) Izquierdo-Sandoval, D.; Fabregat-Safont, D.; Lacalle-Bergeron, L.; Sancho, J. V.; Hernández, F.; Portoles, T. Benefits of Ion Mobility Separation in GC-APCI-HRMS Screening: From the Construction of a CCS Library to the Application to Real-World Samples. *Anal. Chem.* **2022**, *94* (25), 9040–9047. https://doi.org/10.1021/acs.analchem.2c01118.

(28) Bleiholder, C. Towards Measuring Ion Mobilities in Non-Stationary Gases and Non-Uniform and Dynamic Electric Fields (I). Transport Equation. *Int. J. Mass Spectrom.* **2016**, *399–400*, 1–9. https://doi.org/10.1016/j.ijms.2016.01.003.

(29) Focant, J.-F.; Eppe, G.; Pirard, C.; De Pauw, E. Fast Clean-up for Polychlorinated Dibenzo-p-Dioxins, Dibenzofurans and Coplanar Polychlorinated Biphenyls Analysis of High-Fat-Content Biological Samples. *J. Chromatogr. A* **2001**, *925* (1–2), 207–221. https://doi.org/10.1016/S0021-9673(01)01047-0.

(30) García-Bermejo, Á.; Ábalos, M.; Sauló, J.; Abad, E.; González, M. J.; Gómara, B. Triple Quadrupole Tandem Mass Spectrometry: A Real Alternative to High Resolution Magnetic Sector Instrument for the Analysis of Polychlorinated Dibenzo-p-Dioxins, Furans and Dioxin-like

Polychlorinated Biphenyls. *Anal. Chim. Acta* **2015**, *889*, 156–165. https://doi.org/10.1016/j.aca.2015.07.039.

(31) Benigni, P.; Fernandez-Lima, F. Oversampling Selective Accumulation Trapped Ion Mobility Spectrometry Coupled to FT-ICR MS: Fundamentals and Applications. *Anal. Chem.* **2016**, *88* (14), 7404–7412. https://doi.org/10.1021/acs.analchem.6b01946.

(32) Benigni, P.; Porter, J.; Ridgeway, Mark. E.; Park, Melvin. A.; Fernandez-Lima, F. Increasing Analytical Separation and Duty Cycle with Nonlinear Analytical Mobility Scan Functions in TIMS-FT-ICR MS. *Anal. Chem.* **2018**, *90* (4), 2446–2450. https://doi.org/10.1021/acs.analchem.7b04053.

(33) Meier, F.; Brunner, A.-D.; Frank, M.; Ha, A.; Bludau, I.; Voytik, E.; Kaspar-Schoenefeld, S.; Lubeck, M.; Raether, O.; Bache, N.; Aebersold, R.; Collins, B. C.; Röst, H. L.; Mann, M. diaPASEF: Parallel Accumulation–Serial Fragmentation Combined with Data-Independent Acquisition. *Nat. Methods* **2020**, *17* (12), 1229–1236. https://doi.org/10.1038/s41592-020-00998-0.

(34) Skowronek, P.; Krohs, F.; Lubeck, M.; Wallmann, G.; Itang, E. C. M.; Koval, P.; Wahle, M.; Thielert, M.; Meier, F.; Willems, S.; Raether, O.; Mann, M. Synchro-PASEF Allows Precursor-Specific Fragment Ion Extraction and Interference Removal in Data-Independent Acquisition. *Mol. Cell. Proteomics* **2023**, *22* (2), 100489. https://doi.org/10.1016/j.mcpro.2022.100489.

(35) Lesur, A.; Schmit, P.-O.; Bernardin, F.; Letellier, E.; Brehmer, S.; Decker, J.; Dittmar, G. Highly Multiplexed Targeted Proteomics Acquisition on a TIMS-QTOF. *Anal. Chem.* **2021**, *93* (3), 1383–1392. https://doi.org/10.1021/acs.analchem.0c03180.

4.5 - Supporting information

FIGURES

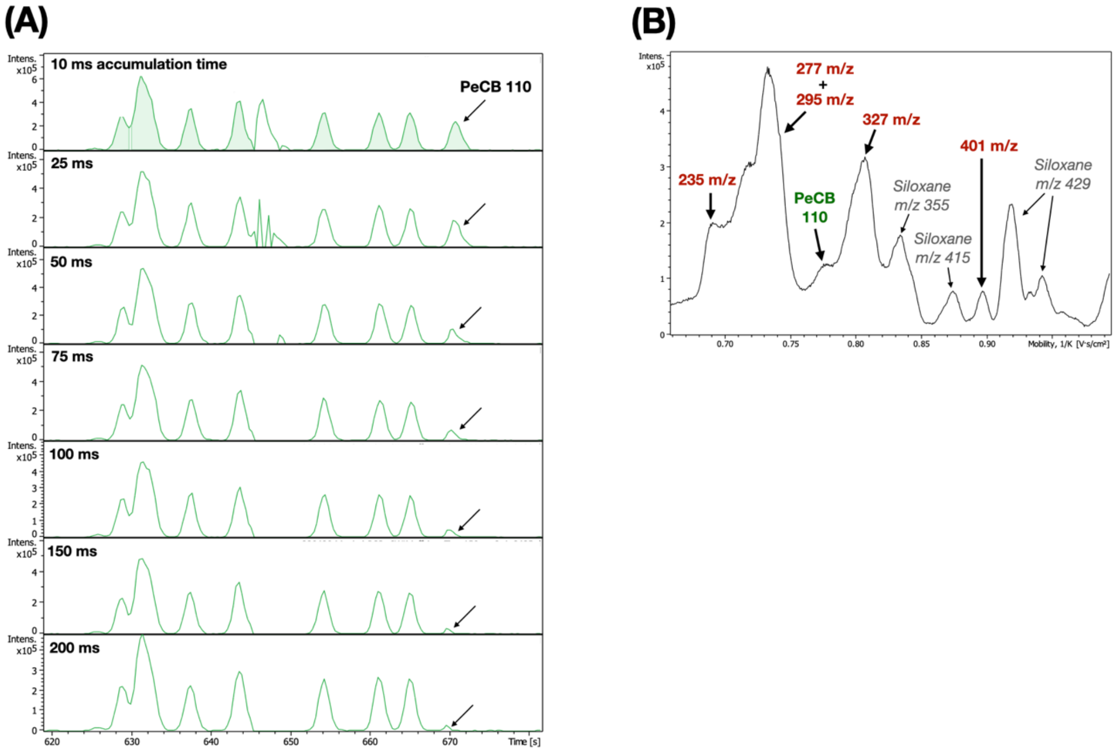

Figure S4.1 – **(A)** Extracted ion chromatograms (EICs) of a mixture of pentachlorobiphenyls (PeCBs) recorded at different accumulation times. The analysis time was fixed at 200 ms. **(B)** Total ion mobilogram (TIM) generated during the elution windows of PeCB 110. Peaks corresponding to the intense coeluting matrix interference are highlighted in dark red. Other peaks in the TIMs are annotated in grey

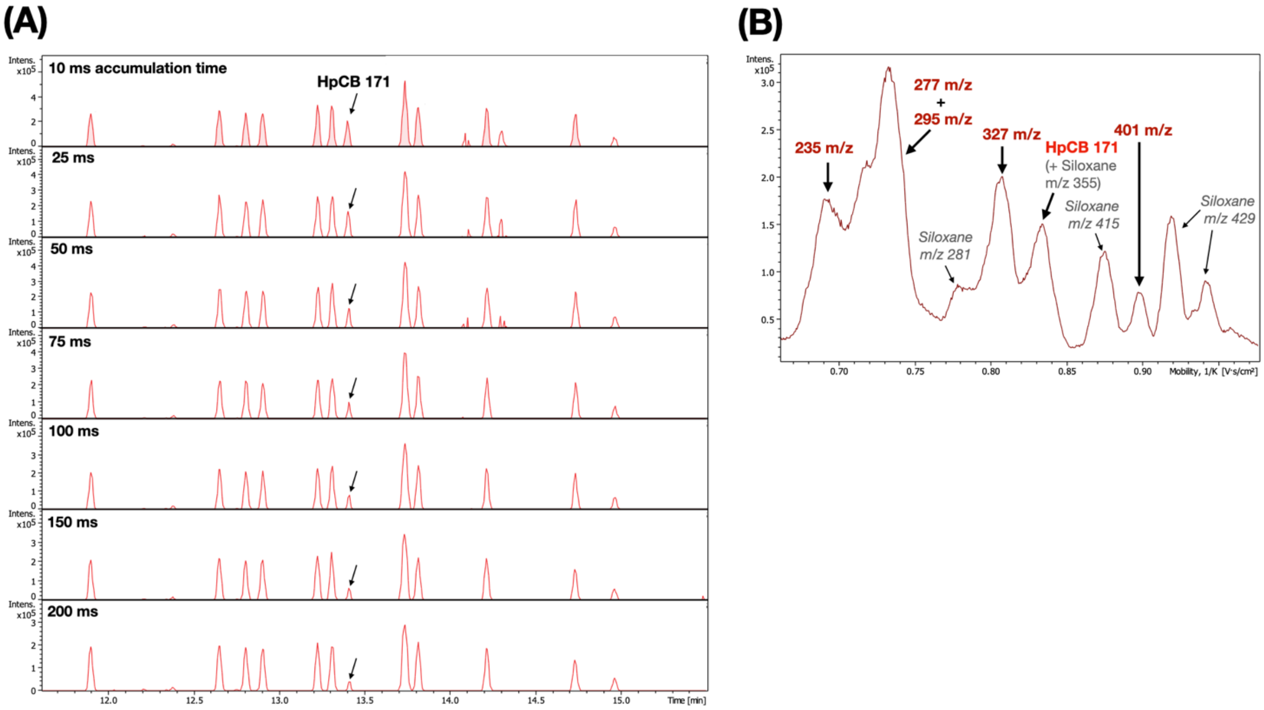

Figure S4.2 – **(A)** Extracted ion chromatograms (EICs) of a mixture of heptachlorobiphenyls (HpCBs) recorded at different accumulation times. The analysis time was fixed at 200 ms. **(B)** Total ion mobilogram (TIM) generated during the elution windows of HpCB 171. Peaks corresponding to the intense coeluting matrix interference are highlighted in dark red. Other peaks in the TIMs are annotated in grey.

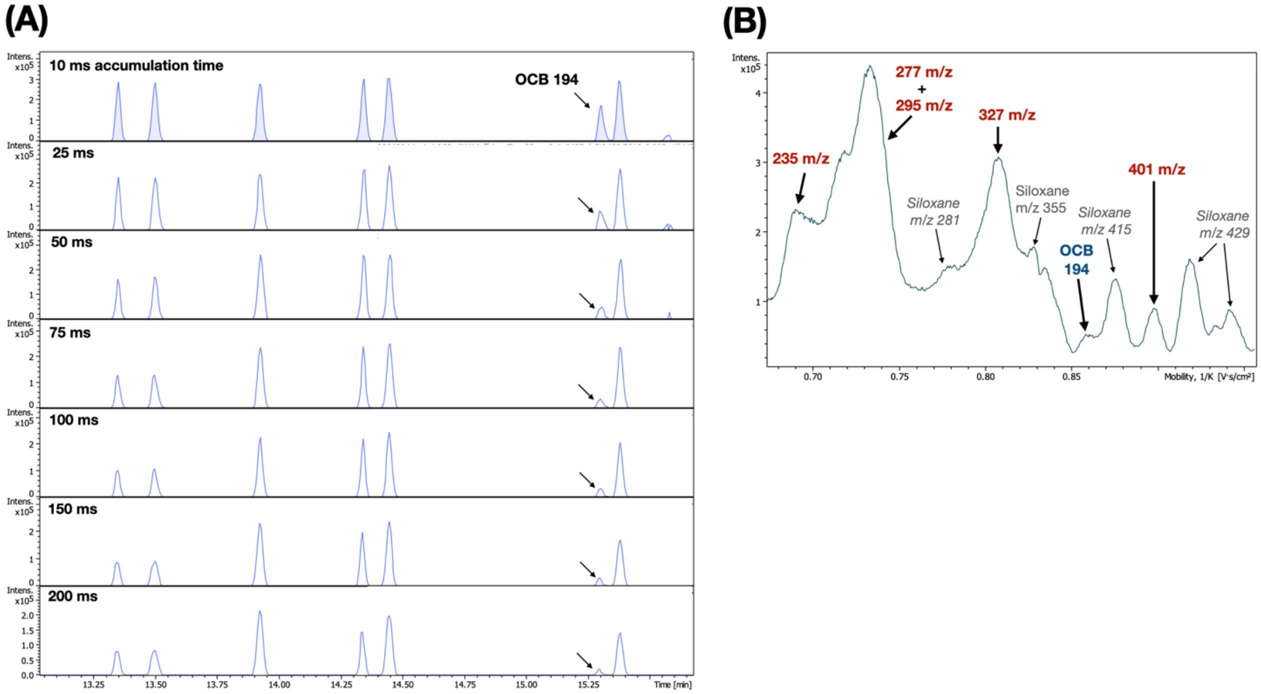

Figure S4.3 – **(A)** Extracted ion chromatograms (EICs) of a mixture of octachlorobiphenyls (OCBs) recorded at different accumulation times. The analysis time was fixed at 200 ms. **(B)** Total ion mobilogram (TIM) generated during the elution windows of OCB 194. Peaks corresponding to the intense coeluting matrix interference are highlighted in dark red. Other peaks in the TIMs are annotated in grey. Interestingly, in this case, the interfering ion appears to be the siloxane ion at m/z 415 rather than one of the five coeluting ionic species highlighted in dark red. While this siloxane ion was present throughout the GC chromatographic run due to column bleed, it was particularly intense at the retention time of OCB 194. This may be due to additional contributions from impurities within the GC system (e.g., injector, caps, septa), beyond those from the column itself.

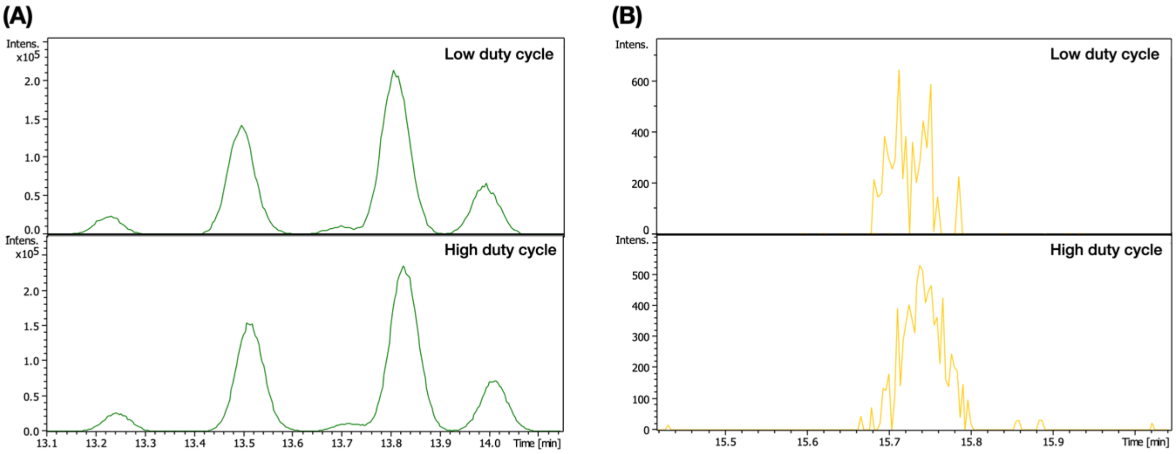

Figure S4.4 –Extracted ion chromatogram (EIC) comparison at low (37%) and high (100%) duty cycle for **(A)** pentachlorobiphenyls (PeCBs) present in high abundance, and **(B)** a tribromodiphenyl ether (TriBDE) present at trace levels. While the chromatograms in (A) are nearly identical, the high duty cycle chromatogram in (B) appears to be of slightly better quality than the one acquired at low duty cycle.

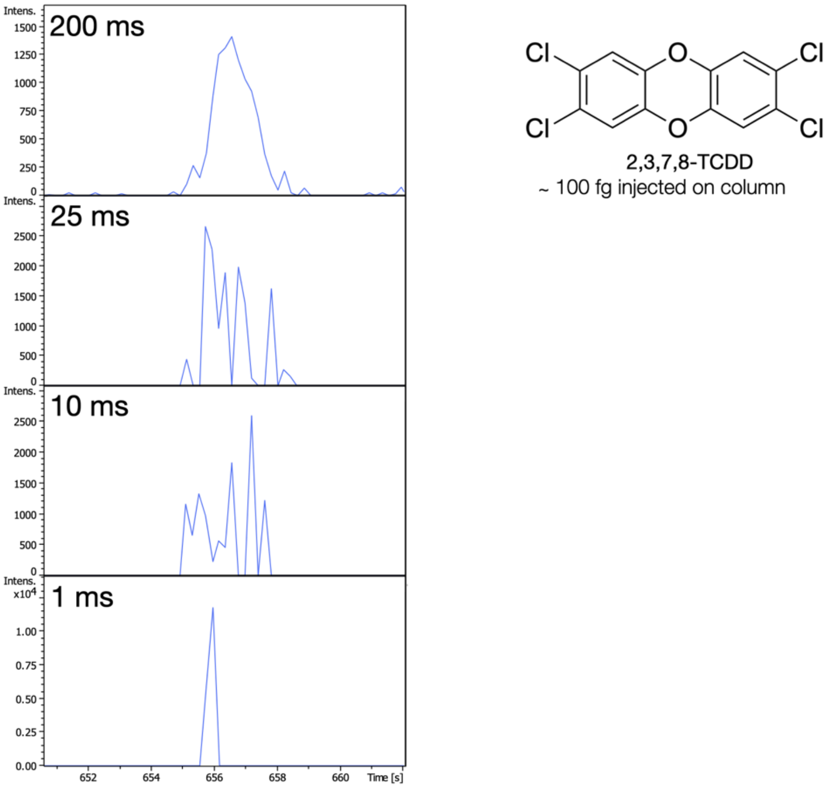

Figure S4.5 – Extracted ion chromatograms (EICs) from the analysis of a low amount (~100 fg) of 2,3,7,8-TCDD at different accumulation times. The analysis time was fixed at 200 ms.

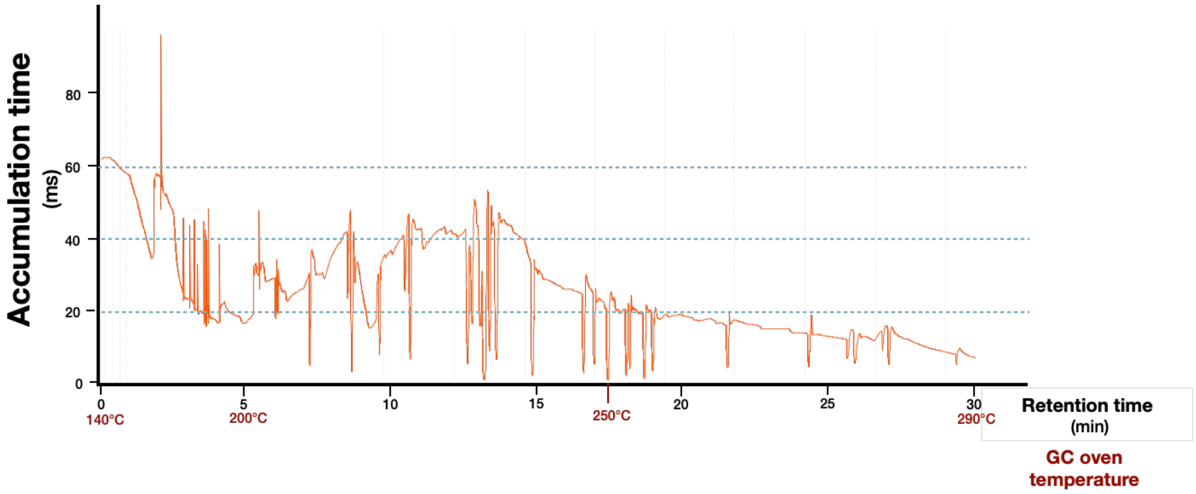

Figure S4.6 - Accumulation time versus retention time and GC oven temperature in ICC mode (7.5 MiO). As can be seen in this figure, the accumulation time already drops to ~60 ms at the start of the GC separation (T=140°C). Between 200 and 250°C, the accumulation time varies between 20 and 50 ms. Above 250°C, it drops below 20 ms and reaches ~10 ms at the end of the separation.

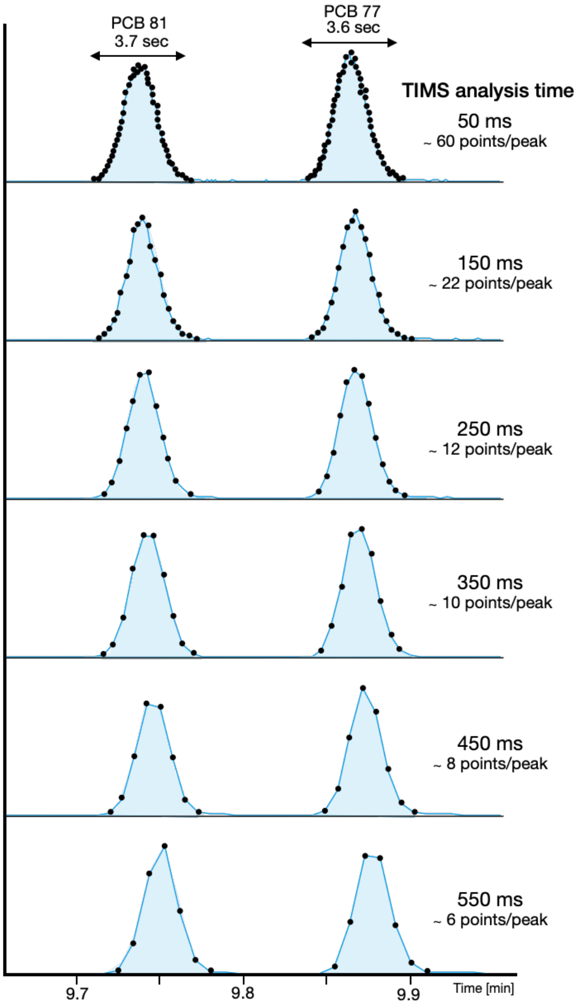

Figure S4.7 – Variation of the chromatographic sampling rate of two tetra PCBs (77 and 81) as a function of the TIMS analysis time. Each black point corresponds to a single TIMS separation.

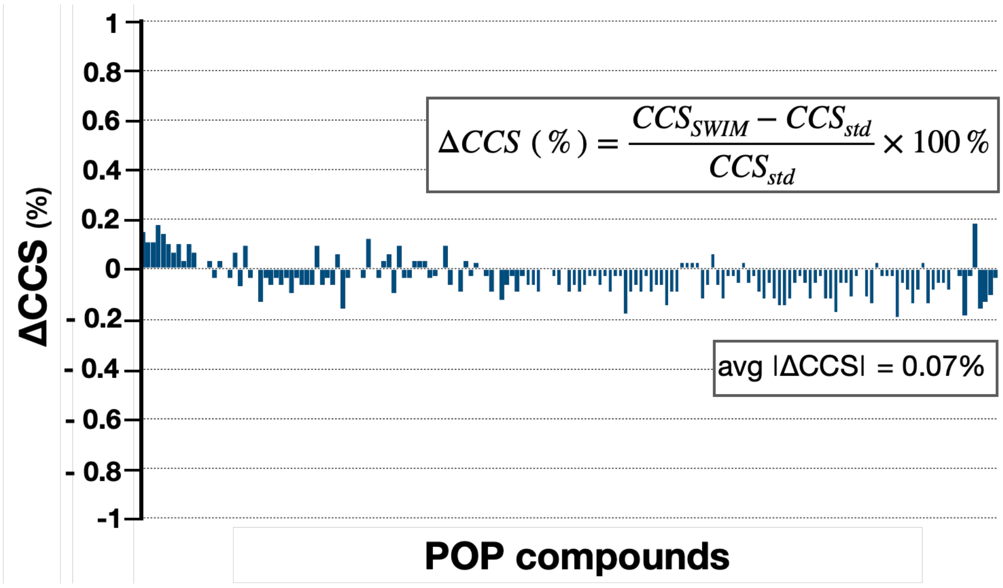

Figure S4.8 – Percentage difference in the measured CCS of the 174 POP standards between the standard and the SWIM mode.

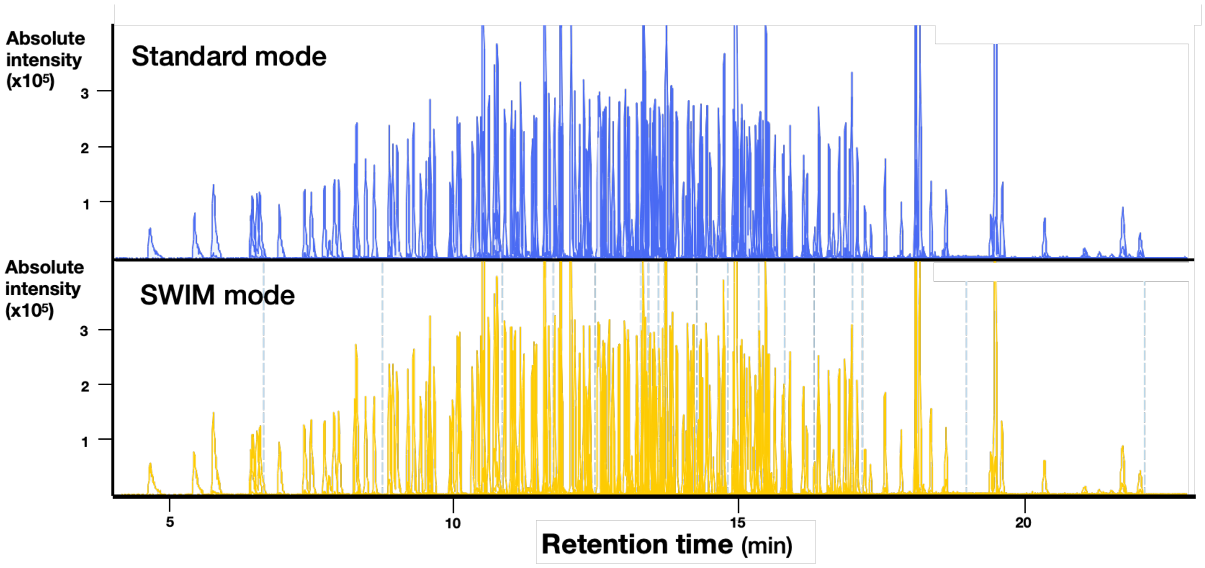

Figure S4.9 – Overlaid extracted ion chromatograms of the 174 POPs in standard (upper chromatogram) and SWIM (lower chromatogram) modes. Overall, signal intensity is of the same order of magnitude in both modes.

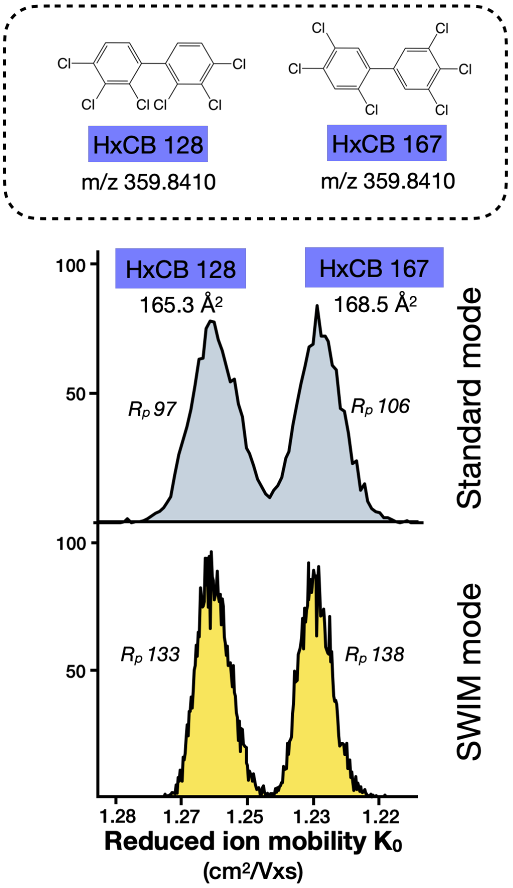

Figure S4.10 – Ion mobility spectra in standard mode (upper spectrum) and SWIM mode (lower spectrum) of two partially coeluting hexachlorobiphenyl isomers (HxCBs). While the two isomers were not completely resolved in the standard mode, a perfect baseline separation was obtained in the SWIM mode.

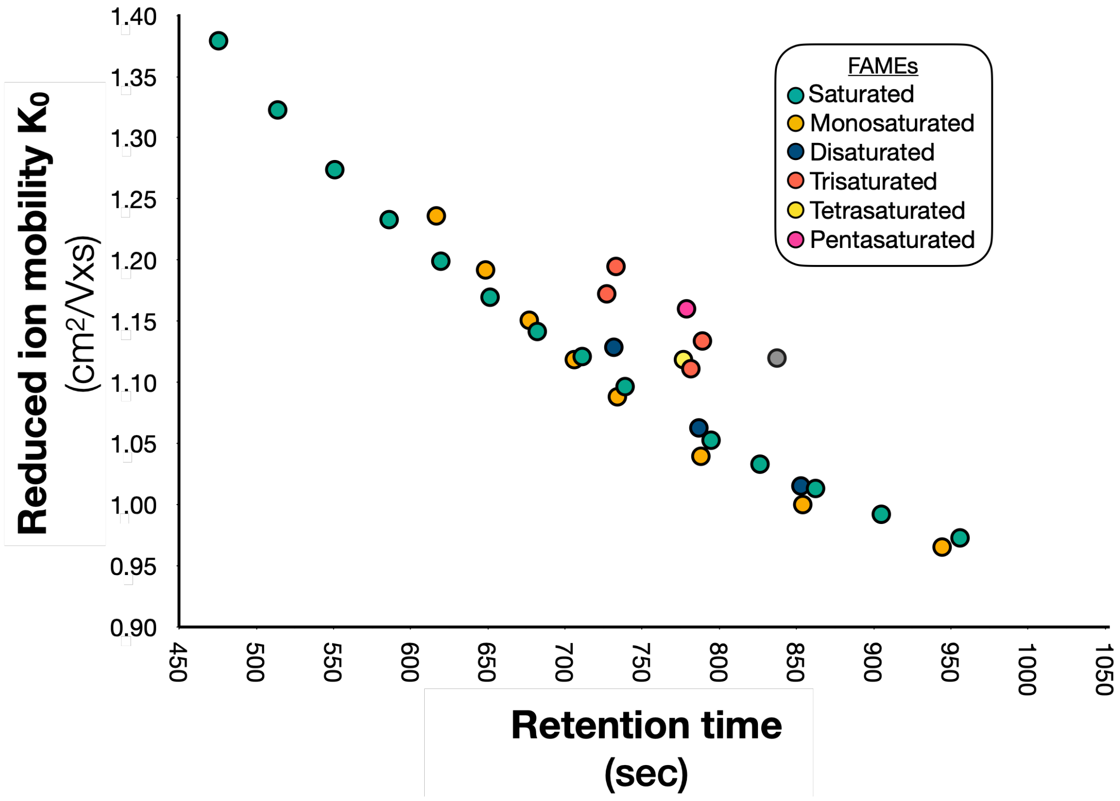

Figure S4.11 – Reduced ion mobility vs retention time plot of a mixture of saturated and (poly)unsaturated fatty acid methyl esters (FAMEs) from C11 to C25 analyzed by GC-TIMS-MS.

TABLES

Table S4.1: Optimized ion mobility windows for the 174 POPs in SWIM mode.

IM windows	RT segments (sec)	Analysis range (K_0)	Analysis range ($1/K_0$)
1	0 – 400	1.67 – 1.41	0.60 – 0.71
2	400 - 525	1.59 – 1.35	0.63 – 0.74
3	525 - 651	1.45 – 1.25	0.69 – 0.80
4	641 - 704	1.41 – 1.22	0.71 – 0.82
5	704 - 748	1.37 – 1.19	0.73 – 0.84
6	748 - 796	1.35 – 1.18	0.74 – 0.85
7	796 - 805	1.33 – 1.16	0.75 – 0.86
8	805 - 815	1.32 – 1.15	0.76 – 0.87
9	815 - 822	1.37 – 1.19	0.73 – 0.84
10	822 - 856	1.33 – 1.16	0.75 – 0.86
11	856 - 888	1.32 – 1.15	0.76 – 0.87
12	888 - 920	1.28 – 1.12	0.78 – 0.89
13	920 - 948	1.30 – 1.14	0.77 – 0.88
14	948 - 979	1.28 – 1.12	0.78 – 0.89
15	979 - 1020	1.23 – 1.09	0.81 – 0.92
16	1020 - 1030	1.25 – 1.10	0.80 – 0.91
17	1030 - 1140	1.23 – 1.09	0.81 – 0.92
18	1140 - 1276	1.18 – 1.04	0.85 – 0.96
19	1276 - 2280	1.12 – 1.00	0.89 – 1.00

Research axis II: Application of GC-APCI-TIMS-TOFMS for the targeted and untargeted analysis of halogenated contaminants

Chapter 5:
Evaluation of the performance of GC-APCI-TIMS-TOFMS for the quantitative analysis of trace contaminants

Portions of this chapter are based on the following publications:

Muller, H. B.; Scholl, G.; Far, J.; De Pauw, E.; Eppe, G. Sliding Windows in Ion Mobility (SWIM): A New Approach to Increase the Resolving Power in Trapped Ion Mobility-Mass Spectrometry Hyphenated with Chromatography. *Anal. Chem.* **2023**, *95* (48), 17586–17594

Muller, H. B.; Scholl, G.; Eppe, G. Gas Chromatography–Trapped Ion Mobility Mass Spectrometry: A Highly Specific and Ultra-Sensitive Platform for Quantifying Sub-ppt Levels of Dioxins and PCBs in Food. *Chemosphere* **2025**, 385, 144557

Chapter 5: Evaluation of the performance of GC-APCI-TIMS-TOFMS for the quantitative analysis of trace contaminants

5.1 - MATERIALS AND METHODS 113

5.1.1 - Chemicals 113

5.1.2 - Sample preparation 113

5.1.3 - Instrumentation 114
- A. GC-APCI-TIMS-TOFMS 114
- B. GC-sectorHRMS 115

5.1.4 - Data treatment 115

5.2 - RESULTS AND DISCUSSION 115

5.2.1 - Quantitative performances evaluation of GC-APCI-TIMS-TOF 115
- A. Linearity and LOQs 115
- B. Precision, trueness and uncertainty 118

5.2.2 - Benefits of ion mobility for the quantitative analysis of contaminants 121
- A. CCS values for analyte confirmation 121
- B. Increased selectivity 122

5.3 - CONCLUSION 125

5.4 - REFERENCES 126

5.5 - SUPPORTING INFORMATION 129

In the field of contaminants and pollutants analysis, the interest in IM-MS platforms is emerging and has been growing significantly in the last 5 years (Section 1.3.5). Indeed, several recent studies have demonstrated the potential of IM as powerful additional technique to improve the analysis of both legacy and emerging contaminants[1,2]. However, while such applications have been mainly qualitative approaches, quantitative applications for pollutant compounds have been comparatively scarce.

Interestingly, some of the earliest reports of quantitative IM-MS applications, across all research fields, dated back to 1999-2000. Theses pioneers studies, conducted by the group of Guevremont, focused on the targeted analysis of disinfection by products (DBPs) such as perchlorate in water using a homebuilt FAIMS device hyphenated to a commercial LC-quadrupole[3–5]. Since then, only a few works have focused on the targeted analysis of contaminants such as per- and polyfluoroalkyl substances (PFAS)[6], organic micropollutants (OMPs)[7], hydroxylated polychlorobiphenyls (PCBs)[8], non-intentionally added substances (NIAS)[9], pesticides[10] and veterinary drug residues[11] have been published. Moreover, while promising preliminary quantitative performance results have been reported in these studies, a thorough validation of the performances of current IM-MS instrumentation for the quantitative analysis of trace contaminants, comparable to the efforts undertaken for other classes of small compounds such as metabolites[12–16], remains lacking.

To address this gap, the present chapter aimed at thoroughly evaluating the capabilities of a modern commercially available IM-MS instrument (timsTOF pro 2 from Bruker) to accurately quantify trace amounts of well-known legacy contaminants, the dioxins and the PCBs, in food samples. Three fat samples (fish oil, palm oil and milk fat) from proficiency tests (PTs) were analyzed on a GC-APCI-TIMS-MS device. After method optimization, analytical performance was assessed in accordance with Commission Regulation (EU) 2017/644 and compared with the reference confirmatory method for dioxins and PCBs, the GC–EI–sector HRMS. Additionally, the benefits of incorporating ion mobility in terms of specificity and peak capacity were evaluated in the context of dioxin and PCB analysis and are discussed in the final section of this chapter.

5.1 - Materials and methods

5.1.1 - Chemicals

All congeners of PCDD/Fs (the seventeen 2,3,7,8-substituted), non-ortho (NO-)PCBs (PCBs 77, 81, 126, 169), mono-ortho (MO-)PCBs (PCBs 105, 114, 118, 123, 156, 157, 167, 189) and non-dioxin like (NDL) indicator PCBs (PCBs 28, 52, 101, 138, 153, 180) were quantitated against their own ^{13}C-uniformly labeled internal standards according to the isotopic dilution method. Native and ^{13}C- labelled standards were purchased from Wellington Laboratories (Ontario, Canada). For the calibration curves, 6 level calibration solutions were prepared for the PCDD/Fs and the NO-PCBs, 8 for the MO-PCBs and 9 for the NDL-PCBs. The detailed concentrations for each calibration level are given in **Tables S5.1**. Recovery rates were checked with recovery standards (1,2,3,4-TCDD for PCDD/Fs and PCB 80 for PCBs). All solvents used were of the highest purity, suitable for the analysis of trace contaminants (Biosolve, Dieuze, France).

5.1.2 - Sample preparation

The oil fat samples analysed in this study were aliquots of PT samples provided by the European Reference Laboratory for Dioxins and PCBs in Food and Feed (EU-RL, Freiburg, Germany). The three matrices were fish oil (EURL-PT-DP_1601-HF), palm oil (EURL-PT-DP_1701-PF) and milk fat (EURL-PT-

DP_1302-MI). These matrices were chosen because they required the same sample preparation procedure and because their profile and level of contamination were different.

The sample preparation was performed according to our ISO17025 accredited protocol for the analysis of PCDD/Fs and PCBs in foodstuffs. Briefly, each fat samples (2 g for fish oil; 4 g for palm oil and milk fat) were dissolved in a mix of 14 mL n-hexane and 1 mL of toluene, spiked with ^{13}C-uniformaly labeled internal standards and then loaded on an automated Dextech Heat system (LCTech, Germany) for multiple column clean-up and fractionation. The samples in hexane were sequentially eluted through $AgNO_3$, H_2SO_4, and KOH supported on silica and basic alumina for lipid breakdown and removal of some interferences. Then, on an activated carbon column, two fractions were collected, a first one with non-planar congeners (MO- and NDL-PCBs, referred to in this text as the "PCBs fraction") and a second one with the planar congeners (PCDD/Fs and NO-PCBs, referred to as the "dioxins fraction"). These fractions were then transferred to GC vials containing n-Nonane as keeper solvent, evaporated under a gentle stream of nitrogen and finally spiked with the recovery standards before analysis. The final volumes were 100 and 9 μL for the PCBs and dioxins fraction, respectively. For each matrix, two sets of six aliquots were taken and prepared according to the abovementioned protocol (one set for GC-TIMS-TOFMS and the other for GC-sectorHRMS). A total of 10 procedural blanks were also prepared in parallel. All the sample preparation was performed by qualified and experienced technicians from our routine trace contaminants laboratory.

5.1.3 - Instrumentation

A. GC-APCI-TIMS-TOFMS

Measurements were performed on a commercial timsTOF Pro 2 mass spectrometer (Bruker, Bremen) equipped with a Scion 456-GC connected to an atmospheric pressure chemical ionization (APCI) source for sample introduction and ionization (GC-APCI II, Bruker, Bremen).

Injections were conducted in splitless mode (injection temperature 275 °C, 1 µL) for the PCBs fraction (MO- and NDL-PCBs) and in solvent vent PTV mode (injection temperature 80 °C, 5 µL) for the dioxins fraction (PCDD/Fs and NO-PCBs). The GC column was a low polarity Rxi-5Sil MS column (30 m × 0.25 mm × 0.25 µm, Restek). Helium (grade 6.0, Air Liquide, Belgium) was used as the carrier gas. More details about the GC conditions are given in **Table S5.2**.

Analytes were ionized in positive APCI mode and were generated mostly as stable radical molecular ions $M^{+\cdot}$, along with a small proportion of protonated $[M+H]^+$ ions (a detailed list of the ionization source parameters used is provided in **Table S5.3**).

A complete list of the optimized TIMS parameters used in this study (voltages, pressure, analysis times, etc.) is provided in **Table S5.4**. The accumulation time for the analysis of the PCBs fraction was set to 75 ms (corresponding to a duty cycle of 30%) to limit space charge effects (Section 4.2.1A). However, for the dioxins fraction, the accumulation time was set to 250 ms (i.e., 100% duty cycle) to ensure more accurate peak integrations (Section 4.2.1A). The TIMS separations were performed in SWIM mode[17] (Section 4.2.2C). More details about the application of SWIM to the analysis of both fractions are given in **Figure S5.1**. The resolving power achieved varied roughly between 100 and 220 depending on the quantity of analyte injected (1 to 500 pg). Ion mobility and m/z calibration were performed according to procedure developed in Section 3.2.1C using siloxane ions from the GC column bleed. The qTOF analyzer was operated at 10 kHz in the range m/z 100−1000 in MS only mode (additional parameters are provided in **Table S5.5**).

B. GC-sectorHRMS

Reference measurements were performed on an Autospec sector mass spectrometer (Waters, Manchester, UK) coupled to an Agilent 7890 gas chromatograph (Palo-Alto, CA, USA). The GC conditions were similar to the injections performed on the timsTOF instrument, with the exception of the GC columns which were different (a 50m J&W VF-5ms column for the dioxins fraction and a 25 m Trajan HT8 column for the PCBs fraction). The ionization was performed in electron impact (EI) at 35 eV. The mass resolving power was set to 10 000 (10% valley definition) in single ion monitoring (SIM) mode.

5.1.4 - Data treatment

For the GC-timsTOFMS analysis, data processing was performed using the software Data-Analysis (Bruker, version 5.3). Two approaches of peak integration were considered: quantitation based on the areas of the ion mobility peaks or quantitation based on the areas of the IM-filtered chromatographic peaks (**Figure S5.2**). Comparison of the quantification results revealed that the latter approach provided slightly more reproductible and accurate results, so this method was chosen. Internal recalibration of both m/z and ion mobilities was performed after each data acquisition. Experimentally measured ion mobility values were converted to CCS values using the fundamental low-field (Mason-Schamp) equation, with T set arbitrarily to 305 K. Ion mobility resolving powers were calculated using the CCS-based definition ($R_p = CCS/\Delta_{fwhm}CCS$)[18].

For the GC-sectorHRMS analysis, data processing was performed using TargetLynx (Waters, version 4.1). The chromatographic area of the two most intense isotopologues of the molecular cluster was used for quantification and confirmation.

5.2 - Results and discussion

5.2.1 - Quantitative performances evaluation of GC-APCI-TIMS-TOF

The assessment of the quantitative performances of our method was performed according to protocols and criteria from the European Regulation 2017/644[19], which states the basic requirements that need to be met by analytical method for the confirmatory analysis of dioxins and PCBs in food. The following criteria were evaluated in this study: linearity, LOQ, precision, trueness and measurement uncertainty. They are discussed in the following subsections. For comparison purposes, the precision, trueness and uncertainty were also determined on our validated GC-EI-sectorHRMS instrument.

A. Linearity and LOQs

Linearity is commonly evaluated using the coefficient of determination (R^2). However, in the field of dioxin and PCB analysis, where isotope dilution is the reference quantification approach, a more statistically robust method involves assessing linearity through the precision (expressed as RSD) of the relative response factor (RRF), calculated at each calibration level. To determine the linear dynamic range of our method, calibration solutions were analyzed in triplicate over three separate days. For each level, the mean RRF was calculated, and the RSD (%) of these average RRFs was determined. In accordance with regulatory requirements, the RSD must remain below 20% to confirm acceptable linearity. The linear ranges that met this criterion are summarized in **Table 5.1** for each analyte, along with the corresponding RSD values of the average RRF$_{avg}$. For most PCDDs and PCDFs, the lowest calibration level fell outside the linear range and was excluded. Similarly, for MO and NDL PCBs, the first two calibration points had to be removed to achieve an RSD below 20% (Table S5.1).

Table 5.1: Linearity and LOQs obtained with the GC-APCI-TIMS-TOFMS instrumentation for the different analytes.

Analyte	RSD RRF$_{avg}$ (%)	Linear range (pg/μL)	RSD lowest calibration point (n=3, %)	Deviation lowest calibration point compared to RRF$_{avg}$ (%)	iLOQ (pg/μL)	mLOQ (pg/g)	
						2g	4g
2,3,7,8-TCDD	4.9	0.1-10	5.3	-1.2	0.1	0.1	0.05
1,2,3,7,8-PeCDD	4.4	0.1-10	12.4	+7.1	0.1	0.1	0.05
1,2,3,4,7,8-HxCDD	4.4	0.2-20	4.7	-2.1	0.2	0.2	0.1
1,2,3,6,7,8-HxCDD	5.3	0.2-20	12.7	-1.0	0.2	0.2	0.1
1,2,3,7,8,9-HxCDD	4.2	0.2-20	5.2	-2.9	0.2	0.2	0.1
1,2,3,4,6,7,8-HpCDD	4.8	0.2-20	14.2	+6.7	0.2	0.2	0.1
OCDD	5.0	0.5-50	8.1	-1.8	0.5	0.5	0.25
2,3,7,8-TCDF	3.0	0.1-10	9.9	+3.9	0.1	0.1	0.05
1,2,3,7,8-PeCDF	4.1	0.1-10	4.1	+1.6	0.1	0.1	0.05
2,3,4,7,8-PeCDF	3.7	0.1-10	3.8	-3.1	0.1	0.1	0.05
1,2,3,4,7,8-HxCDF	3.6	0.2-20	9.8	+5.0	0.2	0.2	0.1
1,2,3,6,7,8-HxCDF	2.7	0.2-20	1.8	+1.0	0.2	0.2	0.1
2,3,4,6,7,8-HxCDF	4.0	0.2-20	4.0	-5.9	0.2	0.2	0.1
1,2,3,7,8,9-HxCDF	2.8	0.2-20	2.8	-0.3	0.2	0.2	0.1
1,2,3,4,6,7,8-HpCDF	4.1	0.2-20	4.1	-1.3	0.2	0.2	0.1
1,2,3,4,7,8,9-HpCDF	4.9	0.2-20	14.3	+3.3	0.2	0.2	0.1
OCDF	4.0	0.5-50	4.0	-2.7	0.5	0.5	0.25
TCB 81	6.3	0.5-20	0.7	+3.7	0.5	2.7	1.35
TCB 77	5.4	0.5-20	1.8	+5.6	0.5	13.1	6.5
PeCB 126	2.0	0.5-20	4.7	-0.7	0.5	0.5	0.25
HxCB 169	5.5	0.5-20	11.0	+1.0	0.5	0.5	0.25
PeCB 123	2.5	4-140	1.2	-1.1	4	5.7	2.85
PeCB 118	6.5	4-140	10.1	+12.7	4	144	72
PeCB 114	1.5	4-140	4.9	+1.1	4	4.8	2.4
PeCB 105	2.5	4-140	9.0	+2.9	4	53.5	26.75
HxCB 167	3.5	4-140	2.8	-2.7	4	4	2
HxCB 156	5.6	4-140	5.6	-1.1	4	4.0	2.0
HxCB 157	2.0	4-140	3.9	-1.4	4	4	2
HpCB 189	3.1	4-140	4.6	+0.8	4	4	2
TriCB 28	7.8	4-500	4.5	+12.9	4	1299	649.5

TCB 52	9.6	4-500	4.5	+18.4	4	2379	1189.5
PeCB 101	3.0	4-500	1.4	+3.7	4	636	318
HxCB 153	4.2	4-500	5.8	-2.5	4	121	60.5
HxCB 138	3.2	4-500	4.3	-2.3	4	68	34
HpCB 180	4.7	4-500	4.0	-4.9	4	15	7.5

Concerning the limit of quantification (LOQ), two types were determined in this work: the instrumental LOQ (iLOQ) which depends purely on the instrumental performances and the method LOQ (mLOQ) which takes into account the blank levels[20]. The determination of the iLOQ was based on the definition of the LOQ in the regulation[19], where it is stated that it corresponds to "the concentration of an analyte in the extract of a sample which produces an instrumental response at two different ions to be monitored with a S/N (signal/noise) ratio of 3:1 for the less intensive raw data signal". Moreover, the regulation specifies that "if for technical reasons the signal-to-noise calculation does not provide reliable results" the LOQ can be defined as "the lowest concentration point on a calibration curve that gives an acceptable (≤30 %) and consistent (measured at least at the start and at the end of an analytical series of samples) deviation to the average relative response factor calculated for all points on the calibration curve in each series of samples". While the S/N-based definition is commonly used with traditional GC-sectorHRMS methods, we found it unsuitable for the GC-TIMS-TOF system. The additional ion mobility separation effectively acts as a noise filter, suppressing background signals to such an extent that calculating a representative noise level (and consequently, a reliable signal-to-noise ratio) is no longer feasible (**Figure S5.3**). A similar limitation has already been reported for GC-QqQ systems[20]. Therefore, the iLOQ in this work was determined according to the second regulatory definition. Specifically, it was set as the lowest calibration point for which the average RRF, measured over three different days, met two criteria: (i) a relative standard deviation (RSD) ≤ 15%, and (ii) a deviation of less than 30% from the overall average RRF across the entire calibration range.

The resulting iLOQs are displayed in Table 5.1. For all analytes, the lowest calibration point within the linear range satisfied both criteria and was thus designated as the iLOQ. These results demonstrate that the GC-APCI-TIMS-TOF platform offers sufficient intrinsic sensitivity to quantify analytes at sub-ppt levels, with absolute concentrations in the range of a few hundreds of femtograms per μL, i.e. concentrations typically encountered in injection vials after sample preparation of food samples.

As regards to the mLOQ, it was calculated as the mean contamination levels in 10 procedural blanks plus ten times standards deviations. Procedural blanks were prepared weekly to reflect routine laboratory conditions. For the NO PCB 169 and all the PCDD/Fs which were not found in the procedural blanks, the mLOQ was set equal to the corresponding iLOQ. The conversion from iLOQ to mLOQ assumed a final extract volume of 10 µL, an injection volume of 5 µL, and 100% recovery. For a few compounds detected in the blanks, specifically PeCB 126, HxCB 167, HxCB 157, and HpCB 189, the calculated mLOQ based on contamination levels was lower than the value derived from the iLOQ (**Table S5.6**). In these cases, the higher of the two values was retained to ensure conservativeness. The resulting mLOQs are reported in Table 5.1, based on sample masses of 2 g (fish oil) and 4 g (palm oil and milk fat).

Overall, the mLOQs were in the high fg/g for the dioxins and ranged from a few pg to hundreds of pg/g for the dioxin like PCBs. The mLOQs for the NDL PCBs were much higher owing to their relatively high level in the procedural blanks, in particular for the PCBs 28, 52 and 101. It is important to emphasize that, for most PCB congeners, the mLOQs reported in Table 5.1 do not reflect the sensitivity of the TIMS-TOF Pro2 instrument itself, but rather the background contamination observed in our laboratory environment, which severely penalizes the achievable LOQs for these congeners.

B. Precision, trueness and uncertainty

The precision, trueness, and uncertainty of the method were evaluated using a set of samples from proficiency tests for which consensus concentration values of the target congeners were available. Six aliquots of each matrix (palm oil, fish oil, and milk fat) were analyzed over five days under intermediate reproducibility conditions using the GC-TIMS-TOF method. For comparison, an additional set of six aliquots per matrix was prepared and analyzed under the same conditions using our reference GC-sectorHRMS instrument.

Intermediate precision (RSD$_R$) was estimated for each congener by calculating the relative standard deviation across the six replicate measurements. The resulting RSD$_R$ values for both the TIMS and magnetic sector methods are plotted as a function of analyte concentration in **Figures 5.1a** and **5.1b**, respectively. These plots clearly show that, in the vast majority of cases (97%), the RSD$_R$ values obtained with the TIMS method remained below the regulatory thresholds of 15% for PCDD/Fs and DL PCBs, and 20% for NDL PCBs. Moreover, comparison of Figures 5.1a and 5.1b indicates that the precision achieved with the TIMS method was broadly comparable to that of the magnetic sector instrument. On average, the RSD$_R$ was slightly higher with the TIMS method for dioxins (8.9% vs. 6.1%), but slightly lower for the NDL PCBs (5.0% vs. 8.1%) (**Table S5.7**). It was similar for MO PCBs (4.8% vs. 5.4%). As expected, for both techniques, RSD$_R$ values tended to approach the regulatory thresholds at lower analyte concentrations.

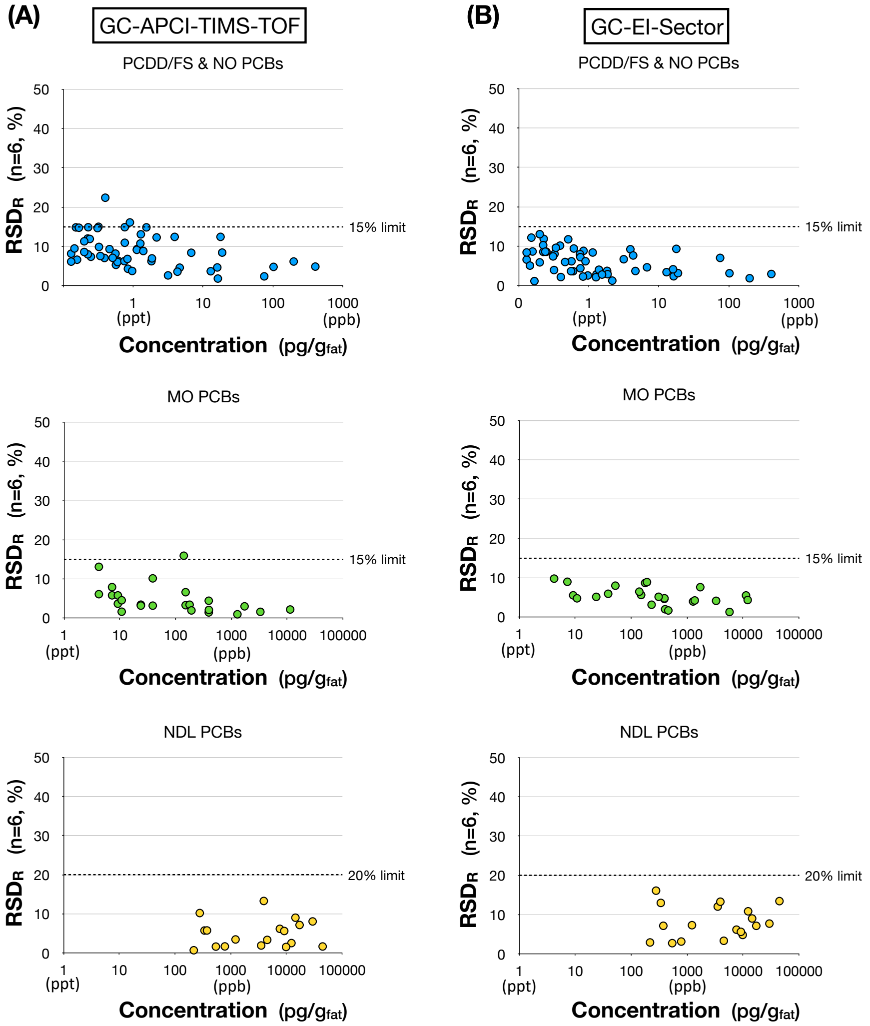

Figure 5.1: Plot of RSD versus concentrations of the analytes in the different samples for **(A)** the GC-APCI-TIMS-TOFMS and **(B)** GC-EI-Sector methods.

Trueness was assessed through the calculation of the bias of the measured values with respect to the consensus values from the PTs. The resulting biases for PCDD/Fs, DL PCBs and NDL PCBs are plotted against analyte concentration in **Figure 5.2a** (TIMS) and **5.3b** (magnetic sector). With regards to the PCDD/Fs fraction, the plot indicates that the calculated biases with the TIMS instrumentation globally complied with the European requirements (79.9% of biases were within the +/- 20% threshold, Table S5.7). Although a notable portion of biases exceeded this threshold, especially at lower concentrations (around the ppt level and below), this high compliance rate for trueness remains very encouraging, particularly given the complexity of the matrix and the ultra-trace levels of PCDD/Fs involved. This trend contrasts with the performance of the magnetic sector instrument, where nearly all biases (99.7%) were within regulatory limits, although a slight increase in variability was observed at the lowest concentration levels. Accordingly, the mean absolute bias for dioxins was almost twice as high with the TIMS system compared to the magnetic sectorHRMS method (13.1% vs. 7.3%, Table S5.7), suggesting a limitation of the current TIMS configuration in accurately quantifying PCDD/Fs at ultra-trace levels close to the mLOQ.

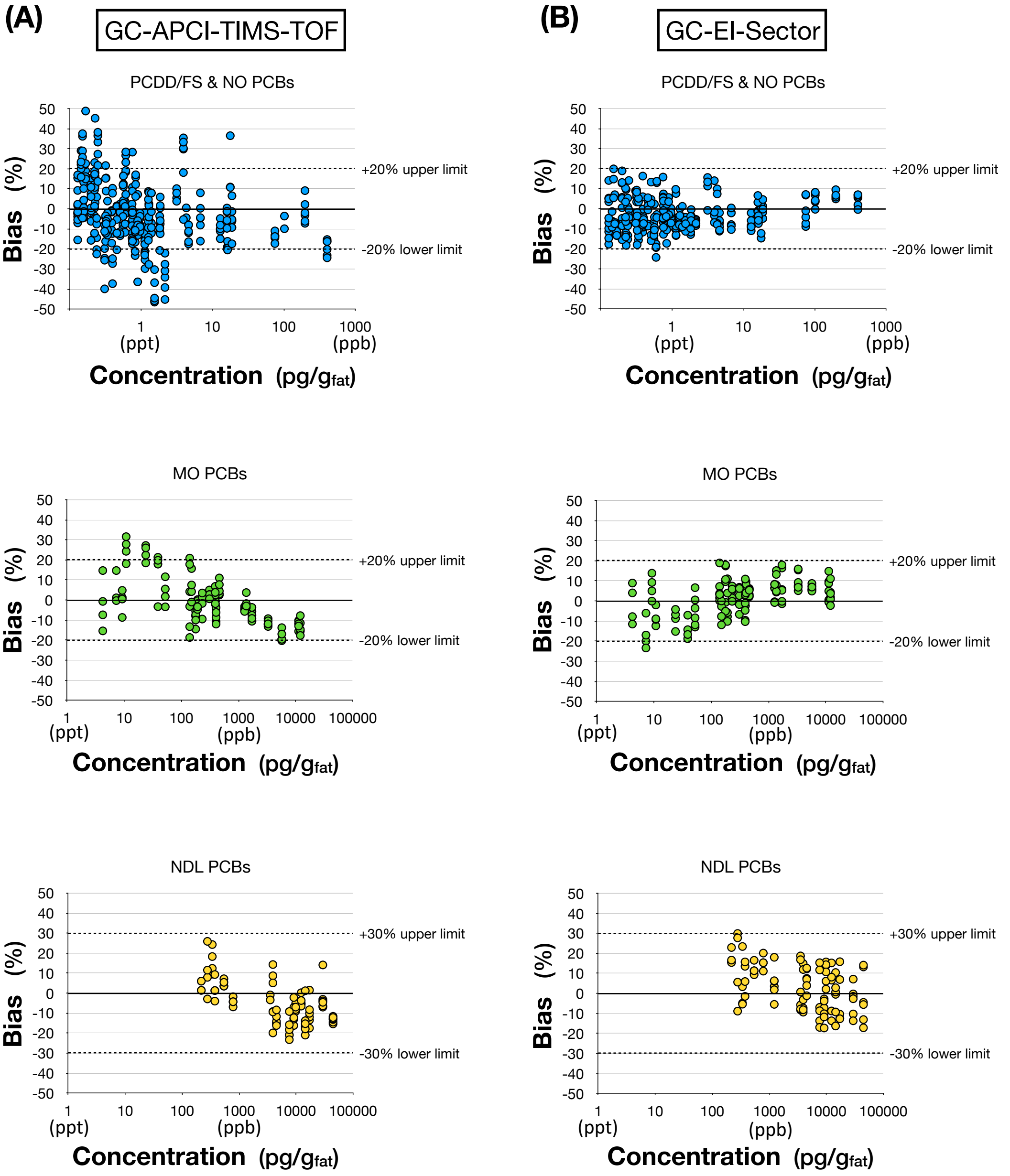

Figure 5.2: Plot of bias versus concentrations of the analytes in the different samples for **(A)** the GC-APCI-TIMS-TOFMS and **(B)** GC-EI-Sector methods.

For the PCBs fraction, biases were generally well within the regulatory acceptance criteria: 87.2% of values fell within ±20% for MO PCBs, and 93.0% within ±30% for NDL PCBs. These results compared favourably with the magnetic sectorHRMS method, with mean absolute biases of 8.9% vs. 7.1% for MO PCBs, and 9.8% vs. 10.3% for NDL PCBs (Table S5.7), confirming the trueness performances of the GC-TIMS-TOF platform for PCBs quantification across a broad concentration range.

Measurement uncertainty was estimated using the top-down approach developed by the EURL POPs[21], based on intermediate precision and trueness. As illustrated in the bar graph in **Figure S5.4A**, the calculated expended uncertainty U (with a coverage factor of 2) for PCDDs and PCDFs with the TIMS method was generally higher than that observed for PCBs. Moreover, for approximately half of the dioxin congeners, the calculated uncertainties were moderately to significantly higher (e.g., 1,2,3,7,8,9-HpCDF, OCDF) than the EURL recommended value[21] ($U \leq 38\%$). These findings are primarily attributed to a greater contribution of trueness at very low concentrations, which becomes more pronounced for PCDD/Fs in the TIMS method. In contrast, uncertainties for PCBs were generally comparable between the two techniques.

Finally, the precision, trueness and uncertainty were also evaluated for the summed WHO$_{2005}$-TEQ concentrations of PCDD/Fs and DL PCBs, as well as the sum concentrations of NDL PCBs. For each matrix, all performance criteria complied with the regulation requirements (**Table S5.8** and Figure S5.4B) and the total TEQ concentrations measured with both instruments were in close agreement (**Figure 5.3**). Importantly, both methods led to the same compliance conclusions for all three samples with respect to their respective PCDD/Fs and PCBs maximum limits[22], demonstrating the reliability of the TIMS approach compared to the reference magnetic sector field instrument at ppt levels. One exception to this consistency was observed for the milk fat sample, where the summed TEQ concentrations of dioxins and DL-PCBs, as well as the summed NDL-PCB concentration, were classified as compliant using the TIMS method, but as non-compliant with the magnetic sector instrument (Figure 5.3 and Table S5.8). In both cases, the concentrations measured in TIMS were above the respective maximum levels, consistent with the magnetic sector instrument. However, since the measured values were only slightly above the regulatory thresholds, and the expanded uncertainty associated with TIMS was slightly larger, the compliance decision fell within the uncertainty range, resulting in a classification as compliant. In such borderline cases, the alternative approach using TIMS would trigger the need for confirmatory analysis, as required by regulation. This clearly demonstrates that TIMS fulfilled its intended role as a reliable alternative screening method at the maximum level decision, and that, in any case, the appropriate decision had been made for the sum of PCDD/Fs in this milk fat sample limiting the risk of false non-compliance.

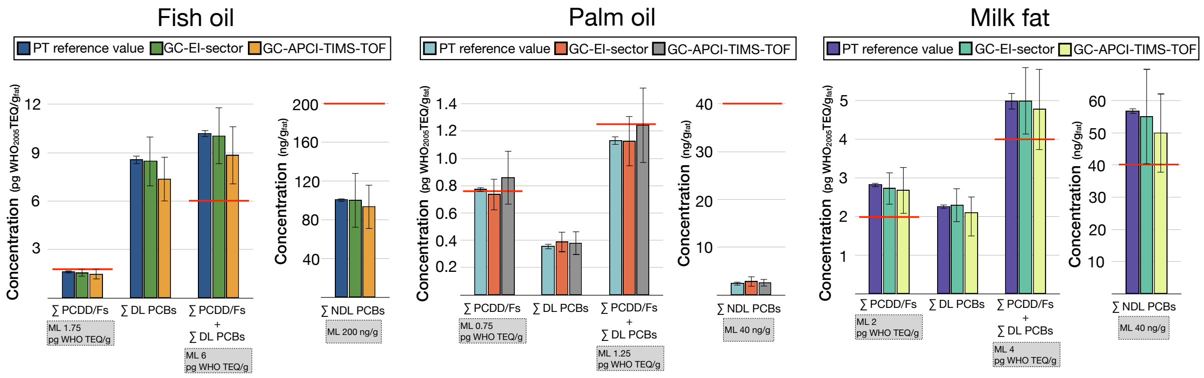

Figure 5.3: Comparison of total upper bound WHO$_{2005}$ TEQ concentrations of dioxins (PCDDs + PCDFs) and dioxin like PCBs (NO + MO PCBs) and summed concentrations of NDL PCBs measured by GC-EI-sector and GC-APCI-TIMS-TOF in the different matrices. The horizontal red lines correspond to the maximum limits based on WHO$_{2005}$ TEF values according to commission regulation EU 2023/915[22]. The error bars correspond to the expended measurement uncertainties (Figure S5.4).

5.2.2 - Benefits of ion mobility for the quantitative analysis of contaminants

A. CCS values for analyte confirmation

The identification of an analyte by targeted GC-MS methods is usually confirmed through retention times comparison between the analyte and its isotopically labelled standard analogue (e.g., <0.15%) as well as compliance of the ion abundance ratios (e.g., +/- 15% around the theoretical value)[19]. The addition of an ion mobility step within this workflow provides an additional means to correctly confirm the identity of the analyte and thus avoid false positives. In screening and non-targeted approaches, comparison between experimental CCS and references values from libraries (built in-house or made available from other laboratories) has already shown great promises to improve confidence in analyte assignment. Indeed, it was demonstrated that CCS values are not affected by the sample matrix[23,24] and generally display good reproducibility across different instrumental designs[25–27] (Section 1.3.4B). As a result, a 2% variation between experimental and reference database value has been suggested several times in the literature as a plausible cut-off value for identity confirmation of the analytes[23,28,29].

In targeted analysis performed with the isotopic dilution method, the CCS values can directly be compared between the analyte and its isotopically labelled standard, since both are present simultaneously in a given sample. In this work, we found the CCS of the native and corresponding labelled standard to be really close. On average, the CCS difference between native and standard at the different calibration levels varied from a minimum of 0.00% to a maximum of 0.21% (**Figure S5.5**). The differences were greatest for lower chlorinated PCBs, especially those with three and four chlorine atoms (**Figure 5.4a**) but decreased with increasing halogenation degree. Moreover, they were not significant for the PCDDs and the PCDFs (Figure 5.4b). It is noteworthy that, when present, the differences in CCS were consistently attributable to the isotopically labelled standard exhibiting a slightly higher CCS in comparison to the native analyte (Figures 5.4a and S5.5). This systematic behaviour is akin to the relative differences in the GC retention times where the ^{13}C labelled standards always elute a few seconds before their native analogues. The reason for these small deviations in CCS could be due to isotopic effects (i.e., isotopologue effect[30]).

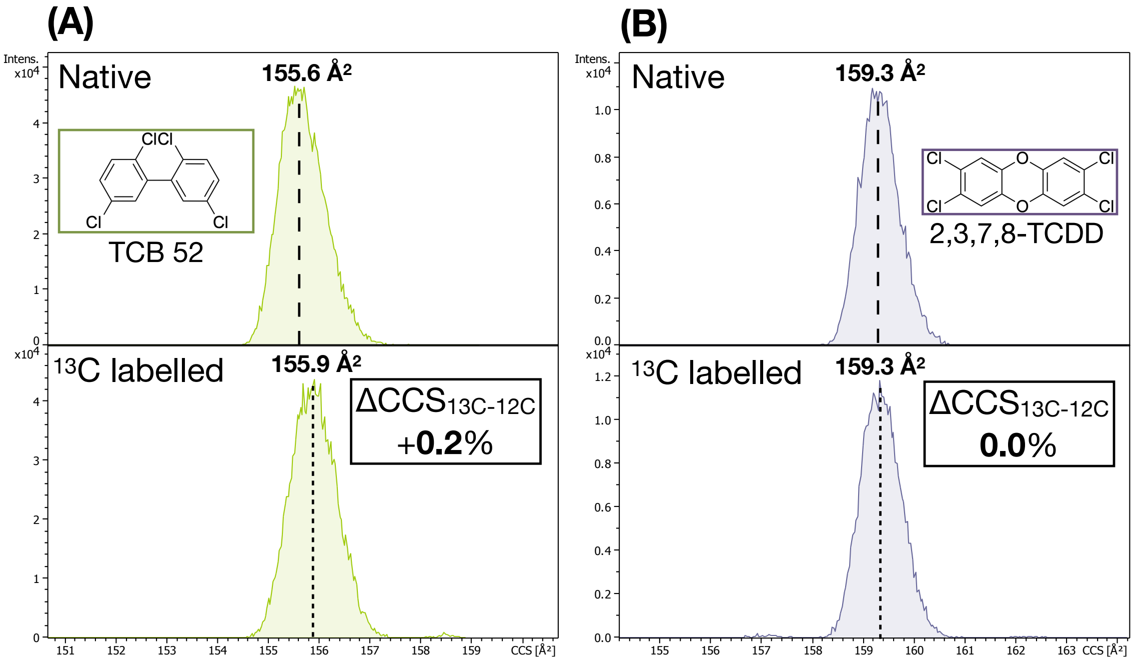

Figure 5.4: Overlayed ion mobility spectra of the native and ^{13}C uniformly labelled standards of **(A)** TCB 52 and **(B)** 2,3,7,8-TCDD (calibration level 5 in each case). A slight difference in CCS between the two standards can be seen in the case of the TCB 52.

In addition, a gradual CCS shift towards higher values was observed for the PCBs starting at the calibration level 7 (corresponding to an injection of 80 pg of native + 20 pg of labelled standard, Figure S5.5). These shifts are likely the result of space charge effects arising from increased ion density at the trapping region within the TIMS tunnel[31]. However, since these CCS shifts affected both the native analytes and their isotopically labelled analogues, the relative CCS differences between them were generally preserved. Only minor increases in ΔCCS were observed for a few analytes, with the largest shift reaching 0.45% for TCB 52 (**Figure S5.6**).

In light of these findings, we propose that a conservative cut-off of 0.5% for the maximum allowable CCS difference between an analyte and its labelled internal standard could serve as an additional identity confirmation criterion when using isotope dilution for quantification.

B. Increased selectivity

The occurrence of coeluting isobars and isomers remains a significant challenge for the identification and quantification of pollutants in complex samples using chromatographic-based MS analysis. Coeluting isobars, which have the same nominal mass, require high mass resolving power or tandem MS for differentiation, while coeluting isomers cannot be distinguished if they have identical or similar fragmentation spectra[32]. Although several papers have highlighted the potential of ion mobility for separating isomeric and isobaric species[33–35], fewer have explored its utility when such species are poorly separated in the chromatographic dimension[29,36,37].

In this work, most of the 35 target analytes were not impacted by potential interferences. This is due to a combination of a very thorough sample preparation which destroys and removes the great majority of the matrix and a high resolution separation in both the chromatographic and the mass spectrometric dimension (R_{FWHM} > 40 000). However, a number of interferences were still observed in some matrices. These were, for the great majority, partial coelution of isomeric congeners. For instance in the palm oil sample, numerous TCDDs were present in the sample and one of them was partially coeluting with the 2,3,7,8-TCDD (**Figure 5.5a**). However, in the IM dimension, the 2,3,7,8-TCDD was baseline separated from this interference (Figure 5.5c) and this interference could be removed in the corresponding IM-filtered chromatogram (Figure 5.5b). Similar cases were also observed for the NDL-PCBs 52, 101 and 153 in the different matrices (**Figure S5.7**). In the case of the TriCB 28, while a single peak was observed in the chromatographic dimension, the corresponding ion mobility spectrum strongly suggested the presence of an interfering compound (**Figure S5.8**). Only partial separation was achieved in this case. According to the model developed by McLean et al.[18], baseline separation of these two PCB isomers, which are characterized by a CCS difference of no more than 0.6%, would require an ion mobility resolving power of approximately 350, which exceeds the capabilities of the current GC-TIMS-MS configuration. The TriCB 31 is a well known coeluting interference of TriCB 28. This coelution was resolved with the magnetic sector instrumentation by using a specific GC column (HT-8). For the TIMS configuration, a classic and more versatile column was used (DB5-MS). With the exceptions of these few cases, overall most of the partially coeluting isomers observed in the different samples could not be further separated in the IM dimension, despite the high resolving power of the method (**Figure S5.9**).

Besides coeluting isomers, another type of interference that was observed was the case of two coeluting isobars, the 1,2,3,7,8-PeCDD and the HxCB 169 (**Figure S5.10**). Here, the M+6 isotopologue of the PeCDD (m/z 359.8485) interferes with the most intense isotopologue of the HxCB used for quantification (M+2, m/z 359.8410). The same isobaric interference is observed between the corresponding isotopically labelled standards (m/z 371.8885 vs m/z 371.8812). However, these interferences were completely resolved in the ion mobility dimension, the CCS of the hexachloro substituted PCB being significantly larger than that of the pentachloro substituted PCDD (Figure S5.10).

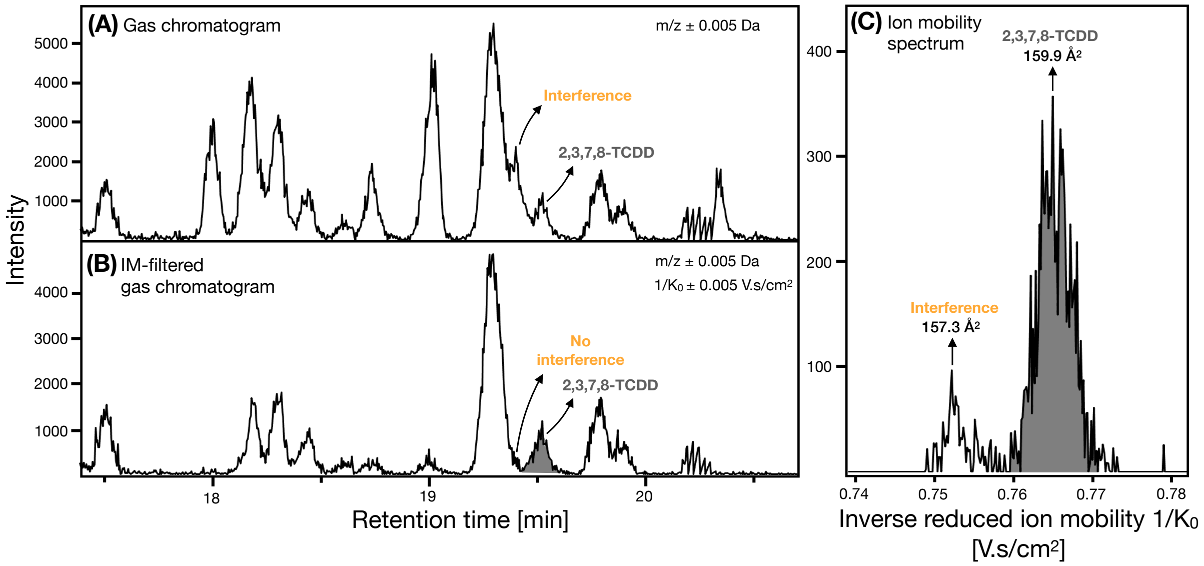

Figure 5.5: Unfiltered (A) and IM-filtered (B) gas chromatograms of 2,3,7,8-TCDD in the palm oil sample. (C) Corresponding ion mobility spectrum of 2,3,7,8-TCDD.

Finally, a last type of interference was noticed in the case of the MO-PCB 123 (**Figure 5.6**). This PeCB was partially coeluting with two other PCB congeners, a PeCB and an HxCB (Figure 5.6a). The difference in CCS between the two PeCBs was too small to obtain an appreciable separation, leaving the interfering PeCB appear as a small shoulder on the right of the ion mobility peak of PCB 123 (Figure 5.6b). Concerning the HxCB, this type of coelution is not, a priori, an issue, since in positive APCI, the soft ionization mechanism gives mostly rise to intense parent ions (～85% $[M]^{+\cdot}$ and ～15% $[M+H]^{+}$, Section 3.3.2A) that can be readily distinguished in the m/z dimension (i.e., m/z 325.8799 for PeCBs and m/z 359.8410 for HxCBs). However, the small extent of PCBs fragmentation into $[M+H-Cl]^{+\cdot}$ and $[M-Cl]^{+\cdot}$ fragment ions can turn out problematic in the event of a coelution between two PCB congeners that differ by one degree of chlorination, especially if the most chlorinated congener is much more present in the sample compared to the other. Indeed, in this situation these fragments become isomeric/isobaric interferences with regard to the less chlorinated PCB. This was typically the case here with the PeCB 123 and the coeluting HxCB congener which had a signal intensity more than an order of magnitude higher.

However, the additional ion mobility dimension can, at least partially, resolve this issue. Indeed, depending on the moment the fragmentation takes relative to the ion mobility separation, some separation can be achieved between the analyte and the interfering fragment ions (**Figure S5.11**, Section 3.2.2B). In the case of fragmentations taking place before or during the separation (e.g., in source, in transit to the IM cell, etc.), the fragment ions go through the TIMS cell, become trapped and elute at a later time compared to their precursor ions since they are characterized by lower CCS values (in TIMS, ions with the highest CCS elute first, Figure S5.11a). Moreover, since these fragments are isomeric/isobaric to the analyte ion, the probability that they share a similar CCS is high. Therefore in this case, IM separation of the analyte ion and the fragment ions is not likely. However, in the case of fragmentations occurring after the IM separation (in transit to the TOF MS), the ion mobility of the fragments match that of their precursor ions (Figure S5.11b). This time, the separation between the analyte ion and the isomeric/isobaric fragment ions is much more likely since two PCBs congeners differing by one chlorine atom are usually characterized by CCS that are sufficiently different to obtain a baseline separation at the resolving power of the TIMS (Section 3.2.2C).

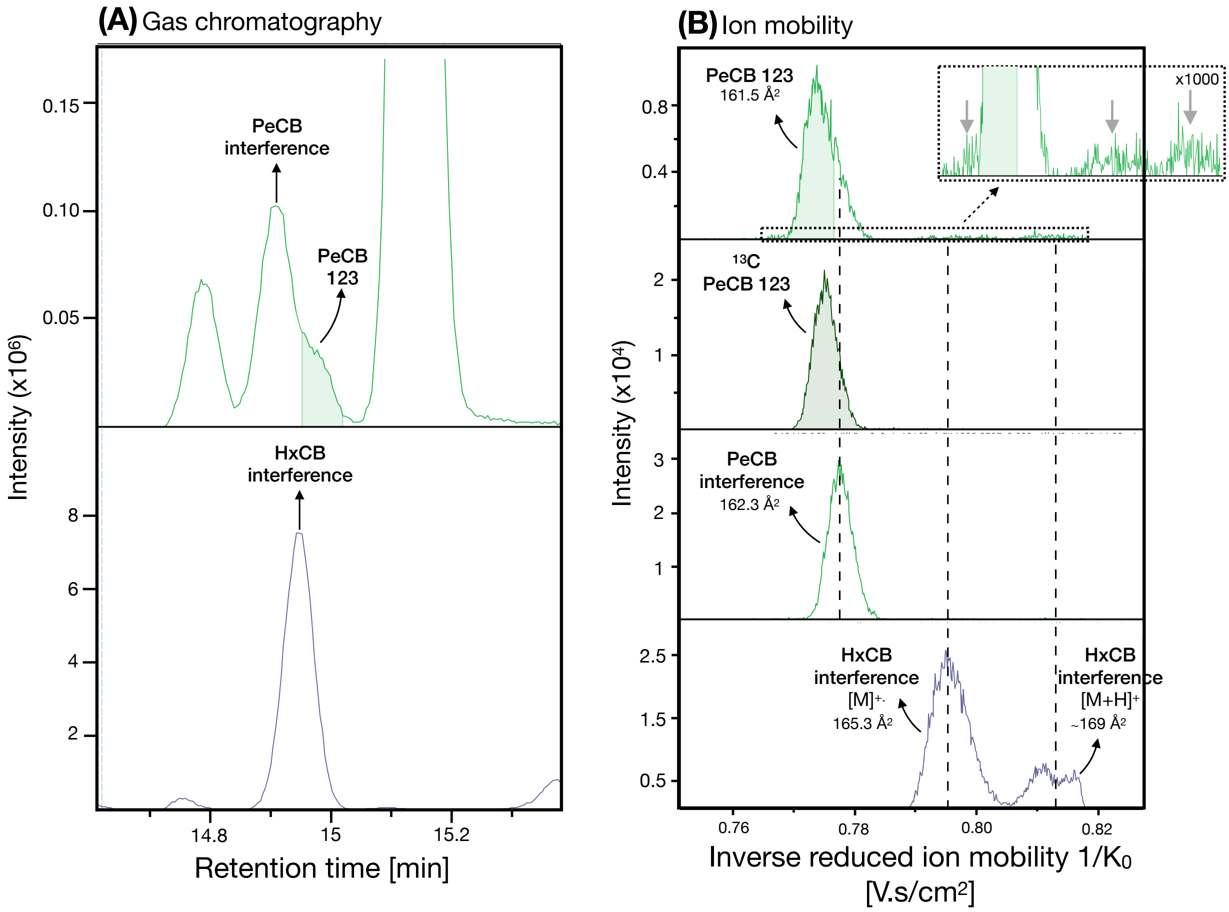

Figure 5.6: **(A)** Overlaid chromatograms of PeCBs and HxCBs close to the retention time of PeCB 123 (milk fat sample). **(B)** Overlaid ion mobility spectra of PeCB 123, its ^{13}C standard analog, the coeluting PeCB interference and the coeluting HxCB interference. For the HxCB intereference, the IM peaks from both types of precursor ions ($[M]^{+\cdot}$ and $[M+H]^+$) are shown in the spectrum since both can give rise to isomeric/isobaric fragments.

This is indeed what is observed in Figure 5.6b. In the mobility spectrum of the PeCB 123 $[M]^{+\cdot}$ ion, a series of peaks of small intensity can be seen on the right side of the major peak at higher CCS values (see inset in Figure 5.6b). These are the signal corresponding to the post-IM fragmentation of the coeluting HxCB interference. This is confirmed by the alignment of those signals with the ion mobility peaks of their precursor $[M]^{+\cdot}$ and $[M+H]^+$ ions (bottom ion mobility spectrum in Figure 5.6b). As for the series of low intensity peaks on the left side of the major peak (see inset), they could be attributed to signal originating from the pre/intra IM fragmentation of the coeluting HxCB. Some of this signal may not be visible due to overlap with that of the PeCB 123 $[M]^{+\cdot}$ ion.

Clearly, in this example, the impact of the HxCB isomeric fragment ions is negligible due to the low relative intensity of their signal. However, such types of interference could become significantly more pronounced in samples where the intensity difference between the interfering fragment and the target analyte is smaller, or in the case of compound classes that exhibit a higher degree of fragmentation under positive APCI conditions (e.g., PCDDs, Section 3.2.2B). In such scenarios, the additional selectivity offered by the ion mobility dimension could prove particularly beneficial, enabling the separation of the interfering fragment species and thus improving the accuracy and reliability of the quantification.

Overall, these results indicate that the separation of (partially) coeluting POPs isomers is generally not achieved in the ion mobility (IM) dimension, even at very high resolving power (R_p ~200). This observation is consistent with findings from another study[29], as well as with results obtained during the analysis of the POPs mixture in the optimization of the SWIM method presented in the previous chapter (Section 4.2.2C). In the latter case, all (partially) coeluting isobaric standard species were baseline-separated in the IM dimension, even at the lower resolving power provided by the standard TIMS method (R_p ~100, **Figure S5.12**). This reflects the fact that, despite having nearly identical mass, these POP isobars exhibit significantly different three-dimensional structures due to variations in the central aromatic core and the number and type of halogen atoms. In contrast, most of the (partially) coeluting isomeric pairs produced a single, convoluted peak in the ion mobility spectra (**Figure S5.13**), even when analyzed individually using a very slow scan rate (**Figure S5.14**), suggesting minimal, if any, differences in CCS. Consequently, while ion mobility appears as a powerful tool for separating coeluting isobars, often even at moderate resolving powers around 100, its ability to discriminate coeluting isomers is limited by their structural and conformational similarity, which leads to nearly identical CCS values.

5.3 - Conclusion

In this chapter, the potential of a modern IM-MS platform, namely a TIMS-TOF instrument, to perform quantitative analysis of trace and ultra-trace contaminants was assessed. The performance evaluation conducted demonstrated that the GC-APCI-TIMS-TOF method we developed broadly met the requirements of EU Regulation 2017/644 in terms of linearity, LOQs, precision, trueness, and measurement uncertainty for PCDD/Fs and PCBs in three different fat and oil samples. Although a non-negligible fraction of individual PCDD/F congeners present at very low levels (around ppt and below) showed accuracies falling outside the tolerated range, this had only a limited impact on the overall method performance: all regulatory criteria were fulfilled for the summed TEQ concentrations, which are the key metrics for regulatory compliance. Compared to the reference GC-sector HRMS method, performances were similar or slightly lower for PCBs, and slightly to significantly lower for most PCDD/Fs. However, the added ion mobility separation dimension of the GC-APCI-TIMS-TOF method brought significant advantages in terms of analyte identification (with CCS values serving as an additional identification point in targeted analysis) and peak capacity (enabling separation of some partially coeluting isomers, isobars, and isomeric fragment ions). This improved selectivity for dioxins and PCBs could potentially allow for simplified sample preparation procedures, resulting in reduced preparation times and costs. Overall, this study highlights the promising potential of the TIMS-TOF platform and IM-MS technologies more generally for the quantitative analysis of a broad range of contaminants in complex matrices.

5.4 - References

(1) Song, X.-C.; Canellas, E.; Dreolin, N.; Goshawk, J.; Lv, M.; Qu, G.; Nerin, C.; Jiang, G. Application of Ion Mobility Spectrometry and the Derived Collision Cross Section in the Analysis of Environmental Organic Micropollutants. *Environ. Sci. Technol.* **2023**, *57* (51), 21485–21502. https://doi.org/10.1021/acs.est.3c03686.

(2) Celma, A.; Alygizakis, N.; Belova, L.; Bijlsma, L.; Fabregat-Safont, D.; Menger, F.; Gil-Solsona, R. Ion Mobility Separation Coupled to High-Resolution Mass Spectrometry in Environmental Analysis – Current State and Future Potential. *Trends Environ. Anal. Chem.* **2024**, *43*, e00239. https://doi.org/10.1016/j.teac.2024.e00239.

(3) Barnett, D. A.; Guevremont, R.; Purves, R. W. Determination of Parts-per-Trillion Levels of Chlorate, Bromate, and Iodate by Electrospray Ionization/High-Field Asymmetric Waveform Ion Mobility Spectrometry/Mass Spectrometry. *Appl. Spectrosc.* **1999**, *53* (11), 1367–1374. https://doi.org/10.1366/0003702991945984.

(4) Ells, B.; Barnett, D. A.; Purves, R. W.; Guevremont, R. Trace Level Determination of Perchlorate in Water Matrices and Human Urine Using ESI-FAIMS-MS. *J. Environ. Monit.* **2000**, *2* (5), 393–397. https://doi.org/10.1039/b005601o.

(5) Handy, R.; Barnett, D. A.; Purves, R. W.; Horlick, G.; Guevremont, R. Determination of Nanomolar Levels of Perchlorate in Water by ESI-FAIMS-MS. *J. Anal. At. Spectrom.* **2000**, *15* (8), 907–911. https://doi.org/10.1039/b002306j.

(6) Gonzalez De Vega, R.; Cameron, A.; Clases, D.; Dodgen, T. M.; Doble, P. A.; Bishop, D. P. "Simultaneous Targeted and Non-Targeted Analysis of per- and Polyfluoroalkyl Substances in Environmental Samples by Liquid Chromatography-Ion Mobility-Quadrupole Time of Flight-Mass Spectrometry and Mass Defect Analysis." *J. Chromatogr. A* **2021**, *1653*, 462423. https://doi.org/10.1016/j.chroma.2021.462423.

(7) Hinnenkamp, V.; Balsaa, P.; Schmidt, T. C. Quantitative Screening and Prioritization Based on UPLC-IM-Q-TOF-MS as an Alternative Water Sample Monitoring Strategy. *Anal. Bioanal. Chem.* **2019**, *411* (23), 6101–6110. https://doi.org/10.1007/s00216-019-01994-w.

(8) Adams, K. J.; Smith, N. F.; Ramirez, C. E.; Fernandez-Lima, F. Discovery and Targeted Monitoring of Polychlorinated Biphenyl Metabolites in Blood Plasma Using LC-TIMS-TOF MS. *Int. J. Mass Spectrom.* **2018**, *427*, 133–140. https://doi.org/10.1016/j.ijms.2017.11.009.

(9) Yan, M.; Zhang, N.; Li, X.; Xu, J.; Lei, H.; Ma, Q. Integrating Post-Ionization Separation via Differential Mobility Spectrometry into Direct Analysis in Real Time Mass Spectrometry for Toy Safety Screening. *Anal. Chem.* **2024**, *96* (1), 265–271. https://doi.org/10.1021/acs.analchem.3c03915.

(10) Shi, Y.; Jin, H.-F.; Shi, M.-Z.; Cao, J.; Ye, L.-H. Carbon Black-Assisted Miniaturized Solid-Phase Extraction of Carbamate Residues from Ginger by Supercritical Fluid Chromatography Combined with Ion Mobility Quadrupole Time-of-Flight Mass Spectrometry. *Microchem. J.* **2023**, *194*, 109335. https://doi.org/10.1016/j.microc.2023.109335.

(11) Ray, J. A.; Kushnir, M. M.; Yost, R. A.; Rockwood, A. L.; Wayne Meikle, A. Performance Enhancement in the Measurement of 5 Endogenous Steroids by LC–MS/MS Combined with Differential Ion Mobility Spectrometry. *Clin. Chim. Acta* **2015**, *438*, 330–336. https://doi.org/10.1016/j.cca.2014.07.036.

(12) Moehnke, K.; Kemp, J.; Campbell, M. R.; Singh, R. J.; Tebo, A. E.; Maus, A. Using Differential Mobility Spectrometry to Improve the Specificity of Targeted Measurements of 2,3-Dinor 11β-Prostaglandin F2α. *Clin. Biochem.* **2024**, *126*, 110745. https://doi.org/10.1016/j.clinbiochem.2024.110745.

(13) Lerner, R.; Baker, D.; Schwitter, C.; Neuhaus, S.; Hauptmann, T.; Post, J. M.; Kramer, S.; Bindila, L. Four-Dimensional Trapped Ion Mobility Spectrometry Lipidomics for High Throughput Clinical Profiling of Human Blood Samples. *Nat. Commun.* **2023**, *14* (1), 937. https://doi.org/10.1038/s41467-023-36520-1.

(14) Fan, R.-J.; Zhang, F.; Chen, X.-P.; Qi, W.-S.; Guan, Q.; Sun, T.-Q.; Guo, Y.-L. High-Throughput Screening and Quantitation of Guanidino and Ureido Compounds Using Liquid Chromatography-Drift Tube Ion Mobility Spectrometry-Mass Spectrometry. *Anal. Chim. Acta* **2017**, *961*, 82–90. https://doi.org/10.1016/j.aca.2017.01.036.

(15) Chai, Y.; Grebe, S. K. G.; Maus, A. Improving LC-MS/MS Measurements of Steroids with Differential Mobility Spectrometry. *J. Mass Spectrom. Adv. Clin. Lab* **2023**, *30*, 30–37. https://doi.org/10.1016/j.jmsacl.2023.10.001.

(16) Oranzi, N. R.; Lei, J.; Kemperman, R. H. J.; Chouinard, C. D.; Holmquist, B.; Garrett, T. J.; Yost, R. A. Rapid Quantitation of 25-Hydroxyvitamin D2 and D3 in Human Serum Using Liquid Chromatography/Drift Tube Ion Mobility-Mass Spectrometry. *Anal. Chem.* **2019**, *91* (21), 13555–13561. https://doi.org/10.1021/acs.analchem.9b02683.

(17) Muller, H. B.; Scholl, G.; Far, J.; De Pauw, E.; Eppe, G. Sliding Windows in Ion Mobility (SWIM): A New Approach to Increase the Resolving Power in Trapped Ion Mobility-Mass Spectrometry Hyphenated with Chromatography. *Anal. Chem.* **2023**, *95* (48), 17586–17594. https://doi.org/10.1021/acs.analchem.3c03039.

(18) Dodds, J. N.; May, J. C.; McLean, J. A. Correlating Resolving Power, Resolution, and Collision Cross Section: Unifying Cross-Platform Assessment of Separation Efficiency in Ion Mobility Spectrometry. *Anal. Chem.* **2017**, *89* (22), 12176–12184. https://doi.org/10.1021/acs.analchem.7b02827.

(19) COMMISSION REGULATION (EU) 2017/ 644 - of 5 April 2017 - Laying down Methods of Sampling and Analysis for the Control of Levels of Dioxins, Dioxin-like PCBs and Non-Dioxin-like PCBs in Certain Foodstuffs and Repealing Regulation (EU) No 589 / 2014. *J Eur Union L* **2017**, *92*, 9–34.

(20) L'Homme, B.; Scholl, G.; Eppe, G.; Focant, J.-F. Validation of a Gas Chromatography–Triple Quadrupole Mass Spectrometry Method for Confirmatory Analysis of Dioxins and Dioxin-like Polychlorobiphenyls in Feed Following New EU Regulation 709/2014. *J. Chromatogr. A* **2015**, *1376*, 149–158. https://doi.org/10.1016/j.chroma.2014.12.013.

(21) Working Group for Measurement Uncertainty in PCDD/F and PCB Analysis. Guidance Document on Measurement Uncertainty for Laboratories Performing PCDD/F and PCB Analysis Using Isotope Dilution Mass Spectrometry. **2017**.

(22) COMMISSION REGULATION (EU) 2023/915 of 25 April 2023 on Maximum Levels for Certain Contaminants in Food and Repealing Regulation (EC) No 1881/2006. *J Eur Union L* **2023**, *119*, 103–157.

(23) Goscinny, S.; Joly, L.; De Pauw, E.; Hanot, V.; Eppe, G. Travelling-Wave Ion Mobility Time-of-Flight Mass Spectrometry as an Alternative Strategy for Screening of Multi-Class Pesticides in Fruits and Vegetables. *J. Chromatogr. A* **2015**, *1405*, 85–93. https://doi.org/10.1016/j.chroma.2015.05.057.

(24) Regueiro, J.; Negreira, N.; Berntssen, M. H. G. Ion-Mobility-Derived Collision Cross Section as an Additional Identification Point for Multiresidue Screening of Pesticides in Fish Feed. *Anal. Chem.* **2016**, *88* (22), 11169–11177. https://doi.org/10.1021/acs.analchem.6b03381.

(25) Hinnenkamp, V.; Klein, J.; Meckelmann, S. W.; Balsaa, P.; Schmidt, T. C.; Schmitz, O. J. Comparison of CCS Values Determined by Traveling Wave Ion Mobility Mass Spectrometry and Drift Tube Ion Mobility Mass Spectrometry. *Anal. Chem.* **2018**, *90* (20), 12042–12050. https://doi.org/10.1021/acs.analchem.8b02711.

(26) Belova, L.; Celma, A.; Van Haesendonck, G.; Lemière, F.; Sancho, J. V.; Covaci, A.; Van Nuijs, A. L. N.; Bijlsma, L. Revealing the Differences in Collision Cross Section Values of Small Organic Molecules Acquired by Different Instrumental Designs and Prediction Models. *Anal. Chim. Acta* **2022**, *1229*, 340361. https://doi.org/10.1016/j.aca.2022.340361.

(27) Belova, L.; Caballero-Casero, N.; Ballesteros, A.; Poma, G.; Van Nuijs, A. L. N.; Covaci, A. Trapped and Drift-tube Ion-mobility Spectrometry for the Analysis of Environmental Contaminants:

Comparability of Collision Cross-section Values and Resolving Power. *Rapid Commun. Mass Spectrom.* **2024**, *38* (21), e9901. https://doi.org/10.1002/rcm.9901.

(28) Celma, A.; Sancho, J. V.; Schymanski, E. L.; Fabregat-Safont, D.; Ibáñez, M.; Goshawk, J.; Barknowitz, G.; Hernández, F.; Bijlsma, L. Improving Target and Suspect Screening High-Resolution Mass Spectrometry Workflows in Environmental Analysis by Ion Mobility Separation. *Environ. Sci. Technol.* **2020**, *54* (23), 15120–15131. https://doi.org/10.1021/acs.est.0c05713.

(29) Celma, A.; Ahrens, L.; Gago-Ferrero, P.; Hernández, F.; López, F.; Lundqvist, J.; Pitarch, E.; Sancho, J. V.; Wiberg, K.; Bijlsma, L. The Relevant Role of Ion Mobility Separation in LC-HRMS Based Screening Strategies for Contaminants of Emerging Concern in the Aquatic Environment. *Chemosphere* **2021**, *280*, 130799. https://doi.org/10.1016/j.chemosphere.2021.130799.

(30) Gabelica, V.; Marklund, E. Fundamentals of Ion Mobility Spectrometry. *Curr. Opin. Chem. Biol.* **2018**, *42*, 51–59. https://doi.org/10.1016/j.cbpa.2017.10.022.

(31) Silveira, J. A.; Ridgeway, M. E.; Laukien, F. H.; Mann, M.; Park, M. A. Parallel Accumulation for 100% Duty Cycle Trapped Ion Mobility-Mass Spectrometry. *Int. J. Mass Spectrom.* **2017**, *413*, 168–175. https://doi.org/10.1016/j.ijms.2016.03.004.

(32) Ayala-Cabrera, J. F.; Santos, F. J.; Moyano, E. Recent Advances in Analytical Methodologies Based on Mass Spectrometry for the Environmental Analysis of Halogenated Organic Contaminants. *Trends Environ. Anal. Chem.* **2021**, *30*, e00122. https://doi.org/10.1016/j.teac.2021.e00122.

(33) Dodds, J. N.; May, J. C.; McLean, J. A. Investigation of the Complete Suite of the Leucine and Isoleucine Isomers: Toward Prediction of Ion Mobility Separation Capabilities. *Anal. Chem.* **2017**, *89* (1), 952–959. https://doi.org/10.1021/acs.analchem.6b04171.

(34) Zheng, X.; Dupuis, K. T.; Aly, N. A.; Zhou, Y.; Smith, F. B.; Tang, K.; Smith, R. D.; Baker, E. S. Utilizing Ion Mobility Spectrometry and Mass Spectrometry for the Analysis of Polycyclic Aromatic Hydrocarbons, Polychlorinated Biphenyls, Polybrominated Diphenyl Ethers and Their Metabolites. *Anal. Chim. Acta* **2018**, *1037*, 265–273. https://doi.org/10.1016/j.aca.2018.02.054.

(35) Wu, Q.; Wang, J.-Y.; Han, D.-Q.; Yao, Z.-P. Recent Advances in Differentiation of Isomers by Ion Mobility Mass Spectrometry. *TrAC Trends Anal. Chem.* **2020**, *124*, 115801. https://doi.org/10.1016/j.trac.2019.115801.

(36) Dodds, J. N.; Hopkins, Z. R.; Knappe, D. R. U.; Baker, E. S. Rapid Characterization of Per- and Polyfluoroalkyl Substances (PFAS) by Ion Mobility Spectrometry–Mass Spectrometry (IMS-MS). *Anal. Chem.* **2020**, *92* (6), 4427–4435. https://doi.org/10.1021/acs.analchem.9b05364.

(37) Causon, T. J.; Hann, S. Theoretical Evaluation of Peak Capacity Improvements by Use of Liquid Chromatography Combined with Drift Tube Ion Mobility-Mass Spectrometry. *J. Chromatogr. A* **2015**, *1416*, 47–56. https://doi.org/10.1016/j.chroma.2015.09.009.

5.5 - Supporting information

TABLES

Tables S5.1: Concentrations (in pg/μL) of the calibration solutions.

PCDDs	Calibration level					
	1	2	3	4	5	6
2,3,7,8-TCDD	0.05	0.1	0.5	1	5	10
1,2,3,7,8-PeCDD	0.05	0.1	0.5	1	5	10
1,2,3,4,7,8-HxCDD	0.1	0.2	1	2	10	20
1,2,3,6,7,8-HxCDD	0.1	0.2	1	2	10	20
1,2,3,7,8,9-HxCDD	0.1	0.2	1	2	10	20
1,2,3,4,6,7,8-HpCDD	0.1	0.2	1	2	10	20
OCDD	0.25	0.5	2.5	5	25	50

PCDFs	Calibration level					
	1	2	3	4	5	6
2,3,7,8-TCDF	0.05	0.1	0.5	1	5	10
1,2,3,7,8-PeCDF	0.05	0.1	0.5	1	5	10
2,3,4,7,8-PeCDF	0.05	0.1	0.5	1	5	10
1,2,3,4,7,8-HxCDF	0.1	0.2	1	2	10	20
1,2,3,6,7,8-HxCDF	0.1	0.2	1	2	10	20
1,2,3,7,8,9-HxCDF	0.1	0.2	1	2	10	20
2,3,4,6,7,8-HxCDF	0.1	0.2	1	2	10	20
1,2,3,4,6,7,8-HpCDF	0.1	0.2	1	2	10	20
1,2,3,4,7,8,9-HpCDF	0.1	0.2	1	2	10	20
OCDF	0.25	0.5	2.5	5	25	50

NO PCBs	Calibration level					
	1	2	3	4	5	6
TCB 77	0.5	1	2	5	10	20
TCB 81	0.5	1	2	5	10	20
PeCB 126	0.5	1	2	5	10	20
HxCB 169	0.5	1	2	5	10	20

MO PCBs	Calibration level							
	1	2	3	4	5	6	7	8
PeCB 105	0.04	0.1	4	10	20	40	80	140
PeCB 114	0.04	0.1	4	10	20	40	80	140
PeCB 118	0.04	0.1	4	10	20	40	80	140
PeCB 123	0.04	0.1	4	10	20	40	80	140
HxCB 156	0.04	0.1	4	10	20	40	80	140
HxCB 157	0.04	0.1	4	10	20	40	80	140
HxCB 167	0.04	0.1	4	10	20	40	80	140
HpCB 189	0.04	0.1	4	10	20	40	80	140

NDL PCBs	Calibration level								
	1	2	3	4	5	6	7	8	9

TriCB 28	0.04	0.1	4	10	20	40	80	140	500
TCB 52	0.04	0.1	4	10	20	40	80	140	500
PeCB 101	0.04	0.1	4	10	20	40	80	140	500
HxCB 138	0.04	0.1	4	10	20	40	80	140	500
HxCB 153	0.04	0.1	4	10	20	40	80	140	500
HpCB 180	0.04	0.1	4	10	20	40	80	140	500

Table S5.2: Additional GC parameters (TIMS-TOF instrument).

	Fraction	
	1 MO & NDL PCBs	2 PCDD/Fs & NO PCBs
Gas flow	0.8 mL/min	1 mL/min
Temperature program	• 140°C, held 1 min • 220°C @ 15°C/min, held 7.5 min • 250°C @ 8°C/min • 262°C @ 2°C/min • 310°C @ 15°C/min, held 4.2 min ⇒ Total: 30 min	• 80°C, held 3 min • 200°C @ 70°C/min • 250°C @ 2°C/min, held 7 min • 310°C @ 15°C/min, held 4.3 min ⇒ Total: 45 min

Table S5.3: GC-APCI source parameters.

Transfer line temperature	300°C
Source temperature	300°C
End plate offset	-500 V
Capillary	-4500 V
Corona	+1000 nA
Nebulizer	2.4 Bar
Dry gas	1.5 L/min
Dry temperature	175°C

Table S5.4: TIMS parameters.

		Fraction	
		1 MO & NDL PCBs	2 PCDD/Fs & NO PCBs
Accumulation time (duty cycle %)		75 ms ($30\%_{dc}$)	250 ms ($100\%_{dc}$)
Ramp time (spectra rate)		250 ms (3.9 Hz)	
Accumulation range		Same as analysis range	
Analysis range		Variable (SWIM mode cfr. Figure S2) $\Delta 1/K_0 = 0.07$	Variable (SWIM mode cfr. Figure S2) $\Delta 1/K_0 = 0.06$
Tunnel pressure	Entrance(P1)	3.04 mBar	
	Exit (P2)	0.84 mBar	

	ΔP	2.20 mBar
IM cell temperature		Not available
RF voltage		250 V_{pp}
Transfer voltages	D1	-20 V
	D2	-120 V
	D3	50 V
	D4	20 V
	D5	0 V
	D6	100 V

Table S5.5: qTOF parameters. Three sets of parameters were used at different times during the analysis to optimize the transmission of both lower and higher m/z ions (F1 = PCBs fraction; F2 = dioxins fraction).

	Set 1 F1: Start - 14.6 min F2: Start - 17.0 min	Set 2 F1: 14.6 - 26.6 min F2: 17.0 - 40.4 min	Set 3 F1: 26.6 min - End F2: 40.4 min - End
Funnel 2 RF	200 V_{pp}	250 V_{pp}	300 V_{pp}
Multipole RF	200 V_{pp}	250 V_{pp}	300 V_{pp}
Collision RF	800 V_{pp}	1000 V_{pp}	1200 V_{pp}
Quadrupole energy	8 eV	9 eV	10 eV
Collision cell energy	8 eV	9 eV	10 eV
Collision cell in	190 V	190 V	190 V
Transfert time	55 µs	60 µs	70 µs
Prepulse storage	7 µs	9 µs	11 µs

Table S5.6 – Comparison of calculated mLOQ values using the two approaches: blank-level contamination and instrument LOQ.

Analyte	mLOQ (pg/g) 2g of sample		mLOQ (pg/g) 4g of sample	
	iLOQ	Blank level	iLOQ	Blank level
TCB 81	0.5	2.7	0.25	1.35
TCB 77	0.5	13.1	0.25	6.5
PeCB 126	0.5	0.4	0.25	0.2
PeCB 123	4	5.7	2	2.85
PeCB 118	4	144	2	72
PeCB 114	4	4.8	2	2.4
PeCB 105	4	53.5	2	26.75
HxCB 167	4	1.8	2	0.9
HxCB 156	4	4.0	2	2.0
HxCB 157	4	2.0	2	1.0
HpCB 189	4	0.7	2	0.35

TriCB 28	4	1299	2	649.5
TCB 52	4	2379	2	1189.5
PeCB 101	4	636	2	318
HxCB 153	4	121	2	60.5
HxCB 138	4	68	2	34
HpCB 180	4	15	2	7.5

Table S5.7: Mean RSD$_R$ and bias measured for the dioxins and PCBs in the different matrices with the two instrumentations.

		Mean RSD$_R$ (% RSD$_R$ <15%) [20% for NDL PCBs]		Mean absolute bias (% $\vert$bias$\vert$ $\leq$ 20%) [30% for NDL PCBs]	
		TIMS TOF	Sector	TIMS TOF	Sector
PCDD/Fs + NO PCBs	Fish oil	7.0% (100%)	7.3% (100%)	10.5% (88%)	7.9% (100%)
	Palm oil	8.8% (100%)	7.6% (100%)	14.3% (77%)	9.3% (99%)
	Milk fat	10.4% (90%)	3.7% (100%)	13.8% (77%)	5.7% (100%)
	Total	**8.9% (96%)**	**6.1% (100%)**	**13.1% (80%)**	**7.3% (99%)**
MO PCBs	Fish oil	3.9% (88%)	6.3% (100%)	7.8% (98%)	7.2% (100%)
	Palm oil	6.6% (100%)	6.3% (100%)	12.1% (71%)	9.4% (97%)
	Milk fat	3.9% (100%)	3.7% (100%)	7.7% (87%)	5.6% (90%)
	Total	**4.8% (96%)**	**5.4% (100%)**	**8.9% (87%)**	**7.1% (95%)**
NDL PCBs	Fish oil	3.2% (100%)	9.4% (100%)	7.4% (100%)	9.0% (100%)
	Palm oil	4.3% (100%)	7.5% (100%)	7.5% (92%)	13.6% (79%)
	Milk fat	7.5% (100%)	7.5% (100%)	13.0% (89%)	9.4% (100%)
	Total	**5.0% (100%)**	**8.1% (100%)**	**9.8% (93%)**	**10.3% (95%)**

Tables S5.8: Total WHO$_{2005}$ TEQ concentrations of dioxins (PCDDs + PCDFs) and dioxin like PCBs (NO + MO PCBs) and summed concentrations of NDL PCBs measured by GC-EI-sector and GC-APCI-TIMS-TOF in the different matrices. RSD$_R$ and relative bias values that comply with the criteria from the European Regulation 2017/644 are highlighted in green.

Fish oil	Certified TEQ concentration PT [pg WHO$_{2005}$ TEQ/g$_{fat}$]	Mean concentration [pg WHO$_{2005}$ TEQ/g$_{fat}$] (Relative bias %)		RSD$_R$ (%)		Compliance regarding maximum level (EU 2023/915)		
		TIMS	Sector	TIMS	Sector	PT	TIMS	Sector
∑ PCDD/Fs	1.62	1.48 (-8.7)	1.54 (-4.8)	5.0	5.5	Compliant	Compliant	Compliant
∑ DL PCBs	8.57	7.37 (-13.9)	8.49 (-0.39)	1.3	6.4			

∑ PCDD/Fs + DL PCBs	10.19	8.85 (-13.1)	10.03 (-1.5)	0.2	5.9	Non compliant	Non compliant	Non compliant
	Certified concentration PT [ng /g$_{fat}$]	Mean concentration [ng /g$_{fat}$] (Relative bias %)		RSD$_R$ (%)				
		TIMS	Sector	TIMS	Sector			
∑ NDL PCBs	100.98	93.79 (-7.1)	100.43 (-0.5)	3.2	9.9	Compliant	Compliant	Compliant

Palm oil	Certified TEQ concentration PT [pg WHO$_{2005}$ TEQ/g$_{fat}$]	Mean concentration [pg WHO$_{2005}$ TEQ/g$_{fat}$] (Relative bias %)		RSD$_R$ (%)		Compliance regarding maximum level (EU 2023/915)		
		TIMS	Sector	TIMS	Sector	PT	TIMS	Sector
∑ PCDD/Fs	0.77	0.86 (+11.4)	0.74 (-4.7)	5.8	3.2	Compliant	Compliant	Compliant
∑ DL PCBs	0.36	0.38 (+6.2)	0.39 (+8.6)	2.2	6.4			
∑ PCDD/Fs + DL PCBs	1.13	1.24 (+9.8)	1.13 (-0.5)	5.1	2.4	Compliant	Compliant	Compliant
	Certified concentration PT [ng /g$_{fat}$]	Mean concentration [ng /g$_{fat}$] (Relative bias %)		RSD$_R$ (%)				
		TIMS	Sector	TIMS	Sector			
∑ NDL PCBs	2.53	2.63 (+3.7)	2.86 (+12.9)	3.2	4.5	Compliant	Compliant	Compliant

Milk fat	Certified TEQ concentration PT [pg WHO$_{2005}$ TEQ/g$_{fat}$]	Mean concentration [pg WHO$_{2005}$ TEQ/g$_{fat}$] (Relative bias %)		RSD$_R$ (%)		Compliance regarding maximum level (EU 2023/915)		
		TIMS	Sector	TIMS	Sector	PT	TIMS	Sector
∑ PCDD/Fs	2.83	2.68 (-5.2)	2.73 (-3.5)	3.8	1.3	Non compliant	Non compliant	Non compliant
∑ DL PCBs	2.27	2.10 (-7.1)	2.29 (+1.3)	3.7	3.6			
∑ PCDD/Fs + DL PCBs	5.10	4.79 (-6.1)	5.03 (-1.4)	2.7	1.9	Non compliant	Compliant	Non compliant
	Certified concentration PT [ng /g$_{fat}$]	Mean concentration [ng /g$_{fat}$] (Relative bias %)		RSD$_R$ (%)				
		TIMS	Sector	TIMS	Sector			
∑ NDL PCBs	56.88	50.13 (-11.9)	55.11 (-3.1)	6.1	9.5	Non compliant	Compliant	Non compliant

FIGURES

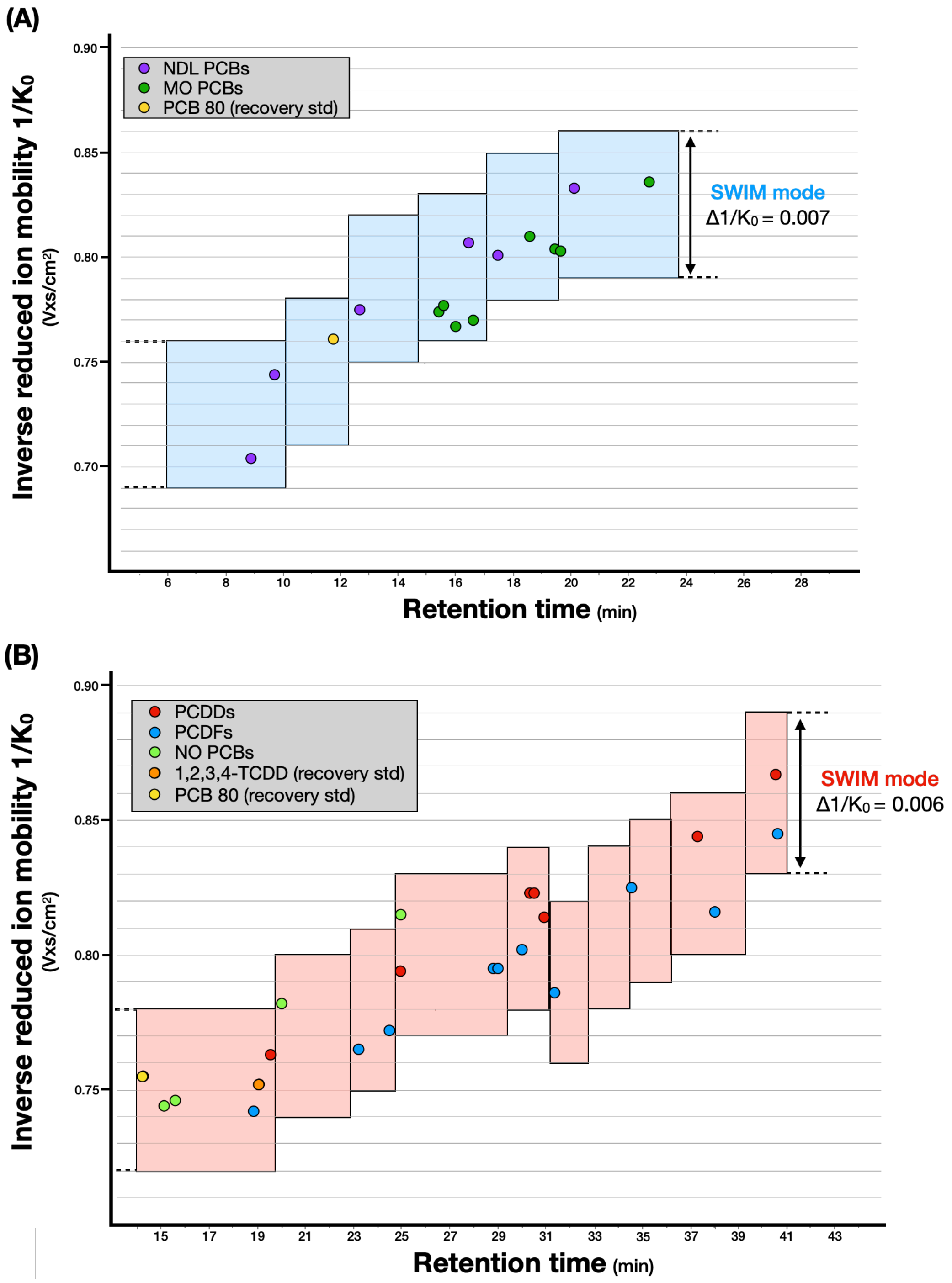

Figure S5.1: SWIM method applied to **(A)** the PCBs fraction and **(B)** the dioxins fraction. The ion mobility range of analysis (represented by the rectangles) is changed during the course of the chromatographic separation to adapt to the CCS of the analytes (represented by the coloured dots) that elute during a given retention time window. This avoids the use of a wider (and therefore less resolvable) ion mobility range that would have been necessary if that range had been constant over time (in order to include all the analytes).

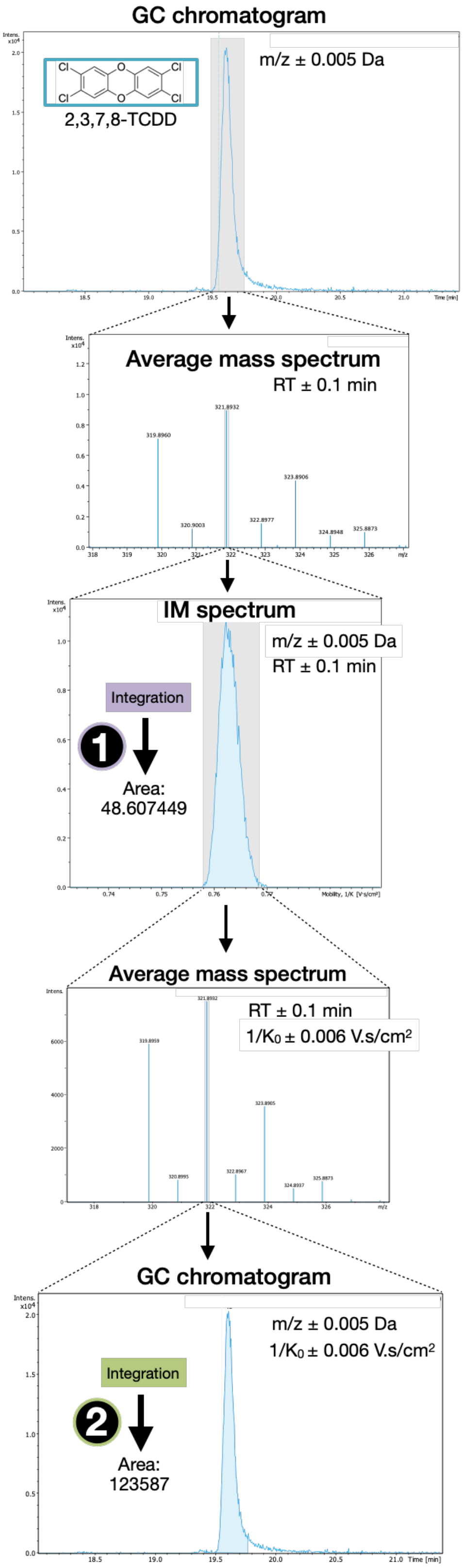

Figure S5.2: Illustration of the two signal integration procedures that were tested in this study. First, an average mass spectrum was generated over the elution time of the analyte of interest. Then, the ion mobility spectrum of the most intense isotopologue of the isotopic pattern was generated and integrated and the resulting area was used in the quantification process (procedure #1). For the second procedure, an average mass spectrum was generated over the elution time and the ion mobility range of the analyte of interest. A mobility filtered extracted ion chromatogram was then generated based on this mass spectra. The resulting chromatographic peak was integrated and used in the quantification process (procedure #2).

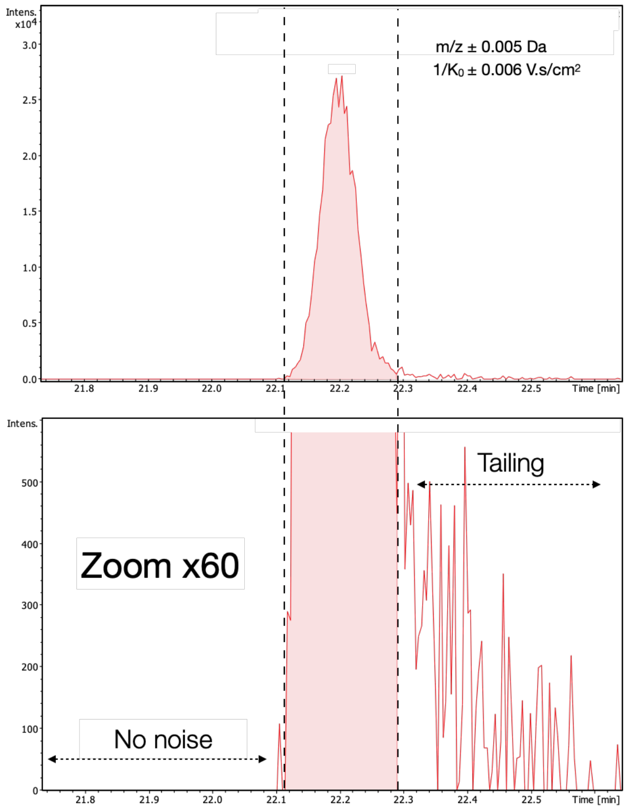

Figure S5.3: IM-filtered chromatogram of HpCB 189 (4 pg injected) with (lower spectrum) and without (upper spectrum) zoom.

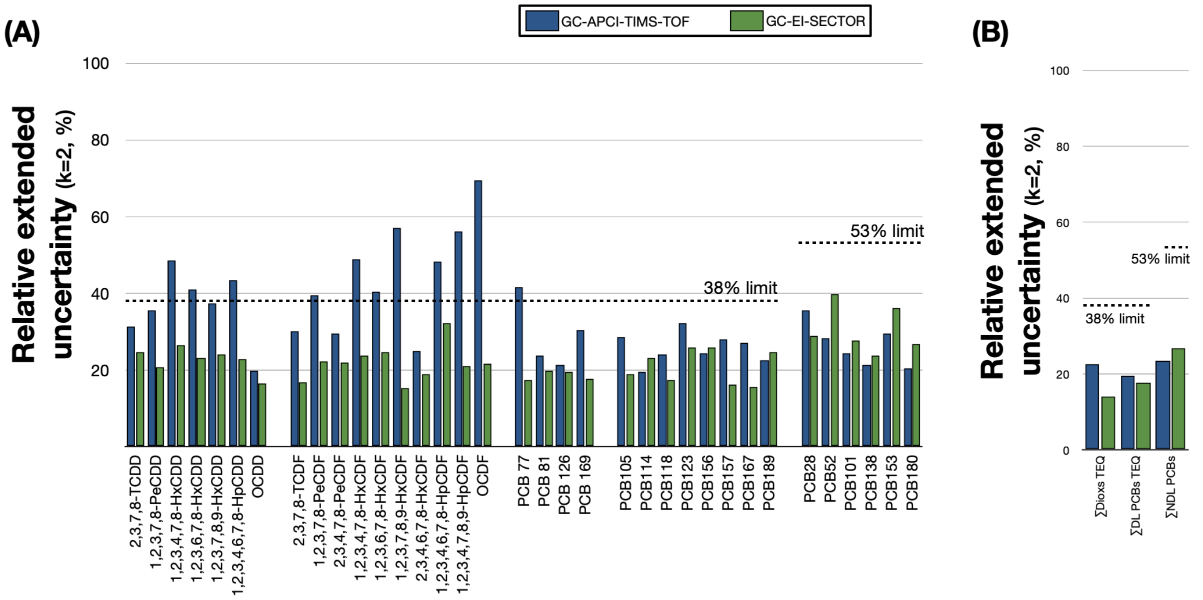

Figure S5.4: Expanded measurement uncertainty U calculated for the different dioxins and PCBs congeners **(A)** and the sum TEQ concentrations **(B)** with the TIMS (blue) and sector (green) systems.

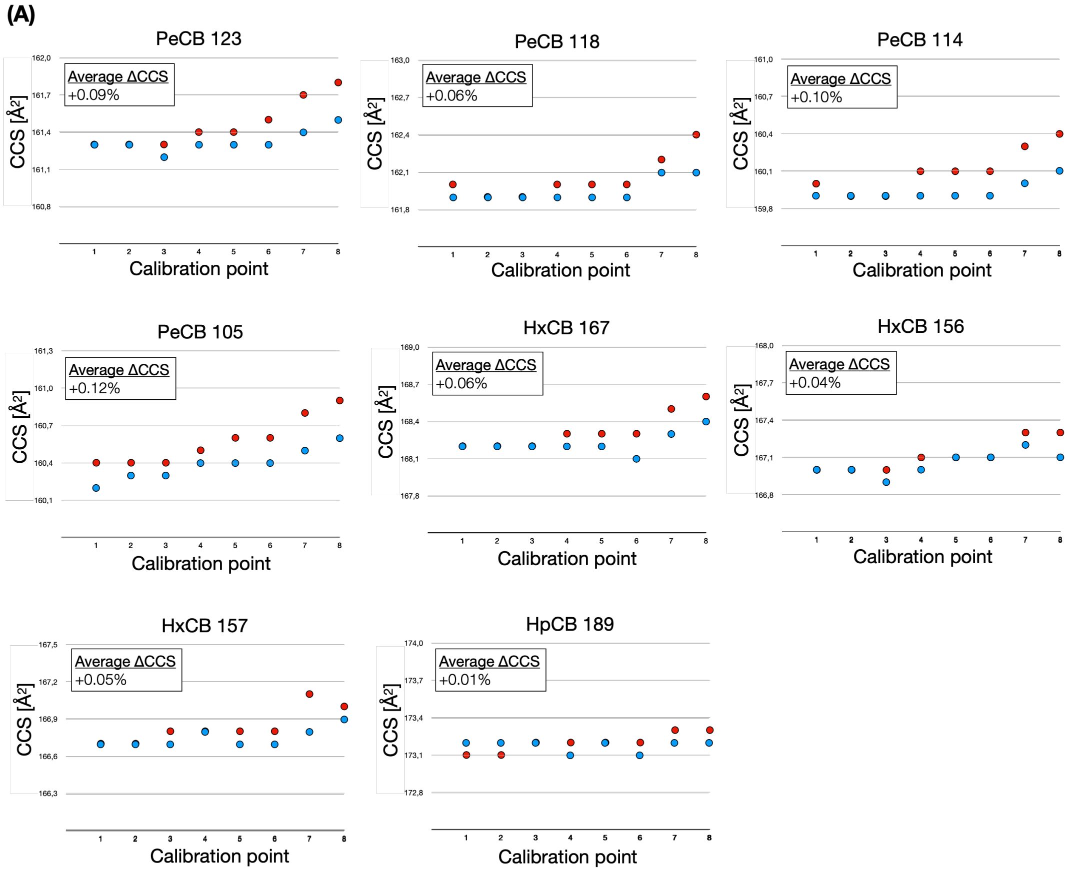
(A)
PeCB 123
Average ΔCCS
+0.09%
PeCB 118
Average ΔCCS
+0.06%
PeCB 114
Average ΔCCS
+0.10%
PeCB 105
Average ΔCCS
+0.12%
HxCB 167
Average ΔCCS
+0.06%
HxCB 156
Average ΔCCS
+0.04%
HxCB 157
Average ΔCCS
+0.05%
HpCB 189
Average ΔCCS
+0.01%
CCS [Å2]
Calibration point
1 2 3 4 5 6 7 8

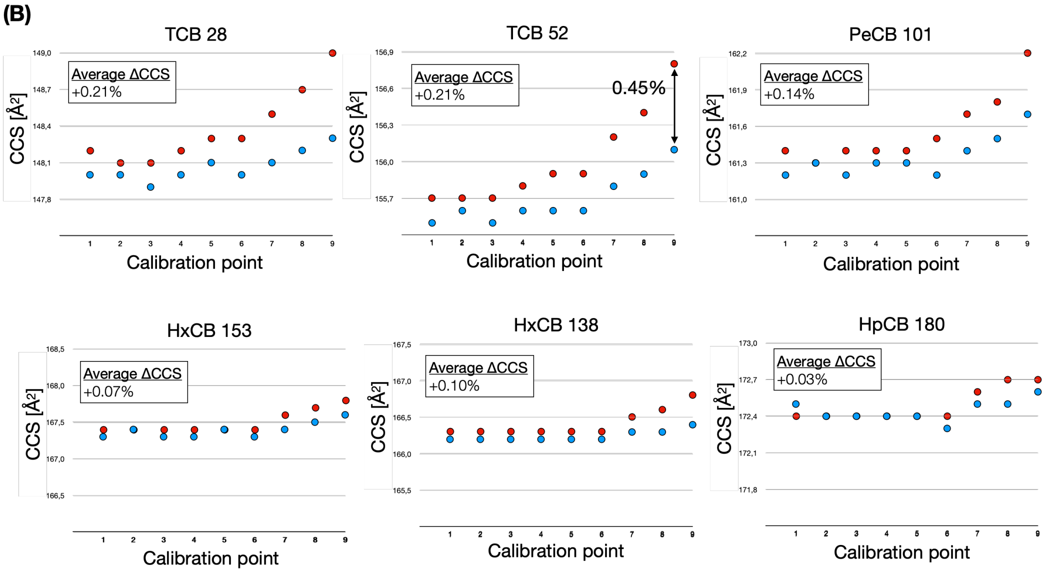
(B)
TCB 28
Average ΔCCS
+0.21%
TCB 52
Average ΔCCS
+0.21%
0.45%
PeCB 101
Average ΔCCS
+0.14%
HxCB 153
Average ΔCCS
+0.07%
HxCB 138
Average ΔCCS
+0.10%
HpCB 180
Average ΔCCS
+0.03%
CCS [Å2]
Calibration point
1 2 3 4 5 6 7 8 9

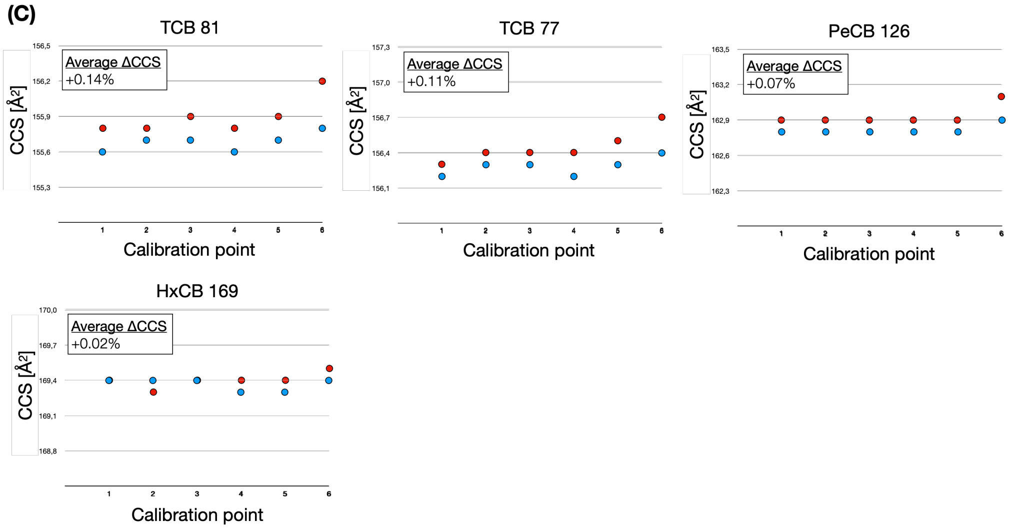
(C)
TCB 81
Average ΔCCS
+0.14%
156,5
156,2
155,9
155,6
155,3
CCS [Å²]
1
2
3
4
5
6
Calibration point
TCB 77
Average ΔCCS
+0.11%
157,3
157,0
156,7
156,4
156,1
CCS [Å²]
1
2
3
4
5
6
Calibration point
PeCB 126
Average ΔCCS
+0.07%
163,5
163,2
162,9
162,6
162,3
CCS [Å²]
1
2
3
4
5
6
Calibration point
HxCB 169
Average ΔCCS
+0.02%
170,0
169,7
169,4
169,1
168,8
CCS [Å²]
1
2
3
4
5
6
Calibration point

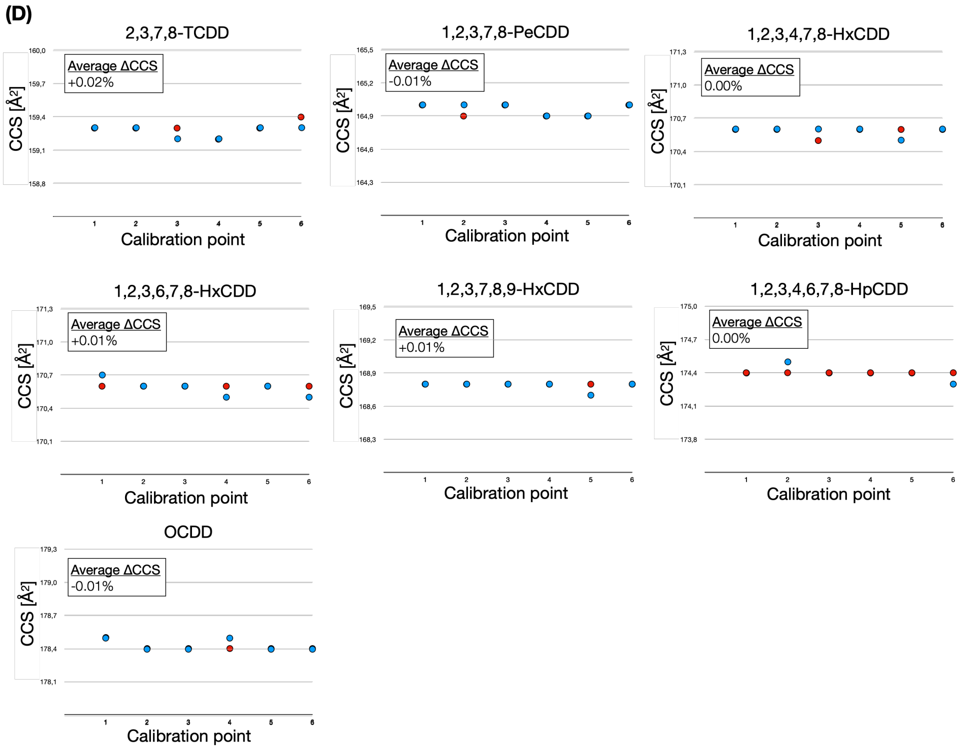
(D)
2,3,7,8-TCDD
Average ΔCCS
+0.02%
160,0
159,7
159,4
159,1
158,8
CCS [Å²]
1
2
3
4
5
6
Calibration point
1,2,3,7,8-PeCDD
Average ΔCCS
-0.01%
165,5
165,2
164,9
164,6
164,3
CCS [Å²]
1
2
3
4
5
6
Calibration point
1,2,3,4,7,8-HxCDD
Average ΔCCS
0.00%
171,3
171,0
170,7
170,4
170,1
CCS [Å²]
1
2
3
4
5
6
Calibration point
1,2,3,6,7,8-HxCDD
Average ΔCCS
+0.01%
171,3
171,0
170,7
170,4
170,1
CCS [Å²]
1
2
3
4
5
6
Calibration point
1,2,3,7,8,9-HxCDD
Average ΔCCS
+0.01%
169,5
169,2
168,9
168,6
168,3
CCS [Å²]
1
2
3
4
5
6
Calibration point
1,2,3,4,6,7,8-HpCDD
Average ΔCCS
0.00%
175,0
174,7
174,4
174,1
173,8
CCS [Å²]
1
2
3
4
5
6
Calibration point
OCDD
Average ΔCCS
-0.01%
179,3
179,0
178,7
178,4
178,1
CCS [Å²]
1
2
3
4
5
6
Calibration point

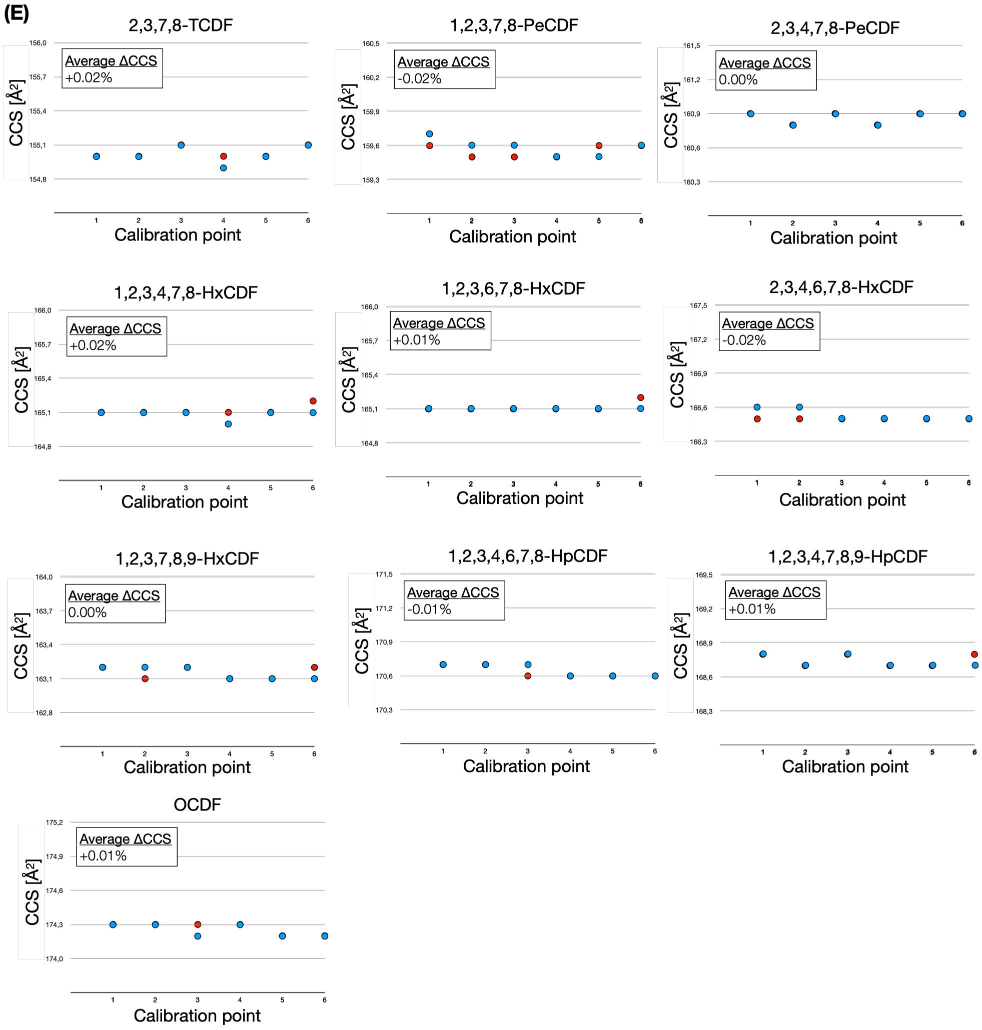

Figure S5.5: Experimentally measured CCS of both native (blue dots) and ^{13}C isotopically labelled standards (red dots) at the different calibration levels for: **(A)** MO PCBs; **(B)** NDL PCBs; **(C)** NO PCBs; **(D)** PCDDs and **(E)** PCDFs. The ΔCCS corresponds to the difference between the CCS value of the ^{13}C and the native standards, expressed as a percentage relative to the CCS of the native standard. The ΔCCS were calculated at each concentration levels and averaged to yield the average ΔCCS value displayed for each analyte in the graphs.

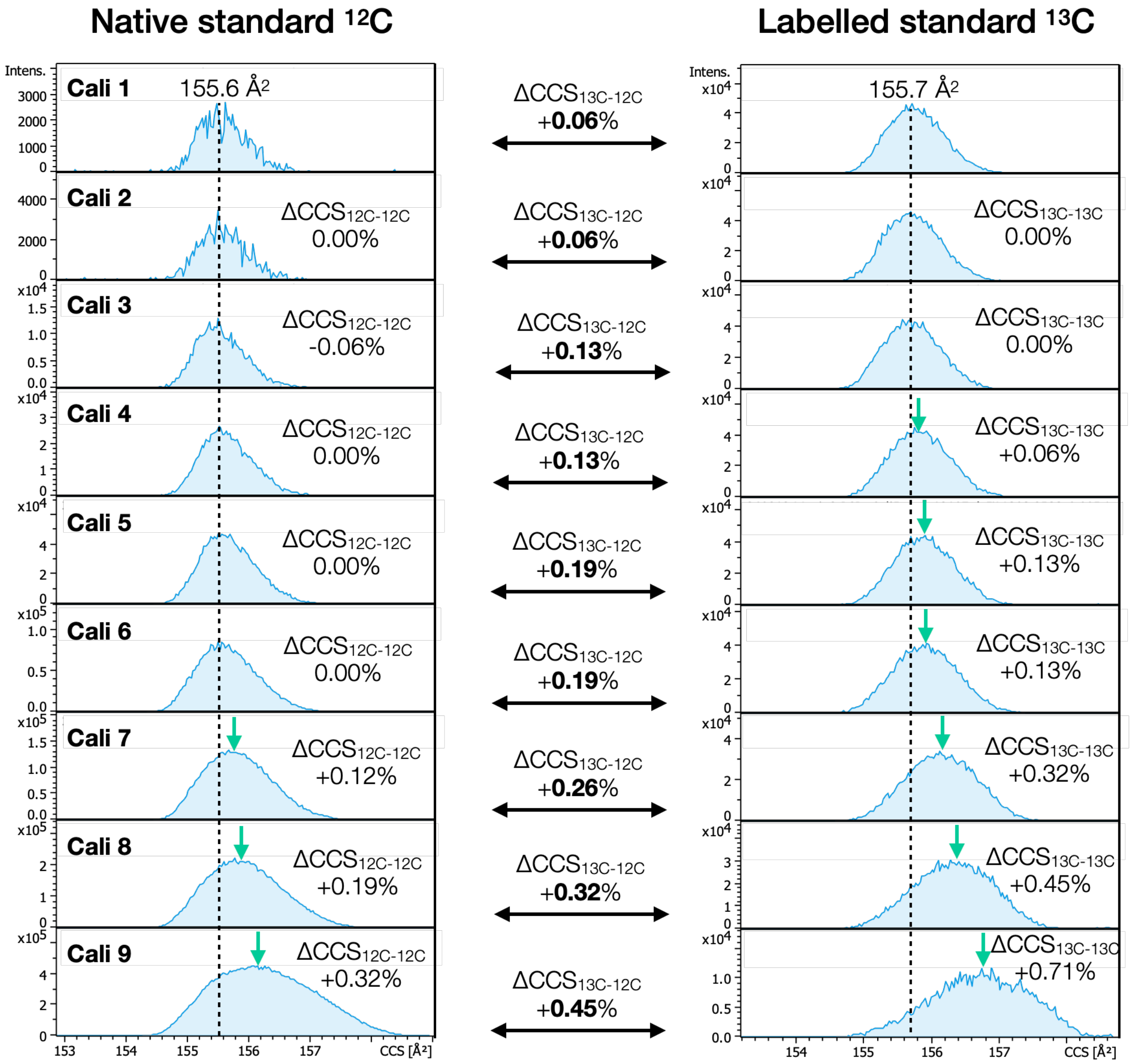

Figure S5.6: Superposition of the ion mobility spectra of the native and labelled standard of PCB 52 obtained at the different calibration levels. This figure highlights the shift of the ion mobility peaks towards higher CCS values at higher concentration levels for both the native and the labelled standard. It can be seen that the shift occurs earlier and to a greater extent for the labelled standard ($\Delta CCS_{13C\text{-}13C}$) compared to the native standard ($\Delta CCS_{12C\text{-}12C}$), ultimately resulting in an increase in the CCS difference between native and labelled standard ($\Delta CCS_{13C\text{-}12C}$) with increasing concentration levels. Once again, we believe this unequal extent in peak shifts could be attributed to space charge effects.

(A)

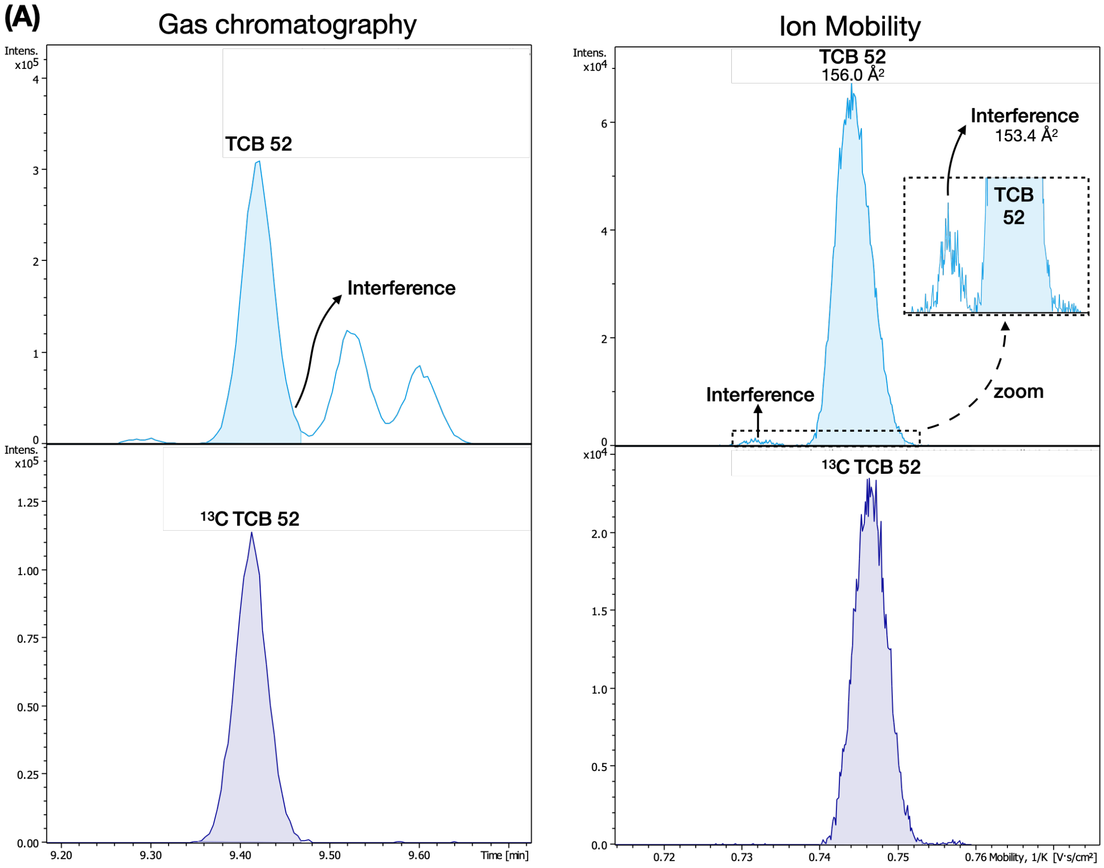
Gas chromatography
Ion Mobility
Intens. x10^5
TCB 52
Interference
13C TCB 52
9.20
9.30
9.40
9.50
9.60
Time [min]
Intens. x10^4
TCB 52
156.0 Å²
Interference
153.4 Å²
TCB 52
Interference
zoom
13C TCB 52
0.72
0.73
0.74
0.75
0.76 Mobility, 1/K [V·s/cm²]

(B)

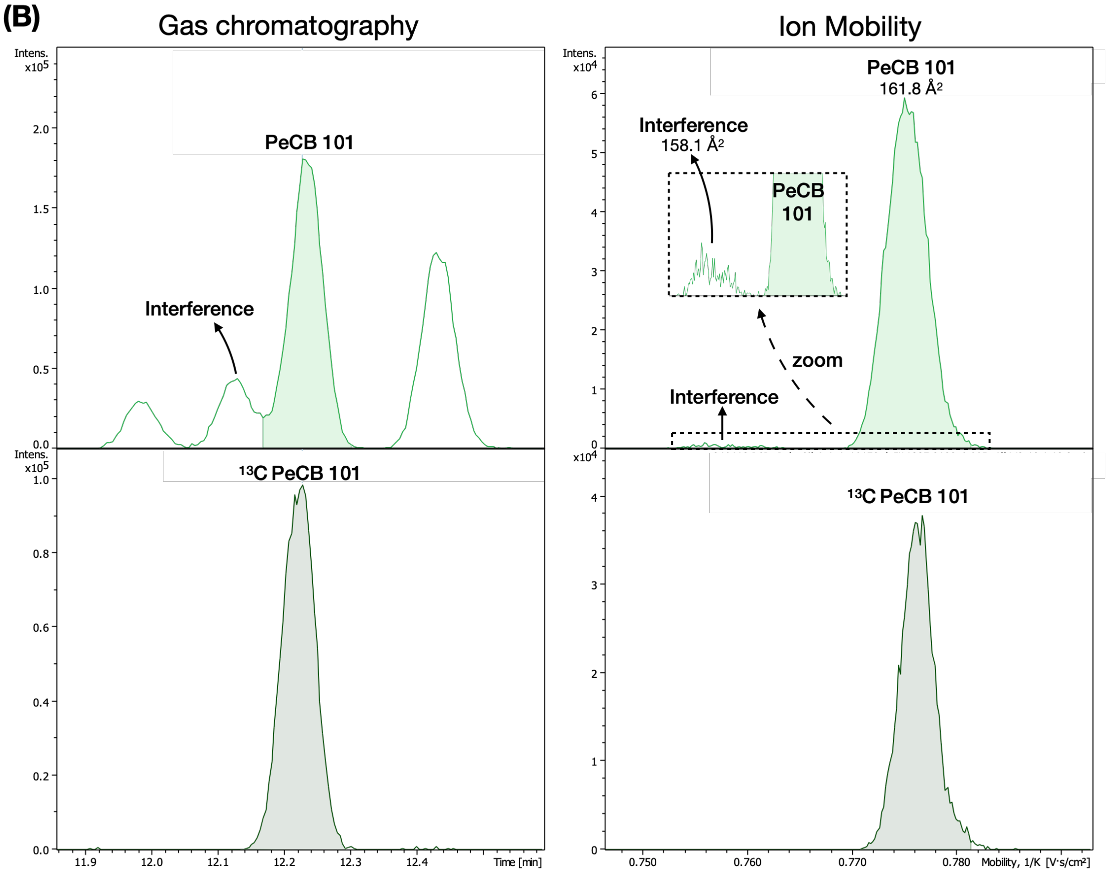
Gas chromatography
Ion Mobility
Intens. x10^5
PeCB 101
Interference
13C PeCB 101
11.9
12.0
12.1
12.2
12.3
12.4
Time [min]
Intens. x10^4
PeCB 101
161.8 Å²
Interference
158.1 Å²
PeCB 101
zoom
Interference
13C PeCB 101
0.750
0.760
0.770
0.780
Mobility, 1/K [V·s/cm²]

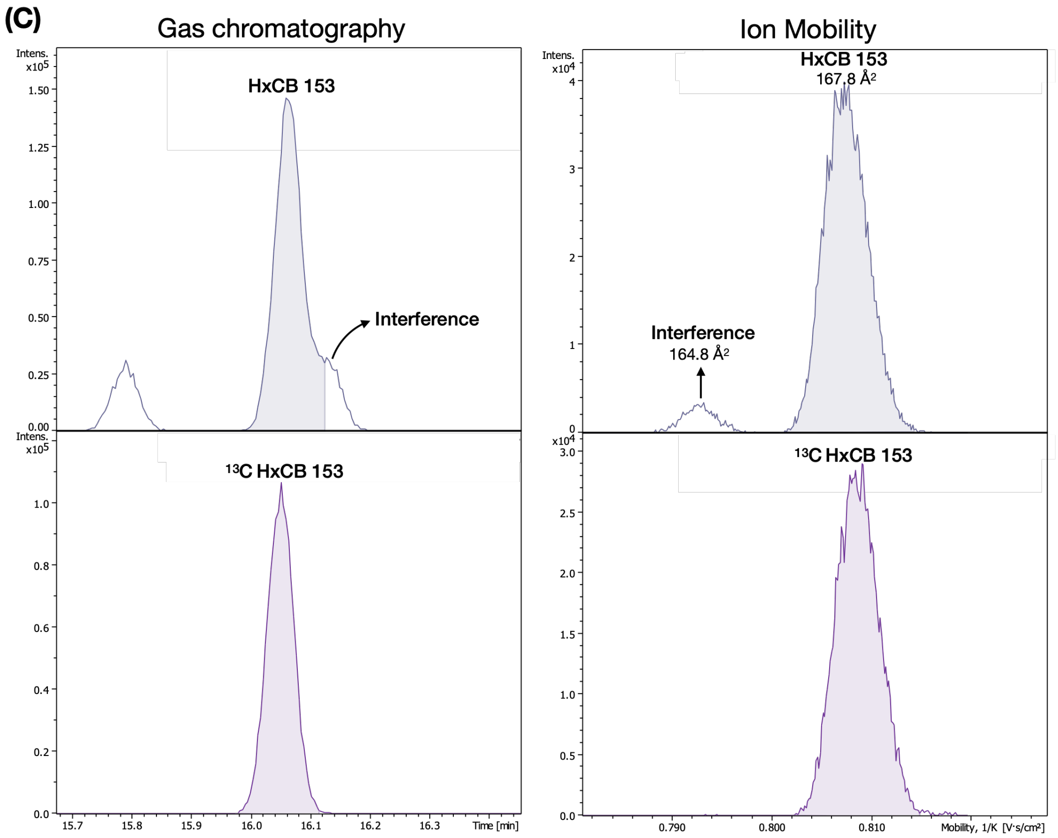

Figure S5.7: Overlayed chromatograms (left) and ion mobility spectra (right) of native and isotopically labelled standard for **(A)** TCB 52, **(B)** PeCB 101 and **(C)** HxCB 153 (palm oil sample). In each case, the (partially) coeluting isomeric interference in the GC dimension was baseline separated in the ion mobility dimension.

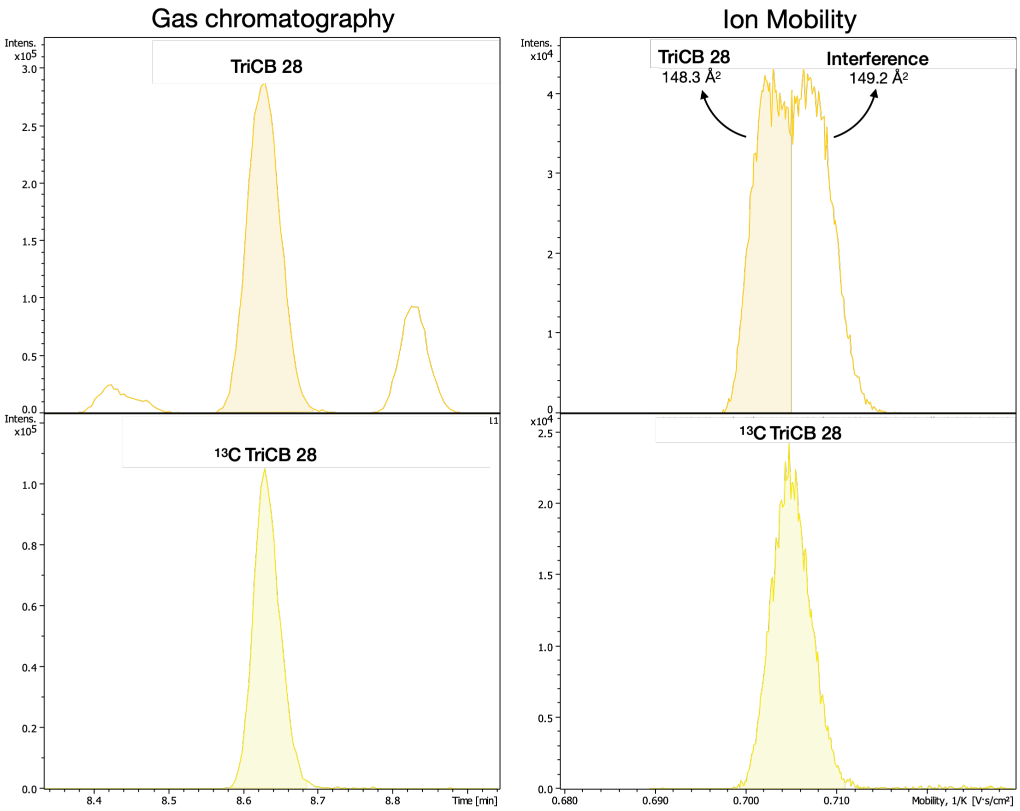

Figure S5.8: Overlayed chromatograms (left) and ion mobility spectra (right) of native and isotopically labelled standard for TriCB 28 (palm oil sample).

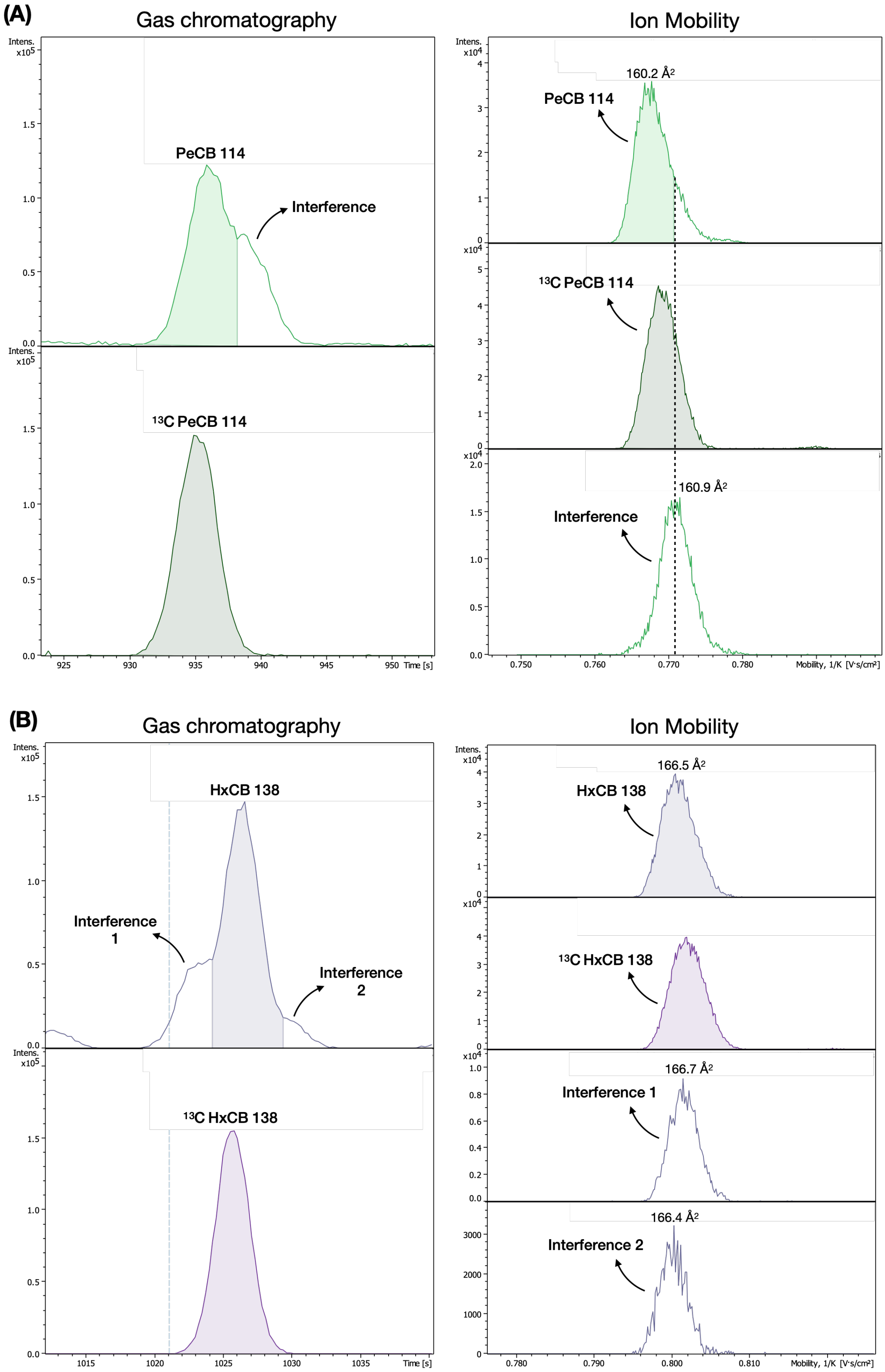
(A)
Gas chromatography
Ion Mobility
Intens. x10^5
PeCB 114
Interference
13C PeCB 114
925
930
935
940
945
950
Time [s]
Intens. x10^4
160.2 Å2
PeCB 114
13C PeCB 114
160.9 Å2
Interference
0.750
0.760
0.770
0.780
Mobility, 1/K [V·s/cm²]
(B)
Gas chromatography
Ion Mobility
HxCB 138
Interference 1
Interference 2
13C HxCB 138
1015
1020
1025
1030
1035
Time [s]
166.5 Å2
HxCB 138
13C HxCB 138
166.7 Å2
Interference 1
166.4 Å2
Interference 2
0.780
0.790
0.800
0.810
Mobility, 1/K [V·s/cm²]

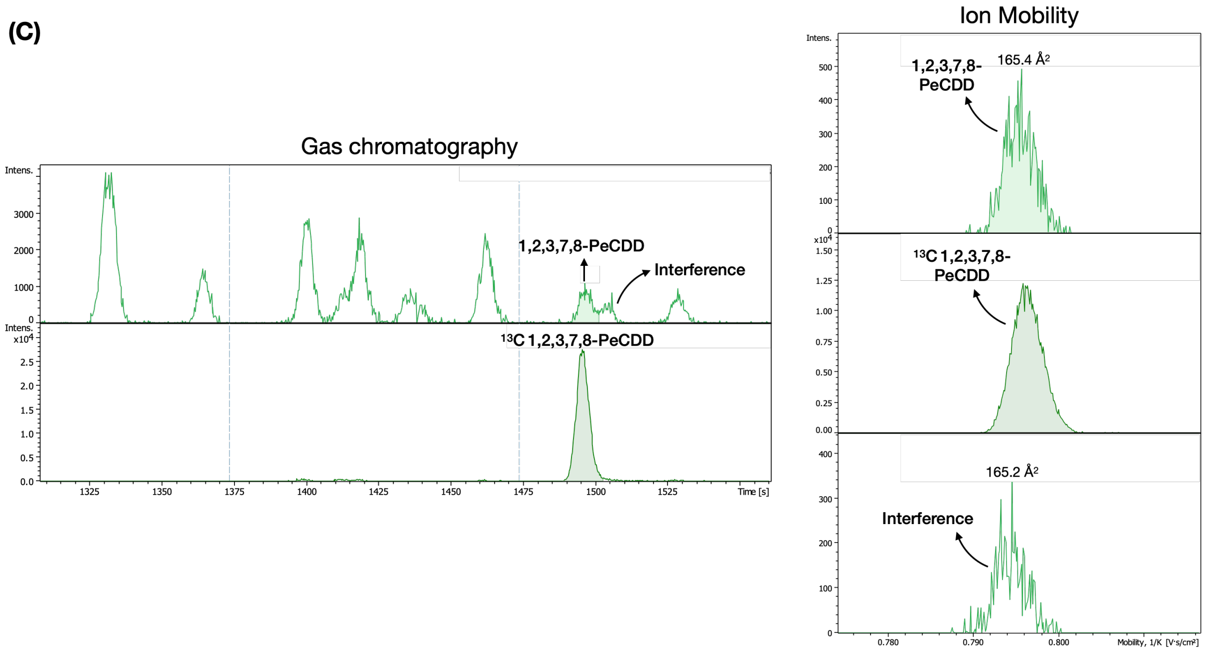
(C)
Gas chromatography
Intens.
3000
2000
1000
0
1,2,3,7,8-PeCDD
Interference
Intens.
x10^4
2.5
2.0
1.5
1.0
0.5
0.0
^{13}C 1,2,3,7,8-PeCDD
1325
1350
1375
1400
1425
1450
1475
1500
1525
Time [s]
Ion Mobility
Intens.
500
400
300
200
100
0
1,2,3,7,8-PeCDD
165.4 Å^2
x10^4
1.50
1.25
1.00
0.75
0.50
0.25
0.00
^{13}C 1,2,3,7,8-PeCDD
400
300
200
100
0
165.2 Å^2
Interference
0.780
0.790
0.800
Mobility, 1/K [V·s/cm²]

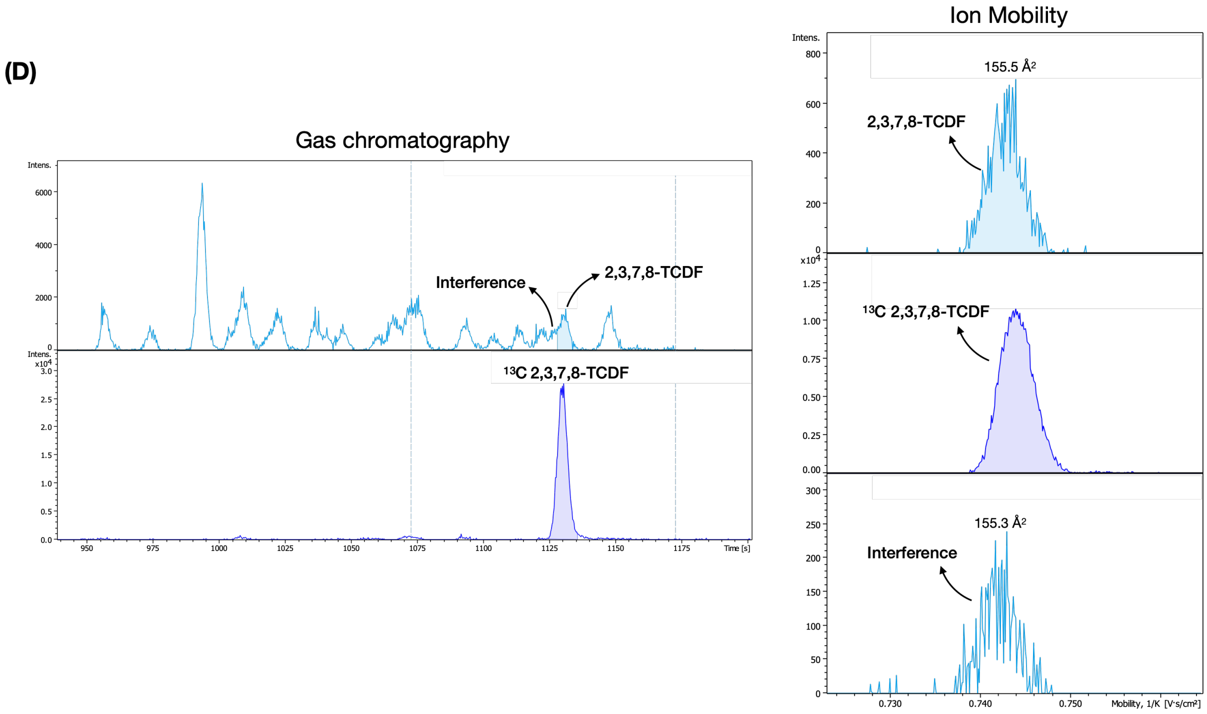
(D)
Gas chromatography
Intens.
6000
4000
2000
0
Interference
2,3,7,8-TCDF
Intens.
x10^4
3.0
2.5
2.0
1.5
1.0
0.5
0.0
^{13}C 2,3,7,8-TCDF
950
975
1000
1025
1050
1075
1100
1125
1150
1175
Time [s]
Ion Mobility
Intens.
800
600
400
200
0
155.5 Å^2
2,3,7,8-TCDF
x10^4
1.25
1.00
0.75
0.50
0.25
0.00
^{13}C 2,3,7,8-TCDF
300
250
200
150
100
50
0
155.3 Å^2
Interference
0.730
0.740
0.750
Mobility, 1/K [V·s/cm²]

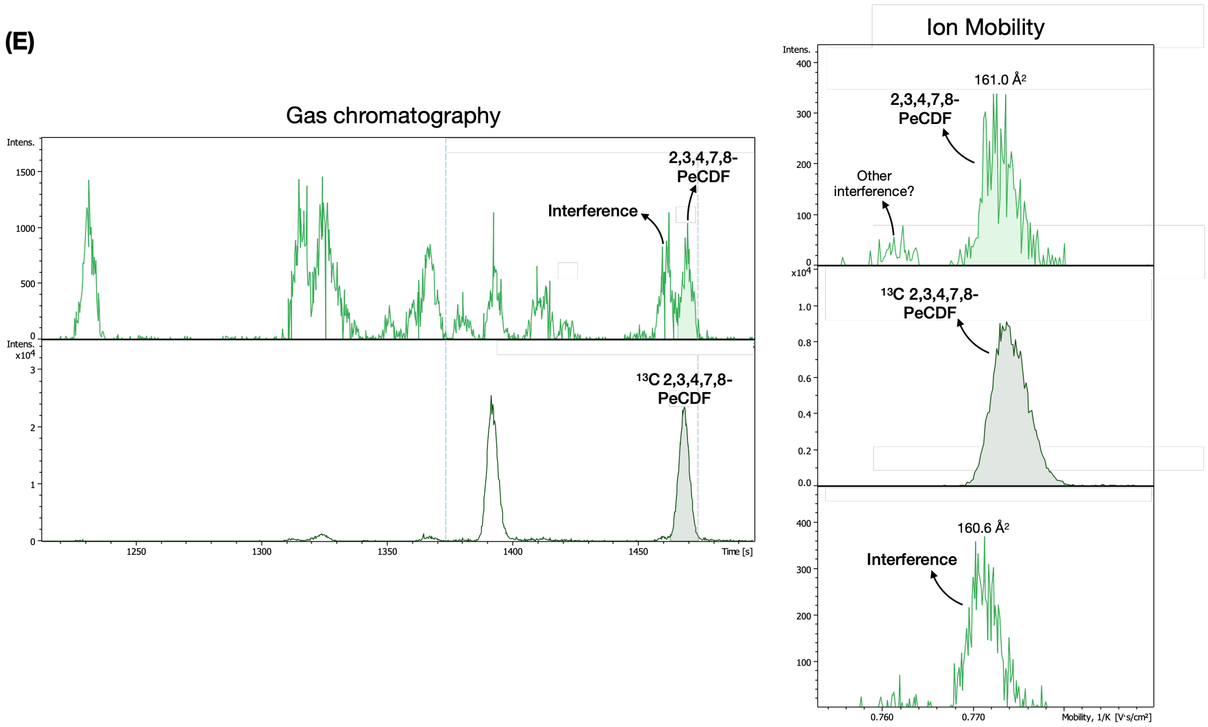

Figure S5.9: Overlayed chromatograms (left) and ion mobility spectra (right) of native, isotopically labelled standard and interference(s) for **(A)** PeCB 114 in milk fat, **(B)** HxCB 138 in palm oil, **(C)** 1,2,3,7,8-PeCDD in palm oil, **(D)** 2,3,7,8-TCDF in palm oil and **(E)** PeCDF 2,3,4,7,8-PeCDF in palm oil. While no significant separation between the analytes and the interferences could be achieved in the IM dimension, most compounds were reasonably separated in the GC dimension. Consequently, the quantification results were not impacted significantly by the presence of these interferences.

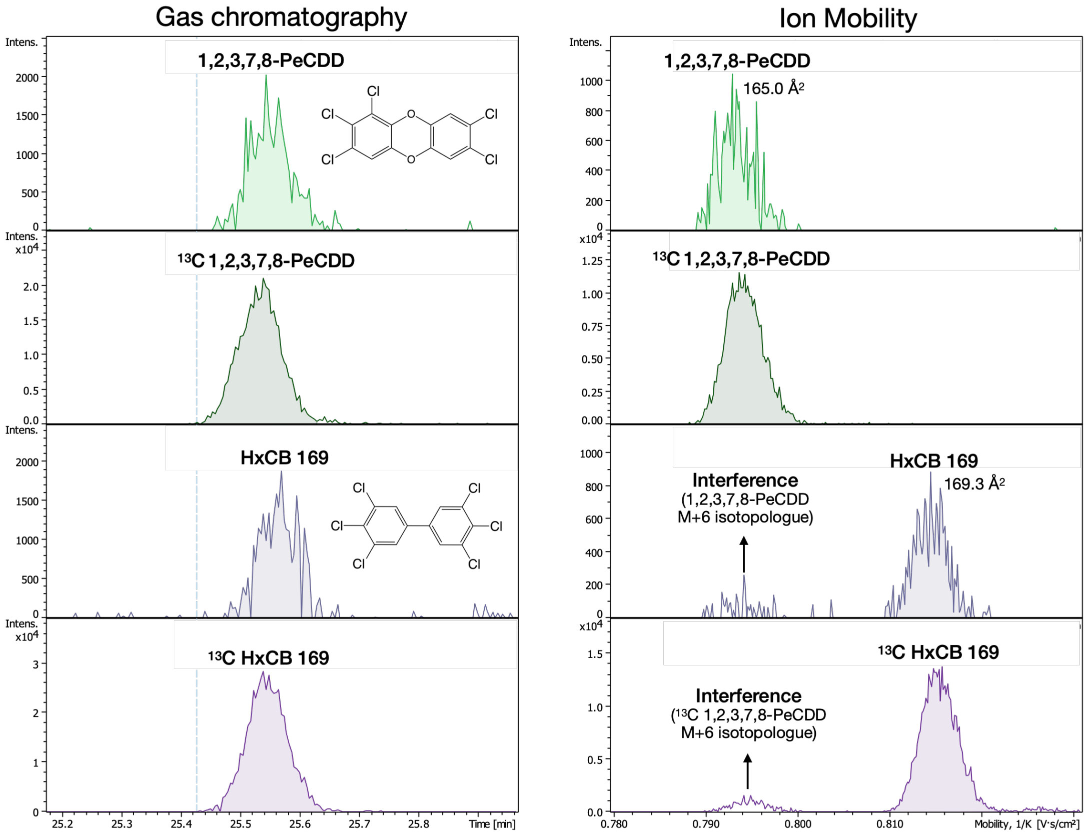

Figure S5.10: Overlayed chromatograms (left) and ion mobility spectra (right) of native and isotopically labelled standard for the coeluting isobars 1,2,3,7,8-PeCDD and HxCB 169 (milk fat sample).

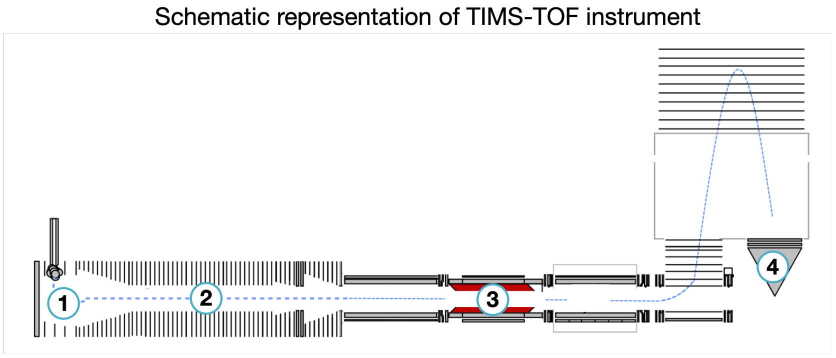

(A) Pre/intra TIMS fragmentation

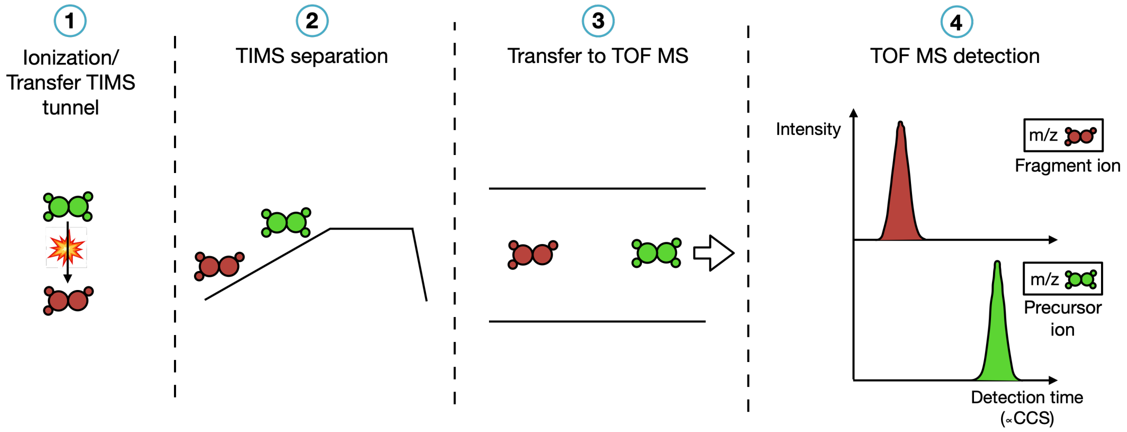

(B) Post TIMS fragmentation

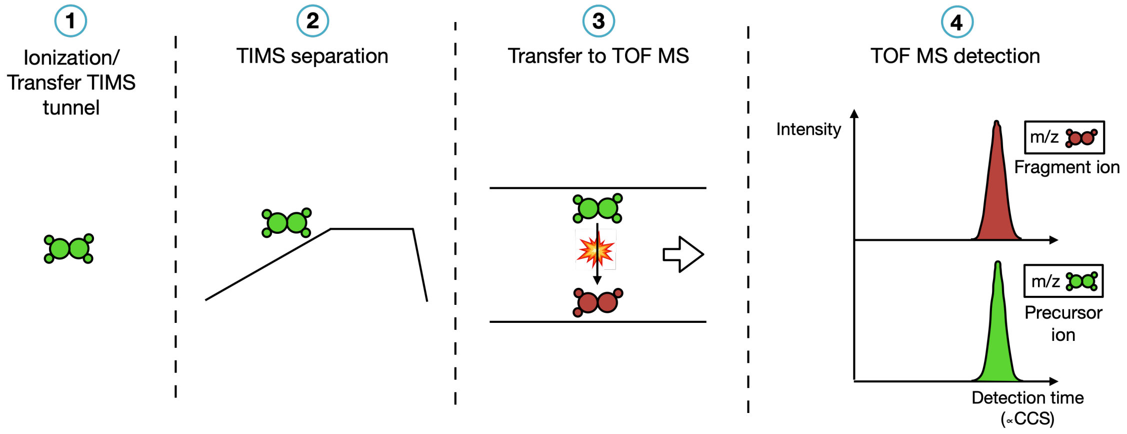

Figure S5.11: Schematic representation of the TIMS analysis of a parent ion (e.g., $M^{+\cdot}$ or $[M+H]^+$) and its fragment ion (e.g., $[M+H-Cl]^{+\cdot}$ or $[M-Cl]^+$) when fragmentation occurs either **(A)** before/during or **(B)** after TIMS separation. Precursor ions and their fragments are represented in green and red, respectively. In this figure, the TIMS-MS experiment was divided in 4 successive events. The approximate location of a specific event is shown in the schematic representation of the TIMS TOF instrument on top of the figure.

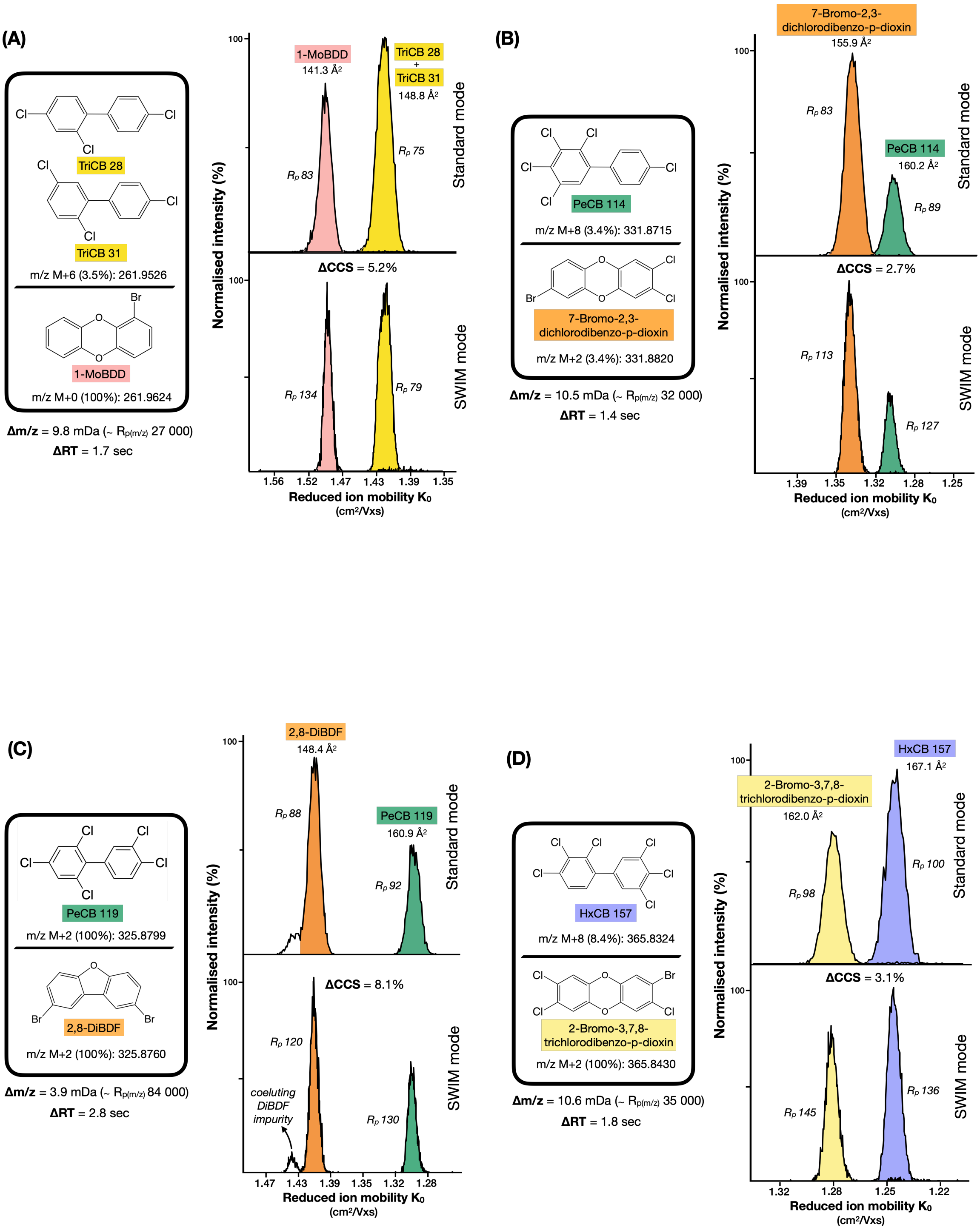
(A)
Cl
Cl
Cl
TriCB 28
Cl
Cl
Cl
TriCB 31
m/z M+6 (3.5%): 261.9526
Br
O
O
1-MoBDD
m/z M+0 (100%): 261.9624
Δm/z = 9.8 mDa (~ Rp(m/z) 27 000)
ΔRT = 1.7 sec
1-MoBDD
141.3 Å²
TriCB 28
+
TriCB 31
148.8 Å²
Rp 83
Rp 75
Standard mode
ΔCCS = 5.2%
Rp 134
Rp 79
SWIM mode
100
100
Normalised intensity (%)
1.56
1.52
1.47
1.43
1.39
1.35
Reduced ion mobility K₀
(cm²/Vxs)
(B)
Cl
Cl
Cl
Cl
Cl
PeCB 114
m/z M+8 (3.4%): 331.8715
O
O
Cl
Cl
Br
7-Bromo-2,3-dichlorodibenzo-p-dioxin
m/z M+2 (3.4%): 331.8820
Δm/z = 10.5 mDa (~ Rp(m/z) 32 000)
ΔRT = 1.4 sec
7-Bromo-2,3-dichlorodibenzo-p-dioxin
155.9 Å²
Rp 83
PeCB 114
160.2 Å²
Rp 89
Standard mode
ΔCCS = 2.7%
Rp 113
Rp 127
SWIM mode
100
100
Normalised intensity (%)
1.39
1.35
1.32
1.28
1.25
Reduced ion mobility K₀
(cm²/Vxs)
(C)
Cl
Cl
Cl
Cl
Cl
PeCB 119
m/z M+2 (100%): 325.8799
O
Br
Br
2,8-DiBDF
m/z M+2 (100%): 325.8760
Δm/z = 3.9 mDa (~ Rp(m/z) 84 000)
ΔRT = 2.8 sec
2,8-DiBDF
148.4 Å²
Rp 88
PeCB 119
160.9 Å²
Rp 92
Standard mode
ΔCCS = 8.1%
Rp 120
coeluting
DiBDF
impurity
Rp 130
SWIM mode
100
100
Normalised intensity (%)
1.47
1.43
1.39
1.35
1.32
1.28
Reduced ion mobility K₀
(cm²/Vxs)
(D)
Cl
Cl
Cl
Cl
Cl
Cl
HxCB 157
m/z M+8 (8.4%): 365.8324
Cl
Cl
Cl
Br
O
O
2-Bromo-3,7,8-trichlorodibenzo-p-dioxin
m/z M+2 (100%): 365.8430
Δm/z = 10.6 mDa (~ Rp(m/z) 35 000)
ΔRT = 1.8 sec
HxCB 157
167.1 Å²
2-Bromo-3,7,8-trichlorodibenzo-p-dioxin
162.0 Å²
Rp 98
Rp 100
Standard mode
ΔCCS = 3.1%
Rp 145
Rp 136
SWIM mode
100
100
Normalised intensity (%)
1.32
1.28
1.25
1.22
Reduced ion mobility K₀
(cm²/Vxs)

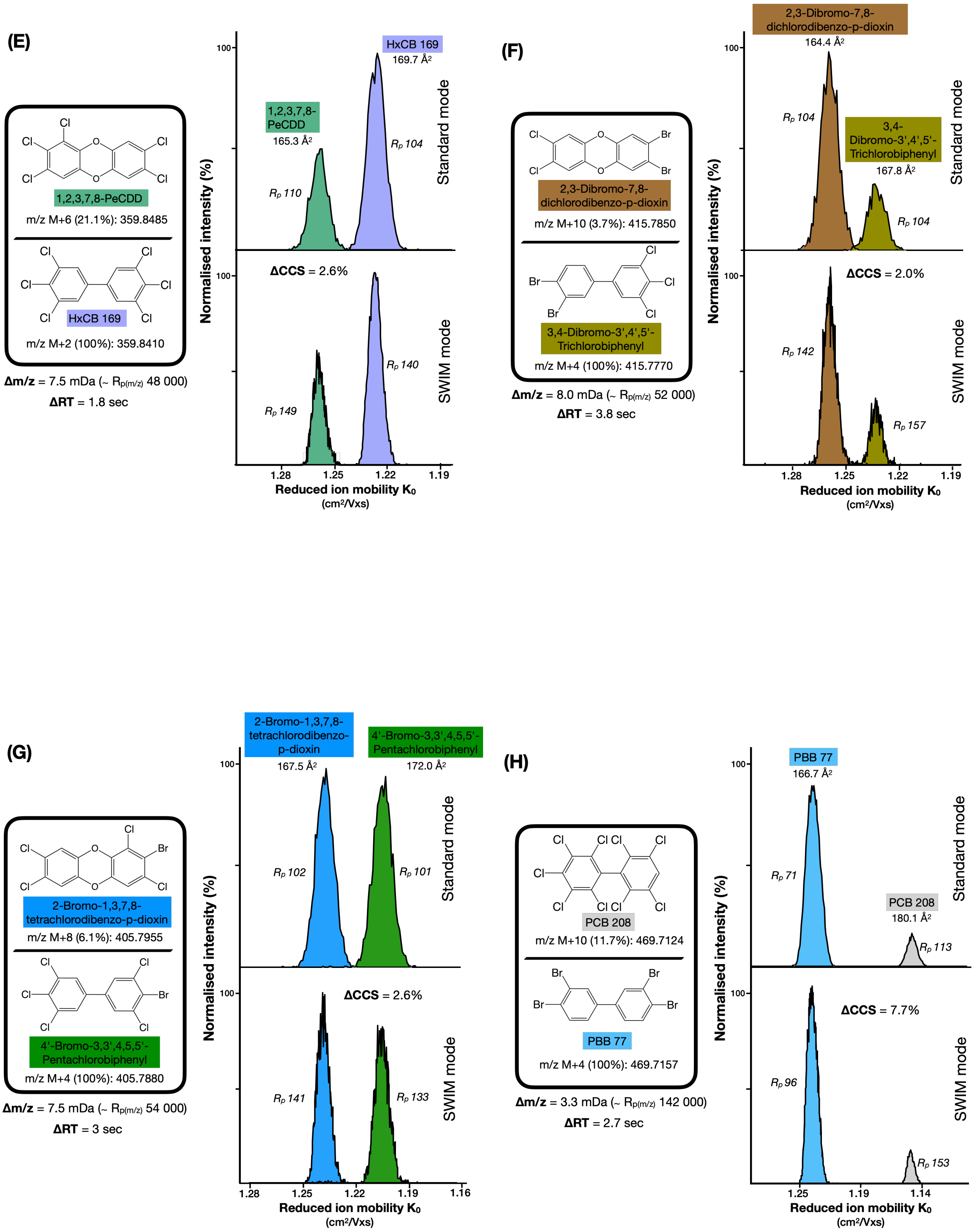

Figure S5.12 – Ion mobility spectra (in both standard and SWIM modes) of critical isobaric coelutions from the analysis of the POP standard mix in Section 4.2.2C. The minimum mass resolving power ($R_{p(m/z)}$) required to resolve the two signal in the m/z dimension is specified in each case, along with the ion mobility resolving power (R_p), CCS values and % difference in CCS.

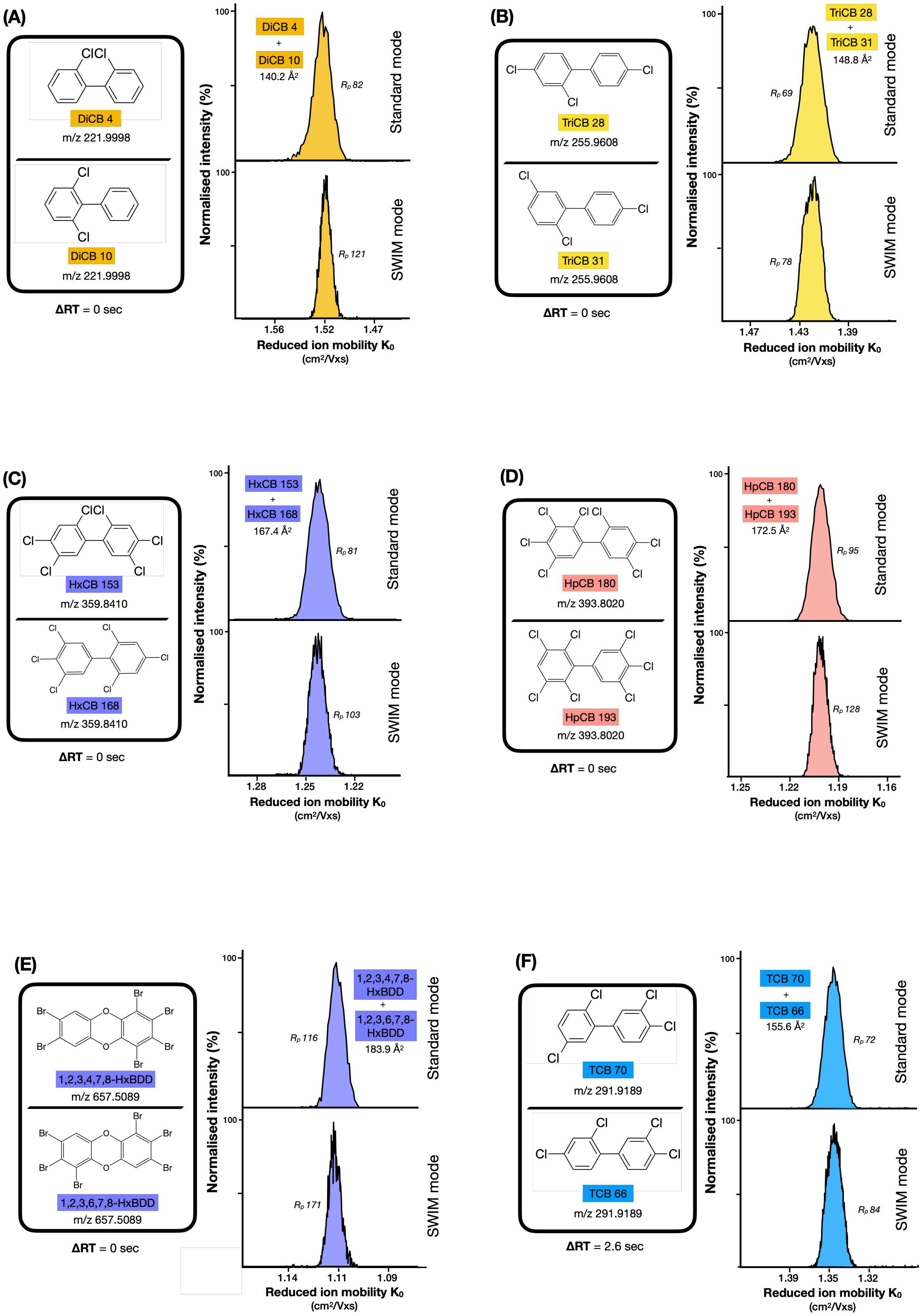
(A)
DiCB 4
m/z 221.9998
DiCB 10
m/z 221.9998
ΔRT = 0 sec
DiCB 4 + DiCB 10
140.2 Å²
Rp 82
Rp 121
Standard mode
SWIM mode
Normalised intensity (%)
Reduced ion mobility K₀ (cm²/Vxs)
1.56 1.52 1.47
(B)
TriCB 28
m/z 255.9608
TriCB 31
m/z 255.9608
ΔRT = 0 sec
TriCB 28 + TriCB 31
148.8 Å²
Rp 69
Rp 78
1.47 1.43 1.39
(C)
HxCB 153
m/z 359.8410
HxCB 168
m/z 359.8410
ΔRT = 0 sec
HxCB 153 + HxCB 168
167.4 Å²
Rp 81
Rp 103
1.28 1.25 1.22
(D)
HpCB 180
m/z 393.8020
HpCB 193
m/z 393.8020
ΔRT = 0 sec
HpCB 180 + HpCB 193
172.5 Å²
Rp 95
Rp 128
1.25 1.22 1.19 1.16
(E)
1,2,3,4,7,8-HxBDD
m/z 657.5089
1,2,3,6,7,8-HxBDD
m/z 657.5089
ΔRT = 0 sec
1,2,3,4,7,8-HxBDD + 1,2,3,6,7,8-HxBDD
183.9 Å²
Rp 116
Rp 171
1.14 1.11 1.09
(F)
TCB 70
m/z 291.9189
TCB 66
m/z 291.9189
ΔRT = 2.6 sec
TCB 70 + TCB 66
155.6 Å²
Rp 72
Rp 84
1.39 1.35 1.32

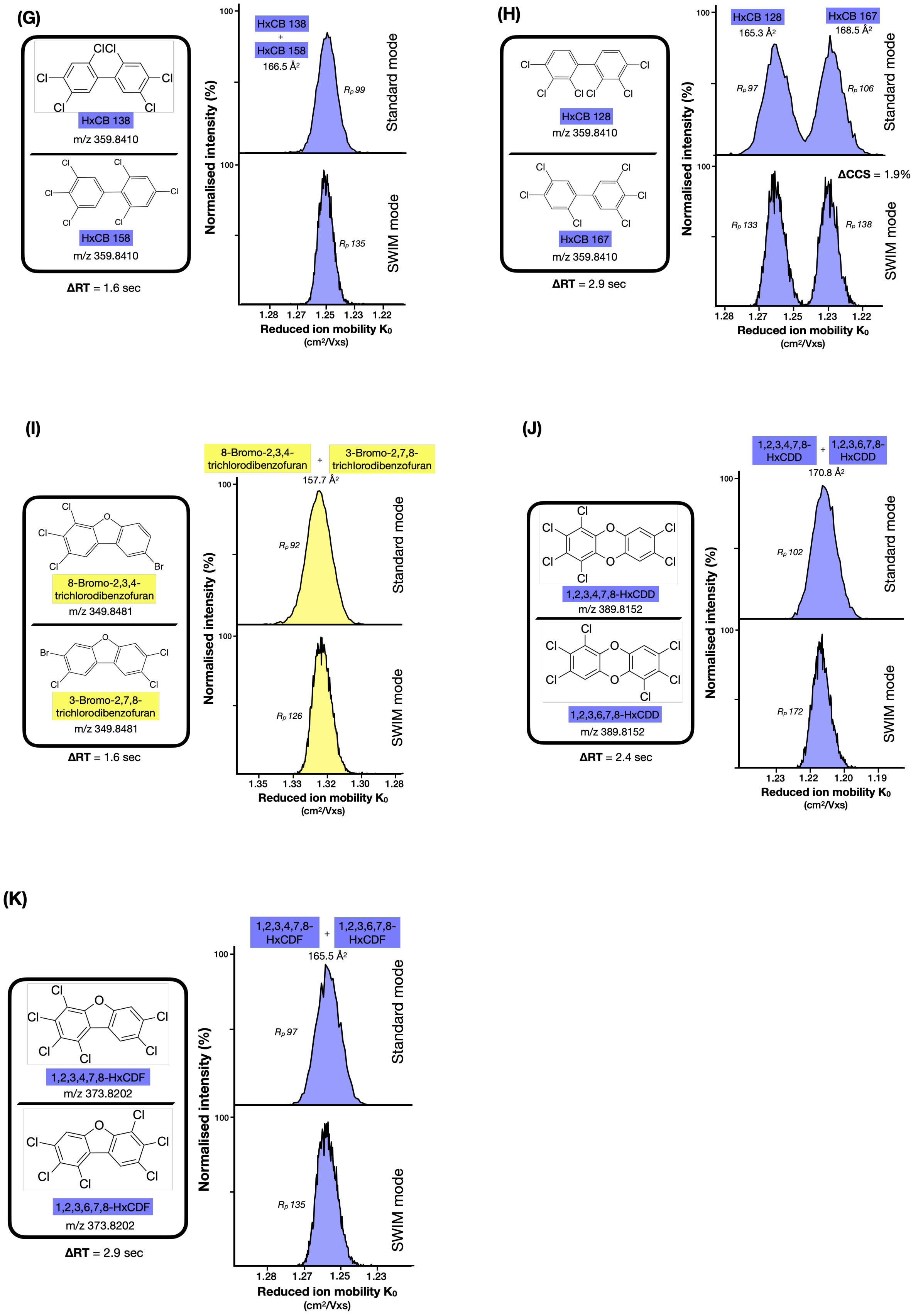

Figure S5.13 – Ion mobility spectra (in both standard and SWIM modes) of perfectly coeluting and partially coeluting isomers from the analysis of the POP standard mix in Section 4.2.2C. The ion mobility resolving power (R_p) and CCS values are specified in each case.

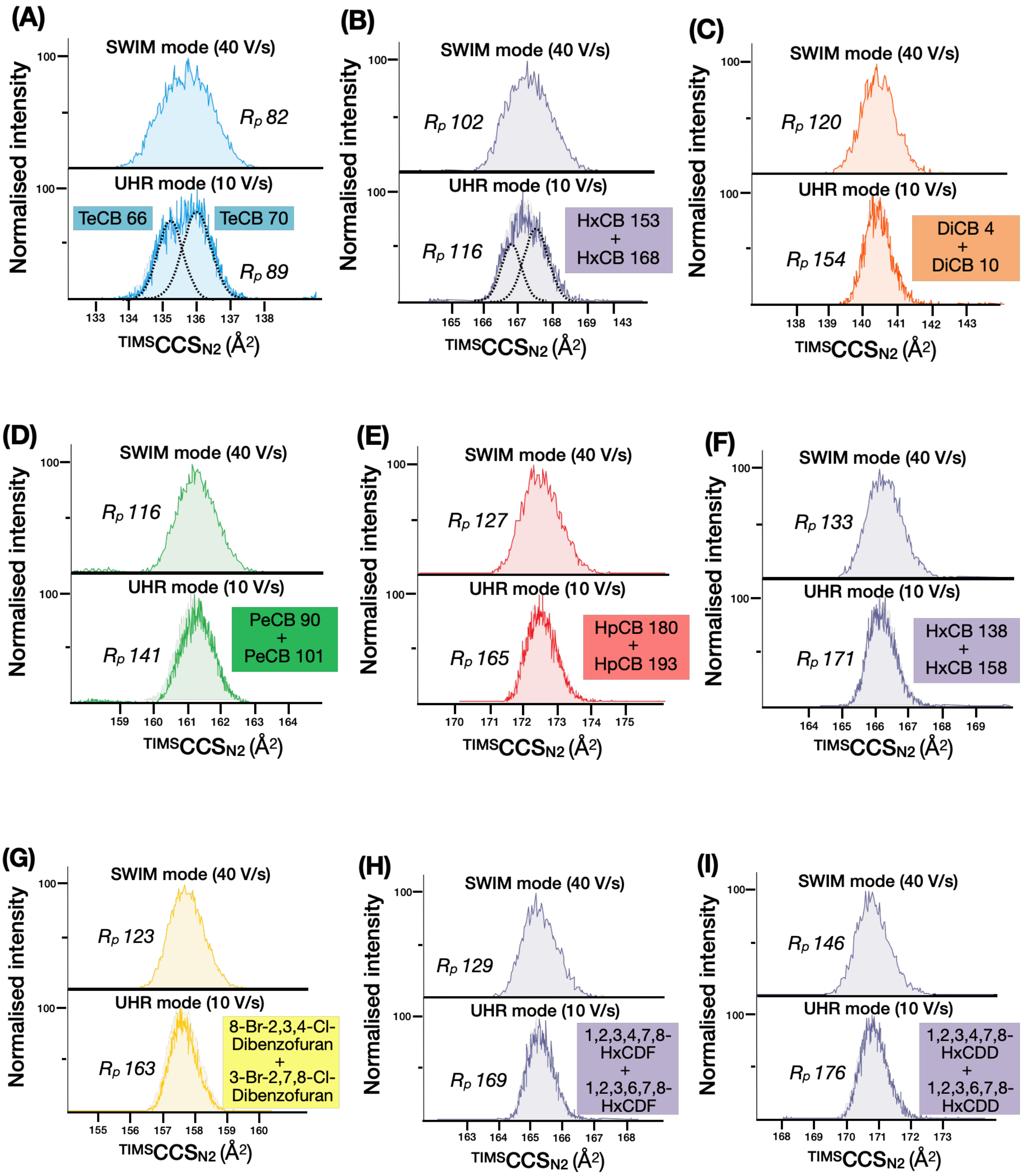

Figure S5.1 – Lower spectra: ion mobility spectra resulting from the individual ultra high resolution (UHR) analysis (β_V = 10 V/s) of each of the unresolved coeluting isomeric pairs from Figure S13. Upper spectra: original ion mobility spectra acquired in SWIM mode (β_V = 40 V/s), for comparison.

Chapter 6:
Non targeted analysis of halogenated compounds in a stranded killer whale using TIMS hyphenated with GC-HRMS

Chapter 6: Non targeted analysis of halogenated compounds in a stranded killer whale using TIMS hyphenated with GC-HRMS

6.1 - MATERIALS AND METHODS 156

6.1.1 - Sample preparation 156

6.1.2 - Analysis 156

6.1.3 - Data processing 156

6.2 - RESULTS AND DISCUSSION 157

6.2.1 - Leveraging an additional dimension of separation: mass vs mobility space 157
  A. Prioritization Strategy 157
  B. Optimized DDA selectivity 160

6.2.2 - Classes of halogenated compounds tentatively identified in the killer whale's blubber 161

6.2.3 - Evaluation of machine learning tools for predicting CCS of polyhalogenated pollutants 163

6.3 - CONCLUSION 165

6.4 - REFERENCES 165

6.5 - SUPPORTING INFORMATION 171

Currently, cetaceans face significant survival threats due to various factors directly or indirectly linked to human activities. These include acoustic disturbances, ship strikes, reduced prey availability from overfishing and climate change, and increased susceptibility to disease from biotoxins and infectious pathogens[1]. Additionally, since the initial release of human-made chemicals into marine environments, cetaceans have been widely exposed to high levels of pollutants[2,3], the oceans acting as a major sink for many of them[4].

Among cetaceans, the killer whale (*Orcinus orca*) is particularly notable for being one of the most contaminated marine mammals globally[3,5]. This is largely due to its high trophic level, long lifespan (up to 90 years), and limited metabolic capacity for breaking down pollutants[6,7]. Extremely high concentrations of contaminants, especially legacy POPs such as PCBs and OCPs, have been detected in lipid-rich tissues like the blubber[8]. These concentrations vary significantly depending on factors such as diet (fish-based vs. marine mammal-based), age, location (e.g., proximity to industrialized areas), and sex, as females can offload a substantial portion of their contaminant burden during lactation[1,3,9]. Numerous studies have demonstrated that elevated POP levels may cause a range of adverse effects in marine mammals[10]. Notably, a recent report[11] projected that up to 50% of current killer whale populations could collapse within the next century solely due to PCB exposure, which is strongly associated with immunosuppression.

To date, the monitoring of contaminants in killer whales has primarily focused on targeted analyses of legacy persistent organic pollutants[12]. These include PCBs[13]; organochlorine pesticides[14] such as dichlorodiphenyltrichloroethanes (DDTs), chlordanes, and toxaphenes; flame retardants such as polybrominated diphenyl ethers (PBDEs), hexabromocyclododecane (HBCDD), and polybrominated biphenyls (PBBs)[15,16]; polychlorinated naphthalenes (PCNs)[7,15]; and polychlorinated dibenzo-p-dioxins and dibenzofurans (PCDD/Fs)[3,17]. More recently, targeted analyses have also included emerging contaminants such as novel flame retardants[18,19] (e.g., DPTE, PBEB, PBT, HBB, Dechloranes), chlorinated paraffins[20], and per- and polyfluoroalkyl substances (PFAS)[16]. These studies revealed that killer whales are also exposed to emerging contaminants, although the levels found were typically much lower than legacy POPs.

In contrast, non-targeted approaches have been largely absent from the study of killer whale contamination. To date, only a single study has applied a non-targeted screening workflow to investigate additional contaminants in this species[21]. Using liquid chromatography coupled to a quadrupole time-of-flight mass spectrometer in both positive and negative electrospray ionization modes, the study tentatively identified several compounds, including antioxidants, PFAS, and alkylphenols. Similar NTS studies conducted on other marine mammals have revealed a wide array of potentially harmful and unregulated substances[22–24]. Collectively, these findings underscore the value of non-targeted approaches in uncovering both known and previously unidentified contaminants that may contribute to the toxic burden in marine mammals, beyond the well-characterized legacy POPs.

In this context, the aim of this chapter was to investigate the presence of additional GC-amenable halogenated substances in the blubber of a killer whale that stranded on the beach of De Panne, Belgium, using a non-targeted approach. To achieve this, a non-targeted screening method using a GC-APCI-TIMS-MS/MS system was developed. Recently, the integration of ion mobility into traditional GC- and LC-HRMS suspect and non-targeted workflows has demonstrated its capability to enhance data processing across all stages - from feature detection[25] (e.g., separation of isomers and isobars), to prioritization[26,27] (e.g., filtering using collision cross section vs m/z), and ultimately identification[26,28,29] (e.g., cleaner MS and MS/MS spectra; identification of trendlines in CCS, m/z, and mass defect space; and comparison of experimental CCS values with reference or predicted data). Here, we will discuss how we specifically leveraged the additional separation provided by ion mobility to filter features in the mobility vs. m/z space, but also to optimize the precursor selection during the tandem MS step using parallel accumulation–serial fragmentation (PASEF), a DDA fragmentation mode specific to TIMS technology[30]. Additionally, we also evaluate the performance of machine learning–based CCS prediction tools as a means to enhance structural elucidation of halogenated compounds when experimental CCS values are unavailable.

6.1 - Materials and methods

6.1.1 - Sample preparation

Approximately 130 mg were collected from the blubber of a subadult male killer whale that stranded on the beach of De Panne, Belgium, in October 2023. Sample preparation involved accelerated solvent extraction (ASE) to isolate the lipophilic fraction, followed by clean-up using an acid-silica (44%) and sodium sulfate column to remove lipids and residual water. The cleaned extract was then transferred to a GC vial containing *n*-nonane and stored at -18 °C until analysis. A procedural blank was also prepared in parallel. A detailed description of the sample preparation is provided in **Figure S6.1**.

6.1.2 - Analysis

The analyses were performed on a timsTOF Pro 2 mass spectrometer (Bruker, Bremen), equipped with a GC-APCI source (GC-APCI II, Bruker, Bremen) for sample separation and ionization prior to ion mobility–mass spectrometry (IM-MS) analysis. Generic GC, IM, and MS parameters were applied to maximize the detection coverage of compounds (see **Tables S6.1-S6.4**).

Tandem MS was carried out in data-dependent acquisition (DDA) mode using parallel accumulation–serial fragmentation (PASEF)[30] (specific parameters in **Table S6.5**). Further details on this acquisition mode are provided in the Results and Discussion section. To complement the selective DDA data, an additional analysis was conducted in data-independent acquisition (DIA) mode using broad-band collision-induced dissociation (bbCID). This non-selective fragmentation mode fragments all ions simultaneously, enabling the acquisition of complete isotopic patterns for the fragments. These patterns supported the determination of fragment chemical formulas by revealing the number and types of halogen atoms present.

6.1.3 - Data processing

Due to the lack of open-access software tailored for IM-MS data processing in the field of environmental analysis, data treatment was carried out manually using DataAnalysis (v5.3, Bruker). An overview of the non-targeted screening (NTS) processing workflow is shown below in **Figure 6.1**. As a first step, the raw data were recalibrated in terms of m/z and ion mobility using the procedure described in Section 3.2.1C. Next, peak picking was manually performed based on the prioritization strategy outlined in the Results and Discussion section (Section 6.2.1A). In the final step, the filtered features were tentatively identified.

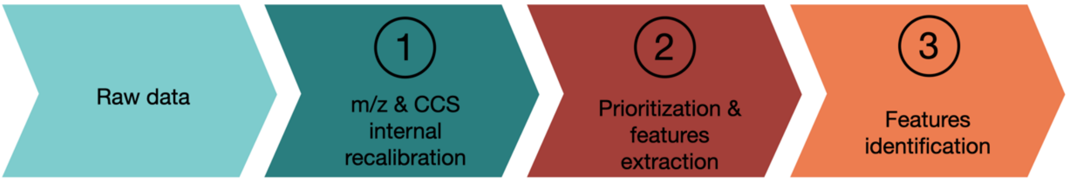

Figure 6.1 - Overview of the non-targeted processing workflow.

The identification procedure is summarized in **Figure S6.2**. First, the number and types of halogen atoms were inferred from the retention time- and ion mobility-filtered isotopic pattern of the molecular ions. When available, tandem MS spectra and in-source fragments also provided valuable information in this regard (particularly for mixed halogenated compounds containing both Cl and Br; see feature 10 in Annex A for instance) since such compounds typically undergo characteristic halogen losses during collision-induced and in-source fragmentation.

Second, the inferred halogen composition was used to query the PubChem database for candidate structures containing the same combination of halogen atoms. To reduce the number of hits, a molecular weight filter was applied. The retrieved candidates were then further refined by evaluating the match between theoretical and experimental isotopic patterns, as well as the mass accuracy. For some features with no matching candidates in PubChem, molecular formulae were estimated using the SmartFormula tool in DataAnalysis, which generates formula candidates based on experimental accurate mass and isotopic pattern.

Third, remaining candidates were further filtered using all available experimental information: comparison of experimental CCS with in-house database values; plausibility of ionization efficiency, retention time, and GC amenability; metadata; characteristics of IM spectra (peak shape, number of peaks); proportion of protonated ion vs. radical molecular ion…

6.2 - Results and discussion

6.2.1 - Leveraging an additional dimension of separation: mass vs mobility space

Figure 6.2 presents the m/z vs $1/K_0$ heatmap of all signals recorded during the full GC analysis of the killer whale blubber extract. Two clearly distinct regions are visible, as indicated by the dotted lines. As detailed in Section 3.2.2C, this separation reflects the differentiation between halogenated and non-halogenated compounds: halogenated compounds, due to their higher molecular density, predominantly appear in the lower region of the plot[27]. In addition, a series of straight lines can be observed at the bottom of the heatmap. These artifact signals originate from higher-mass ions with $1/K_0$ values exceeding the set upper limit of 1.0 V.s/cm^2. Since they are not retained by the electric field gradient, these ions continuously pass through the TIMS cell during the accumulation phase (100 ms), resulting in the appearance of continuous bands.

In the following section, we describe how the distinct region in the m/z vs $1/K_0$ space, characteristic of halogenated species, was leveraged to prioritize complex data and enhance precursor ion selection during tandem MS acquisition using the DDA PASEF mode.

A. Prioritization Strategy

Several powerful strategies have been commonly used to prioritize halogenated features in complex samples. Among the most well-known are the mass defect and Kendrick mass defect plots, which exploit the relatively low (negative) mass defect of halogenated compounds[31]. These plots facilitate a simplified visualization of complex HRMS data, enabling halogenated features to be isolated from non-halogenated ones, and allowing homologous compounds within a chemical class to align horizontally[32]. Other strategies are based on the characteristic isotopic patterns of Cl- and Br-containing compounds, which enable their selective filtering from complex MS datasets[33,34].

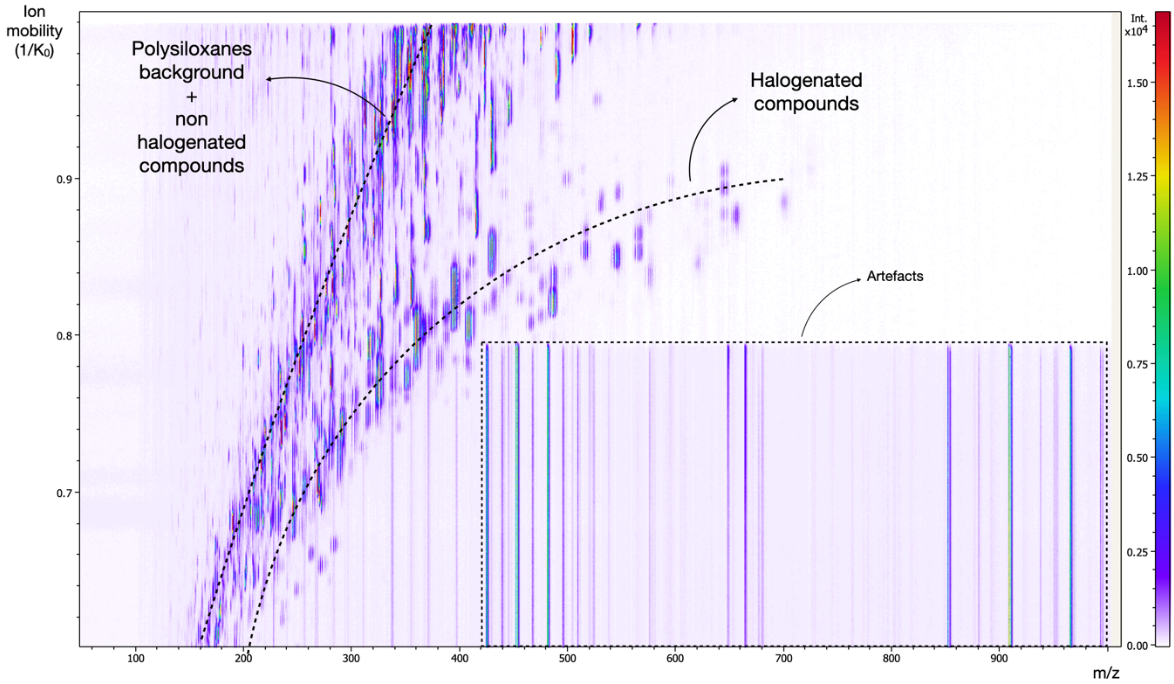

Figure 6.2 - Ion mobility (1/K_0) vs m/z heatmap of signal from the killer whale's blubber recorded over the entire GC analysis.

More recently, CCS-based strategies have been developed. These take advantage of the higher density of halogenated compounds, resulting in their specific localization in m/z vs CCS or mobility plots[26,35]. For instance, MacNeil et al.[27] applied a CCS-based prioritization strategy during GC-IM-MS analysis of an indoor dust sample. In their approach, they defined a region in the m/z vs CCS space in which only features with CCS values below a limit defined by '100 Å² + (m/z ÷ 5)' were retained for further identification.

In our study, we applied a similar CCS-based strategy to filter out non-halogenated features, such as background ions (e.g., siloxanes) and biological compounds. However, instead of applying a fixed linear cutoff as in the study by MacNeil et al., our boundary was empirically defined based on the signal distribution pattern of background ions signals in the m/z vs 1/K_0 heatmap (**Figure 6.3**). All signals located above this boundary were considered to originate from non-halogenated compounds and were excluded from further analysis. The validity of this boundary was supported by superposing the plot of reference 1/K_0 values of halogenated standards measured in Section 3.2.2; the majority of these standards indeed fell below the defined threshold (**Figure S6.3**).

Additionally, unlike MacNeil et al., we did not apply this filtering strategy following an automated peak picking. Instead, peak picking was performed manually via visual inspection of individual heatmaps generated during the analysis of the blubber extract. When a signal was observed below the boundary at a given retention time, its mass spectrum was extracted and its chromatographic peak was integrated, resulting in the creation of a feature (**Figure 6.4**). To simplify this process, each heatmap was limited to a 100 m/z range at a time (e.g., 300–400 m/z, 400–500 m/z, etc.). A minimum chromatographic intensity cutoff of 2000 was also applied to eliminate low-intensity signals with poor-quality spectra.

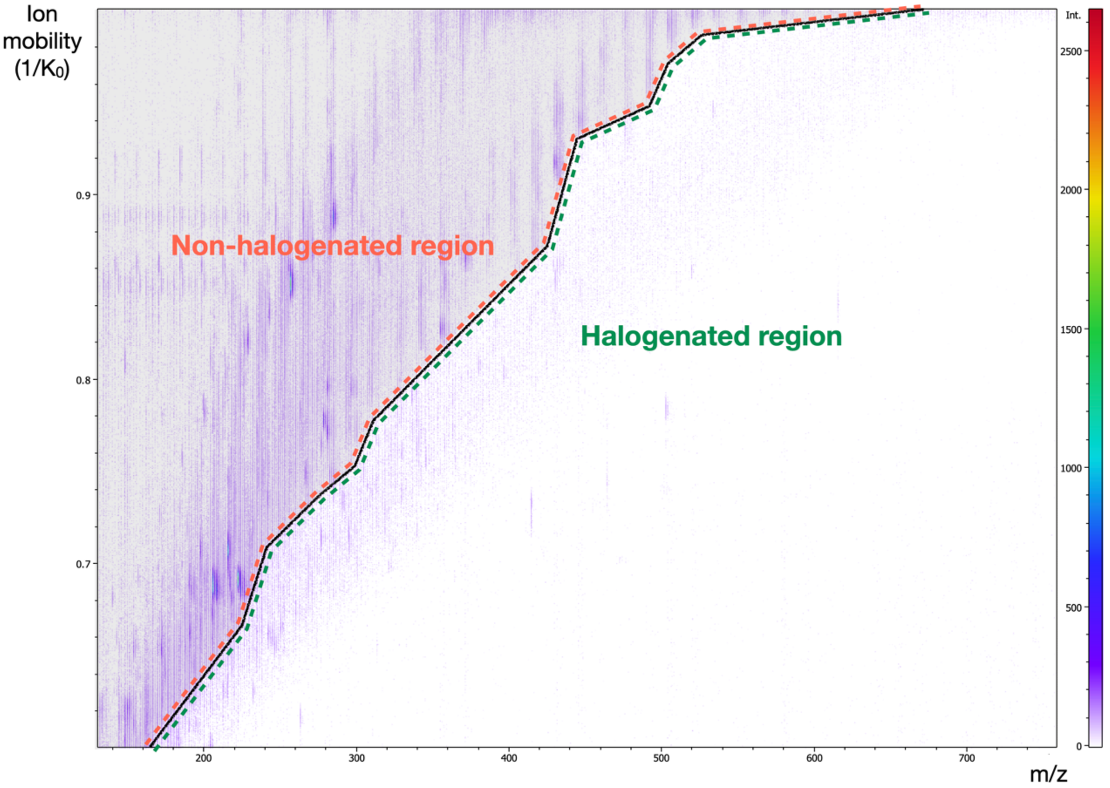

Figure 6.3 – Empirical boundary between halogenated and non-halogenated signals in the $1/K_0$ vs m/z space, defined based on background signals from GC column bleed (siloxane compounds). The heatmap was generated from the analysis of the GC column bleed at 200°C.

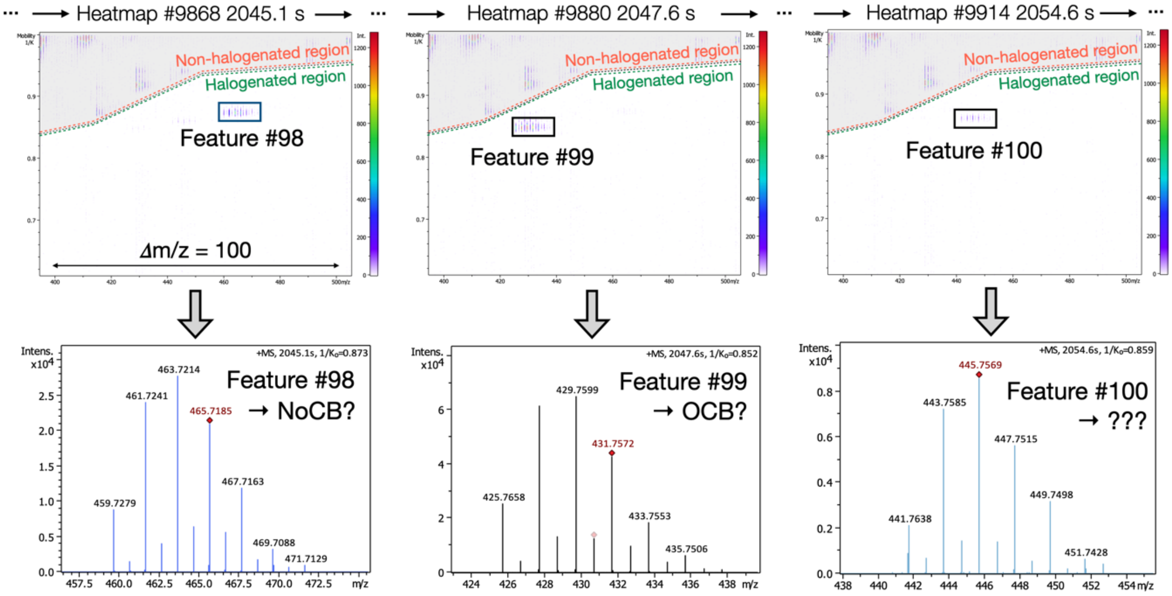

Figure 6.4 –Illustration of the visual peak-picking process for three features in the 400–500 m/z range.

This visual approach proved especially effective for identifying in-source fragments, as precursor ions and their corresponding in-source fragments appeared simultaneously within the same heatmap. Post-TIMS fragment ions could also be easily recognized, since they were aligned with their precursor ions along the mobility dimension. **Figure S6.4** illustrates these cases for a specific feature.

Altogether, this prioritization strategy enabled the manual extraction of a total of 202 tentative classes of halogenated compounds and their associated fragments (**Figures 6.5** and **S6.5**).

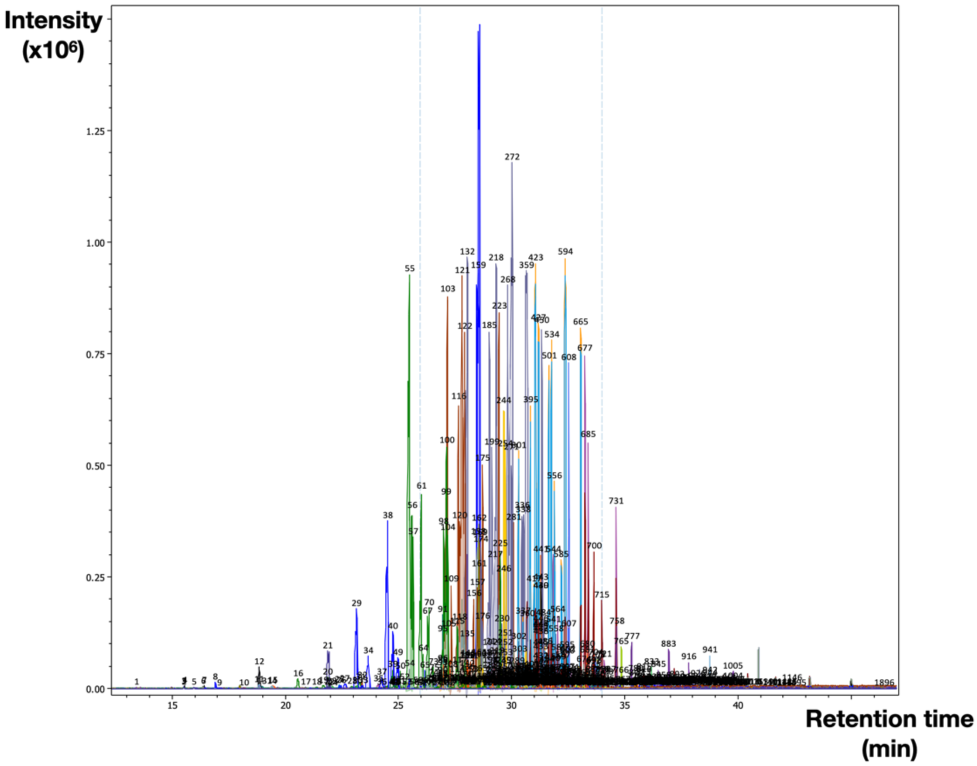

Figure 6.5 – Overlaid extracted ion chromatograms (EICs) of the 202 classes of halogenated compounds isolated using the prioritization strategy introduced in this chapter.

B. Optimized DDA selectivity

Data-dependent acquisition (DDA) modes in non-targeted analysis enable the automated and selective isolation and fragmentation of precursor ions, resulting in clean tandem mass spectra. These spectra can often be directly compared to reference MS/MS libraries or interpreted manually or in silico, in contrast to data-independent acquisition (DIA) approaches, which provide more comprehensive but more complex datasets[36].

In conventional DDA, precursor selection typically follows a “Top N” approach, where the N most intense ions in the full MS survey scan are selected for fragmentation[36]. While effective, this method tends to favor the most abundant ions, often at the expense of lower-intensity, potentially relevant analytes[37]. Furthermore, although exclusion lists can be applied to omit known background m/z values from fragmentation, the method remains limited in its ability to discriminate between meaningful and irrelevant signals, such as those arising from the sample matrix[36,37].

In TIMS, a specific DDA fragmentation strategy termed ‘parallel accumulation – serial fragmentation (PASEF)’ was devised in 2015 by Mann et al[38]. In conventional qTOF-based DDA, all ions arrive simultaneously at the quadrupole, but only one precursor (typically the most intense) is selected for fragmentation per scan. In contrast, in DDA-PASEF, implemented on a TIMS-qTOF platform, ions are first separated based on their mobility before they reach the quadrupole. By synchronizing the quadrupole selection with the ion elution order from the TIMS cell, PASEF enables the sequential fragmentation of multiple precursor ions in a single scan cycle. This greatly increases both the MS/MS acquisition rate and precursor ion coverage[30,38].

In addition, PASEF allows to specifically isolate precursor ions in a defined region of the mobility versus m/z space. In proteomics, for example, this allows exclusion of singly charged peptide ions that occupy a specific region of the plot, enabling preferential selection of multiply charged, more informative precursors[30].

In this study, we leveraged this capability to selectively target halogenated precursor ions. A precursor selection region was defined in the m/z vs. $1/K_0$ space, centered around the halogenated zone described in the previous section. As illustrated in **Figure 6.6**, this DDA-PASEF strategy successfully restricted precursor selection to ions within the halogenated region, excluding non-halogenated and background ions. This approach allowed even low-intensity halogenated signals to be selected for MS/MS fragmentation. These signals would likely have been overlooked in a traditional intensity-based DDA scheme, where more abundant matrix-derived ions would dominate precursor selection (see for instance the case of feature 31 in Annex A).

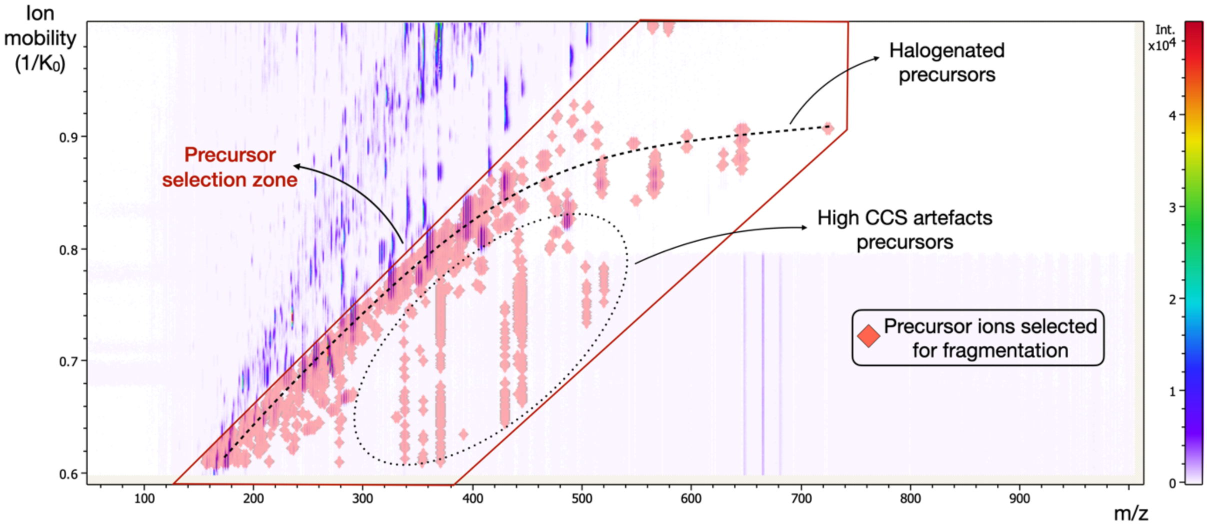

Figure 6.6 – Overview of precursor ions selected for MS/MS analysis using the developed DDA-PASEF strategy. Note that some artifact ions located within the precursor selection zone were also subjected to fragmentation.

6.2.2 - Classes of halogenated compounds tentatively identified in the killer whale's blubber

Out of the 202 classes of halogenated compounds extracted from the m/z vs. $1/K_0$ heatmap, 23 classes (~11%) have reached the final step of the non-targeted workflow: tentative identification. Work is still ongoing for the remaining classes. In this section, we provide an overview of the identifications performed to date.

These 23 classes comprised a total of 42 individual features. The experimental data used in the identification process are provided in a PDF document attached to this thesis (Annex A). For each feature, it includes: the m/z vs. $1/K_0$ heatmap, chromatogram, full-scan and tandem mass spectra, and the ion mobility spectra of the (quasi)molecular ions and their fragments (when present). When relevant, the chemical structure of the tentatively identified compound was also included.

More than half of the features could be classified as Level 3 according to the Schymanski scale[39] (i.e., tentative structures, **Figure 6.7**). In addition to accurate mass, isotopic pattern, and characteristic fragments, supporting evidence for these annotations included the GC amenability of the proposed structures. For instance, some candidate compounds contained alcohol functional groups, making them less likely to be detected by non-polar GC (features 2, 3, 6, 12–16, and 24 in Annex A), although this criterium would require further validation. Moreover, most of these annotations corresponded to well-known classes of substances that have already been reported in several targeted studies of killer whale samples. These included legacy POPs (e.g., PBDEs: features 2–3, 12–16; PBBs: features 4–5, 17–23, Annex A) as well as naturally produced halogenated compounds (e.g., methoxylated PBDEs: features 6, 35–36; halogenated methyl bipyrroles: features 7, 25–27, Annex A). These natural halogenated products (HNPs) are biosynthesized by marine organisms such as sponges, algae, and bacteria, and some exhibit POP-like properties comparable to anthropogenic halogenated compounds[22,40,41]. Finally, the high relative intensity of the protonated ion $[M+H]^+$ observed for some features provided additional evidence for the presence of strongly basic sites prone to protonation, such as heteroatoms like nitrogen or sulfur. The brominated methyl bipyrroles (features 7, 25–27, Annex A) serve as a representative example.

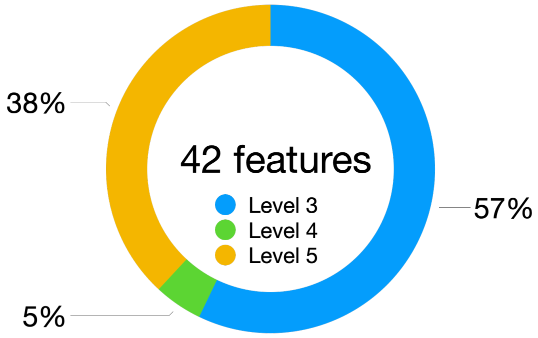

Figure 6.7 – Overview of the confidence levels assigned to the features based on the Schymanski classification system[39].

Additional evidence for the identification was provided by the added dimension of separation introduced by ion mobility. For example, the positions of tentatively identified PBDE and PBB features in the mobility vs m/z space were aligned with their respective characteristic trendlines defined in Section 3.2.2C, providing further confidence in their classification[26,42] (**Figure S6.6**). Note that two $^{TIMS}CCS_{N2}$ values for the tentatively identified HxBDEs are rather far from the expected values based on the trendline fit. However, the trendline was created from the CCS of only 18 PBDEs out of the 209 existing congeners, and is therefore not fully representative of the structural diversity within the class. As such, deviations may arise due to differences in substitution patterns and molecular conformations that are not captured by the limited calibration set. Further expansion of the reference database would help improve confidence in CCS-based identifications for these PBDEs (see next section).

Moreover, for most of these features, the ion mobility peak of the radical molecular ion ($M^{+\cdot}$) appeared as a single symmetric peak, suggesting either a rigid molecular structure or a rapidly interconverting flexible conformation (Section 3.2.2A), consistent with the proposed candidate structures. In contrast, some features exhibited asymmetric or multiple peaks in their ion mobility spectra, which may indicate more complex ion structures with multiple conformers (e.g., features 33, 34, and 41; Section 3.2.2A), or the presence of coeluting isomers that are separated in the ion mobility dimension. This last case is exemplified in the ion mobility spectra of the putative HxBDE (feature 13) and HpBDE (feature 2).

Finally, the overall profile of the ion mobility spectra of both precursor and fragment ions for the tentative PBDEs was consistent with the behavior observed for the PBDE standards in Section 3.2.2B. Specifically: the CCS of the protonated ion $[M+H]^+$ was slightly higher than that of the corresponding radical ion $M^{+\cdot}$; a significant fraction of pre/intra-TIMS fragmentation was observed; post-TIMS fragment ions had mobility peaks aligned with those of the $[M+H]^+$ precursor ion; the CCS of the $[M+H-Br]^{+\cdot}$ fragments matched the expected CCS values - those of PeBDEs for HxBDEs fragments and those of HxBDEs for HpBDEs fragments. These observations confirm the valuable additional identification information provided by all types of ions, both precursor and fragment ions[43]. Altogether, the ion mobility spectra of those ions act as a "fingerprint" for each class of pollutants, enhancing confidence in structural annotations.

Besides these tentative structural assignments, the remaining features were classified at confidence levels 4 (i.e., unequivocal molecular formula) and 5 (i.e., exact mass) according to the Schymanski scale[39] (Figure 6.7). For these features, although plausible combinations of halogen atoms were identified that matched the experimental isotopic patterns, no corresponding PubChem hits were found during the second step of the identification workflow. With the exception of one case (feature 10), these unknown features exhibited low signal intensity (<5000), which suggest that some of them may potentially represent emerging contaminants recently released into the environment and subsequently accumulated in the blubber of the killer whale.

6.2.3 - Evaluation of machine learning tools for predicting CCS of polyhalogenated pollutants

As we have seen in the cases of the legacy POPs features, CCS are highly valuable parameters that enhances confidence in compound class identification by allowing their comparison to experimental class-specific trendlines. The experimental CCS of features for which one (level 2) or multiple exact structure (level 3) were found can also be directly compared to their corresponding database CCS values[29,44] (Section 1.3.4B). It is currently accepted that a difference below 2% gives extra confidence in support of the candidate structure[45,46]. However, the number of available empirical CCS values remains limited, primarily due to the scarcity of analytical standards and the time-intensive nature of CCS measurements[37,47,48]. To address this limitation, recently several machine learning (ML)-based tools have been developed to predict CCS values for small molecules on a large scale, achieving low to moderate prediction errors[47,49] (Section 1.3.4B). ML predicted CCS are now available for every compound included in the PubChem Lite database[50,51].

Current open-access machine learning–based software for CCS prediction includes AllCCS2[52], CCSbase[53], CCSP 2.0[54], DeepCCS[55], and CCSondemand[56]. Most of these models follow a common approach[49]: they use algorithms trained on a dataset of compounds with known CCS values (the training set) and a corresponding set of molecular descriptors (numerical values that characterize the physicochemical properties of a molecule, such as exact mass, polarizability, log K_{OW}, and more). Once trained and validated, the model can rapidly predict the CCS of compounds not included in the original training dataset. In most cases, only the SMILES and/or InChi representation of a compound is required to generate a CCS prediction.

To further assess the accuracy of the level 3 candidate structures proposed in the previous section, predicted CCS values were calculated. To determine which ML-based software would be most suitable for this task, CCS values for eight halogenated compounds (with CCS previously measured on our timsTOF instrument) were predicted using four commonly used models: AllCCS2, CCSbase, CCSP 2.0, and CCSondemand.

The predicted CCS values and corresponding errors relative to the experimental values for each halogenated compound are shown in **Figure 6.8**. As illustrated, the performance varied significantly across the different software tools. One model that clearly stood out was CCSP 2.0, which consistently achieved the highest prediction accuracy, with errors always below 1%. AllCCS2 and CCSondemand displayed similar performance, with prediction errors under 6% and 4%, respectively. In contrast, CCSbase showed the poorest performance: while half of its predictions had errors below 4%, the remainder exhibited much larger deviations, reaching up to 21%.

The reason for these outlier values remains unclear. However, the superior performance of the CCSP 2.0 model is likely due to its training dataset[54]. Unlike the other models, which were primarily trained on CCS values of non-halogenated metabolite compounds, CCSP 2.0 was trained on a custom dataset comprising 184 ^{TIMS}CCS values of halogenated compounds from our in-house database. This comparison highlights a well-known key limitation of ML-based CCS prediction tools: the accuracy of predictions depends heavily on the relevance of the training data[29,53]. Therefore, for halogenated compounds, significantly better results are obtained using models trained specifically on halogenated structures[57].

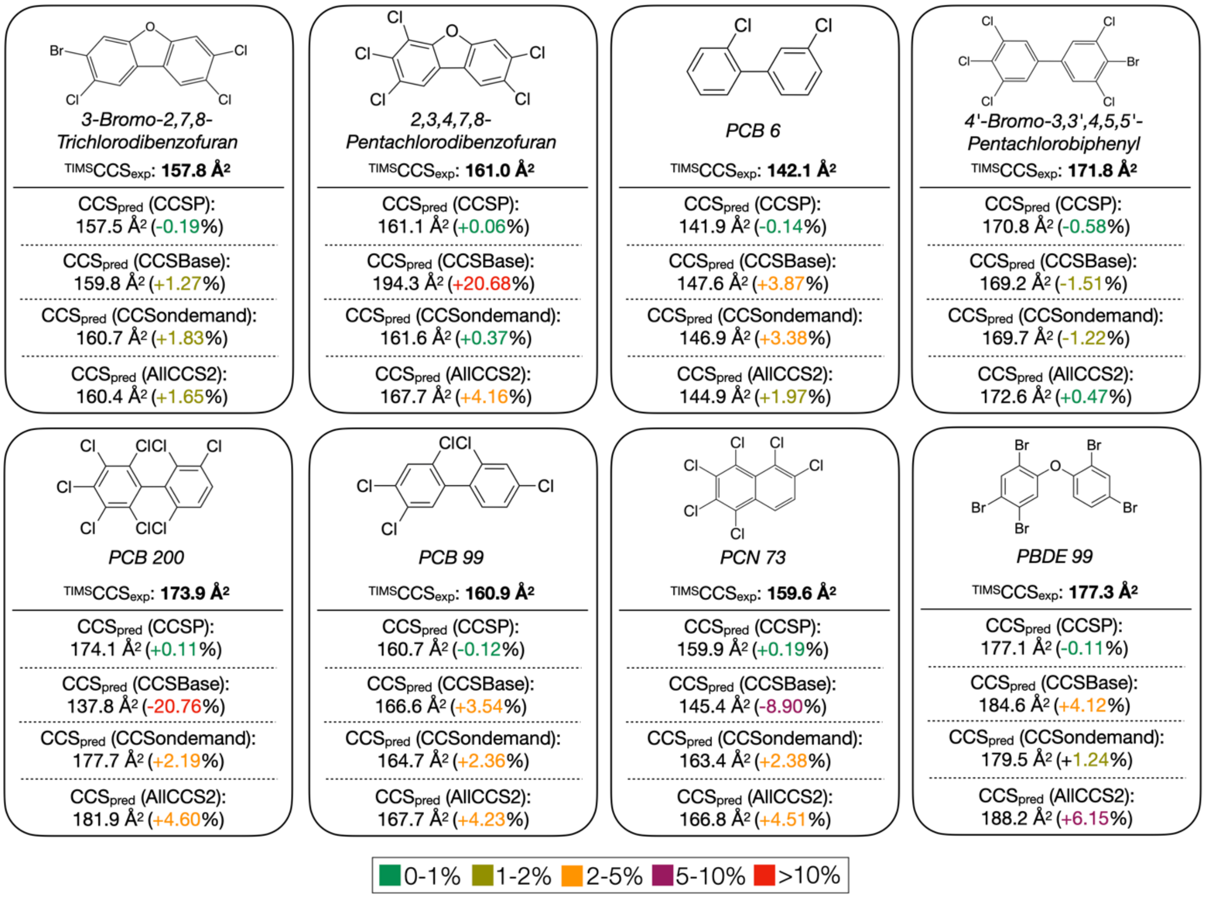

Figure 6.8 – Comparison of experimental $^{TIMS}CCS_{N2}$ values for eight selected halogenated contaminants with predicted values from various machine learning tools. The percentage prediction error is shown in parentheses.

Predicted CCS values using the CCSP 2.0 model were calculated for each tentative level 3 structure (see "CCS pred" in Annex A). For HNP features (6, 7, 24, 25–27, and 35–36), which lacked experimental CCS values in existing libraries, the predicted values were consistently in agreement with the experimentally measured CCS, falling within ±5% bias, providing additional confidence in their tentative identification. Notably, for feature 6, the prediction error for the HNP dimethoxy hexaBDE candidate was significantly lower than that for an alternative isomeric candidate (+2.9% vs. +13.1%), further supporting the proposed chemical class. However, for feature 24 (tentative dimethoxy pentaBDE), features 12–16 (tentative hexaBDEs), and features 17–23 (tentative hexaBBs), the predicted CCS values for other isomeric candidate classes were also within ±5% of the experimental

values. In these cases, the predicted CCS values were therefore not discriminative enough to rule out the alternative candidate structures.
Additionally, predicted CCS values were generated for the missing congeners of the HpBDE, HpBB, HxBDE, and HxBB classes (features 2–3, 4–5, 12–16, and 17–23), enabling the extension of their expected CCS ranges in CCS vs. m/z space compared to those established previously based solely on experimental values (**Figure S6.7**). These extended ranges supported the tentative identifications proposed in the previous section for features corresponding to HxBBs, HpBDEs, and HpBBs, whose experimental CCS values fell within their respective expected ranges. In the case of the tentative HxBDE features, all but one (the feature with the lowest CCS) were within (or very close to) the predicted range, confirming the earlier suspicion that this feature may belong to a different compound class.

6.3 - Conclusion

In this study, we evaluated the capabilities of gas chromatography-ion mobility-mass spectrometry (GC-IM-MS) combined with CCS-based prioritization and advanced data-dependent acquisition strategies, for the non-targeted analysis of halogenated pollutants in complex biological matrices. By leveraging the distinct separation of halogenated and non-halogenated features in the m/z vs $1/K_0$ space, we developed a selective approach to prioritize both relevant features for further data processing and precursor ions for tandem MS acquisition.

Altogether, the preliminary non-targeted data acquired from the blubber of this killer whale using the developed workflow strongly suggest the presence of a wide diversity of both known and likely unknown halogenated substances. These findings support the continued tentative identification of the remaining 179 classes and, more broadly, highlight the potential of IM-based non-targeted screening approaches for comprehensive environmental analysis.

An automated workflow for the identification step would be desirable to accelerate the overall process. Confidence in structural annotations could also be enhanced by integrating additional identification criteria, such as the comparison of acquired tandem mass spectra with spectral libraries or in silico interpretation tools[36] (e.g., MetFrag[58]), as well as the determination of retention time indices (RTIs, such as PAH-based Lee indices[59]) for comparison with experimental or predicted values.

6.4 - References

(1) Jepson, P. D.; Deaville, R.; Barber, J. L.; Aguilar, À.; Borrell, A.; Murphy, S.; Barry, J.; Brownlow, A.; Barnett, J.; Berrow, S.; Cunningham, A. A.; Davison, N. J.; Ten Doeschate, M.; Esteban, R.; Ferreira, M.; Foote, A. D.; Genov, T.; Giménez, J.; Loveridge, J.; Llavona, Á.; Martin, V.; Maxwell, D. L.; Papachlimitzou, A.; Penrose, R.; Perkins, M. W.; Smith, B.; De Stephanis, R.; Tregenza, N.; Verborgh, P.; Fernandez, A.; Law, R. J. PCB Pollution Continues to Impact Populations of Orcas and Other Dolphins in European Waters. *Sci. Rep.* **2016**, *6* (1), 18573. https://doi.org/10.1038/srep18573.
(2) Law, R. J. An Overview of Time Trends in Organic Contaminant Concentrations in Marine Mammals: Going up or Down? *Mar. Pollut. Bull.* **2014**, *82* (1–2), 7–10. https://doi.org/10.1016/j.marpolbul.2014.03.024.
(3) Ross, P. S.; Ellis, G. M.; Ikonomou, M. G.; Barrett-Lennard, L. G.; Addison, R. F. High PCB Concentrations in Free-Ranging Pacific Killer Whales, Orcinus Orca: Effects of Age, Sex and Dietary Preference. *Mar. Pollut. Bull.* **2000**, *40* (6), 504–515. https://doi.org/10.1016/S0025-326X(99)00233-7.

(4) Jones, K. C. Persistent Organic Pollutants (POPs) and Related Chemicals in the Global Environment: Some Personal Reflections. *Environ. Sci. Technol.* **2021**, *55* (14), 9400–9412. https://doi.org/10.1021/acs.est.0c08093.

(5) Formigaro, C.; Henríquez-Hernandez, L. A.; Zaccaroni, A.; Garcia-Hartmann, M.; Camacho, M.; Boada, L. D.; Zumbado, M.; Luzardo, O. P. Assessment of Current Dietary Intake of Organochlorine Contaminants and Polycyclic Aromatic Hydrocarbons in Killer Whales (Orcinus Orca) through Direct Determination in a Group of Whales in Captivity. *Sci. Total Environ.* **2014**, *472*, 1044–1051. https://doi.org/10.1016/j.scitotenv.2013.11.127.

(6) Andvik, C.; Jourdain, E.; Ruus, A.; Lyche, J. L.; Karoliussen, R.; Borgå, K. Preying on Seals Pushes Killer Whales from Norway above Pollution Effects Thresholds. *Sci. Rep.* **2020**, *10* (1), 11888. https://doi.org/10.1038/s41598-020-68659-y.

(7) Desforges, J.-P.; Ferguson, S. H.; Remili, A.; McKinney, M. A.; Watt, C. A.; Matthews, C. J. D. Assessment of Persistent Organic Pollutants in Killer Whales (Orcinus Orca) of the Canadian Arctic: Implications for Subsistence Consumption and Conservation Strategies. *Environ. Res.* **2024**, *244*, 117992. https://doi.org/10.1016/j.envres.2023.117992.

(8) Desforges, J.-P.; Levin, M.; Jasperse, L.; De Guise, S.; Eulaers, I.; Letcher, R. J.; Acquarone, M.; Nordøy, E.; Folkow, L. P.; Hammer Jensen, T.; Grøndahl, C.; Bertelsen, M. F.; St. Leger, J.; Almunia, J.; Sonne, C.; Dietz, R. Effects of Polar Bear and Killer Whale Derived Contaminant Cocktails on Marine Mammal Immunity. *Environ. Sci. Technol.* **2017**, *51* (19), 11431–11439. https://doi.org/10.1021/acs.est.7b03532.

(9) Remili, A.; Dietz, R.; Sonne, C.; Samarra, F. I. P.; Letcher, R. J.; Rikardsen, A. H.; Ferguson, S. H.; Watt, C. A.; Matthews, C. J. D.; Kiszka, J. J.; Rosing-Asvid, A.; McKinney, M. A. Varying Diet Composition Causes Striking Differences in Legacy and Emerging Contaminant Concentrations in Killer Whales across the North Atlantic. *Environ. Sci. Technol.* **2023**, *57* (42), 16109–16120. https://doi.org/10.1021/acs.est.3c05516.

(10) Williams, R. S.; Brownlow, A.; Baillie, A.; Barber, J. L.; Barnett, J.; Davison, N. J.; Deaville, R.; Ten Doeschate, M.; Murphy, S.; Penrose, R.; Perkins, M.; Spiro, S.; Williams, R.; Jepson, P. D.; Curnick, D. J.; Jobling, S. Spatiotemporal Trends Spanning Three Decades Show Toxic Levels of Chemical Contaminants in Marine Mammals. *Environ. Sci. Technol.* **2023**, *57* (49), 20736–20749. https://doi.org/10.1021/acs.est.3c01881.

(11) Desforges, J.-P.; Hall, A.; McConnell, B.; Rosing-Asvid, A.; Barber, J. L.; Brownlow, A.; De Guise, S.; Eulaers, I.; Jepson, P. D.; Letcher, R. J.; Levin, M.; Ross, P. S.; Samarra, F.; Víkingson, G.; Sonne, C.; Dietz, R. Predicting Global Killer Whale Population Collapse from PCB Pollution. *Science* **2018**, *361* (6409), 1373–1376. https://doi.org/10.1126/science.aat1953.

(12) Ross, P. S. Fireproof Killer Whales (*Orcinus Orca*): Flame-Retardant Chemicals and the Conservation Imperative in the Charismatic Icon of British Columbia, Canada. *Can. J. Fish. Aquat. Sci.* **2006**, *63* (1), 224–234. https://doi.org/10.1139/f05-244.

(13) Noël, M.; Barrett-Lennard, L.; Guinet, C.; Dangerfield, N.; Ross, P. S. Persistent Organic Pollutants (POPs) in Killer Whales (Orcinus Orca) from the Crozet Archipelago, Southern Indian Ocean. *Mar. Environ. Res.* **2009**, *68* (4), 196–202. https://doi.org/10.1016/j.marenvres.2009.06.009.

(14) Haraguchi, K.; Hisamichi, Y.; Endo, T. Accumulation and Mother-to-Calf Transfer of Anthropogenic and Natural Organohalogens in Killer Whales (Orcinus Orca) Stranded on the Pacific Coast of Japan. *Sci. Total Environ.* **2009**, *407* (8), 2853–2859. https://doi.org/10.1016/j.scitotenv.2009.01.003.

(15) Rayne, S.; Ikonomou, M. G.; Ross, P. S.; Ellis, G. M.; Barrett-Lennard, L. G. PBDEs, PBBs, and PCNs in Three Communities of Free-Ranging Killer Whales (*Orcinus Orca*) from the Northeastern Pacific Ocean. *Environ. Sci. Technol.* **2004**, *38* (16), 4293–4299. https://doi.org/10.1021/es0495011.

(16) Lee, K.; Alava, J. J.; Cottrell, P.; Cottrell, L.; Grace, R.; Zysk, I.; Raverty, S. Emerging Contaminants and New POPs (PFAS and HBCDD) in Endangered Southern Resident and Bigg's (Transient) Killer Whales (*Orcinus Orca*): *In Utero* Maternal Transfer and Pollution Management Implications. *Environ. Sci. Technol.* **2023**, *57* (1), 360–374. https://doi.org/10.1021/acs.est.2c04126.

(17) Kajiwara, N.; Kunisue, T.; Kamikawa, S.; Ochi, Y.; Yano, S.; Tanabe, S. Organohalogen and Organotin Compounds in Killer Whales Mass-Stranded in the Shiretoko Peninsula, Hokkaido, Japan. *Mar. Pollut. Bull.* **2006**, *52* (9), 1066–1076. https://doi.org/10.1016/j.marpolbul.2006.01.011.

(18) Andvik, C.; Jourdain, E.; Ruus, A.; Lyche, J. L.; Karoliussen, R.; Borgå, K. Preying on Seals Pushes Killer Whales from Norway above Pollution Effects Thresholds. *Sci. Rep.* **2020**, *10* (1), 11888. https://doi.org/10.1038/s41598-020-68659-y.

(19) Andvik, C.; Jourdain, E.; Lyche, J. L.; Karoliussen, R.; Borgå, K. High Levels of Legacy and Emerging Contaminants in Killer Whales (*Orcinus Orca*) from Norway, 2015 to 2017. *Environ. Toxicol. Chem.* **2021**, *40* (7), 1848–1858. https://doi.org/10.1002/etc.5064.

(20) Andvik, C.; Jourdain, E.; Borgen, A.; Lyche, J. L.; Karoliussen, R.; Haug, T.; Borgå, K. Intercorrelations of Chlorinated Paraffins, Dechloranes, and Legacy Persistent Organic Pollutants in 10 Species of Marine Mammals from Norway, in Light of Dietary Niche. *Environ. Sci. Technol.* **2024**, *58* (33), 14797–14811. https://doi.org/10.1021/acs.est.4c02625.

(21) Pedersen, A. F.; Bayen, S.; Liu, L.; Dietz, R.; Sonne, C.; Rosing-Asvid, A.; Ferguson, S. H.; McKinney, M. A. Nontarget and Suspect Screening Reveals the Presence of Multiple Plastic-Related Compounds in Polar Bear, Killer Whale, Narwhal and Long-Finned Pilot Whale Blubber from East Greenland. *Environ. Pollut.* **2024**, *357*, 124417. https://doi.org/10.1016/j.envpol.2024.124417.

(22) Shaul, N. J.; Dodder, N. G.; Aluwihare, L. I.; Mackintosh, S. A.; Maruya, K. A.; Chivers, S. J.; Danil, K.; Weller, D. W.; Hoh, E. Nontargeted Biomonitoring of Halogenated Organic Compounds in Two Ecotypes of Bottlenose Dolphins (*Tursiops Truncatus*) from the Southern California Bight. *Environ. Sci. Technol.* **2015**, *49* (3), 1328–1338. https://doi.org/10.1021/es505156q.

(23) Rebryk, A.; Gallampois, C.; Haglund, P. A Time-Trend Guided Non-Target Screening Study of Organic Contaminants in Baltic Sea Harbor Porpoise (1988–2019), Guillemot (1986–2019), and White-Tailed Sea Eagle (1965–2017) Using Gas Chromatography–High-Resolution Mass Spectrometry. *Sci. Total Environ.* **2022**, *829*, 154620. https://doi.org/10.1016/j.scitotenv.2022.154620.

(24) Rebryk, A.; Haglund, P. Non-Targeted Screening Workflows for Gas Chromatography–High-Resolution Mass Spectrometry Analysis and Identification of Biomagnifying Contaminants in Biota Samples. *Anal. Bioanal. Chem.* **2021**, *413* (2), 479–501. https://doi.org/10.1007/s00216-020-03018-4.

(25) Benigni, P.; Fernandez-Lima, F. Oversampling Selective Accumulation Trapped Ion Mobility Spectrometry Coupled to FT-ICR MS: Fundamentals and Applications. *Anal. Chem.* **2016**, *88* (14), 7404–7412. https://doi.org/10.1021/acs.analchem.6b01946.

(26) Kirkwood-Donelson, K. I.; Dodds, J. N.; Schnetzer, A.; Hall, N.; Baker, E. S. Uncovering Per- and Polyfluoroalkyl Substances (PFAS) with Nontargeted Ion Mobility Spectrometry–Mass Spectrometry Analyses. *Sci. Adv.* **2023**, *9* (43), eadj7048. https://doi.org/10.1126/sciadv.adj7048.

(27) MacNeil, A.; Li, X.; Amiri, R.; Muir, D. C. G.; Simpson, A.; Simpson, M. J.; Dorman, F. L.; Jobst, K. J. Gas Chromatography-(Cyclic) Ion Mobility Mass Spectrometry: A Novel Platform for the Discovery of Unknown Per-/Polyfluoroalkyl Substances. *Anal. Chem.* **2022**, *94* (31), 11096–11103. https://doi.org/10.1021/acs.analchem.2c02325.

(28) Menger, F.; Celma, A.; Schymanski, E. L.; Lai, F. Y.; Bijlsma, L.; Wiberg, K.; Hernández, F.; Sancho, J. V.; Ahrens, L. Enhancing Spectral Quality in Complex Environmental Matrices: Supporting Suspect and Non-Target Screening in Zebra Mussels with Ion Mobility. *Environ. Int.* **2022**, *170*, 107585. https://doi.org/10.1016/j.envint.2022.107585.

(29) Zhou, Z.; Luo, M.; Chen, X.; Yin, Y.; Xiong, X.; Wang, R.; Zhu, Z.-J. Ion Mobility Collision Cross-Section Atlas for Known and Unknown Metabolite Annotation in Untargeted Metabolomics. *Nat. Commun.* **2020**, *11* (1), 4334. https://doi.org/10.1038/s41467-020-18171-8.

(30) Meier, F.; Brunner, A.-D.; Koch, S.; Koch, H.; Lubeck, M.; Krause, M.; Goedecke, N.; Decker, J.; Kosinski, T.; Park, M. A.; Bache, N.; Hoerning, O.; Cox, J.; Räther, O.; Mann, M. Online Parallel Accumulation–Serial Fragmentation (PASEF) with a Novel Trapped Ion Mobility Mass Spectrometer. *Mol. Cell. Proteomics* **2018**, *17* (12), 2534–2545. https://doi.org/10.1074/mcp.TIR118.000900.

(31) Merel, S. Critical Assessment of the Kendrick Mass Defect Analysis as an Innovative Approach to Process High Resolution Mass Spectrometry Data for Environmental Applications. *Chemosphere* **2023**, *313*, 137443. https://doi.org/10.1016/j.chemosphere.2022.137443.

(32) Jobst, K. J.; Shen, L.; Reiner, E. J.; Taguchi, V. Y.; Helm, P. A.; McCrindle, R.; Backus, S. The Use of Mass Defect Plots for the Identification of (Novel) Halogenated Contaminants in the Environment. *Anal. Bioanal. Chem.* **2013**, *405* (10), 3289–3297. https://doi.org/10.1007/s00216-013-6735-2.

(33) Léon, A.; Cariou, R.; Hutinet, S.; Hurel, J.; Guitton, Y.; Tixier, C.; Munschy, C.; Antignac, J.-P.; Dervilly-Pinel, G.; Le Bizec, B. HaloSeeker 1.0: A User-Friendly Software to Highlight Halogenated Chemicals in Nontargeted High-Resolution Mass Spectrometry Data Sets. *Anal. Chem.* **2019**, *91* (5), 3500–3507. https://doi.org/10.1021/acs.analchem.8b05103.

(34) Zhang, X.; Di Lorenzo, R. A.; Helm, P. A.; Reiner, E. J.; Howard, P. H.; Muir, D. C. G.; Sled, J. G.; Jobst, K. J. Compositional Space: A Guide for Environmental Chemists on the Identification of Persistent and Bioaccumulative Organics Using Mass Spectrometry. *Environ. Int.* **2019**, *132*, 104808. https://doi.org/10.1016/j.envint.2019.05.002.

(35) Foster, M.; Rainey, M.; Watson, C.; Dodds, J. N.; Kirkwood, K. I.; Fernández, F. M.; Baker, E. S. Uncovering PFAS and Other Xenobiotics in the Dark Metabolome Using Ion Mobility Spectrometry, Mass Defect Analysis, and Machine Learning. *Environ. Sci. Technol.* **2022**, *56* (12), 9133–9143. https://doi.org/10.1021/acs.est.2c00201.

(36) Hollender, J.; Schymanski, E. L.; Ahrens, L.; Alygizakis, N.; Béen, F.; Bijlsma, L.; Brunner, A. M.; Celma, A.; Fildier, A.; Fu, Q.; Gago-Ferrero, P.; Gil-Solsona, R.; Haglund, P.; Hansen, M.; Kaserzon, S.; Kruve, A.; Lamoree, M.; Margoum, C.; Meijer, J.; Merel, S.; Rauert, C.; Rostkowski, P.; Samanipour, S.; Schulze, B.; Schulze, T.; Singh, R. R.; Slobodnik, J.; Steininger-Mairinger, T.; Thomaidis, N. S.; Togola, A.; Vorkamp, K.; Vulliet, E.; Zhu, L.; Krauss, M. NORMAN Guidance on Suspect and Non-Target Screening in Environmental Monitoring. *Environ. Sci. Eur.* **2023**, *35* (1), 75. https://doi.org/10.1186/s12302-023-00779-4.

(37) Monge, M. E.; Dodds, J. N.; Baker, E. S.; Edison, A. S.; Fernández, F. M. Challenges in Identifying the Dark Molecules of Life. *Annu. Rev. Anal. Chem.* **2019**, *12* (1), 177–199. https://doi.org/10.1146/annurev-anchem-061318-114959.

(38) Meier, F.; Beck, S.; Grassl, N.; Lubeck, M.; Park, M. A.; Raether, O.; Mann, M. Parallel Accumulation–Serial Fragmentation (PASEF): Multiplying Sequencing Speed and Sensitivity by Synchronized Scans in a Trapped Ion Mobility Device. *J. Proteome Res.* **2015**, *14* (12), 5378–5387. https://doi.org/10.1021/acs.jproteome.5b00932.

(39) Schymanski, E. L.; Jeon, J.; Gulde, R.; Fenner, K.; Ruff, M.; Singer, H. P.; Hollender, J. Identifying Small Molecules via High Resolution Mass Spectrometry: Communicating Confidence. *Environ. Sci. Technol.* **2014**, *48* (4), 2097–2098. https://doi.org/10.1021/es5002105.

(40) Cariou, R.; Méndez-Fernandez, P.; Hutinet, S.; Guitton, Y.; Caurant, F.; Le Bizec, B.; Spitz, J.; Vetter, W.; Dervilly, G. Nontargeted LC/ESI-HRMS Detection of Polyhalogenated Compounds in Marine Mammals Stranded on French Atlantic Coasts. *ACS EST Water* **2021**, *1* (2), 309–318. https://doi.org/10.1021/acsestwater.0c00091.

(41) Singh, R. R.; Aminot, Y.; Héas-Moisan, K.; Preud'homme, H.; Munschy, C. Cracked and Shucked: GC-APCI-IMS-HRMS Facilitates Identification of Unknown Halogenated Organic Chemicals in French Marine Bivalves. *Environ. Int.* **2023**, *178*, 108094. https://doi.org/10.1016/j.envint.2023.108094.

(42) Picache, J. A.; Rose, B. S.; Balinski, A.; Leaptrot, K. L.; Sherrod, S. D.; May, J. C.; McLean, J. A. Collision Cross Section Compendium to Annotate and Predict Multi-Omic Compound Identities. *Chem. Sci.* **2019**, *10* (4), 983–993. https://doi.org/10.1039/C8SC04396E.

(43) Palm, E. H.; Engelhardt, J.; Tshepelevitsh, S.; Weiss, J.; Kruve, A. Gas Phase Reactivity of Isomeric Hydroxylated Polychlorinated Biphenyls. *J. Am. Soc. Mass Spectrom.* **2024**, *35* (5), 1021–1029. https://doi.org/10.1021/jasms.4c00035.

(44) Dodds, J. N.; Baker, E. S. Ion Mobility Spectrometry: Fundamental Concepts, Instrumentation, Applications, and the Road Ahead. *J. Am. Soc. Mass Spectrom.* **2019**, *30* (11), 2185–2195. https://doi.org/10.1007/s13361-019-02288-2.

(45) Celma, A.; Sancho, J. V.; Schymanski, E. L.; Fabregat-Safont, D.; Ibáñez, M.; Goshawk, J.; Barknowitz, G.; Hernández, F.; Bijlsma, L. Improving Target and Suspect Screening High-Resolution Mass Spectrometry Workflows in Environmental Analysis by Ion Mobility Separation. *Environ. Sci. Technol.* **2020**, *54* (23), 15120–15131. https://doi.org/10.1021/acs.est.0c05713.

(46) Goscinny, S.; Joly, L.; De Pauw, E.; Hanot, V.; Eppe, G. Travelling-Wave Ion Mobility Time-of-Flight Mass Spectrometry as an Alternative Strategy for Screening of Multi-Class Pesticides in Fruits and Vegetables. *J. Chromatogr. A* **2015**, *1405*, 85–93. https://doi.org/10.1016/j.chroma.2015.05.057.

(47) Celma, A.; Ahrens, L.; Gago-Ferrero, P.; Hernández, F.; López, F.; Lundqvist, J.; Pitarch, E.; Sancho, J. V.; Wiberg, K.; Bijlsma, L. The Relevant Role of Ion Mobility Separation in LC-HRMS Based Screening Strategies for Contaminants of Emerging Concern in the Aquatic Environment. *Chemosphere* **2021**, *280*, 130799. https://doi.org/10.1016/j.chemosphere.2021.130799.

(48) Izquierdo-Sandoval, D.; Fabregat-Safont, D.; Lacalle-Bergeron, L.; Sancho, J. V.; Hernández, F.; Portoles, T. Benefits of Ion Mobility Separation in GC-APCI-HRMS Screening: From the Construction of a CCS Library to the Application to Real-World Samples. *Anal. Chem.* **2022**, *94* (25), 9040–9047. https://doi.org/10.1021/acs.analchem.2c01118.

(49) Zhou, Z.; Tu, J.; Zhu, Z.-J. Advancing the Large-Scale CCS Database for Metabolomics and Lipidomics at the Machine-Learning Era. *Curr. Opin. Chem. Biol.* **2018**, *42*, 34–41. https://doi.org/10.1016/j.cbpa.2017.10.033.

(50) Schymanski, E. L.; Kondić, T.; Neumann, S.; Thiessen, P. A.; Zhang, J.; Bolton, E. E. Empowering Large Chemical Knowledge Bases for Exposomics: PubChemLite Meets MetFrag. *J. Cheminformatics* **2021**, *13* (1), 19. https://doi.org/10.1186/s13321-021-00489-0.

(51) Elapavalore, A.; Ross, D. H.; Grouès, V.; Aurich, D.; Krinsky, A. M.; Kim, S.; Thiessen, P. A.; Zhang, J.; Dodds, J. N.; Baker, E. S.; Bolton, E. E.; Xu, L.; Schymanski, E. L. PubChemLite Plus Collision Cross Section (CCS) Values for Enhanced Interpretation of Nontarget Environmental Data. *Environ. Sci. Technol. Lett.* **2025**, *12* (2), 166–174. https://doi.org/10.1021/acs.estlett.4c01003.

(52) Zhang, H.; Luo, M.; Wang, H.; Ren, F.; Yin, Y.; Zhu, Z.-J. AllCCS2: Curation of Ion Mobility Collision Cross-Section Atlas for Small Molecules Using Comprehensive Molecular Representations. *Anal. Chem.* **2023**, *95* (37), 13913–13921. https://doi.org/10.1021/acs.analchem.3c02267.

(53) Ross, D. H.; Cho, J. H.; Xu, L. Breaking Down Structural Diversity for Comprehensive Prediction of Ion-Neutral Collision Cross Sections. *Anal. Chem.* **2020**, *92* (6), 4548–4557. https://doi.org/10.1021/acs.analchem.9b05772.

(54) Rainey, M. A.; Watson, C. A.; Asef, C. K.; Foster, M. R.; Baker, E. S.; Fernández, F. M. CCS Predictor 2.0: An Open-Source Jupyter Notebook Tool for Filtering Out False Positives in Metabolomics. *Anal. Chem.* **2022**, *94* (50), 17456–17466. https://doi.org/10.1021/acs.analchem.2c03491.

(55) Plante, P.-L.; Francovic-Fontaine, É.; May, J. C.; McLean, J. A.; Baker, E. S.; Laviolette, F.; Marchand, M.; Corbeil, J. Predicting Ion Mobility Collision Cross-Sections Using a Deep Neural Network: DeepCCS. *Anal. Chem.* **2019**, *91* (8), 5191–5199. https://doi.org/10.1021/acs.analchem.8b05821.

(56) Broeckling, C. D.; Yao, L.; Isaac, G.; Gioioso, M.; Ianchis, V.; Vissers, J. P. C. Application of Predicted Collisional Cross Section to Metabolome Databases to Probabilistically Describe the Current and Future Ion Mobility Mass Spectrometry. *J. Am. Soc. Mass Spectrom.* **2021**, *32* (3), 661–669. https://doi.org/10.1021/jasms.0c00375.

(57) Song, X.-C.; Dreolin, N.; Canellas, E.; Goshawk, J.; Nerin, C. Prediction of Collision Cross-Section Values for Extractables and Leachables from Plastic Products. *Environ. Sci. Technol.* **2022**, *56* (13), 9463–9473. https://doi.org/10.1021/acs.est.2c02853.

(58) Ruttkies, C.; Schymanski, E. L.; Wolf, S.; Hollender, J.; Neumann, S. MetFrag Relaunched: Incorporating Strategies beyond in Silico Fragmentation. *J. Cheminformatics* **2016**, *8* (1), 3. https://doi.org/10.1186/s13321-016-0115-9.

(59) Lee, M. L.; Vassilaros, D. L.; White, C. M. Retention Indices for Programmed-Temperature Capillary-Column Gas Chromatography of Polycyclic Aromatic Hydrocarbons. *Anal. Chem.* **1979**, *51* (6), 768–773. https://doi.org/10.1021/ac50042a043.

6.5 - Supporting information

TABLES

Table S6.1: GC parameters.

Gas flow	1.5 mL/min, Helium
Injection	1 μL, splitless
Injector temperature	275°C
Temperature program	• 40°C, held 1 min • 310°C @ 7°C/min, held 20 min ⇒ Total: 59.6 min

Table S6.2: GC-APCI source parameters.

Transfer line temperature	300°C
Source temperature	300°C
End plate offset	-500 V
Capillary	-4500 V
Corona	+1000 nA
Nebulizer	2.4 Bar
Dry gas	1.5 L/min
Dry temperature	175°C

Table S6.3: TIMS parameters.

Accumulation time (duty cycle %)		100 ms (50%)
Ramp time (spectra rate)		200 ms (~5 Hz)
Accumulation range		Same as analysis range
Analysis range	$1/K_0$	0.6 – 1.0 $1/K_0$ $\Delta 1/K_0 = 0.40$
Tunnel pressure	Entrance (P1)	3.04 mBar
	Exit (P2)	0.85 mBar
	ΔP	2.19 mbar
IM cell temperature		Not available
RF voltage		250 V_{pp}
Transfer voltages	D1	- 20 V
	D2	- 120 V
	D3	50 V
	D4	20 V
	D5	0 V
	D6	100 V

Table S6.4: qTOF parameters. Three sets of parameters were used at different times during the analysis to optimize the transmission of both lower and higher m/z ions

	Set 1 Start – 26 min	Set 2 26 min – 34 min	Set 3 34 min – end
Funnel 2 RF	200 V_{pp}	250 V_{pp}	300 V_{pp}
Multipole RF	200 V_{pp}	250 V_{pp}	300 V_{pp}
Collision RF	800 V_{pp}	1000 V_{pp}	1200 V_{pp}
Quadrupole energy	8 eV	9 eV	10 eV
Collision cell energy	8 eV	9 eV	10 eV
Collision cell in	190 V	190 V	190 V
Transfert time	55 µs	60 µs	70 µs
Prepulse storage	7 µs	9 µs	11 µs

Table S6.5: PASEF parameters.

PASEF scan	1 (cycle time 0,41 sec)
Precursor ion	MS repetition 1; cycle overlap 1
Charge range	Polygon centered on halogenated POPs
Intensity threshold	2000
Scheduling	Target intensity 20000
Active exclusion	ON: release after 6s; reconsider if ratio ≥4
Exclusion window	0.015 m/z - 0.015 1/K_0
Isolation width	1 m/z (200 Da) - 2 m/z (800 Da)
Collision energy	40 eV (0.6 1/K_0) - 50 eV (1 1/K_0)
Mobilogram	Summation width 25, max number of peaks 3

FIGURES

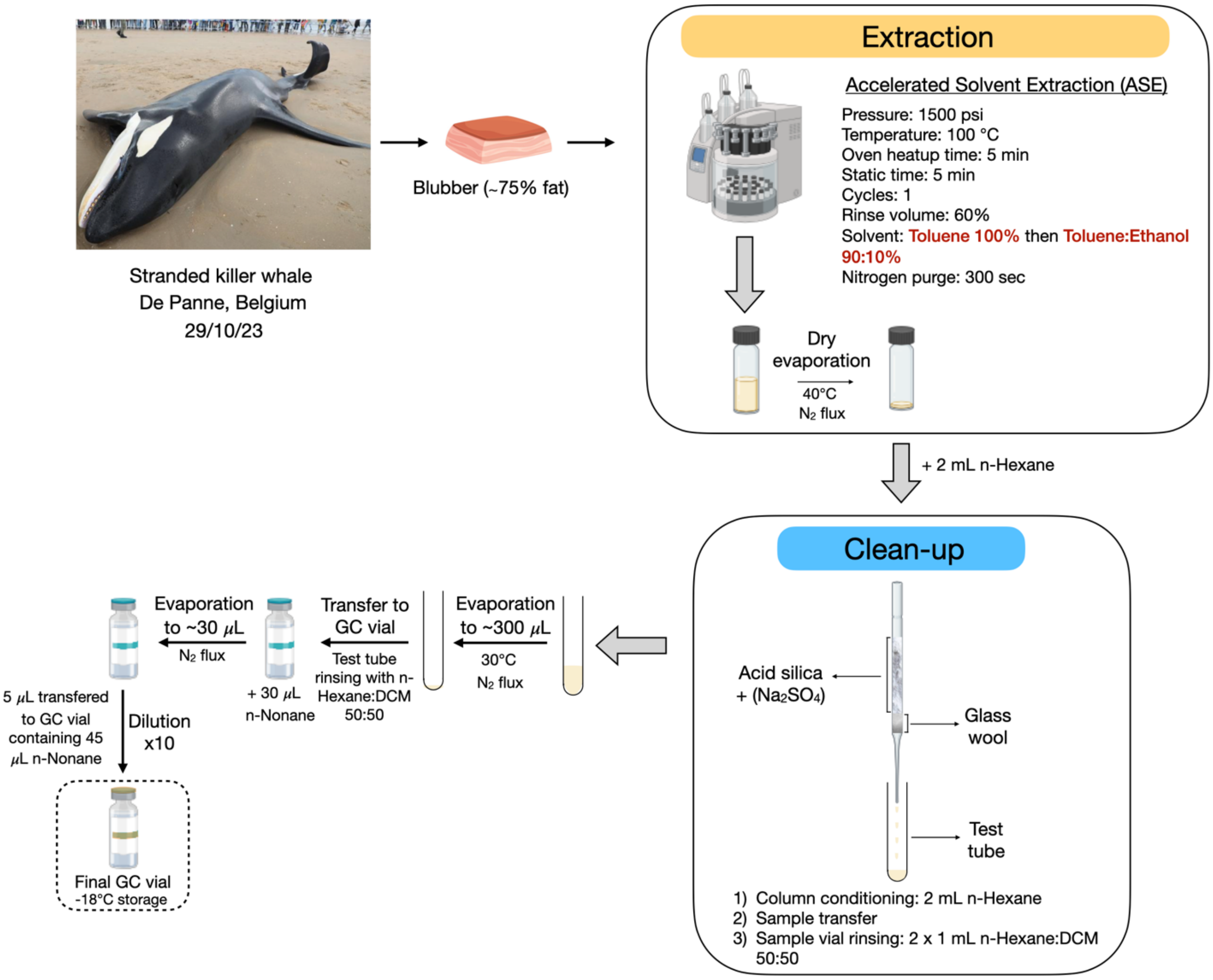

Figure S6.1 – Schematic overview of the sample preparation workflow.

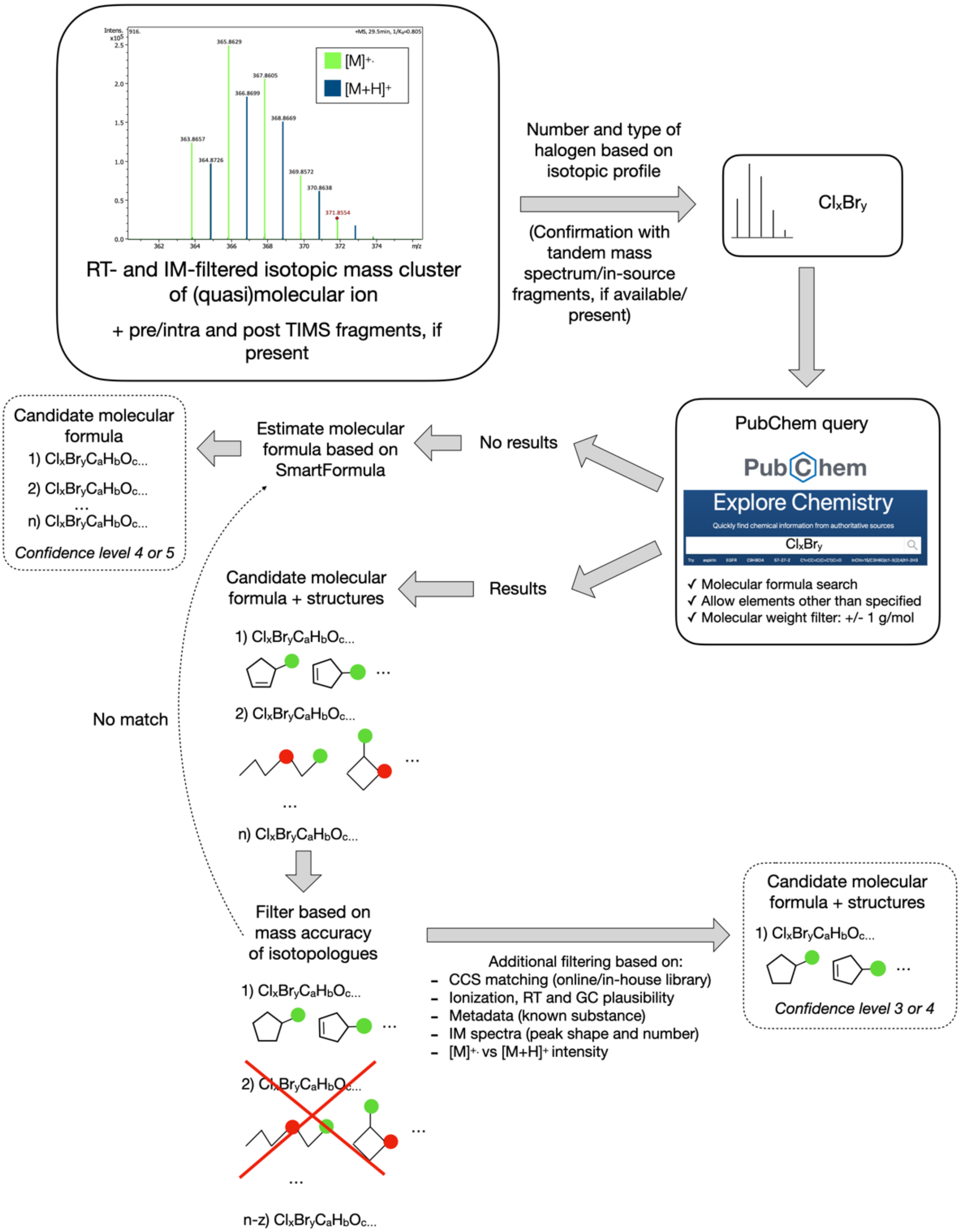

Figure S6.2 – Schematic overview of the feature identification workflow.

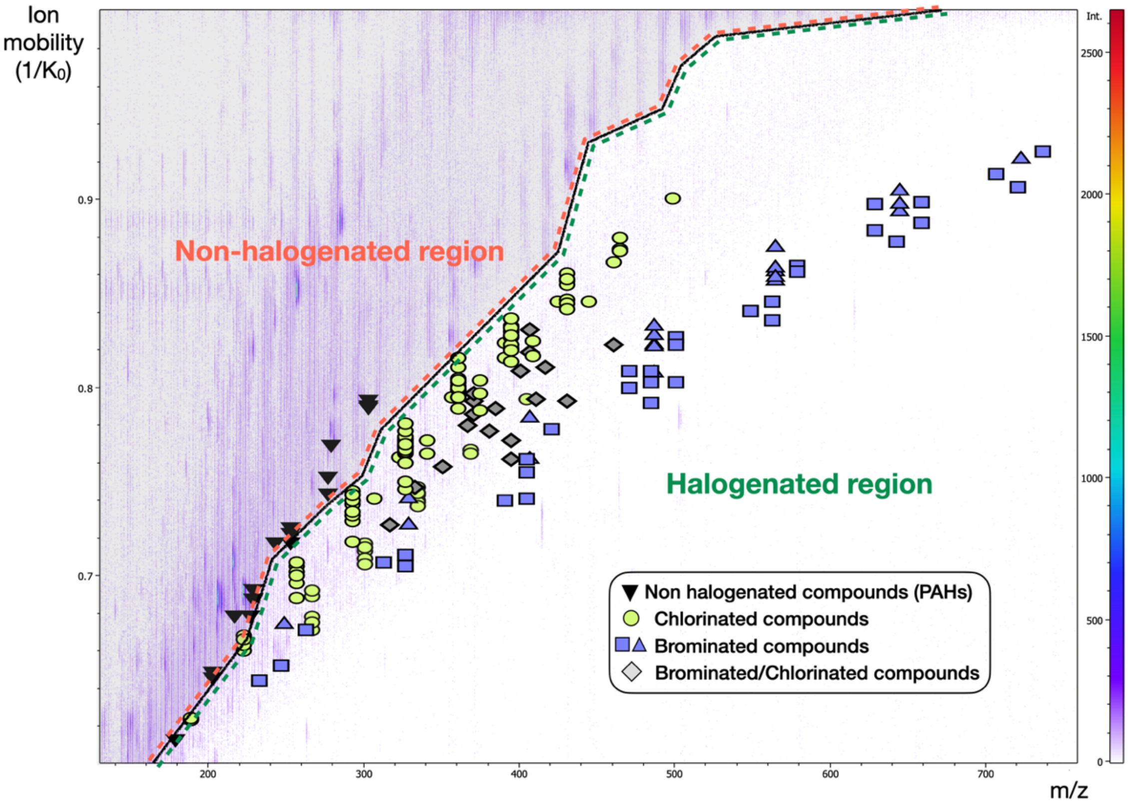

Figure S6.3 – Superposition of in-house 1/K$_0$ reference values from ca. 200 halogenated compounds and 21 PAH standards onto the heatmap shown in Figure 3.

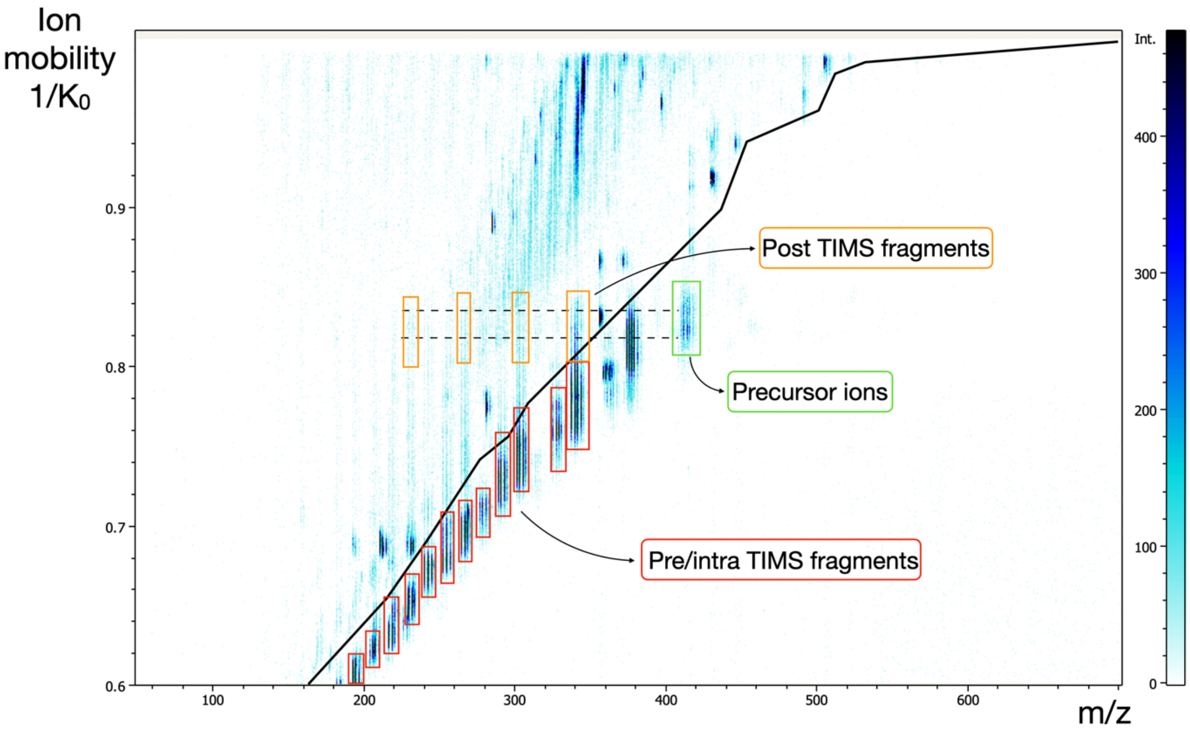

Figure S6.4 – Heatmap #9074 showing feature m/z 412.812 and its associated pre/intra and post TIMS fragments.

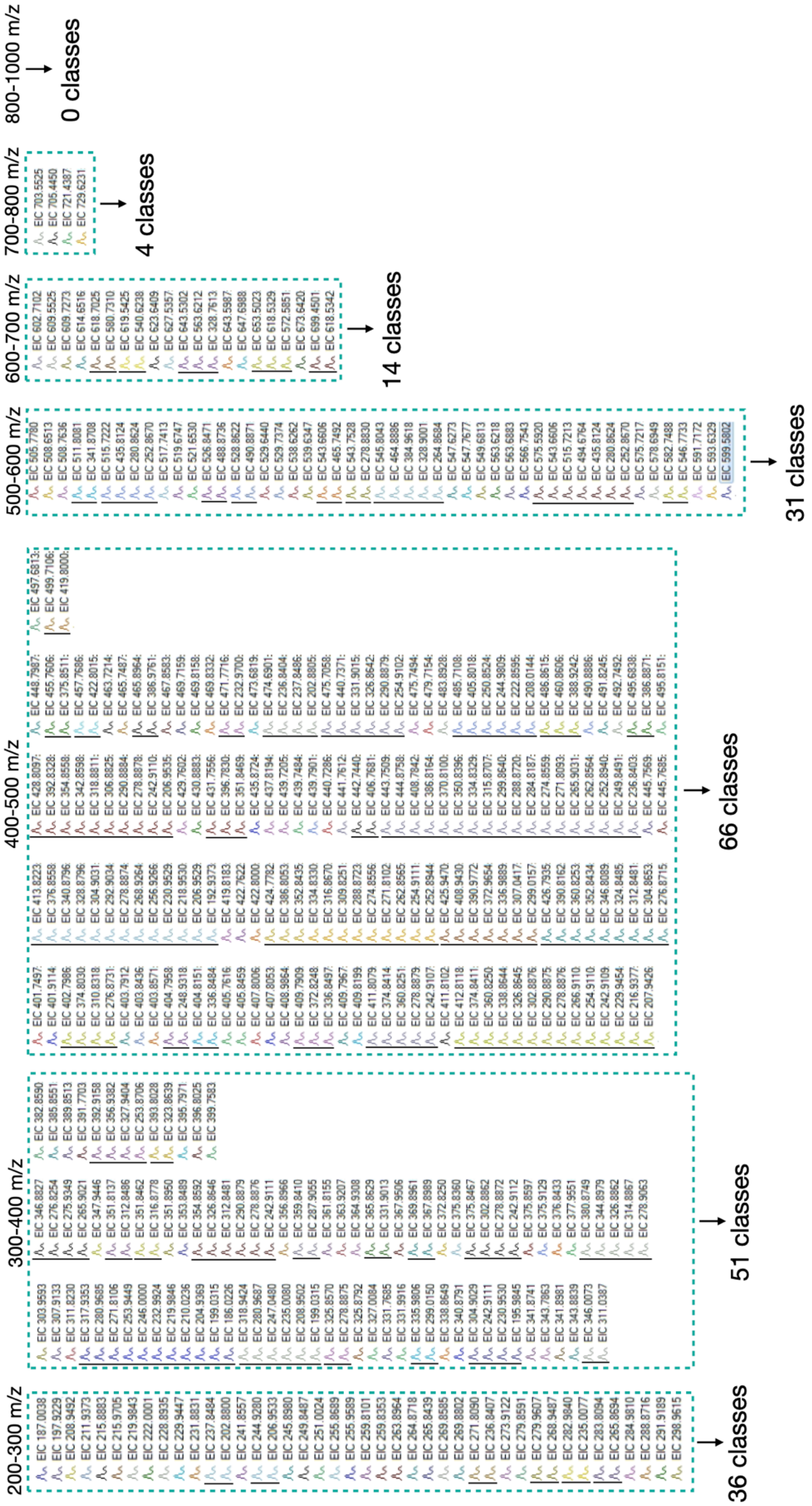

Figure S6.5 –List of the mass-to-charge ratios of the 202 classes of halogenated compounds and their corresponding fragments. Precursor ions and their associated fragment(s) were grouped together, as indicated by the black lines.

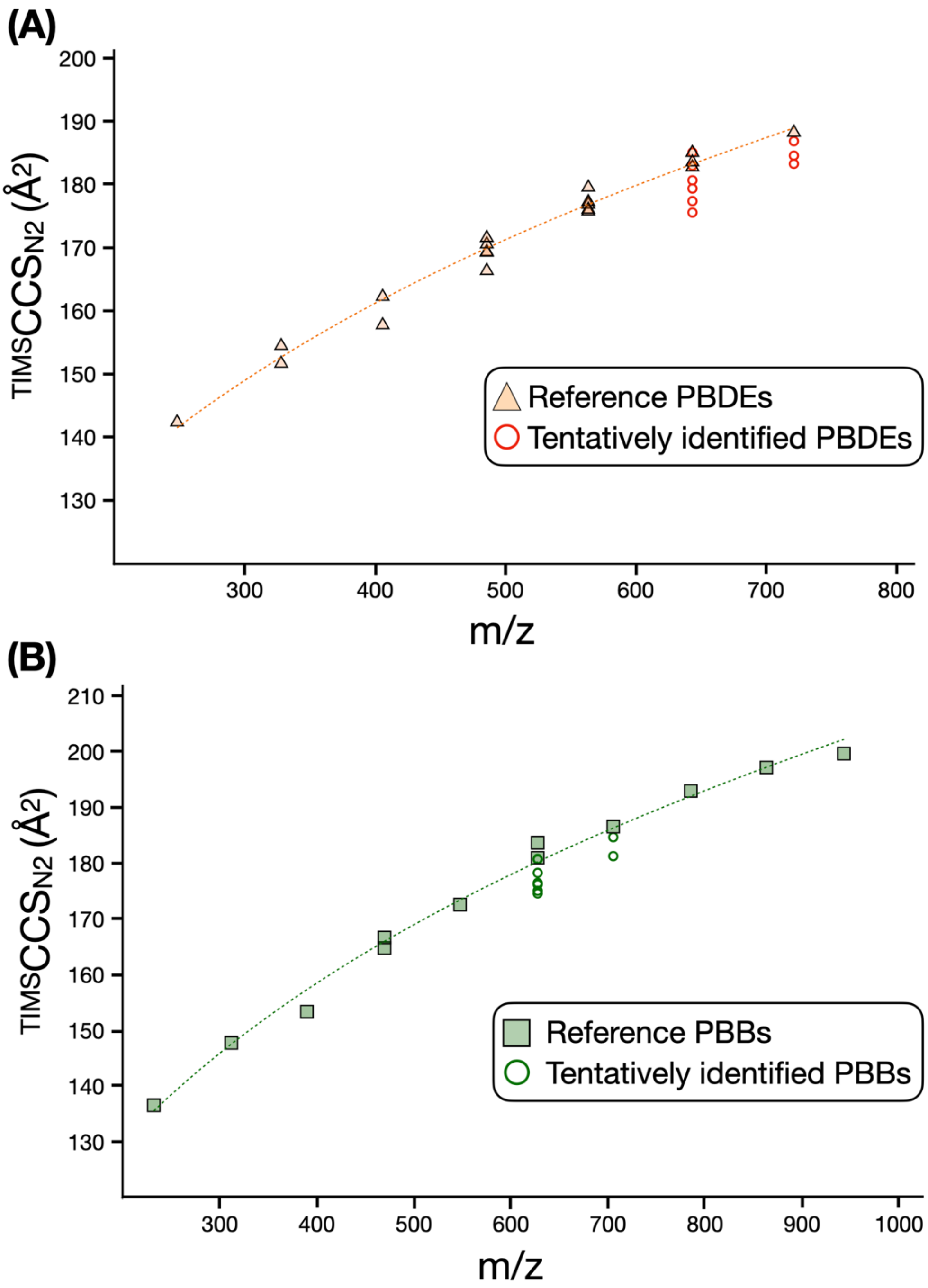

Figure S6.6 – Comparison of the $^{TIMS}CCS_{N2}$ values of the tentatively identified PBDEs **(A)** and PBBs **(B)** with those of the reference in-house values (found in Appendix F) in the CCS vs m/z space.

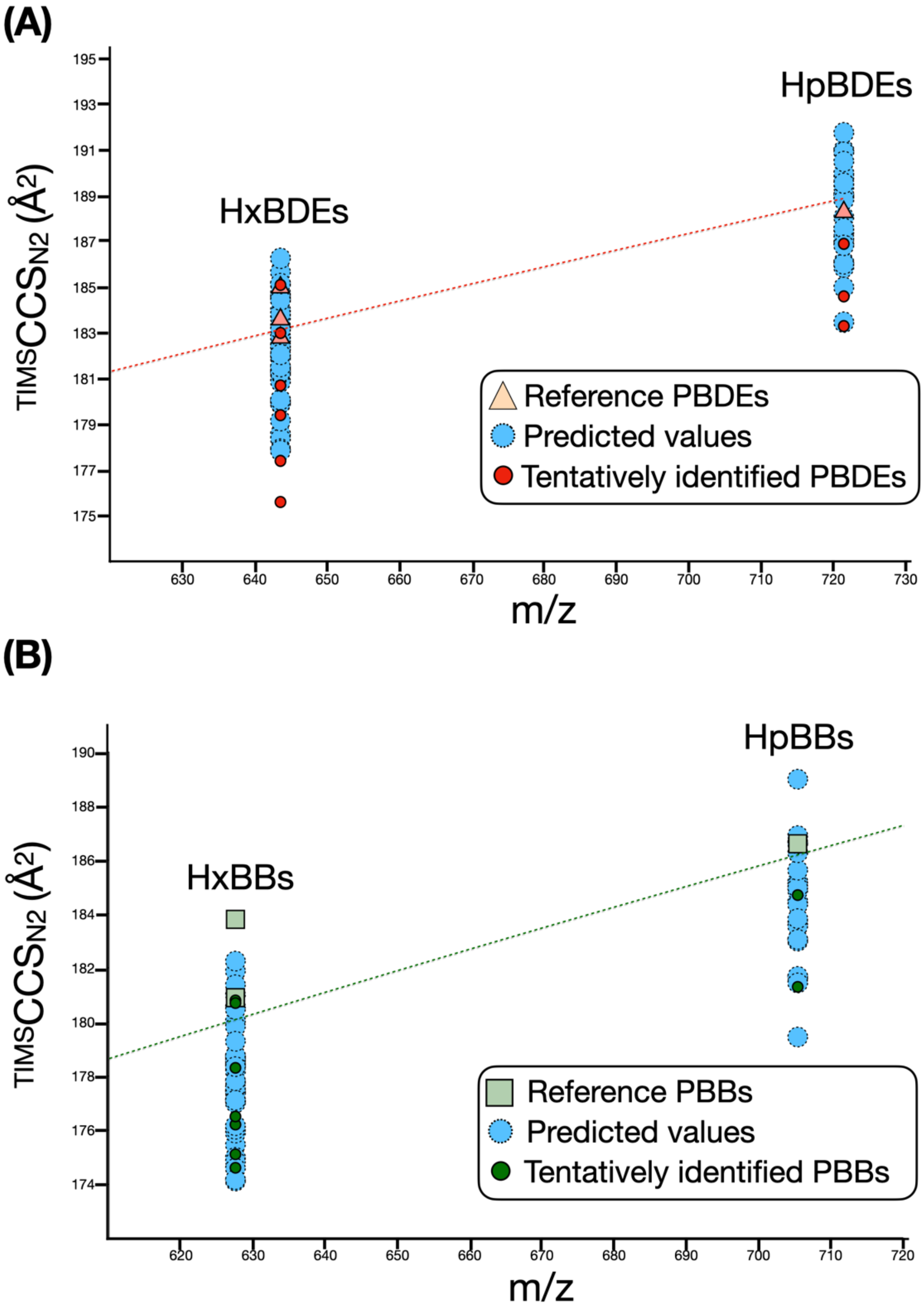

Figure S6.7 –Comparison of the $^{TIMS}CCS_{N2}$values of the tentatively identified HxBDEs–HpBDEs (A) and HxBBs–HpBBs (B) with both in-house reference values and machine learning–predicted values in CCS vs. m/z space. Predicted CCS values for HxBDEs (n = 39), HpBDEs (n = 23), HxBBs (n = 40) and HpBBs (n = 22) were generated using the CCSP 2.0 model.

Chapter 7:
General conclusion and outlook

The initial aims and objectives of this thesis were rooted in the context of environmental contamination by chemical pollutants - a persistent global issue, particularly concerning halogenated persistent organic pollutants[1,2]. These substances are well known for their toxicity, environmental persistence, and bioaccumulative nature. The introductory chapter provided a broad overview of the current strategies for monitoring and regulating such compounds, highlighting the need for analytical techniques that are both sensitive and selective[3]. Over the past decades, gas chromatography coupled with mass spectrometry (GC-MS) has remained the benchmark for the detection and quantification of semi-volatile POPs[4]. In particular, GC-quadrupole (GC-Q), triple quadrupole (GC-QqQ), and sector field MS configurations have been extensively employed in both regulatory frameworks and scientific research[5].

In addition, the thesis introduced ion mobility spectrometry (IMS) as an emerging and promising complementary separation technique[6]. When coupled with mass spectrometry (IM-MS), IMS adds a valuable orthogonal separation dimension, improving selectivity and increasing confidence in compound identification, particularly in complex matrices. Despite its potential, however, the application of IM–MS for environmental contaminant analysis, especially when hyphenated with gas chromatography, was still at a nascent stage when this doctoral research began[7,8]. Most existing applications were restricted to liquid chromatography-compatible compounds such as pesticides and pharmaceuticals, relied on lower-resolution IMS technologies (e.g., drift tube and travelling wave IMS), and were generally limited to qualitative analyses.

This doctoral research was therefore undertaken to address these limitations and to expand the capabilities of IM-MS within the field of environmental chemistry. The research conducted to achieve these objectives is summarized and discussed in the following sections.

Objective I: development and optimization of a GC-hyphenated IM-MS system suitable for GC-amenable compounds

The methods were developed on a Bruker timsTOF pro 2 hyphenated to a gas chromatograph via a GC-APCI interface. First of all, it was found that the establishment of a robust CCS calibration procedure for this type of configuration proved to be essential due to the specific challenges introduced by the GC-APCI ion source (Section 3.2.1). The inability to perform direct infusion-based calibrations, as commonly done with standard ESI or LC-APCI sources, necessitated the development of alternative strategies. Initial efforts focused on transferring calibration coefficients determined with a different ion source (Section 3.2.1A). However, these experiments revealed that installing the GC-APCI source led to measurable shifts in ion mobility values. These shifts were primarily attributed to changes in the analytical drift gas properties, particularly a decrease in the entrance pressure caused by the high operating temperature of the GC-APCI source.

To address this, an external calibration strategy using polycyclic aromatic hydrocarbons (PAHs) was first implemented, showing strong linearity between measured TIMS CCS values and reference DTIMS values (Section 3.2.1B). However, the method's practical drawbacks (such as high cost, toxicity, lengthy analysis time, and lack of real-time calibration) motivated the search for a better alternative. Consequently, background siloxane ions, naturally present during GC runs, were investigated as internal calibrants (Section 3.2.1C). Five siloxane ions, whose CCS and $1/K_0$ were determined based on the external PAHs calibration, were eventually selected. The resulting internal calibration strategy provides a fast, cost-free, and real-time calibration solution that also enables post-acquisition correction and extends to mass calibration, making them well suited for the analysis of halogenated POPs.

However, the accuracy of the developed calibration strategy was not evaluated. Although the CCS values obtained using this procedure were found to be highly reproducible over time, a quantitative assessment of reproducibility was also not performed. To evaluate the accuracy of the method, one possible approach would be to compare the collision cross sections of ions measured on the developed system with those obtained from a reference DTIMS instrument. Any discrepancies between the two sets of values could be explained by the empirical nature of the calibration procedure[9], as the $^{TIMS}CCS_{N2}$ PAHs values used in the external calibration procedure may have been acquired under different experimental conditions (e.g., temperature, E/N regime) than those present in the reference DTIMS system[10]. Additionally, the CCS values of the siloxane ions were derived from a secondary calibration, which may introduce further bias. One way to improve this would be to directly measure the CCS of these siloxane ions on a reference DTIMS instrument. Regarding the assessment of reproducibility, the most robust approach would be to conduct an interlaboratory trial[11].

Second, the influence of multiple instrumental parameters on the performance of the TIMS analyzer in terms of resolving power, ion transmission, and fragmentation was systematically evaluated (Section 4.2.1). Among these, accumulation time emerged as a particularly sensitive parameter, requiring a careful balance between maximizing sensitivity and minimizing space charge effects (Section 4.2.1A). For most POP-related applications, accumulation times between 50 and 100 ms provided an optimal compromise, as longer times led to saturation (due to the presence of background siloxane ions) and signal suppression. However, in trace-level analyses, longer accumulation times, approaching the GC analysis time, remained advantageous for improving signal quality, despite the associated reduction in resolving power. It is expected that the enhanced ion storage capacity of next-generation TIMS cells will mitigate these limitations by enabling the trapping of a larger number of ions (e.g., Mobility Range Enhancement (MoRE) acquisition mode on the novel dual-stage TIMS-MX cell[12]).

Ion confinement via the Funnel 1 RF voltage was found to have a mass-dependent impact on resolving power (Section 4.2.1B). Intermediate RF settings (150–250 V_{pp}) offered the best performance, ensuring efficient transmission across a wide m/z range while minimizing peak broadening from axial spreading and preventing peak tailing due to insufficient confinement of high-mass ions.

Finally, DC voltages applied within the TIMS cell and downstream ion optics (quadrupole and collision cell) had a strong influence on ion transmission and fragmentation (Sections 4.2.1C and 4.2.1D). Careful tuning of these voltages was critical for maintaining efficient ion transport while limiting the extent of fragmentation. In particular, increasing the ‘collision cell in’ voltage markedly improved resolving power and reduced fragmentation by accelerating ion transit and enhancing extraction efficiency in the collision cell (Section 4.2.1E).

Third, through systematic investigation of key experimental parameters including buffer gas velocity, ion accumulation and scan rate, we demonstrated how the TIMS resolving power could be significantly enhanced (Section 4.2.2). Notably, we showed that for small molecules like POPs, the entrance pressure of the TIMS cell which regulates the buffer gas velocity could be set a value higher than that recommended by the manufacturer, resulting in an increased resolving power while not affecting other performances (Section 4.2.2A). Next, we also found that the resolving power was strongly influenced by the quantity of compound analyzed, and would drastically drop with increasing quantities, even at lower accumulation times (Section 4.2.2B). Finally, we introduced and validated the sliding windows in ion mobility (SWIM) strategy[13] (Section 4.2.2C). This method leverages the predictable correlation between retention time and collisional cross section among halogenated POPs to narrow the ion mobility range scanned in each retention time segment, thereby substantially improving resolving power. The concept enabled a ~40% increase in resolving power relative to standard TIMS operation, all while maintaining accurate CCS measurements and consistent signal intensity.

While the SWIM method was successfully applied to multiple subclasses of GC-amenable halogenated POPs in this thesis (10 subclasses in total), it also holds promise for broader application. The approach is particularly suitable for compound classes that exhibit well-defined trends in CCS versus retention time. In addition to the POPs analyzed in this study, we observed similar trends for saturated and unsaturated fatty acid methyl esters (FAMEs; see Figure S4.11). Literature reports suggest that other classes, including PFAS[14], PBDE metabolites[15] and PAHs[16], also exhibit such behavior. Preliminary work is already underway in our group to adapt the SWIM strategy to the analysis of LC-amenable PFAS. However, when applied to pesticides, published CCS vs RT plots revealed weaker correlations[17,18], likely due to the greater structural diversity of this compound class compared to the more homologous POPs investigated in this work. Moving forward, the availability of predictive models for both CCS[19] and retention time[20] could be useful in assessing the feasibility of applying the SWIM methodology to additional compound classes across food, environmental and biological matrices.

Objective II: characterization of the ion mobilities and collision cross sections of halogenated POPs

The ion mobility and fragmentation behavior of a broad range of halogenated POPs were systematically characterized using the developed GC-APCI-TIMS-MS platform (Section 3.2.2). The study revealed consistent patterns in ionization mechanisms, with charge transfer always prevailing over proton transfer (Section 3.2.2A). These mechanisms were shown to significantly influence ion mobility behavior. Radical molecular ions typically produced simpler, single-peak mobility spectra, whereas protonated species often exhibited more complex signatures, likely reflecting the presence of multiple protomers or conformers and/or dynamic adduct equilibria. For more structurally complex compounds, such as dechloranes and most organochlorine pesticides (e.g., Drines, Chlordanes and Endosulfans), the ion mobility spectra of the radical molecular ions usually displayed multiple peaks. This observation may also indicate the presence of several stable gas-phase conformers. The fact that some ions are characterized by multiple or a distribution of peaks raises important questions about the appropriate representation of such species in CCS reference libraries (see Table A2 in Appendix E).

Fragmentation patterns further distinguished compound classes (Section 3.2.2B). Simpler structures, such as dioxins and PCBs, yielded only a few fragment ions, whereas more complex compounds produced intricate ion mobility spectra with numerous fragments. Notably, the alignment of post-TIMS fragment ions with their corresponding precursor ions underscored the utility of ion mobility in elucidating simple fragmentation pathways. Collectively, the ion mobility spectra of (quasi)molecular precursor ions and their associated fragments may offer an additional layer of structural evidence to support compound identification in non-targeted environmental analyses (as demonstrated in Section 6.2.2).

Finally, the CCS values of halogenated POPs were examined and compared across multiple structural levels (Section 3.2.2C). At the halogen type level, we observed a clear segregation in the m/z vs. CCS space between non-halogenated, chlorinated, and brominated compounds, which could be rationalized by differences in their 'molecular densities'. At the contaminant class level, specific trends in the m/z vs CCS space were identified for each class of contaminants. Furthermore, it was found that for a given halogenation degree and type, halogenated dibenzo-p-dioxins and diphenyl ethers exhibited higher CCS values than their dibenzofuran and biphenyl counterparts, while halogenated naphthalenes displayed the lowest CCS values. At the congener level, halogenation degree was confirmed as the dominant factor influencing CCS. However, the high resolution of the TIMS technology also revealed subtle CCS differences among isomeric congeners. For some compound classes, these variations followed recognizable patterns - for instance, ortho substitution effects in halogenated biphenyls or substitution symmetry in halogenated dioxins and furans. Additional insights into the structural basis of these patterns could be gained through molecular modeling and conformational analysis[21,22].

In the future, continued ion mobility characterization of additional classes of halogenated POPs will contribute to the development of more comprehensive and structurally informative CCS libraries, ultimately enhancing the capabilities of both targeted and non-targeted screening workflows for these environmental contaminants (including the prediction accuracies of machine learning CCS prediction tools).

Objective III: evaluation of the analytical benefits of using a high-resolution IM technology, TIMS, for both the targeted and untargeted analysis of halogenated contaminants

A central focus of this thesis was the evaluation of the high-resolution ion mobility method developed to address GC coeluting isobaric and isomeric species, which remain a significant challenge in the identification and quantification of pollutants in complex matrices using chromatographic–mass spectrometric techniques. Overall, the results demonstrated that ion mobility is a powerful tool for discriminating coeluting isobars, even at moderate resolving powers around 100 (Section 5.2.2B). The method also showed promise in partially resolving isomeric fragment interferences. However, it was found that most coeluting isomeric POPs could not be separated, even when the instrument was operated in (ultra)high-resolution mode (~200), due to their minimal CCS differences, typically well below 1%. While emerging cyclic and SLIM TWIMS platforms have demonstrated exceptionally high resolving powers[23,24] (>500) which could potentially resolve some of these coelutions, their effective implementation in front-end chromatographic hyphenation applications has yet to be established[25,26].

Additionally, in the non-targeted analysis of halogenated compounds in the blubber of a stranded killer whale, the clear separation of halogenated from non-halogenated compounds in the m/z vs $1/K_0$ space enabled the development of a selective prioritization strategy to extract halogenated features, as well as an effective exclusion of background and non-halogenated signals during precursor ion selection using the advanced DDA-PASEF tandem MS mode (Section 6.2.1). While the prioritization approach was highly effective in capturing relevant halogenated signals (including in-source fragments) the visual, manual data curation process was notably labor-intensive and would greatly benefit from automation. One potential improvement could involve implementing a post-peak-picking filtering strategy, similar to the one introduced by MacNeil et al[26].

In terms of compound identification, CCS values proved highly beneficial for both targeted and non-targeted approaches. In the quantitative analysis of dioxins and PCBs in fat and oil samples, the small difference in CCS (<0.5%) between the native analytes and their corresponding ^{13}C-labeled internal standards strongly supported the use of CCS as an additional confirmation criterion, either in conjunction with or as an alternative to retention time differences (ΔRT) and isotopic ratios (Section 5.2.2A). In the non-targeted analysis of the killer whale sample, the comparison of experimental CCS values of tentative PBDE and PBB features with their corresponding reference CCS vs m/z trendlines provided further confidence in their classification (Section 6.2.2).

The performance of machine learning-based CCS prediction tools as a means to enhance structural elucidation were also evaluated (Section 6.2.3). Among the four models tested, CCSP 2.0 showed superior performance, likely due to its training on halogenated compounds. This outcome highlighted a critical limitation of ML models: prediction accuracy is highly dependent on the relevance of the training data to the chemical class of interest.

As such, CCSP 2.0 was used to predict CCS values for level 3 candidate structures. These predicted CCS values provided additional confidence in the tentative identification of several features, especially for the halogenated natural products that were lacking reference data in CCS libraries. In one case, predictions were discriminative enough to support a specific structural assignment over another. However, in others, predicted CCS values were consistent for multiple isomeric candidates and could not rule out alternative structures.

Additionally, missing CCS values for congeners of the HpBDE, HpBB, HxBDE, and HxBB classes were predicted and used to extend their expected CCS ranges. These extended ranges further supported previous annotations and confirmed the presence of one outlier among the HxBDE features, which may belong to a different compound class.

Finally, beyond CCS values, additional information derived from ion mobility spectra was shown to add value in the structural elucidation process (Section 6.2.2). This included the shape and number of peaks, as well as the relative positions and alignment of IM peaks for both precursor ions (radical and protonated) and their corresponding fragment ions. Taken together, these ion mobility spectra can serve as a kind of “fingerprint” specific to a given compound or compound class.

Objective IV: assessment of the platform’s performance for quantifying trace levels of halogenated pollutants in complex matrices.

The quantitative capabilities of the developed GC-APCI trapped ion mobility TOF platform were evaluated for the determination of ultra-trace levels of polychlorinated dibenzo-p-dioxins and polychlorinated biphenyls in three fat-based proficiency test samples (fish oil, palm oil, and milk fat), in accordance with the criteria set by Commission Regulation (EU) 2017/644[27] (Section 5.2.1).

Linearity was confirmed across broad dynamic ranges, and both instrumental and method limits of quantification reached low levels consistent with concentrations typically found for these contaminants (Section 5.2.1A). Intermediate precision (RSD_R) remained within regulatory thresholds in 97% of cases. Additionally, 80% of PCDD/F and over 87% of PCB measurements met trueness requirements, with summed WHO_{2005}-TEQ and NDL-PCB concentrations closely aligning with the reference proficiency test values (Section 5.2.1B).

Overall, while the method showed slightly reduced performance for ultra-trace dioxins compared to the reference GC-HRMS sector instrument, it delivered accurate quantification and enhanced selectivity. These results highlight the strong potential of TIMS-TOF technology for quantitative contaminant analysis in food safety applications. This supports and encourages the development of quantitative analyses for other types of contaminants/matrices, as well as for alternative IM-MS platforms.

Conclusion

This thesis has demonstrated the strong potential of a GC-APCI-TIMS-MS platform for the advanced analysis of halogenated persistent organic pollutants. From developing a robust calibration strategy and optimizing key instrumental parameters to introducing the SWIM approach and characterizing ion mobility behavior across multiple POP classes, the work has expanded both the technical capabilities and applications of IM-MS. The added selectivity and confidence in identification, coupled with regulatory-compliant quantification in complex food matrices, underline the platform’s value for both targeted and non-targeted applications. These findings not only validate GC-IM-MS as a powerful tool for halogenated contaminant analysis but also encourage its broader adoption across diverse analyte classes and IM-MS technologies. This is further reinforced by recent developments of GC-IM-MS platforms for environmental screening[16,26,28–30]. Altogether, such powerful multidimensional analytical platforms will offer a promising solution to the enduring challenge of detecting pollutants in complex samples.

References

(1) Jones, K. C.; De Voogt, P. Persistent Organic Pollutants (POPs): State of the Science. *Environ. Pollut.* **1999**, *100* (1–3), 209–221. https://doi.org/10.1016/S0269-7491(99)00098-6.

(2) Jones, K. C. Persistent Organic Pollutants (POPs) and Related Chemicals in the Global Environment: Some Personal Reflections. *Environ. Sci. Technol.* **2021**, *55* (14), 9400–9412. https://doi.org/10.1021/acs.est.0c08093.

(3) Ayala-Cabrera, J. F.; Santos, F. J.; Moyano, E. Recent Advances in Analytical Methodologies Based on Mass Spectrometry for the Environmental Analysis of Halogenated Organic Contaminants. *Trends Environ. Anal. Chem.* **2021**, *30*, e00122. https://doi.org/10.1016/j.teac.2021.e00122.

(4) Li, D.-X.; Gan, L.; Bronja, A.; Schmitz, O. J. Gas Chromatography Coupled to Atmospheric Pressure Ionization Mass Spectrometry (GC-API-MS): Review. *Anal. Chim. Acta* **2015**, *891*, 43–61. https://doi.org/10.1016/j.aca.2015.08.002.

(5) *Mass Spectrometry in Food and Environmental Chemistry*; Picó, Y., Campo, J., Eds.; The Handbook of Environmental Chemistry; Springer International Publishing: Cham, 2023; Vol. 119. https://doi.org/10.1007/978-3-031-19093-3.

(6) Gabelica, V. CHAPTER 1. Ion Mobility–Mass Spectrometry: An Overview. In *New Developments in Mass Spectrometry*; Ashcroft, A. E., Sobott, F., Eds.; Royal Society of Chemistry: Cambridge, 2021; pp 1–25. https://doi.org/10.1039/9781839162886-00001.

(7) Song, X.-C.; Canellas, E.; Dreolin, N.; Goshawk, J.; Lv, M.; Qu, G.; Nerin, C.; Jiang, G. Application of Ion Mobility Spectrometry and the Derived Collision Cross Section in the Analysis of Environmental Organic Micropollutants. *Environ. Sci. Technol.* **2023**, *57* (51), 21485–21502. https://doi.org/10.1021/acs.est.3c03686.

(8) Celma, A.; Alygizakis, N.; Belova, L.; Bijlsma, L.; Fabregat-Safont, D.; Menger, F.; Gil-Solsona, R. Ion Mobility Separation Coupled to High-Resolution Mass Spectrometry in Environmental Analysis – Current State and Future Potential. *Trends Environ. Anal. Chem.* **2024**, *43*, e00239. https://doi.org/10.1016/j.teac.2024.e00239.

(9) Gabelica, V.; Shvartsburg, A. A.; Afonso, C.; Barran, P.; Benesch, J. L. P.; Bleiholder, C.; Bowers, M. T.; Bilbao, A.; Bush, M. F.; Campbell, J. L.; Campuzano, I. D. G.; Causon, T.; Clowers, B. H.; Creaser, C. S.; De Pauw, E.; Far, J.; Fernandez-Lima, F.; Fjeldsted, J. C.; Giles, K.; Groessl, M.; Hogan, C. J.; Hann, S.; Kim, H. I.; Kurulugama, R. T.; May, J. C.; McLean, J. A.; Pagel, K.; Richardson, K.; Ridgeway, M. E.; Rosu, F.; Sobott, F.; Thalassinos, K.; Valentine, S. J.; Wyttenbach, T. Recommendations for Reporting Ion Mobility Mass Spectrometry Measurements. *Mass Spectrom. Rev.* **2019**, *38* (3), 291–320. https://doi.org/10.1002/mas.21585.

(10) Zheng, X.; Dupuis, K. T.; Aly, N. A.; Zhou, Y.; Smith, F. B.; Tang, K.; Smith, R. D.; Baker, E. S. Utilizing Ion Mobility Spectrometry and Mass Spectrometry for the Analysis of Polycyclic Aromatic Hydrocarbons, Polychlorinated Biphenyls, Polybrominated Diphenyl Ethers and Their Metabolites. *Anal. Chim. Acta* **2018**, *1037*, 265–273. https://doi.org/10.1016/j.aca.2018.02.054.

(11) Stow, S. M.; Causon, T. J.; Zheng, X.; Kurulugama, R. T.; Mairinger, T.; May, J. C.; Rennie, E. E.; Baker, E. S.; Smith, R. D.; McLean, J. A.; Hann, S.; Fjeldsted, J. C. An Interlaboratory Evaluation of Drift Tube Ion Mobility–Mass Spectrometry Collision Cross Section Measurements. *Anal. Chem.* **2017**, *89* (17), 9048–9055. https://doi.org/10.1021/acs.analchem.7b01729.

(12) *timsMetabo*. Bruker. https://www.bruker.com/en/products-and-solutions/mass-spectrometry/timstof/timsmetabo.html (accessed 2025-07-01).

(13) Muller, H. B.; Scholl, G.; Far, J.; De Pauw, E.; Eppe, G. Sliding Windows in Ion Mobility (SWIM): A New Approach to Increase the Resolving Power in Trapped Ion Mobility-Mass Spectrometry Hyphenated with Chromatography. *Anal. Chem.* **2023**, *95* (48), 17586–17594. https://doi.org/10.1021/acs.analchem.3c03039.

(14) Dodds, J. N.; Hopkins, Z. R.; Knappe, D. R. U.; Baker, E. S. Rapid Characterization of Per- and Polyfluoroalkyl Substances (PFAS) by Ion Mobility Spectrometry–Mass Spectrometry (IMS-MS). *Anal. Chem.* **2020**, *92* (6), 4427–4435. https://doi.org/10.1021/acs.analchem.9b05364.

(15) Ma, Q.; Wang, C.; Bai, H.; Xi, H.-W.; Xi, G.-C.; Ren, X.-M.; Yang, Y.; Guo, L.-H. Comprehensive Two-Dimensional Separation of Hydroxylated Polybrominated Diphenyl Ethers by Ultra-Performance Liquid Chromatography Coupled with Ion Mobility-Mass Spectrometry. *J. Am. Soc. Mass Spectrom.* **2011**, *22* (10), s13361-011-0200–0202. https://doi.org/10.1007/s13361-011-0200-2.

(16) Olanrewaju, C. A.; Ramirez, C. E.; Fernandez-Lima, F. Comprehensive Screening of Polycyclic Aromatic Hydrocarbons and Similar Compounds Using GC–APLI–TIMS–TOFMS/GC–EI–MS. *Anal. Chem.* **2021**, *93* (15), 6080–6087. https://doi.org/10.1021/acs.analchem.0c04525.

(17) Regueiro, J.; Negreira, N.; Berntssen, M. H. G. Ion-Mobility-Derived Collision Cross Section as an Additional Identification Point for Multiresidue Screening of Pesticides in Fish Feed. *Anal. Chem.* **2016**, *88* (22), 11169–11177. https://doi.org/10.1021/acs.analchem.6b03381.

(18) Goscinny, S.; Joly, L.; De Pauw, E.; Hanot, V.; Eppe, G. Travelling-Wave Ion Mobility Time-of-Flight Mass Spectrometry as an Alternative Strategy for Screening of Multi-Class Pesticides in Fruits and Vegetables. *J. Chromatogr. A* **2015**, *1405*, 85–93. https://doi.org/10.1016/j.chroma.2015.05.057.

(19) Kartowikromo, K. Y.; Olajide, O. E.; Hamid, A. M. Collision Cross Section Measurement and Prediction Methods in Omics. *J. Mass Spectrom.* **2023**, *58* (9), e4973. https://doi.org/10.1002/jms.4973.

(20) Hollender, J.; Schymanski, E. L.; Ahrens, L.; Alygizakis, N.; Béen, F.; Bijlsma, L.; Brunner, A. M.; Celma, A.; Fildier, A.; Fu, Q.; Gago-Ferrero, P.; Gil-Solsona, R.; Haglund, P.; Hansen, M.; Kaserzon, S.; Kruve, A.; Lamoree, M.; Margoum, C.; Meijer, J.; Merel, S.; Rauert, C.; Rostkowski, P.; Samanipour, S.; Schulze, B.; Schulze, T.; Singh, R. R.; Slobodnik, J.; Steininger-Mairinger, T.; Thomaidis, N. S.; Togola, A.; Vorkamp, K.; Vulliet, E.; Zhu, L.; Krauss, M. NORMAN Guidance on Suspect and Non-Target Screening in Environmental Monitoring. *Environ. Sci. Eur.* **2023**, *35* (1), 75. https://doi.org/10.1186/s12302-023-00779-4.

(21) Lalli, P. M.; Corilo, Y. E.; Fasciotti, M.; Riccio, M. F.; De Sa, G. F.; Daroda, R. J.; Souza, G. H. M. F.; McCullagh, M.; Bartberger, M. D.; Eberlin, M. N.; Campuzano, I. D. G. Baseline Resolution of Isomers by Traveling Wave Ion Mobility Mass Spectrometry: Investigating the Effects of Polarizable Drift Gases and Ionic Charge Distribution. *J. Mass Spectrom.* **2013**, *48* (9), 989–997. https://doi.org/10.1002/jms.3245.

(22) Schneiders, A. L.; Far, J.; Belova, L.; Fry, A.; Covaci, A.; Baker, E. S.; De Pauw, E.; Eppe, G. Structural Characterization of Dimeric Perfluoroalkyl Carboxylic Acid Using Experimental and Theoretical Ion Mobility Spectrometry Analyses. *J. Am. Soc. Mass Spectrom.* **2025**, *36* (4), 850–861. https://doi.org/10.1021/jasms.5c00007.

(23) Giles, K.; Ujma, J.; Wildgoose, J.; Pringle, S.; Richardson, K.; Langridge, D.; Green, M. A Cyclic Ion Mobility-Mass Spectrometry System. *Anal. Chem.* **2019**, *91* (13), 8564–8573. https://doi.org/10.1021/acs.analchem.9b01838.

(24) Garimella, S. V. B.; Nagy, G.; Ibrahim, Y. M.; Smith, R. D. Opening New Paths for Biological Applications of Ion Mobility - Mass Spectrometry Using Structures for Lossless Ion Manipulations. *TrAC Trends Anal. Chem.* **2019**, *116*, 300–307. https://doi.org/10.1016/j.trac.2019.04.021.

(25) May, J. C.; Leaptrot, K. L.; Rose, B. S.; Moser, K. L. W.; Deng, L.; Maxon, L.; DeBord, D.; McLean, J. A. Resolving Power and Collision Cross Section Measurement Accuracy of a Prototype High-Resolution Ion Mobility Platform Incorporating Structures for Lossless Ion Manipulation. *J. Am. Soc. Mass Spectrom.* **2021**, *32* (4), 1126–1137. https://doi.org/10.1021/jasms.1c00056.

(26) MacNeil, A.; Li, X.; Amiri, R.; Muir, D. C. G.; Simpson, A.; Simpson, M. J.; Dorman, F. L.; Jobst, K. J. Gas Chromatography-(Cyclic) Ion Mobility Mass Spectrometry: A Novel Platform for the Discovery of Unknown Per-/Polyfluoroalkyl Substances. *Anal. Chem.* **2022**, *94* (31), 11096–11103. https://doi.org/10.1021/acs.analchem.2c02325.

(27) COMMISSION REGULATION (EU) 2017/ 644 - of 5 April 2017 - Laying down Methods of Sampling and Analysis for the Control of Levels of Dioxins, Dioxin-like PCBs and Non-Dioxin-like PCBs in Certain Foodstuffs and Repealing Regulation (EU) No 589 / 2014. *J Eur Union L* **2017**, *92*, 9–34.

(28) Izquierdo-Sandoval, D.; Fabregat-Safont, D.; Lacalle-Bergeron, L.; Sancho, J. V.; Hernández, F.; Portoles, T. Benefits of Ion Mobility Separation in GC-APCI-HRMS Screening: From the Construction of a CCS Library to the Application to Real-World Samples. *Anal. Chem.* **2022**, *94* (25), 9040–9047. https://doi.org/10.1021/acs.analchem.2c01118.

(29) Singh, R. R.; Aminot, Y.; Héas-Moisan, K.; Preud'homme, H.; Munschy, C. Cracked and Shucked: GC-APCI-IMS-HRMS Facilitates Identification of Unknown Halogenated Organic Chemicals in French Marine Bivalves. *Environ. Int.* **2023**, *178*, 108094. https://doi.org/10.1016/j.envint.2023.108094.

(30) Shi, X.; Langberg, H. A.; Sobek, A.; Benskin, J. P. Exploiting Molecular Ions for Screening Hydrophobic Contaminants in Sediments Using Gas Chromatography-Atmospheric Pressure Chemical Ionization-Ion Mobility-Mass Spectrometry. *Environ. Sci. Technol.* **2025**, *59* (9), 4699–4708. https://doi.org/10.1021/acs.est.4c13059.

Curriculum Vitae

Personalia:

Name: Hugo Muller
Date of birth: 13th January 1996
Place of birth: Limassol, Cyprus

Education:

- 09/2021 – …

  PhD candidate in Chemistry

  University of Liège, Belgium

- 09/2019 – 06/2021

  Master in Chemistry

  University of Liège, Belgium

  Master thesis: "Investigating Dioxins and PCBs analysis by APGC-Trapped Ion Mobility-Mass Spectrometry"
  http://hdl.handle.net/2268.2/11747

- 09/2016 – 06/2019

  Bachelor in Chemistry

  University of Liège, Belgium

Publications in peer-reviewed journals:

Muller, H. B.; Scholl, G.; Eppe, G. «Gas Chromatography–Trapped Ion Mobility Mass Spectrometry: A Highly Specific and Ultra-Sensitive Platform for Quantifying Sub-ppt Levels of Dioxins and PCBs in Food» *Chemosphere* **2025**, 385, 144557
https://doi.org/10.1016/j.chemosphere.2025.144557
https://hdl.handle.net/2268/334310

Muller, H. B.; Scholl, G.; Far, J.; De Pauw, E.; Eppe, G. «Sliding Windows in Ion Mobility (SWIM): A New Approach to Increase the Resolving Power in Trapped Ion Mobility-Mass Spectrometry Hyphenated with Chromatography». *Anal. Chem.* **2023**, *95* (48), 17586–17594.
https://doi.org/10.1021/acs.analchem.3c03039
https://hdl.handle.net/2268/309886

Oral presentation at international conferences:

Muller, H. B.; Scholl, G.; Far, J.; De Pauw, E.; Eppe, G. «Sliding windows in ion mobility (SWIM): a new approach to increase the separation power in trapped ion mobility-mass spectrometry hyphenated with chromatography»
Presented at the 5th Joint NVMS/BSMS conference on Mass Spectrometry, Rolduc Abbey, Netherlands, 29 April 2024
https://hdl.handle.net/2268/321830

Muller, H. B.; Scholl, G.; Far, J.; De Pauw, E.; Eppe, G. «Sliding windows in ion mobility (SWIM): a new approach to increase the separation power in trapped ion mobility-mass spectrometry hyphenated with chromatography»
Presented at the 43rd International Symposium on Halogenated Persistent Organic Pollutants (Dioxin), Maastricht, Netherlands, 11 September 2023
https://hdl.handle.net/2268/311093

Muller, H. B.; Scholl, G.; Far, J.; De Pauw, E.; Eppe, G. «Assessing the performance of high resolution ion mobility-mass spectrometry for the separation of GC coeluting isomeric and isobaric halogenated persistent organic pollutants»
Presented at the 43rd International Symposium on Halogenated Persistent

Organic Pollutants (Dioxin), Maastricht, Netherlands, 11 September 2023
https://hdl.handle.net/2268/311092

Muller, H. B.; Scholl, G.; Far, J.; De Pauw, E.; Eppe, G. «Sliding windows in ion mobility (SWIM): a new approach to increase the separation power in trapped ion mobility-mass spectrometry hyphenated with chromatography»
Presented at the 32nd International Conference on Ion Mobility Spectrometry (ISIMS), Maastricht, Netherlands, 21 August 2023
https://hdl.handle.net/2268/311091

Muller, H. B.; Scholl, G.; Far, J.; De Pauw, E.; Eppe, G. «Separation of coeluting isomer and isobar compounds from complex halogenated pollutant mixtures by GC-APCI-TIMS-TOFMS»
Presented at the 24th International Mass Spectrometry Conference (IMSC), Maastricht, Netherlands, 1 September 2022
https://hdl.handle.net/2268/300727

Poster presentation at international conferences:

Muller, H. B.; Das, K.; Scholl, G.; Schymanski, E.; Eppe, G. «Suspect and non-targeted screening of halogenated contaminants in a stranded killer whale (Orcinus orca) using GC-HRMS hyphenated with TIMS»
Presented at the 35th Society of Environmental Toxicology and Chemistry Europe Annual Meeting (SETAC), Vienna, Austria, 5 May 2025
https://hdl.handle.net/2268/334345

Muller, H. B.; Das, K.; Scholl, G.; Schymanski, E.; Eppe, G. «Suspect and non-targeted screening of halogenated contaminants in a stranded killer whale (Orcinus orca) using GC-HRMS hyphenated with TIMS»
Presented at the 72nd Conference on Mass Spectrometry and Allied Topics (ASMS), Anaheim, USA, 3 June 2024
https://hdl.handle.net/2268/321092

Muller, H. B.; Das, K.; Scholl, G.; Schymanski, E.; Eppe, G. «Suspect and non-targeted screening of halogenated contaminants in a stranded killer whale (Orcinus orca) using GC-HRMS hyphenated with TIMS»
Presented at the 18th International Symposium on Hyphenated Techniques in Chromatography and Separation Technology (HTC), Leuven, Belgium, 30 May

2024
https://hdl.handle.net/2268/321831

Muller, H. B.; Scholl, G.; Far, J.; De Pauw, E.; Eppe, G. «Sliding windows in ion mobility (SWIM): a new approach to increase the separation power in trapped ion mobility-mass spectrometry hyphenated with chromatography»
Presented at the 2nd Advances in Separation Science Workshop, Gembloux, Belgium, 28 June 2023
https://hdl.handle.net/2268/310032

Muller, H. B.; Scholl, G.; Far, J.; De Pauw, E.; Eppe, G. «Separation of coeluting isomer and isobar compounds from complex halogenated POP mixtures by GC-TIMS-MS»
Presented at the 17th International Symposium on Hyphenated Techniques in Chromatography and Separation Technology (HTC), Gent, Belgium, 18 May 2022
https://hdl.handle.net/2268/300703

Appendices

Appendix A: GC-APCI-TIMS-TOF instrumentation and schematics

Figure A1 – Photograph of the GC-APCI-TIMS-TOF instrument setup taken in the laboratory. (1 = Bruker/Varian 456 GC gas chromatograph; 2 = Bruker Apollo GC-APCI II ion source; 3 = Bruker timsTOF pro 2 mass spectrometer)

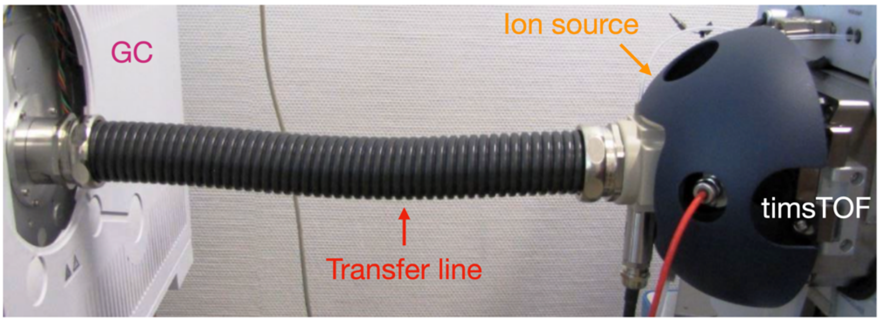

Figure A2 – Close-up photograph of the GC-APCI interface.

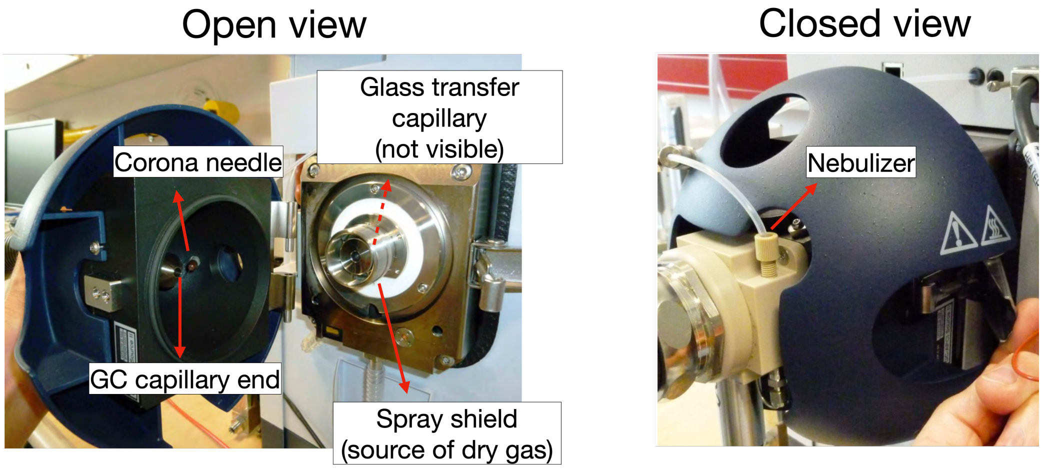

Figure A3 - Close-up photographs of the APCI ion source.

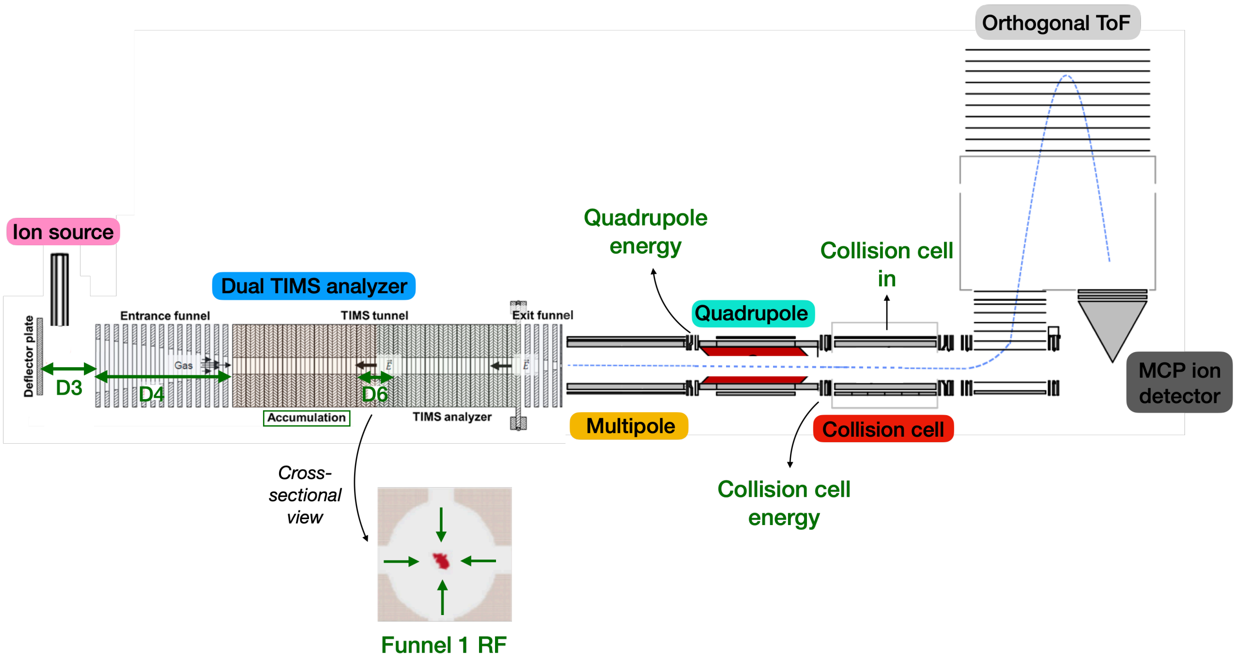

Figure A4 – Schematic of the interior of the timsTOF Pro 2 instrument. Parameters optimized in Chapter I, Part B are highlighted in dark green.

Appendix B: Calibration equation in TIMS

During a TIMS experiment, the total time, t_{tot}, from when an ion of mobility K is trapped to when it is detected by the TOF mass spectrometer, is given by[1]

$$t_{tot} = t_e + t_p + t_{tof} \tag{A1}$$

where:

- t_e is the elution time: the time required for the magnitude of the electric field on the plateau $E_{plateau}$ to reach the trapping electric field E_{trap} value characteristic of that ion during the elution phase (Section 1.3.3D). In other words, it is the time at which the ion will start to elute from the TIMS cell. It is given by:

$$t_e = \frac{E_0 - E_{trap}}{\beta} \tag{A2}$$

  where:
    - E_0 is the initial electric field strength on the plateau during the trapping phase (i.e., before the elution phase).
    - E_{trap} is the electric field magnitude at which the ion is trapped. It is given by equation 1.11
    - β is the scan rate (i.e., the rate at which the electric field on the plateau is linearly decreased in V/m.s during the elution phase)

  Substituting E_{trap} according to equation 1.11 yields:

$$t_e = \frac{E_0 - \frac{v_g}{K}}{\beta} \tag{A3}$$

- t_p is the plateau time: the time required for the ion to traverse the plateau during its elution from the TIMS cell. It is mobility dependent.
- t_{tof} is the time that spans between the moment the ion exits the plateau and the moment it is detected at the MCP detector. It is mass and mobility dependent.

The strength of the electric field on the plateau when an ion hits the detector after a time t_{tot} is therefore given by:

$$E_{detection} = E_0 - \beta t_{tot} \tag{A4}$$

In practice, what is measured is the potential difference across the electrodes of the plateau ΔV, not the electric field. Rewriting equation A4 in terms of voltage gives:

$$\frac{\Delta V_{detection}}{L_p} = \frac{\Delta V_0}{L_p} - \beta t_{tot}$$

$$\Leftrightarrow \Delta V_{detection} = \Delta V_0 - \beta_{\Delta V} t_{tot} \tag{A5}$$

where:

- L_p is the physical length of the plateau region

- $\beta_{\Delta V} = \beta L_p$ is the rate at which the voltage on the plateau is linearly decreased in V/s during the elution phase

Inserting equation A1 gives:

$$\Delta V_{detection} = \Delta V_0 - \beta_{\Delta V}\,(t_e + t_p + t_{tof}) \tag{A6}$$

At this stage, it is relevant to make two approximations[1]:

- t_p can be neglected in comparison to t_e
- t_{tof} can be considered constant for all ions

One then obtains:

$$\Delta V_{detection} \simeq \Delta V_0 - \beta_{\Delta V}\, t_{tof} - \beta_{\Delta V}\, t_e$$

Substituting for t_e:

$$\Delta V_{detection} \simeq \Delta V_0 - \beta_{\Delta V}\, t_{tof} - \beta_{\Delta V}\frac{E_0 - \frac{v_g}{K}}{\beta}$$

$$\Leftrightarrow \Delta V_{detection} \simeq \Delta V_0 - \beta_{\Delta V}\, t_{tof} - L_p(E_0 - \frac{v_g}{K})$$

$$\Leftrightarrow \Delta V_{detection} \simeq \Delta V_0 - \beta_{\Delta V}\, t_{tof} - \Delta V_0 + L_p\frac{v_g}{K}$$

$$\Leftrightarrow \Delta V_{detection} \simeq -\beta_{\Delta V}\, t_{tof} + L_p\frac{v_g}{K}$$

Replacing K by its reduced form $K_0 = K\frac{N}{N_0}$ yields the calibration equation:

$$\Leftrightarrow \Delta V_{detection} \simeq -\beta_{\Delta V}\, t_{tof} + L_p\frac{v_g}{K_0\frac{N_0}{N}}$$

$$\Leftrightarrow \Delta V_{detection} \simeq -\beta_{\Delta V}\, t_{tof} + \frac{L_p v_g N}{N_0}\frac{1}{K_0} \tag{A7}$$

$$\boxed{\Leftrightarrow \Delta V_{detection} \simeq a + b\frac{1}{K_0}} \tag{A8}$$

Appendix C: General principles of gas chromatography[2]

Figure A5 depicts the general appearance of a gas chromatograph and its main components. During a typical GC analysis, the sample containing the compounds to be separated is introduced into the gas chromatograph through the injector port. Separation of compounds then takes place in the heated chromatographic column, at the end of which a detector is located (e.g., MS, FID, ECD).

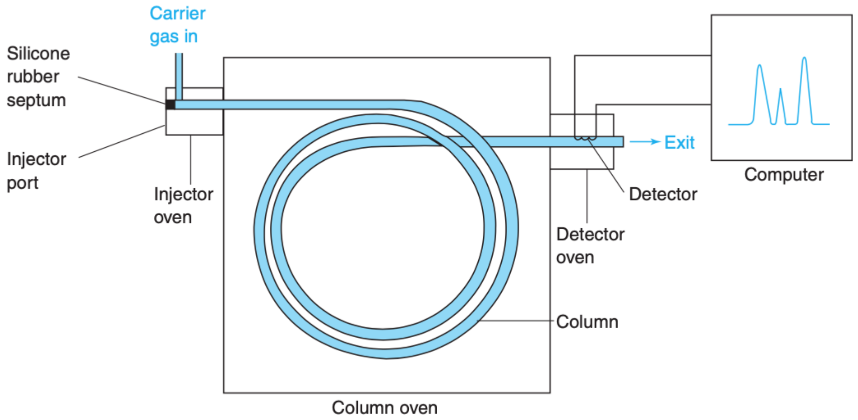

Figure A5 - Schematic representation of a gas chromatograph and its main components. Adapted from reference [2].

Sample injection

Sample introduction is usually carried out by injecting a small volume of diluted liquid or air sample through the septum of the injector port with a microsyringe. This step can be performed either manually or automatically using an autosampler.

Split and splitless injection are the two most common injection techniques (**Figure A6**). In both cases, a liner, which is a silanized glass tube inside the injector, is maintained at a high temperature relative to the boiling temperature of solvent and analytes in order to quickly evaporate them.

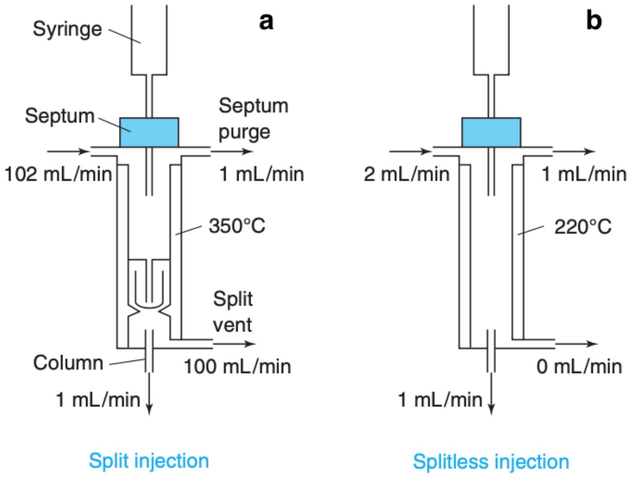

Figure A6 - Split (**A**) and splitless (**B**) injection. The septum purge flow prevents degradation products of the hot rubber septum from contaminating the liner. It also removes excess sample vapor. Adapted from reference [2].

In split injection (Figure A6A), a small fraction (~ 0.2 to 2%) of the vaporized sample is quickly swepted through the chromatographic column with a brisk flow of carrier gas. The proportion of sample that doesn't reach the column, called the split ratio, is defined by the operator by varying the flow of gas exiting the split vent during the injection. This mode of injection is particularly adapted to analyse concentrated and/or dirty samples.

In splitless injection (Figure A6B), the split vent is closed during the injection and most of the sample is eventually transferred to the column (~ 80%). It is therefore more convenient for trace analysis. Because the carrier gas flow is greatly reduced compared to split injection, the residence time of the sample in the liner is much longer. Consequently, to avoid peak broadening, the split vent is opened after a given time (e.g., 45 sec) to flush the remaining sample content out of the liner. Moreover, the initial column temperature is usually maintained at least 40°C below the boiling point of the solvent in order to recondense and focus the analytes at the beginning of the column. This plug of solvent traps the analytes in a narrow band and limits peak broadening.

Chromatographic separation

Chromatographic column

In chromatography, separation of analytes take place in a chromatographic column. In partition gas chromatography, this column is usually a long (15 to 100 m) glass capillary coated on the outside with a polyimide polymer*. Inside this capillary is a stationary phase which is a high molecular weight non volatile liquid bonded on the walls of the column (in the case of wall-coated open tubular columns, **Figure A7A**).

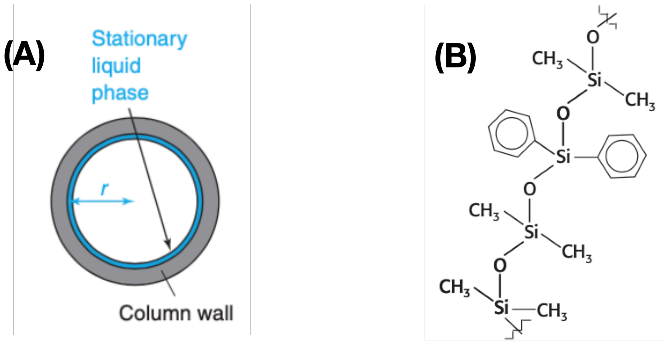

Figure A7 – (**A**) Cross section of a wall-coated open tubular column. (**B**) Representation of the chemical structure of a small part of a (Diphenyl)(dimethyl)-polysiloxane stationary phase. This type of non polar phase only interacts by simple van der Waal forces with the eluting compounds. Adapted from reference [2].

The chemical nature of the stationary phase is an important aspect of GC because it changes the affinity of the column for the analyte through non polar van der Waals forces, dipole-dipole interactions and/or even hydrogen bonding. The choice of the stationary phase will therefore depend on the physico-chemical properties of the analytes under study. Non polar compounds (petroleum products, pesticides, polychlorinated pollutants,…) are more adequately separated on non polar stationary phases whereas more polar molecules (amines, some flavors,…) usually require an intermediate or a strongly polar one. The chemical structure of a widely used non polar stationary phase is shown in Figure A7B.

---

* This heat resistant polymer provides mechanical support and protection from atmospheric moisture.

Basic principles of separation

For most types of chromatography, the procedure of separation relies on the relative time spent by analytes between the mobile phase and the stationary phase. The mobile phase in gas chromatography corresponds to the carrier gas (helium, nitrogen or hydrogen) that transports analytes through the column while the stationary phase is the immobilized high molecular weight non volatile liquid described above. The more time a compound is retained in the stationary phase, the later it will elute from the column (i.e., the greater its retention time t_R will be). In practice, this behaviour is quantified for a given compound by its retention factor k

$$k = \frac{t_{statio}}{t_{mobile}} \tag{A9}$$

where:
- t_{statio} is the time spent by a compound in the stationary phase
- t_{mobile} is the time spent by a compound in the mobile phase

Two important thermodynamic factors govern the retention of a given compound in GC (equation A9). The dominating factor is the enthalpy of vaporization ($\Delta H°_{vap}$) of the particular compound, which is closely related to the boiling point of the compound: the higher the boiling temperature, the higher the enthalpy of vaporization. As a consequence, volatile molecules, which have low boiling points, tend to be less retained than nonvolatile compounds and elute first. However, the second thermodynamic factor, the enthalpy of mixing ($\Delta H°_{mix}$), should also be taken into account. This factor is related to the interactions discussed previously between the stationary phase and the compounds passing along the column: the stronger the interactions between the two, the higher the enthalpy of mixing and the greater the retention.

$$\ln k = \frac{\Delta H_{vap}^{0}}{RT} + \frac{\Delta H_{mix}^{0}}{RT} + constant \tag{A10}$$

Temperature program

Most GC separations are performed using a temperature program, where the oven temperature is gradually increased during the analysis to improve the separation of compounds with different volatilities. Rather than maintaining a constant temperature (isothermal operation), the program begins at a lower temperature to separate volatile compounds, then increases the temperature at a controlled rate to elute heavier or less volatile components more efficiently. This approach enhances resolution, reduces analysis time, and prevents thermal degradation of sensitive analytes, making it ideal for complex mixtures with a wide range of boiling points.

Appendix D: General principles of GC-APCI[3,4]

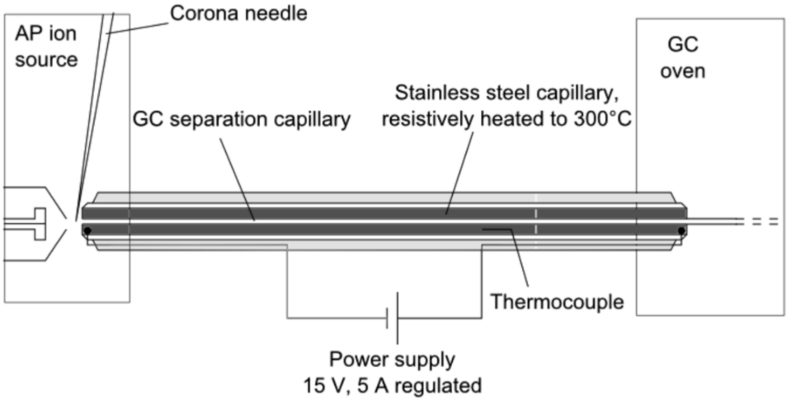

Figure A8 - Schematic representation of a GC-APCI source.

The typical design of a GC-APCI source is shown in **Figure A8**. The gas effluent from the transfer line capillary is introduced into the ionization chamber along with a flow of nitrogen from the nebulizer, which serves as the reagent gas. A plasma of $N^{2+\cdot}$ and $N^{4+\cdot}$ reagent ions is generated at the tip of a high-voltage corona needle positioned directly in front of the capillary. The formation of this nitrogen plasma occurs according to the following scheme:

$$N_2 + e^-_{corona} \rightarrow N_2^{+\cdot} + 2e^-$$

$$N_2^{+\cdot} + N_2 + N_{2\,(3rd\ body)} \rightarrow N_4^{+\cdot} + N_{2\,(3rd\ body)}$$

Ionization of analytes as they pass through the nitrogen plasma can occur through different mechanisms, depending on both the physicochemical properties of the target molecule and the source conditions. In positive mode, ion formation typically occurs via either proton transfer or charge transfer.

Proton transfer

Proton transfer involves the transfer of a proton (H^+) from a proton donor (PD) to the target analyte (M). This process is favored when the gas-phase proton affinity (PA)[†] of the analyte is higher than that of the proton donor.

$$M + [PD + H]^+ \rightarrow [M + H]^+ + PD$$

Proton donors are usually water clusters, although clusters of other protic solvents (such as methanol) can also fulfill this role. These protic solvents may originate from trace impurities in the ionization chamber (for example, water vapor) or can be intentionally introduced by various means (e.g., placing an open vial of solvent inside the ion source).

The sequence of reactions leading to solvent cluster formation in APCI is illustrated below, using water as an example. It begins with an electron transfer between $N^{4+\cdot}$ and a water molecule:

[†] The gas phase proton affinity (PA) is the negative enthalpy change of the transfer of a proton to a molecule M in the gas phase: $M + H^+ \rightarrow [M + H]^+$ PA (M) = $-\Delta H^0_r$

$$N_4^{+\cdot} + H_2O \rightarrow 2\ N_2 + \ H_2O^{+\cdot}$$

The resulting water radical cation then reacts with a neutral water molecule to form the hydronium ion (H_3O^+):

$$H_2O^{+\cdot} + H_2O \rightarrow H_3O^+ + \ OH^{\cdot}$$

This ion subsequently clusters with additional neutral water molecules, forming water clusters of various sizes:

$$H_3O^+ + nH_2O \rightarrow [(H_2O)_n + H]^+$$

The relative abundances of these clusters depend on source conditions such as water concentration, temperature, and dwell time. Smaller water clusters are more acidic, making them more efficient proton donors for the proton transfer process.

Charge transfer

Charge transfer usually occurs with analytes of low polarity which are characterized by an ionization energy (IE) lower than the recombination energy (RE)[‡] of $N^{4+\cdot}$. In this case, electron transfer takes place directly from the nitrogen radical cation to the analyte, resulting in the formation of the molecular ion ($M^{+\cdot}$):

$$M + N_4^{+\cdot} \rightarrow M^{+\cdot} + 2N_2$$

[‡] The recombinaison energy (RE) of the radical cation $X^{+\cdot}$ corresponds to the negative of the enthalpy of its recombinaison with an electron: $X^{+\cdot} + \ e^- \ \rightarrow X$ RE (X) = $-\Delta H^0_r$

Appendix E: General principles of time-of-flight (TOF) mass spectrometry[3]

The basic principle of a time-of-flight (TOF) analyzer is relatively simple: ions are accelerated by a high-voltage pulse, imparting them the same kinetic energy. They then enter a field-free flight tube of fixed length. Because ions with lower mass-to-charge (m/z) ratios travel faster than heavier ones at equal kinetic energy, they reach the detector at the end of the tube earlier (i.e., their flight time is shorter). The direct relationship between flight time and m/z allows for accurate determination of an ion's m/z value. The mathematical relationship between an ion's flight time and its m/z ratio is shown below.

$$t_{flight} = \frac{L}{\sqrt{2e\Delta V}} \times \sqrt{\frac{m}{z}} \tag{A11}$$

where:

- L is the length of the flight tube (in meters)
- e is the electron charge ($1.60217663 \times 10^{-19}$ C)
- ΔV is the acceleration voltage (in Volts)
- m is the ion mass (in kg)
- z is the ion charge (in C)

Due to its inherently pulsed nature, the TOF analyzer is readily compatible with pulsed ionization sources such as MALDI. Nonetheless, TOF analyzers can also be combined with intrinsically non pulsed ionization techniques if there is a mean for periodically extracting the ions in a pulsed manner from the continuous ionic beam generated by these types of sources (e.g., API methods). The design of orthogonal acceleration (oa) TOF analyzers, mainly developed at the beginning of the 1990s, enables such a combination (**Figure A9**).

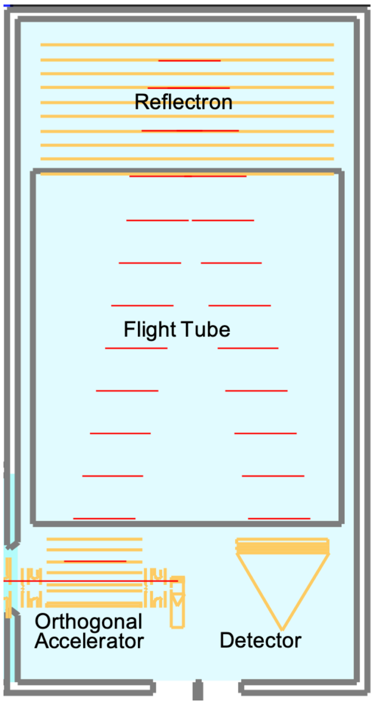

Figure A9 - Schematic representation of an orthogonal acceleration time-of-flight mass spectrometer.

oaTOF analyzers proceed via a two-step cycle :

- Filling phase: ions emitted continuously from the ion source are focused in a narrow, parallel beam by ion optics and ion guides and fill the first stage of the orthogonal accelerator known as the extraction volume. Because this space is initially field-free, ions just follow the initial direction of the ionic beam.
- Extraction phase: periodically, a pulse voltage is applied to a plate that is parallel to the ion beam, pushing a package of ions in a direction nearly orthogonal to their initial motion. These ions then reach the acceleration region where they will be further accelerated before entering the field-free region of the flight tube where TOF separation occurs.

While the TOF separation takes place, the extraction volume is refilled with the continuous ion beam. Once the higher m/z ratio ions have reached the detector, a new pulse voltage is applied to the orthogonal acceleration plate and the next package of ions is sent to the drift tube. Overall, this filling and extraction cycle can be repeated up to several thousands times per second (e.g., 10 kHz).

Modern oaTOF instruments are equipped with so-called reflectrons. These act as ion mirrors to refocus ions with the same m/z ratio but with slightly different kinetic energies, thereby greatly enhancing resolution. Moreover, a quadrupole mass analyzer and a collision cell are sometimes included in front of the TOF analyzer to perform tandem mass experiments (Q-TOF hybrid instruments). The main assets of modern oaTOF instruments are high sensitivity, spectral acquisition rate, resolving power (~30 000 - 100 000) and mass accuracies (a few ppm or less).

References

(1) Hernandez, D. R.; DeBord, J. D.; Ridgeway, M. E.; Kaplan, D. A.; Park, M. A.; Fernandez-Lima, F. Ion Dynamics in a Trapped Ion Mobility Spectrometer. *The Analyst* **2014**, *139* (8), 1913–1921. https://doi.org/10.1039/C3AN02174B.
(2) Harris, D. C.; Lucy, C. A. *Quantitative Chemical Analysis*, Ninth edition.; W.H. Freeman & Company: New York, 2016.
(3) Gross, J. H. *Mass Spectrometry*; Springer International Publishing: Cham, 2017. https://doi.org/10.1007/978-3-319-54398-7.
(4) Li, D.-X.; Gan, L.; Bronja, A.; Schmitz, O. J. Gas Chromatography Coupled to Atmospheric Pressure Ionization Mass Spectrometry (GC-API-MS): Review. *Anal. Chim. Acta* **2015**, *891*, 43–61. https://doi.org/10.1016/j.aca.2015.08.002.

Appendix F: CCS library

Table A1 – Experimental ${}^{TIMS}CCS_{N2}$ of halogenated POP compounds exhibiting low degrees of fragmentation.

Compound class	Compound name	InChiKey	Molecular ion	
			Ion type	${}^{TIMS}CCS_{N2}$ [Å^2]
PCBs	2-Chlorobiphenyl (PCB 1)	LAXBNTIAOJWAOP-UHFFFAOYSA-N	$[M]^{+\cdot}$	133.9
	4-Chlorobiphenyl (PCB 2)	FPWNLURCHDRMHC-UHFFFAOYSA-N	$[M]^{+\cdot}$	134.1
	2,2'-Dichlorobiphenyl (PCB 4)	JAYCNKDKIKZTAF-UHFFFAOYSA-N	$[M]^{+\cdot}$	140.3
	2,4'-Dichlorobiphenyl (PCB 8)	UFNIBRDIUNVOMX-UHFFFAOYSA-N	$[M]^{+\cdot}$	141.0
	2,6-Dichlorobiphenyl (PCB 10)	IYZWUWBAFUBNCH-UHFFFAOYSA-N	$[M]^{+\cdot}$	140.3
	4,4'-Dichlorobiphenyl (PCB 15)	YTBRNEUEFCNVHC-UHFFFAOYSA-N	$[M]^{+\cdot}$	141.8
	2,2',3-Trichlorobiphenyl (PCB 16)	XVIZMMSINIOIQP-UHFFFAOYSA-N	$[M]^{+\cdot}$	146.9
	2,2',5-Trichlorobipheny (PCB 18)	DCMURXAZTZQAFB-UHFFFAOYSA-N	$[M]^{+\cdot}$	147.6
	2,2',6-Trichlorobiphenyl (PCB 19)	MVXIJRBBCDLNLX-UHFFFAOYSA-N	$[M]^{+\cdot}$	145.3
	2,3,4'-Trichlorobiphenyl (PCB 22)	ZMHWQAHZKUPENF-UHFFFAOYSA-N	$[M]^{+\cdot}$	147.8
	2,4,4'-Trichlorobiphenyl (PCB 28)	BZTYNSQSZHARAZ-UHFFFAOYSA-N	$[M]^{+\cdot}$	149.0
	2,4',5-Trichlorobiphenyl (PCB 31)	VAHKBZSAUKPEOV-UHFFFAOYSA-N	$[M]^{+\cdot}$	149.0
	2,3',4'-Trichlorobiphenyl (PCB 33)	RIMXLXBUOQMDHV-UHFFFAOYSA-N	$[M]^{+\cdot}$	148.1
	3,4,4'-Trichlorobiphenyl (PCB 37)	YZANRISAORXTHU-UHFFFAOYSA-N	$[M]^{+\cdot}$	149.2
	2,2',3,3'-Tetrachlorobiphenyl (PCB 40)	VTLYHLREPCPDKX-UHFFFAOYSA-N	$[M]^{+\cdot}$	153.4
	2,2',3,4-Tetrachlorobiphenyl (PCB 41)	SEWHDNLIHDBVDZ-UHFFFAOYSA-N	$[M]^{+\cdot}$	152.9
	2,2',3,5'-Tetrachlorobiphenyl (PCB 44)	ALDJIKXAHSDLLB-UHFFFAOYSA-N	$[M]^{+\cdot}$	154.7
	2,2',4,5'-Tetrachlorobiphenyl (PCB 49)	ZWPVHELAQPIZHO-UHFFFAOYSA-N	$[M]^{+\cdot}$	155.0
	2,2',5,5'-Tetrachlorobiphenyl (PCB 52)	HCWZEPKLWVAEOV-UHFFFAOYSA-N	$[M]^{+\cdot}$	155.8
	2,2',6,6'-Tetrachlorobiphenyl (PCB 54)	PXAGFNRKXSYIHU-UHFFFAOYSA-N	$[M]^{+\cdot}$	150.6

2,3,4,4'-Tetrachlorobiphenyl (PCB 60)	XLDBTRJKXLKYTC-UHFFFAOYSA-N	$[M]^{+\cdot}$	153.8
2,3',4,4'-Tetrachlorobiphenyl (PCB 66)	RKLLTEAEZIJBAU-UHFFFAOYSA-N	$[M]^{+\cdot}$	155.2
2,3',4',5-Tetrachlorobiphenyl (PCB 70)	KENZYIHFBRWMOD-UHFFFAOYSA-N	$[M]^{+\cdot}$	156.1
2,4,4',5-Tetrachlorobiphenyl (PCB 74)	TULCXSBAPHCWCF-UHFFFAOYSA-N	$[M]^{+\cdot}$	155.2
3,3',4,4'-Tetrachlorobiphenyl (PCB 77)	UQMGJOKDKOLIDP-UHFFFAOYSA-N	$[M]^{+\cdot}$	156.4
3,4,4',5-Tetrachlorobiphenyl (PCB 81)	BHWVLZJTVIYLIV-UHFFFAOYSA-N	$[M]^{+\cdot}$	155.9
2,2',3,3',6-Pentachlorobiphenyl (PCB 84)	QVWUJLANSDKRAH-UHFFFAOYSA-N	$[M]^{+\cdot}$	158.5
2,2',3,4,4'-Pentachlorobiphenyl (PCB 85)	LACXVZHAJMVESG-UHFFFAOYSA-N	$[M]^{+\cdot}$	159.9
2,2',3,4,5'-Pentachlorobiphenyl (PCB 87)	OPKYDBFRKPQCBS-UHFFFAOYSA-N	$[M]^{+\cdot}$	160.6
2,2',3,4',5-Pentachlorobiphenyl (PCB 90)	SUOAMBOBSWRMNQ-UHFFFAOYSA-N	$[M]^{+\cdot}$	161.3
2,2',3,5',6-Pentachlorobiphenyl (PCB 95)	GXNNLIMMEXHBKV-UHFFFAOYSA-N	$[M]^{+\cdot}$	159.6
2,2',3,4',5'-Pentachlorobiphenyl (PCB 97)	JTUSORDQZVOEAZ-UHFFFAOYSA-N	$[M]^{+\cdot}$	160.4
2,2',4,5,5'-Pentachlorobiphenyl (PCB 101)	LAHWLEDBADHJGA-UHFFFAOYSA-N	$[M]^{+\cdot}$	161.3
2,2',4,6,6'-Pentachlorobiphenyl (PCB 104)	MTCPZNVSDFCBBE-UHFFFAOYSA-N	$[M]^{+\cdot}$	156.5
2,3,3',4,4'-Pentachlorobiphenyl (PCB 105)	WIDHRBRBACOVOY-UHFFFAOYSA-N	$[M]^{+\cdot}$	160.6
2,3,3',4',6-Pentachlorobiphenyl (PCB 110)	ARXHIJMGSIYYRZ-UHFFFAOYSA-N	$[M]^{+\cdot}$	160.6
2,3,4,4',5-Pentachlorobiphenyl (PCB 114)	SXZSFWHOSHAKMN-UHFFFAOYSA-N	$[M]^{+\cdot}$	160.2
2,3',4,4',5-Pentachlorobiphenyl (PCB 118)	IUTPYMGCWINGEY-UHFFFAOYSA-N	$[M]^{+\cdot}$	162.2
2,3',4,4',6-Pentachlorobiphenyl (PCB 119)	OAEQTHQGPZKTQP-UHFFFAOYSA-N	$[M]^{+\cdot}$	160.9
2,3',4,4',5'-Pentachlorobiphenyl (PCB 123)	YAHNWSSFXMVPOU-UHFFFAOYSA-N	$[M]^{+\cdot}$	161.6
3,3',4,4',5-Pentachlorobiphenyl (PCB 126)	REHONNLQRWTIFF-UHFFFAOYSA-N	$[M]^{+\cdot}$	162.9
2,2',3,3',4,4'-Hexachlorobiphenyl (PCB 128)	BTAGRXWGMYTPBY-UHFFFAOYSA-N	$[M]^{+\cdot}$	165.3
2,2',3,3',4,5-Hexachlorobiphenyl (PCB 129)	VQQKIXKPMJTUMP-UHFFFAOYSA-N	$[M]^{+\cdot}$	165.3
2,2',3,3',5,6'-Hexachlorobiphenyl (PCB 135)	UUTNFLRSJBQQJM-UHFFFAOYSA-N	$[M]^{+\cdot}$	165.4

2,2',3,4,4',5-Hexachlorobiphenyl (PCB 137)	CKLLRBPBZLTGDJ-UHFFFAOYSA-N	$[M]^{+\cdot}$	166.1
2,2',3,4,4',5'-Hexachlorobiphenyl (PCB 138)	RPUMZMSNLZHIGZ-UHFFFAOYSA-N	$[M]^{+\cdot}$	166.4
2,2',3,4,5,5'-Hexachlorobiphenyl (PCB 141)	UCLKLGIYGBLTSM-UHFFFAOYSA-N	$[M]^{+\cdot}$	166.9
2,2',3,4',5',6-Hexachlorobiphenyl (PCB 149)	LKHLFUVHHXCNJH-UHFFFAOYSA-N	$[M]^{+\cdot}$	165.4
2,2',3,5,5',6-Hexachlorobiphenyl (PCB 151)	UHCLFIWDCYOTOL-UHFFFAOYSA-N	$[M]^{+\cdot}$	166.0
2,2',4,4',5,5'-Hexachlorobiphenyl (PCB 153)	MVWHGTYKUMDIHL-UHFFFAOYSA-N	$[M]^{+\cdot}$	167.4
2,2',4,4',6,6'-Hexachlorobiphenyl (PCB 155)	ICOAEPDGFWLUTI-UHFFFAOYSA-N	$[M]^{+\cdot}$	163.9
2,3,3',4,4',5-Hexachlorobiphenyl (PCB 156)	LCXMEXLGMKFLQO-UHFFFAOYSA-N	$[M]^{+\cdot}$	167.2
2,3,3',4,4',5'-Hexachlorobiphenyl (PCB 157)	YTWXDQVNPCIEOX-UHFFFAOYSA-N	$[M]^{+\cdot}$	167.1
2,3,3',4,4',6-Hexachlorobiphenyl (PCB 158)	ZQUPQXINXTWCQR-UHFFFAOYSA-N	$[M]^{+\cdot}$	166.4
2,3',4,4',5,5'-Hexachlorobiphenyl (PCB 167)	AZXHAWRMEPZSSV-UHFFFAOYSA-N	$[M]^{+\cdot}$	168.5
2,3',4,4',5',6-Hexachlorobiphenyl (PCB 168)	PITHIPNORFGJPI-UHFFFAOYSA-N	$[M]^{+\cdot}$	167.4
3,3',4,4',5,5'-Hexachlorobiphenyl (PCB 169)	ZHLICBPIXDOFFG-UHFFFAOYSA-N	$[M]^{+\cdot}$	169.6
2,2',3,3',4,4',5-Heptachlorobiphenyl (PCB 170)	RMPWIIKNWPVWNG-UHFFFAOYSA-N	$[M]^{+\cdot}$	171.4
2,2',3,3',4,4',6-Heptachlorobiphenyl (PCB 171)	TZMHVHLTPWKZCI-UHFFFAOYSA-N	$[M]^{+\cdot}$	170.0
2,2',3,3',4,5,6'-Heptachlorobiphenyl (PCB 174)	ZDLMBNHYTPHDLF-UHFFFAOYSA-N	$[M]^{+\cdot}$	170.2
2,2',3,3',4,5',6'-Heptachlorobiphenyl (PCB 177)	CXOYNJAHPUASHN-UHFFFAOYSA-N	$[M]^{+\cdot}$	170.7
2,2',3,3',5,5',6-Heptachlorobiphenyl (PCB 178)	WCIBKXHMIXUQHK-UHFFFAOYSA-N	$[M]^{+\cdot}$	172.0
2,2',3,4,4',5,5'-Heptachlorobiphenyl (PCB 180)	WBHQEUPUMONIKF-UHFFFAOYSA-N	$[M]^{+\cdot}$	172.6
2,2',3,4,4',5',6-Heptachlorobiphenyl (PCB 183)	KQBFUDNJKCZEDQ-UHFFFAOYSA-N	$[M]^{+\cdot}$	171.4
2,2',3,4',5,5',6-Heptachlorobiphenyl (PCB 187)	UDMZPLROONOSEF-UHFFFAOYSA-N	$[M]^{+\cdot}$	171.9
2,2',3,4',5,6,6'-Heptachlorobiphenyl (PCB 188)	MMTJWDQKGUNSDK-UHFFFAOYSA-N	$[M]^{+\cdot}$	168.7
2,3,3',4,4',5,5'-Heptachlorobiphenyl (PCB 189)	XUAWBXBYHDRROL-UHFFFAOYSA-N	$[M]^{+\cdot}$	173.4
2,3,3',4,4',5',6-Heptachlorobiphenyl (PCB 191)	TVFXBXWAXIMLAQ-UHFFFAOYSA-N	$[M]^{+\cdot}$	172.4

	2,3,3',4',5,5',6-Heptachlorobiphenyl (PCB 193)	SSTJUBQGYXNFFP-UHFFFAOYSA-N	$[M]^{+\cdot}$	172.6
	2,2',3,3',4,4',5,5'-Octachlorobiphenyl (PCB 194)	DTMRKGRREZAYAP-UHFFFAOYSA-N	$[M]^{+\cdot}$	178.0
	2,2',3,3',4,5,5',6'-Octachlorobiphenyl (PCB 199)	HJBYDWKNARZTMJ-UHFFFAOYSA-N	$[M]^{+\cdot}$	177.1
	2,2',3,3',4,5',6,6'-Octachlorobiphenyl (PCB 201)	LJQOBQLZTUSEJA-UHFFFAOYSA-N	$[M]^{+\cdot}$	174.7
	2,2',3,3',5,5',6,6'-Octachlorobiphenyl (PCB 202)	JPOPEORRMSDUIP-UHFFFAOYSA-N	$[M]^{+\cdot}$	175.1
	2,2',3,4,4',5,5',6-Octachlorobiphenyl (PCB 203)	DCPDZFRGNJDWPP-UHFFFAOYSA-N	$[M]^{+\cdot}$	176.7
	2,3,3',4,4',5,5',6-Octachlorobiphenyl (PCB 205)	VXXBCDUYUQKWCK-UHFFFAOYSA-N	$[M]^{+\cdot}$	177.2
	2,2',3,3',4,4',5,5',6-Nonachlorobiphenyl (PCB 206)	JFIMDKGRGPNPRQ-UHFFFAOYSA-N	$[M]^{+\cdot}$	181.7
	2,2',3,3',4,4',5,6,6'-Nonachlorobiphenyl (PCB 207)	YGDPIDTZOQGPAX-UHFFFAOYSA-N	$[M]^{+\cdot}$	180.0
	2,2',3,3',4,5,5',6,6'-Nonachlorobiphenyl (PCB 208)	XIFFTDRFWYFAPO-UHFFFAOYSA-N	$[M]^{+\cdot}$	180.0
	Decachlorobiphenyl (PCB 209)	ONXPZLFXDMAPRO-UHFFFAOYSA-N	$[M]^{+\cdot}$	185.1
PBBs	4-Bromobiphenyl (PBB 3)	PKJBWOWQJHHAHG-UHFFFAOYSA-N	$[M]^{+\cdot}$	136.7
	4,4'-Dibromobiphenyl (PBB 15)	HQJQYILBCQPYBI-UHFFFAOYSA-N	$[M]^{+\cdot}$	147.8
	2,2',5-Tribromobiphenyl (PBB 18)	IYDNWMCMGNRWET-UHFFFAOYSA-N	$[M]^{+\cdot}$	153.5
	2,2',5,5'-Tetrabromobiphenyl (PBB 52)	XEFMFJLRXHQLEM-UHFFFAOYSA-N	$[M]^{+\cdot}$	164.9
	3,3',4,4'-Tetrabromobiphenyl (PBB 77)	BVGDXTYHVRFEQZ-UHFFFAOYSA-N	$[M]^{+\cdot}$	166.6
	2,2',4,5,5'-Pentabromobiphenyl (PBB 101)	OELBLPCWLAWABI-UHFFFAOYSA-N	$[M]^{+\cdot}$	172.6
	2,2',4,4',5,5'-Hexabromobiphenyl (PBB 153)	HMBBJSKXDBUNNT-UHFFFAOYSA-N	$[M]^{+\cdot}$	180.9
	3,3',4,4',5,5'-Hexabromobiphenyl (PBB 169)	UXOOFXUEODCAIP-UHFFFAOYSA-N	$[M]^{+\cdot}$	183.8
	2,2',3,4,4',5,5'-Heptabromobiphenyl (PBB 180)	RPGHQOFAFNAVNA-UHFFFAOYSA-N	$[M]^{+\cdot}$	186.6
	2,2',3,3',4,4',5,5'-Octabromobiphenyl (PBB 194)	HHYHNDNRLUQCEG-UHFFFAOYSA-N	$[M]^{+\cdot}$	193.0
	2,2',3,3',4,4',5,5',6-Nonabromobiphenyl (PBB 206)	QLERKXRXNDBTDM-UHFFFAOYSA-N	$[M]^{+\cdot}$	197.2
	Decabromobiphenyl (PBB 209)	AQPHBYQUCKHJLT-UHFFFAOYSA-N	$[M]^{+\cdot}$	199.7
PXBs	4'-Bromo-2,3',4,5-Tetrachlorobiphenyl	MHNVNUVYEUVATH-UHFFFAOYSA-N	$[M]^{+\cdot}$	164.6

	4'-Bromo-2,3,3',4-Tetrachlorobiphenyl	SCKNNMQTOYXCJZ-UHFFFAOYSA-N	$[M]^{+\cdot}$	163.2
	4'-Bromo-3,3',4,5-Tetrachlorobiphenyl	QFVZROUDMJHONX-UHFFFAOYSA-N	$[M]^{+\cdot}$	165.5
	4'-Bromo-2,3,3',4,5-Pentachlorobiphenyl	PGKMQVRBAIEXHL-UHFFFAOYSA-N	$[M]^{+\cdot}$	169.6
	3,4-Dibromo-3',4'-Dichlorobiphenyl	HXTSQAGEJGCAOR-UHFFFAOYSA-N	$[M]^{+\cdot}$	161.3
	3,4-Dibromo-3',4',5'-Trichlorobiphenyl	PXRDXCVCSPLAIQ-UHFFFAOYSA-N	$[M]^{+\cdot}$	167.9
	3,4-Dichloro-3',4',5'-Tribromobiphenyl	CVRUSNSUIRKGBY-UHFFFAOYSA-N	$[M]^{+\cdot}$	169.8
PCDDs	2,3,7,8-Tetrachlorodibenzo-p-dioxin	HGUFODBRKLSHSI-UHFFFAOYSA-N	$[M]^{+\cdot}$	159.3
	1,2,3,7,8-Pentachlorodibenzo-p-dioxin	FSPZPQQWDODWAU-UHFFFAOYSA-N	$[M]^{+\cdot}$	165.2
	1,2,3,4,7,8-Hexachlorodibenzo-p-dioxin	WCYYQNSQJHPVMG-UHFFFAOYSA-N	$[M]^{+\cdot}$	170.9
	1,2,3,6,7,8-Hexachlorodibenzo-p-dioxin	YCLUIPQDHHPDJJ-UHFFFAOYSA-N	$[M]^{+\cdot}$	170.7
	1,2,3,7,8,9-Hexachlorodibenzo-p-dioxin	LGIRBUBHIWTVCK-UHFFFAOYSA-N	$[M]^{+\cdot}$	169.0
	1,2,3,4,6,7,8-Heptachlorodibenzo-p-dioxin	WCLNVRQZUKYVAI-UHFFFAOYSA-N	$[M]^{+\cdot}$	174.9
	Octachlorodibenzo-p-dioxin	FOIBFBMSLDGNHL-UHFFFAOYSA-N	$[M]^{+\cdot}$	178.9
PBDDs	1-Bromodibenzo-p-dioxin	HEAUGIUDKRRLPJ-UHFFFAOYSA-N	$[M]^{+\cdot}$	141.4
	2,3,7-Tribromodibenzo-p-dioxin	BYNRLLTUMJGOGR-UHFFFAOYSA-N	$[M]^{+\cdot}$	161.0
	1,3,7,8-Tetrabromodibenzo-p-dioxin	DKKJDGGGXMTZKQ-UHFFFAOYSA-N	$[M]^{+\cdot}$	170.2
	1,2,3,4-Tetrabromodibenzo-p-dioxin	AKUPIABWVUYZPX-UHFFFAOYSA-N	$[M]^{+\cdot}$	165.2
	2,3,7,8-Tetrabromodibenzo-p-dioxin	JZLQUWSWOJPCAK-UHFFFAOYSA-N	$[M]^{+\cdot}$	169.4
	1,2,4,7,8-Pentabromodibenzo-p-dioxin	BUTCDYWYGPQTPC-UHFFFAOYSA-N	$[M]^{+\cdot}$	177.4
	1,2,3,7,8-Pentabromodibenzo-p-dioxin	ZIFMQFDZODRVTG-UHFFFAOYSA-N	$[M]^{+\cdot}$	176.7
	1,2,3,4,7,8-Hexabromodibenzo-p-dioxin	JGZILVYVJLWSIH-UHFFFAOYSA-N	$[M]^{+\cdot}$	183.9
	1,2,3,6,7,8-Hexabromodibenzo-p-dioxin	QHJJFBHAYBGEDA-UHFFFAOYSA-N	$[M]^{+\cdot}$	183.9
	1,2,3,7,8,9-Hexabromodibenzo-p-dioxin	BQLIEPWVZAEMQP-UHFFFAOYSA-N	$[M]^{+\cdot}$	181.5
	1,2,3,4,6,7,8-Heptabromodibenzo-p-dioxin	FPCROEVBHPWKPI-UHFFFAOYSA-N	$[M]^{+\cdot}$	188.7

	Octabromodibenzo-p-dioxin	XAHTWKGGNHXJRP-UHFFFAOYSA-N	$[M]^{+\cdot}$	192.9
PXDDs	7-Bromo-2,3-Dichlorodibenzo-p-dioxin	ROEOJLBNCCSIEG-UHFFFAOYSA-N	$[M]^{+\cdot}$	155.9
	2-Bromo-3,7,8-Trichlorodibenzo-p-dioxin	MEDUBLZGNFZMKG-UHFFFAOYSA-N	$[M]^{+\cdot}$	162.0
	2-Bromo-1,3,7,8-Tetrachlorodibenzo-p-dioxin	RMJLHLVWECBHAN-UHFFFAOYSA-N	$[M]^{+\cdot}$	167.4
	2,3-Dibromo-7,8-Dichlorodibenzo-p-dioxin	SBSJXPIUKNBZND-UHFFFAOYSA-N	$[M]^{+\cdot}$	164.4
PCDFs	2,3,7,8-Tetrachlorodibenzofuran	KSMVNVHUTQZITP-UHFFFAOYSA-N	$[M]^{+\cdot}$	155.1
	1,2,3,7,8-Pentachlorodibenzofuran	SBMIVUVRFPGOEB-UHFFFAOYSA-N	$[M]^{+\cdot}$	159.5
	1,2,3,4,7,8-Hexachlorodibenzofuran	LVYBAQIVPKCOEE-UHFFFAOYSA-N	$[M]^{+\cdot}$	165.3
	1,2,3,6,7,8-Hexachlorodibenzofuran	JEYJJJXOFWNEHN-UHFFFAOYSA-N	$[M]^{+\cdot}$	165.4
	2,3,4,6,7,8-Hexachlorodibenzofuran	XTAHLACQOVXINQ-UHFFFAOYSA-N	$[M]^{+\cdot}$	166.7
	1,2,3,7,8,9-Hexachlorodibenzofuran	PYUSJFJVDVSXIU-UHFFFAOYSA-N	$[M]^{+\cdot}$	163.5
	1,2,3,4,6,7,8-Heptachlorodibenzofuran	WDMKCPIVJOGHBF-UHFFFAOYSA-N	$[M]^{+\cdot}$	170.8
	1,2,3,4,7,8,9-Heptachlorodibenzofuran	VEZCTZWLJYWARH-UHFFFAOYSA-N	$[M]^{+\cdot}$	169.1
	Octachlorodibenzofuran	RHIROFAGUQOFLU-UHFFFAOYSA-N	$[M]^{+\cdot}$	174.7
PBDFs	4-Bromodibenzofuran	DYTYBRPMNQQFFL-UHFFFAOYSA-N	$[M]^{+\cdot}$	137.9
	2,4-Dibromodibenzofuran	ARIBSHNUKQULPI-UHFFFAOYSA-N	$[M]^{+\cdot}$	147.0
	2,8-Dibromodibenzofuran	UFCZRCPQBWIXTR-UHFFFAOYSA-N	$[M]^{+\cdot}$	148.4
	1,3,8-Tribromodibenzofuran	NMVVTHPIGSTTDO-UHFFFAOYSA-N	$[M]^{+\cdot}$	156.3
	2,4,7-Tribromodibenzofuran	RQIFVAZCCPQORH-UHFFFAOYSA-N	$[M]^{+\cdot}$	157.8
	2,3,4-Tribromodibenzofuran	PLNFQSTVRAQHRA-UHFFFAOYSA-N	$[M]^{+\cdot}$	153.5
	2,4,6,8-Tetrabromodibenzofuran	HPDRJVPURYBYRT-UHFFFAOYSA-N	$[M]^{+\cdot}$	166.7
	1,2,7,8-Tetrabromodibenzofuran	CUYJKQXKKDTMCW-UHFFFAOYSA-N	$[M]^{+\cdot}$	163.1
	2,3,7,8-Tetrabromodibenzofuran	HCSRVQXNLHZQNM-UHFFFAOYSA-N	$[M]^{+\cdot}$	165.4
	1,2,3,7,8-Pentabromodibenzofuran	QMKPILUKNSMQTD-UHFFFAOYSA-N	$[M]^{+\cdot}$	171.6

	2,3,4,7,8-Pentabromodibenzofuran	KHQDJFUIVSESDP-UHFFFAOYSA-N	$[M]^{+\cdot}$	173.6
	1,2,3,4,7,8-Hexabromodibenzofuran	MAHGKVWEQHQGJI-UHFFFAOYSA-N	$[M]^{+\cdot}$	179.5
	1,2,3,4,6,7,8-Heptabromodibenzofuran	JISOUFWSRUCDMJ-UHFFFAOYSA-N	$[M]^{+\cdot}$	185.2
PXDFs	8-Bromo-2,3-Dichlorodibenzofuran	OXZWQTYEIRTNRS-UHFFFAOYSA-N	$[M]^{+\cdot}$	151.9
	8-Bromo-2,3,4-Trichlorodibenzofuran	HSGAYFKTYSUSKW-UHFFFAOYSA-N	$[M]^{+\cdot}$	157.9
	4-Bromo-2,3,7,8-Tetrachlorodibenzofuran	JVQVVDNPQHZSNJ-UHFFFAOYSA-N	$[M]^{+\cdot}$	163.6
	1,2-Dibromo-7,8-Dichlorodibenzofuran	TUBWDYXLQQTKHJ-UHFFFAOYSA-N	$[M]^{+\cdot}$	158.0
	2,3-Dibromo-7,8-Dichlorodibenzofuran	OTROGRSRJQMCEI-UHFFFAOYSA-N	$[M]^{+\cdot}$	159.9
	1,3-Dibromo-2,7,8-Trichlorodibenzofuran	PPEKUOFMQYAHDM-UHFFFAOYSA-N	$[M]^{+\cdot}$	164.0
PBDES	4-Bromodiphenyl ether (PBDE 3)	JDUYPUMQALQRCN-UHFFFAOYSA-N	$[M]^{+\cdot}$	142.5
	2,4-Dibromodiphenyl ether (PBDE 7)	JMCIHKKTRDLVCO-UHFFFAOYSA-N	$[M]^{+\cdot}$	151.7
	4,4'-Dibromodiphenyl ether (PBDE 15)	YAWIAFUBXXPJMQ-UHFFFAOYSA-N	$[M]^{+\cdot}$	154.5
	2,2',4-Tribromodiphenyl ether (PBDE 17)	VYBFILXLBMWOLI-UHFFFAOYSA-N	$[M]^{+\cdot}$	157.9
	2,4,4'-Tribromodiphenyl ether (PBDE 28)	UPNBETHEXPIWQX-UHFFFAOYSA-N	$[M]^{+\cdot}$	162.3
	2,2',4,4'-Tetrabromodiphenyl ether (PBDE 47)	XYBSIYMGXVUVGY-UHFFFAOYSA-N	$[M]^{+\cdot}$	169.4
	2,2',4,5'-Tetrabromodiphenyl ether (PBDE 49)	QWVDUBDYUPHNHY-UHFFFAOYSA-N	$[M]^{+\cdot}$	169.4
	2,3',4,4'-Tetrabromodiphenyl ether (PBDE 66)	DHUMTYRHKMCVAG-UHFFFAOYSA-N	$[M]^{+\cdot}$	170.5
	3,3',4,6-Tetrabromodiphenyl ether (PBDE 71)	COPAGYRSCJVION-UHFFFAOYSA-N	$[M]^{+\cdot}$	166.4
	3,3',4,4'-Tetrabromodiphenyl ether (PBDE 77)	RYGLOWMCGZHYRQ-UHFFFAOYSA-N	$[M]^{+\cdot}$	171.5
	2,2',3,4,4'-Pentabromodiphenyl ether (PBDE 85)	DMLQSUZPTTUUDP-UHFFFAOYSA-N	$[M]^{+\cdot}$	176.1
	2,2',4,4',6-Pentabromodiphenyl ether (PBDE 100)	NSKIRYMHNFTRLR-UHFFFAOYSA-N	$[M]^{+\cdot}$	175.9
	2,3',4,4',6-Pentabromodiphenyl ether (PBDE 119)	KXEOYBYEJCRPGB-UHFFFAOYSA-N	$[M]^{+\cdot}$	176.9
	3,3',4,4',5-Pentabromodiphenyl ether (PBDE 126)	SJNIIWPIAVQNRK-UHFFFAOYSA-N	$[M]^{+\cdot}$	179.6
	2,2',3,4,4',5'-Hexabromodiphenyl ether (PBDE 138)	IZFQCEZFGCMHOM-UHFFFAOYSA-N	$[M]^{+\cdot}$	183.6

	2,2',4,4',5,5'-Hexabromodiphenyl ether (PBDE 153)	RZXIRSKYBISPGF-UHFFFAOYSA-N	$[M]^{+\cdot}$	185.0
	2,2',4,4',5,6'-Hexabromodiphenyl ether (PBDE 154)	VHNPZYZQKWIWOD-UHFFFAOYSA-N	$[M]^{+\cdot}$	182.8
	2,2',3,4,4',5',6-Hexabromodiphenyl ether (PBDE 183)	ILPSCQCLBHQUEM-UHFFFAOYSA-N	$[M]^{+\cdot}$	188.3
PCNs	1,3,5,7-Tetrachloronaphthalene (PCN 42)	OTTCXKPQKOLSJN-UHFFFAOYSA-N	$[M]^{+\cdot}$	145.0
	1,2,3,5-Tetrachloronaphthalene (PCN 28)	HJJKSUVYCQAMBG-UHFFFAOYSA-N	$[M]^{+\cdot}$	143.2
	1,2,3,4-Tetrachloronaphthalene (PCN 27)	NAQWICRLNQSPPW-UHFFFAOYSA-N	$[M]^{+\cdot}$	141.5
	2,3,6,7-Tetrachloronaphthalene (PCN 48)	XTTLUUBHRXWFSZ-UHFFFAOYSA-N	$[M]^{+\cdot}$	145.3
	1,4,5,8-Tetrachloronaphthalene (PCN 46)	LITCKAVLJAKHOE-UHFFFAOYSA-N	$[M]^{+\cdot}$	142.7
	1,2,3,8-Tetrachloronaphthalene (PCN 31)	UVMHXYSILPJXPK-UHFFFAOYSA-N	$[M]^{+\cdot}$	142.5
	1,2,4,6,7-Pentachloronaphthalene (PCN 60)	GXQUDLBNLKOIQB-UHFFFAOYSA-N	$[M]^{+\cdot}$	150.3
	1,2,3,4,6-Pentachloronaphthalene (PCN 50)	BAOLNVSMVTYGDA-UHFFFAOYSA-N	$[M]^{+\cdot}$	148.9
	1,2,3,5,8-Pentachloronaphthalene (PCN 53)	HVYRFNJXZVEGFK-UHFFFAOYSA-N	$[M]^{+\cdot}$	149.0
	1,2,4,5,8-Pentachloronaphthalene (PCN 59)	FEIKEVSWLMYFFF-UHFFFAOYSA-N	$[M]^{+\cdot}$	148.3
	1,2,3,4,5-Pentachloronaphthalene (PCN 49)	JRZKNHITLINYHV-UHFFFAOYSA-N	$[M]^{+\cdot}$	147.6
	1,2,3,4,6,7-Hexachloronaphthalene (PCN 66)	ZRNSVEOEIWQEMU-UHFFFAOYSA-N	$[M]^{+\cdot}$	155.4
	1,2,3,5,6,8-Hexachloronaphthalene (PCN 68)	FQELOCOACCYGLL-UHFFFAOYSA-N	$[M]^{+\cdot}$	154.5
	1,2,3,5,7,8-Hexachloronaphthalene (PCN 69)	JPQLLIUTUFJWMH-UHFFFAOYSA-N	$[M]^{+\cdot}$	154.5
	1,2,4,5,6,8-Hexachloronaphthalene (PCN 71)	JHKLUUFTHIWTKX-UHFFFAOYSA-N	$[M]^{+\cdot}$	153.7
	1,2,3,4,5,6-Hexachloronaphthalene (PCN 63)	CTLMCQOGOWNFHA-UHFFFAOYSA-N	$[M]^{+\cdot}$	153.4
	1,2,3,4,5,8-Hexachloronaphthalene (PCN 65)	PGCDNPCENWGYMA-UHFFFAOYSA-N	$[M]^{+\cdot}$	153.3
	1,2,3,6,7,8-Hexachloronaphthalene (PCN 70)	WJYZNPLWZGYFIE-UHFFFAOYSA-N	$[M]^{+\cdot}$	154.5
	1,2,3,4,5,6,8-Heptachloronaphthalene (PCN 74)	QYEGXUUXWMKHHS-UHFFFAOYSA-N	$[M]^{+\cdot}$	158.8
	Octachloronaphthalene (PCN 75)	RTNLUFLDZOAXIC-UHFFFAOYSA-N	$[M]^{+\cdot}$	164.0
eBFRs	2,3,5,6-tetrabromo-p-xylene (pTBX)	RXKOKVQKECXYOT-UHFFFAOYSA-N	$[M]^{+\cdot}$	145.3

	1,2,3,4,5-pentabromobenzene (PBBz)	LLVVSBBXENOOQY-UHFFFAOYSA-N	$[M]^{+\cdot}$	145.1
	Pentabromotoluene (PBT)	OZHJEQVYCBTHJT-UHFFFAOYSA-N	$[M]^{+\cdot}$	148.7
	Pentabromoethylbenzene (PBEB)	FIAXCDIQXHJNIX-UHFFFAOYSA-N	$[M]^{+\cdot}$	153.0
	Hexabromobenzene (HBBz)	CAYGQBVSOZLICD-UHFFFAOYSA-N	$[M]^{+\cdot}$	151.5
OCPs	Hexachlorobenzene (HCB)	CKAPSXZOOQJIBF-UHFFFAOYSA-N	$[M]^{+\cdot}$	139.8

Table A2 – Experimentally measured $^{TIMS}CCS_{N2}$ values of halogenated POPs exhibiting high degrees of fragmentation. When multiple fragments were observed, only the two most intense are reported. Underlined values indicate ions whose mobility spectra displayed multiple or distributed peaks (Section 3.2.2A); in such cases, the value corresponds to the most intense peak within the distribution.

Compound class	Compound name	InChiKey	Molecular ion		Fragment 1		Fragment 2	
			Ion type	$^{TIMS}CCS_{N2}$ [Å^2]	Ion type	$^{TIMS}CCS_{N2}$ [Å^2]	Ion type	$^{TIMS}CCS_{N2}$ [Å^2]
eBFRs	1,2-bis(2,4,6-tribromo-phenoxy)ethane (BTBPE)	YATIGPZCMOYEGE-UHFFFAOYSA-N	$[M]^{+\cdot}$	190.6	$[M-C_6H_2OBr_3]^+$	146.6		
	Dechlorane 603	WSEXCYJMFQVEIN-UHFFFAOYSA-N	$[M]^{+\cdot}$	210.6	$[C_7Cl_5H_2]^+$	139.6	$[M-Cl]^+$	205.3
	Syn dechlorane plus	UGQQAJOWXNCOPY-MXYLTYEXSA-N	$[M]^{+\cdot}$	220.6	$[C_5Cl_5]^+$	131.3	$[M-Cl]^+$	202.4
OCPs	p,p'-DDD	AHJKRLASYNVKDZ-UHFFFAOYSA-N	/	/	$[M-CCl_2H]^+$	148.3	$[M-Cl]^+$	156.9
	o,p'-DDD	JWBOIMRXGHLCPP-UHFFFAOYSA-N	/	/	$[M-CCl_2H]^+$	148.3	$[M-Cl]^+$	160.6
	o,p'-DDT	CVUGPAFCQJIYDT-UHFFFAOYSA-N	/	/	$[M-CCl_3]^+$	148.3	$[M-Cl]^+$	161.2
	p,p'-DDT	YVGGHNCTFXOJCH-UHFFFAOYSA-N	/	/	$[M-CCl_3]^+$	148.3	$[M-Cl]^+$	166.5
	o,p'-DDE	ZDYJWDIWLRZXDB-UHFFFAOYSA-N	$[M]^{+\cdot}$	161.6	$[M-Cl]^+$	153.5	$[M-2Cl]^+$	145.6
	p,p'-DDE	UCNVFOCBFJOQAL-UHFFFAOYSA-N	$[M]^{+\cdot}$	166.2	$[M-Cl]^+$	153.7	$[M-2Cl]^+$	145.5
	Perthan	QFMDFTQOJHFVNR-UHFFFAOYSA-N	/	/	$[M-CCl_2H]^+$	155.7	$[M-C_8H_9]^+$	138.2
	Aldrin	QBYJBZPUGVGKQQ-SJJAEHHWSA-N	$[M]^+$	169.4	$[M-Cl]^+$	164.6	$[M-Cl_2H]^+$	152.3
	Isodrin	QBYJBZPUGVGKQQ-DIFDVCDBSA-N	$[M]^{+\cdot}$	158.5	$[M-Cl]^+$	157.0	$[M-Cl_2H]^+$	153.3
	Dieldrin	DFBKLUNHFCTMDC-PICURKEMSA-N	$[M]^{+\cdot}$	166.3	$[M-Cl]^+$	160,4		
	Endrin	DFBKLUNHFCTMDC-GKRDHZSOSA-N	$[M]^{+\cdot}$	159.9	$[M-Cl]^+$	158.2		
	Heptachlor	FRCCEHPWNOQAEU-UHFFFAOYSA-N	$[M]^{+\cdot}$	159.7	$[M-Cl]^+$	165.2	$[C_5Cl_6]^+$	137.7
	Heptachlor epoxide exo	ZXFXBSWRVIQKOD-UOFFAGTMSA-N	$[M]^{+\cdot}$	162.4	$[M-Cl]^+$	160.3	$[M-COCl_2H_2]_+$	148.4
	Heptachlor epoxide endo	ZXFXBSWRVIQKOD-WOBUKFROSA-N	$[M]^{+\cdot}$	162.0	$[M-Cl]^+$	156.8	$[M-COCl_2H_2]_+$	148.3
	Endosulfan sulfate	AAPVQEMYVNZIOO-UHFFFAOYSA-N	$[M]^{+\cdot}$	162.0	$[M-Cl]^+$	167.8	$[M-HSO_4]^+$	151.0
	Hexachloro cyclohexanes (HCHs)	JLYXXMFPNIAWKQ-UHFFFAOYSA-N	/	/	$[M-Cl_2H]^+$	133.5		